

Cancer Cell

Volume 23
Number 2

February 11, 2013

www.cellpress.com



A Master MicroRNA Network for EMT in OvCa

Englerin A Stimulates PKC θ to Inhibit Insulin Signaling and to Simultaneously Activate HSF1: Pharmacologically Induced Synthetic Lethality

Carole Sourbier,¹ Bradley T. Scroggins,¹ Ranjala Ratnayake,³ Thomas L. Prince,¹ Sunmin Lee,² Min-Jung Lee,² Peter Literati Nagy,⁴ Young H. Lee,¹ Jane B. Trepel,² John A. Beutler,³ W. Marston Linehan,¹ and Len Neckers^{1,*}

¹Urologic Oncology Branch

²Medical Oncology Branch

Center for Cancer Research, National Cancer Institute, National Institutes of Health, Bethesda, MD 20892, USA

³Molecular Targets Laboratory, Center for Cancer Research, National Cancer Institute, Frederick, MD 21702, USA

⁴N-Gene Research Laboratories, Inc., 1137 Budapest, Hungary

*Correspondence: neckersl@mail.nih.gov

<http://dx.doi.org/10.1016/j.ccr.2012.12.007>

SUMMARY

The natural product englerin A (EA) binds to and activates protein kinase C- θ (PKC θ). EA-dependent activation of PKC θ induces an insulin-resistant phenotype, limiting the access of tumor cells to glucose. At the same time, EA causes PKC θ -mediated phosphorylation and activation of the transcription factor heat shock factor 1, an inducer of glucose dependence. By promoting glucose addiction, while simultaneously starving cells of glucose, EA proves to be synthetically lethal to highly glycolytic tumors.

INTRODUCTION

Many solid tumors are characterized by an altered metabolic program and display increased dependence on glucose. Several signaling pathways and transcription factors are critical for providing sustained intake of glucose by tumor cells and for enforcing their glycolytic dependence, including the insulin signaling pathway (Leto and Saltiel, 2012) and the heat shock transcription factor heat shock factor 1 (HSF1) (Dai et al., 2007). Whereas a lack of function of the insulin pathway or HSF1 has been linked to diabetes and aging, hyperinsulinemia and HSF1 activation have been linked to the development of cancer (Whitesell and Lindquist, 2009; Gallagher and LeRoith, 2011; Mendillo et al., 2012). Indeed, recent reports suggest that dependence on HSF1 reflects the “nononcogene addiction” of tumor cells for this transcription factor (Solimini et al., 2007).

Molecular mechanisms underlying HSF1-enforced glucose dependence are not well understood. However, effects of the insulin pathway on glucose uptake and utilization have been well characterized. Insulin and insulin-like growth factors activate the PI3K/AKT pathway to stimulate glucose uptake.

Numerous epithelial tumors rely on constitutive activation of this pathway to increase their supply of glucose (Vander Heiden et al., 2009; Leto and Saltiel, 2012). The protein kinase C (PKC) family of kinases exerts both positive and negative effects on this pathway (Nelson et al., 2008). In type II diabetes, activation of some PKCs, including PKC θ , with fatty acids or diacylglycerol can induce insulin resistance via inhibitory phosphorylation of insulin receptor substrate 1 (IRS1) (Griffin et al., 1999; Li et al., 2004). Phosphorylated IRS1 dissociates from the insulin receptor, leading to decreased signaling via PI3K/AKT and reduced glucose uptake (Li et al., 2004; Griffin et al., 1999).

PKC isozymes are divided into three groups: conventional PKCs (PKC α , PKC β I, PKC β II, and PKC γ), novel PKCs (PKC δ , PKC θ , PKC ϵ , and PKC η), and atypical PKCs (PKC ζ and PKC ι). Although PKC α , δ , and ϵ are broadly expressed, other isozymes have a more restricted expression. For example, PKC θ is mainly expressed in T lymphocytes and in some tumors (Marsland and Kopf, 2008; Griner and Kazanietz, 2007). Because of the lack of selectivity of available PKC modulators, the role played by each isozyme in tumorigenesis is not well understood (Griner and Kazanietz, 2007).

Significance

Many epithelial tumors display a glycolytic phenotype characterized by enhanced dependence on glucose. Targeting the abnormal metabolism of such tumors has been a long-term goal of the scientific community. The natural product EA selectively activates PKC θ to induce a metabolic catastrophe in glycolytic tumor cells by promoting insulin resistance and inhibiting glucose uptake, while simultaneously activating the heat shock transcription factor HSF1, thereby enforcing glucose dependence. These data identify EA as a mechanistically unique cytotoxic agent.

Table 1. EA Cytotoxicity Correlates with Glucose Sensitivity in a Panel of Cell Lines

Cell line	Origin of the tissue	EA (IC ₅₀)	2-DG (IC ₅₀)
786-0	Kidney cancer (VHL ^{-/-}) (Williams et al., 1978)	50 nM	60 μ M
786-0/VHL	VHL-restored cell line (Tong et al., 2011)	>10 μ M	>1 mM
UOK257	Kidney cancer (FLCN ^{-/-}) (Yang et al., 2008)	65 nM	285 μ M
UOK257WT	FLCN-restored cell line (Hong et al., 2010)	>10 μ M	721 μ M
UOK262	Kidney cancer metastasis (FH ^{-/-}) (Yang et al., 2010)	35 nM	222 μ M ^a
UOK262WT	FH-restored cell line (Tong et al., 2011)	>10 μ M	>1 mM ^a
HK2	Normal kidney (proximal tubule) (Ryan et al., 1994)	>10 μ M	>1 mM
HEK293	Embryonic epithelial kidney cell (Pear et al., 1993)	>10 μ M	>1 mM
PC3	Prostate cancer (Kaighn et al., 1979)	5 μ M	300 μ M
SKBr3	Breast cancer (Fogh and Trempe, 1975)	3 μ M	n/a

Cells (70% confluence) were treated with a range of EA concentrations (1 nM–10 μ M) in serum-free media. After 48 hr, viability was measured by MTT or manual cell counting. For UOK262 and UOK262WT, viability was only assessed by manual cell counting. Molecularly restored kidney cancer cell lines and normal kidney cell lines did not show significant sensitivity toward EA. Glucose dependence of the cells was similarly assessed by determining sensitivity to 2-deoxyglucose (2-DG, 10 nM–100 μ M). Cells were cultured in DMEM containing 1g/l glucose and were treated with 2-DG for 72 hr (786-0, 786-0/VHL, UOK257, UOK257WT, HK2, HEK293, PC3, and SKBr3), ^aexcept for UOK262 and UOK262WT, which were treated for 24 hr. Viability was assessed by MTT and/or manual cell counting as above. EA sensitivity displays a highly significant positive correlation with glucose dependence, as assessed by determining R² and the Pearson Correlation Coefficient (R² = 0.9126; Pearson Correlation Coefficient = 0.962; p = 0.000003). UOK262 data were not included when determining R² and the Pearson Correlation Coefficient because they were exposed to 2-DG for 24 hr and not 72 hr like the other cell lines.

The epoxyguaiane englerin A (EA) is a natural product that displays selective in vitro cytotoxicity toward kidney cancer cell lines in the NCI-60 cell line panel (Ratnayake et al., 2009). Because EA's cytotoxicity profile suggests a unique mechanism of action, we sought to identify EA's molecular target(s) in order to provide potentially novel therapeutic anticancer strategies.

RESULTS

EA Is Selectively Cytotoxic for a Panel of Genetically Defined Kidney Cancer Cell Lines

Using cell lines derived from three genetically defined kidney cancers (Clear Cell Renal Cell Cancer, 786-0; Hereditary Leiomyomatosis Renal Cell Cancer, UOK262; Birt-Hogg-Dubé Syndrome, UOK257) and their molecularly restored (e.g., stable re-expression of VHL, FH, or Folliculin, respectively; see references in Table 1) nontumorigenic isogenic counterparts, we assessed EA cytotoxicity by MTT assay and/or manual cell counting (Table 1). Whereas the three genetically defined kidney cancer cell lines displayed an IC₅₀ for EA of 35–50 nM, in each case the molecularly restored isogenic counterpart was markedly less sensitive to EA (IC₅₀ > 10 μ M). Two nontumorigenic kidney-derived cell lines, HK2 and HEK293, were similarly insensitive to EA (IC₅₀ > 10 μ M). In contrast, the prostate cancer cell line PC3 and the breast cell line SKBr3 displayed intermediate sensitivity to EA (IC₅₀ = 3–5 μ M). Sensitivity to EA correlated significantly with sensitivity to 2-deoxyglucose (2-DG), an indicator of glucose dependence (Table 1).

EA Selectively Activates PKC θ

Because nothing is known about EA's mechanism of action, we predicted potential target(s) by structure activity relationship analysis (see the Experimental Procedures). Fifteen potential molecular targets were identified, half of which were isoforms

of protein kinase C (PKC) (Table S1 available online). Therefore, we investigated further the potential effect of EA on PKCs, first using a pan-PKC kinase assay. We found that treatment of whole-cell extracts with EA increased pan-PKC activity in a dose-dependent manner (Figure 1A; Figure S1). To identify which PKC isoforms were responsive to EA, we individually silenced expression of PKC- α , - δ , - θ , - η , or - ϵ in 786-0 cells and examined the impact on EA cytotoxicity. Only PKC θ knock-down abrogated EA cytotoxicity (Figure 1B), suggesting that PKC θ may be a target of EA. We confirmed this hypothesis by evaluating the effect of EA on the enzymatic activity of purified PKC θ in vitro. We found that PKC θ -mediated phosphorylation of its substrate IRS1 was dose-dependently enhanced by EA (Figures 1C and 1D).

Because PKC θ is structurally very similar to PKC δ , we asked whether EA's effect on PKC activity is due solely to PKC θ activation. Phorbol esters, including the fluorescent analog sapintoxin D (SAPD), bind to the same pocket in PKCs as does diacylglycerol (DAG) and are well-known PKC activators. Unlike PKC θ and PKC δ , conventional PKCs, including PKC α , require priming with Ca²⁺ in order to bind either DAG or phorbol esters (Luo and Weinstein, 1993; Griner and Kazanietz, 2007). In vitro kinase assay (in the absence of Ca²⁺) using either PKC α , - δ , or - θ proteins confirmed that EA selectively activates PKC θ . In contrast, SAPD activated both PKC δ and PKC θ under the same assay conditions (Figure 1E).

Finally, we took advantage of the fluorescent properties of SAPD to confirm the binding of EA to PKC θ (Figure 1F). Purified PKC θ was incubated for 20 min with EA (1 μ M) or DMSO prior to the addition of SAPD (2 μ M). We found that premixing PKC θ with EA significantly reduced SAPD binding, supporting the hypothesis that EA interacts with a motif in PKC θ , either contiguous with or close to the SAPD/DAG binding domain. Premixing EA with PKC δ had no effect on SAPD binding (data not shown).

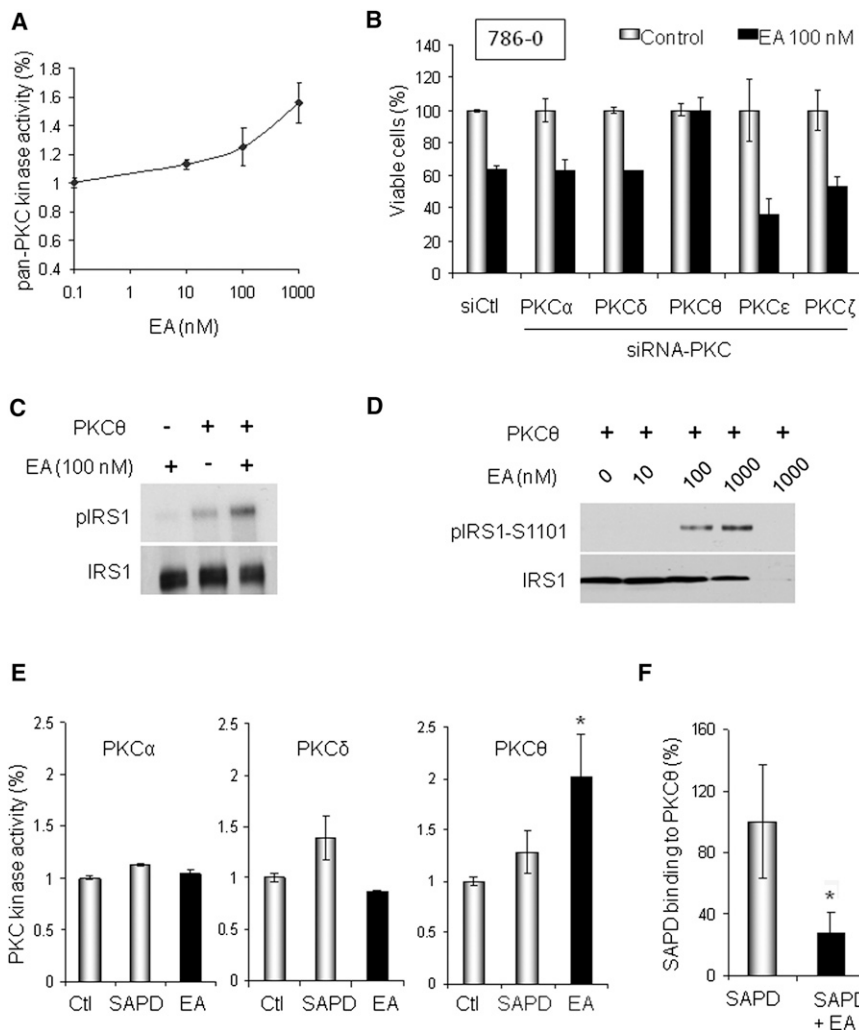


Figure 1. EA Is a Selective PKC θ Activator

(A) Pan-PKC kinase activity was assessed in 786-0 cells following EA treatment. Whole-cell lysates were incubated for 1 hr at 30°C with EA or DMSO in the presence of ATP (10 μ M). PKC kinase activity was quantified by spectrophotometry (see the Experimental Procedures).

(B) Viability (determined by MTT assay) after 24 hr EA treatment (100 nM) of 786-0 cells silenced for different PKC isoforms by RNA interference.

(C) Effect of 30 min EA (100 nM) treatment on PKC θ -mediated phosphorylation of IRS1. A radioactive kinase activity assay was performed in the presence of 6 μ Ci (0.2 μ M) of [32 P]-ATP and 10 μ M nonradioactive ATP using purified PKC θ (50 ng) and its substrate IRS1 (50 ng).

(D) Nonradioactive dose-dependent effects of EA on PKC θ -mediated phosphorylation of IRS1-S1101 using purified proteins were assessed by immunoblotting (1 hr treatment; 10 ng PKC θ , 20 ng IRS1). The last lane omits IRS1 and is a negative control.

(E) Purified PKC α , PKC δ , or PKC θ (5 ng) were incubated for 1 hr with DMSO, SAPD (2 μ M), or EA (1 μ M) in presence of ATP (10 μ M). PKC kinase activity was quantified by spectrophotometry.

(F) EA competes with the fluorescent phorbol ester SAPD for binding to PKC θ . EA (1 μ M) was preincubated for 20 min with 5 ng purified PKC protein prior to addition of SAPD (2 μ M). SAPD fluorescence shifts from 455 nm to 420 nm when it is bound to PKC. Thus, fluorescence emission was measured at 420 nm (excitation at 355 nm) to assess SAPD binding in presence or absence of EA (* p < 0.05). Data are displayed as the mean \pm SD (see also Figure S1 and Table S1).

PKC θ Activation Induces an Insulin-Resistant Phenotype in Tumor Cells

Because we demonstrated that EA enhanced PKC θ -mediated inhibitory phosphorylation of IRS1 (on S1101) in vitro, we hypothesized that EA might induce an insulin-resistant phenotype. EA enhanced the inhibitory phosphorylation of IRS1 in 786-0 cells and led to reduced activating phosphorylations of AKT (T308 and S473) and reduced AKT-mediated phosphorylation of GSK3 β (S9). These effects are PKC θ -dependent because they were ameliorated upon siRNA-mediated silencing of PKC θ (Figure 2A). EA also reduced glucose uptake in 786-0 cells, to a similar degree as the Glut1 inhibitor fasentin (Figure 2B), and decreased cellular ATP content as well (Figure 2C). However, at the concentration used, fasentin only slightly affected 786-0 cell viability (Figure S2A), whereas addition of cell permeable pyruvate (methylpyruvate) abrogates EA cytotoxicity (Figure S2B). These data suggest that glucose uptake inhibition contributes to but does not solely account for EA cytotoxicity.

Next, we assessed the role played by insulin pathway inhibition in EA-mediated inhibition of AKT. We confirmed that the inhibitory effect of EA on AKT activity was IRS1-dependent because EA-mediated AKT inhibition was overcome by the

inclusion of EGF in the culture media (Figure S2C). To confirm the importance of IRS1-dependent AKT inhibition for EA cytotoxicity, we infected 786-0 cells with several AKT viral constructs. As shown in Figure 2D (upper panel), expression of dominant negative AKT (AktDN) enhanced EA cytotoxicity, whereas expression of constitutively active AKT (AktCA) protected cells from EA. These impacts on EA cytotoxicity were consistent with AKT activity status (Figure 2D, lower panel; Figure S2D), and the data clearly implicate IRS1-dependent inhibition of AKT as a necessary component of the cytotoxic response to EA.

To determine whether the in vitro cytotoxicity of EA was obtainable in vivo, we treated athymic mice bearing 786-0 tumor xenografts with EA (5 mg/kg intraperitoneally, daily except Sunday). EA markedly inhibited tumor growth during the 2-week treatment period (Figure 2E). In agreement with our in vitro data, inhibitory phosphorylation of IRS1 was increased, and activity of the PI3K/AKT pathway was decreased in 786-0 tumors excised from mice treated with EA, when compared to tumors from vehicle-treated mice (Figure 2F). Importantly, in a second tumor xenograft model, EA inhibited human prostate tumor growth by up to 60% (Figure S2E), consistent with its

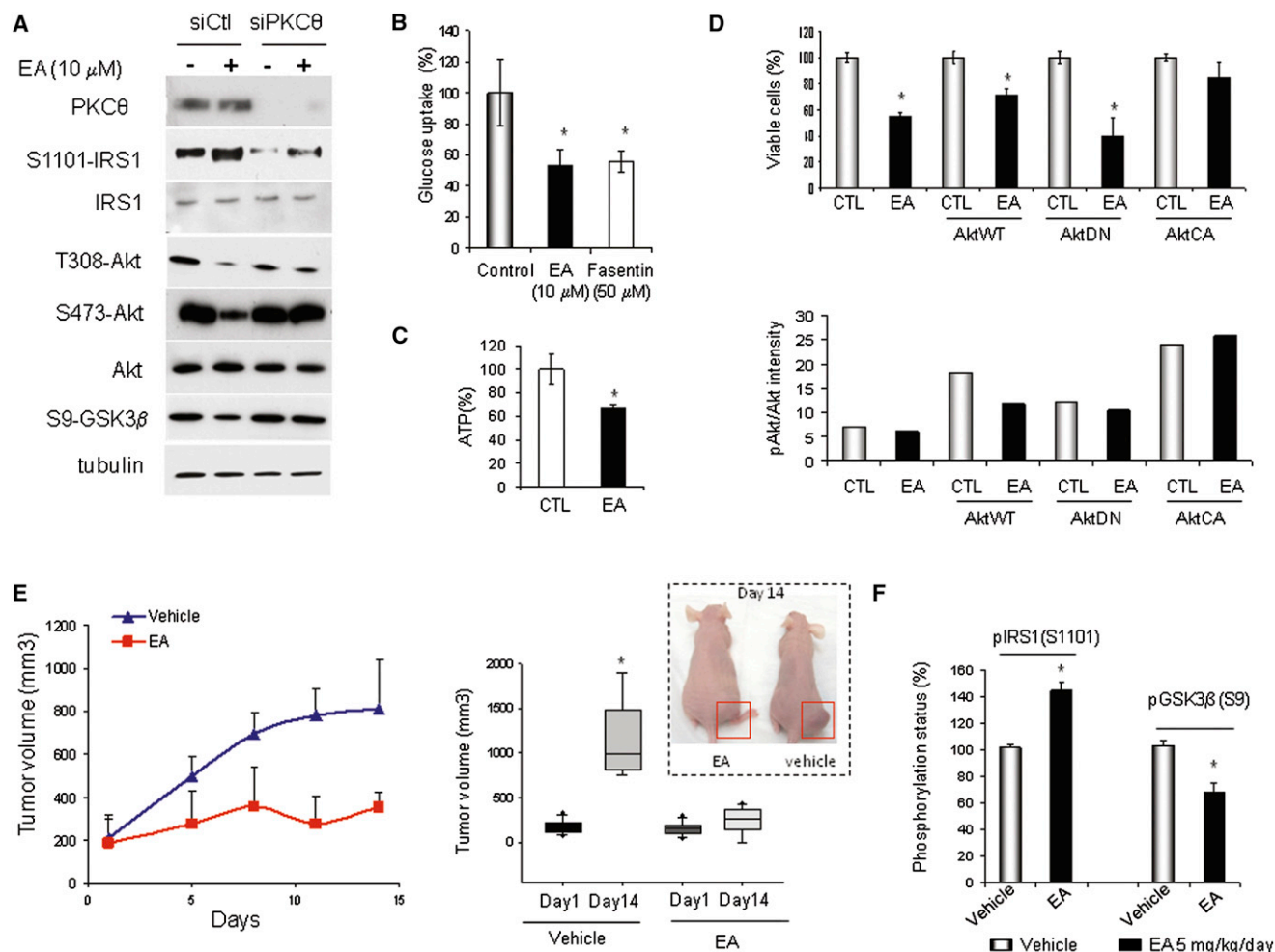


Figure 2. EA Induces Insulin Resistance In Vitro and In Vivo

(A) EA-mediated phosphorylation of IRS1 (S1101), AKT (pT308 and pS473), and GSK3 β (pS9) in 786-0 cells requires PKC θ expression. EA treatment (10 μ M) was for 6 hr.

(B) EA inhibits glucose uptake in 786-0 cells as shown by using the nondegradable fluorescent glucose analog 2-NBDG. The Glut1 inhibitor fasentin (50 μ M) is shown as a positive control. EA and fasentin treatments were for 3 hr.

(C) Effect of EA treatment (6 hr, 1 μ M) on ATP levels in 786-0 cells was measured using ATPlite assay.

(D) Effect of AKT activation on EA cytotoxicity. 786-0 cells were infected 24 hr prior to EA treatment with AKT lentiviral constructs: wild-type AKT (AktWT), dominant negative AKT (AktDN), or constitutively active AKT (AktCA). After treatment with 1 μ M EA for an additional 24 hr, cell viability was assessed by manual cell counting with trypan blue exclusion (upper panel). Impact of lentiviral infections on AKT activity is shown in the lower panel and in Figure S2D. EA inhibits the activity of wild-type but not of constitutively active AKT.

(E) Effect of EA treatment (5 mg/kg, daily except Sunday) on xenograft growth of 786-0 cells in athymic mice (vehicle: PBS/DMSO, 1/1). The left panel displays the growth curve of one of two animal experiments, each with eight animals per group. The right panel represents the averaged mean end point tumor volumes of the two experiments (32 animals in total).

(F) EA treatment in vivo stimulates inhibitory phosphorylation of IRS1 (pS1101) and reduced phosphorylation of the AKT substrate GSK3 β (pS9) in tumor xenografts of treated mice. * $p < 0.05$. Data are displayed as the mean \pm SD (see also Figure S2).

ability to stimulate PKC θ in these cells and with its in vitro toxicity profile (Figure S1; Table 1).

PKC θ Induces Heat-Shock-Independent Activation of HSF1

Because the in vivo data support further evaluation of EA as an anticancer agent, we asked whether treated animals might develop hyperglycemia because of induction of systemic insulin resistance. We measured blood glucose level in mice harboring

either 786-0 or PC3 xenografts before and following a single treatment with either EA or vehicle (PBS/DMSO, 1:1). Surprisingly, mice treated with EA displayed significantly lower blood glucose compared to vehicle-treated mice (Figure 3A).

Chemically induced reduction in blood glucose has been reported previously and is thought to be due to increased HSP70, resulting in sensitization of cells to insulin (Chung et al., 2008; Kavanagh et al., 2011). We observed that in mice treated with EA both plasma and tumor HSP70 were elevated

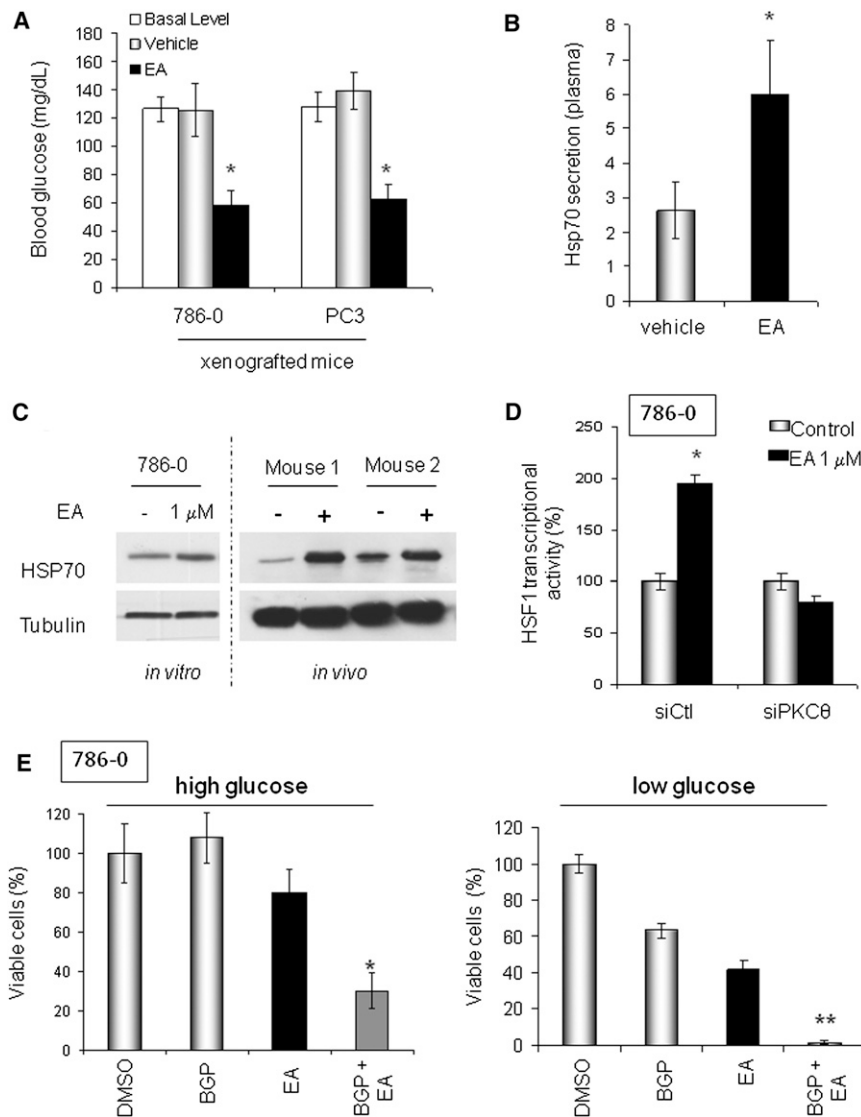


Figure 3. EA Activates HSF1

(A) Effect of EA on blood glucose level in tumor-bearing mice prior to ("basal level") or 5 min after treatment with EA (EA, 5 mg/kg; vehicle: PBS/DMSO, 1/1).

(B) Quantification of plasma HSP70 level in tumor-bearing mice 4 hr following EA treatment (EA: 5 mg/kg; vehicle: PBS/DMSO, 1/1).

(C) HSP70 protein expression following EA treatment of 786-0 cells in vitro (EA, 1 μ M for 8 hr) and in vivo (786-0 xenografts; prior to and 8 hr after EA, 5 mg/kg) was assessed by immunoblotting.

(D) EA stimulation of HSF1 transcriptional activity requires PKC θ expression. HSF1 activity was measured in cells transiently transfected with a HSP70 HSE-promoter GFP-tagged reporter plasmid 6 hr after EA treatment.

(E) EA cytotoxicity is affected by HSF1 activation and extracellular glucose concentration. BGP-15 prolongs the HSF1 transcriptional response. High glucose medium contains 4.5 g/l glucose; low glucose medium contains 1 g/l glucose. BGP-15 was used at 50 μ M (Chung et al., 2008) and EA was used at 1 μ M. Incubation was for 24 hr. Viability was assessed by MTT assay and confirmed by manual cell counting of trypan blue-excluding cells using a hemacytometer. * $p < 0.05$; ** $p < 0.001$. Data are displayed as the mean \pm SD (see also Figure S3).

compared to vehicle-treated mice (Figures 3B and 3C). HSP70 is a marker of cell stress and is a transcriptional target of HSF1 (Trepel et al., 2010). Consistent with these data, we observed that EA induced HSF1 nuclear translocation and upregulated its transcriptional activity in a PKC θ -dependent manner (Figures 3D and S3).

Because HSF1 has recently been identified as a contributing factor for tumorigenesis and likely represents a nononcogene addiction of most tumor cells (Whitesell and Lindquist, 2009; Santagata et al., 2011; Dai et al., 2007; Mendillo et al., 2012; Min et al., 2007), we investigated whether HSF1 activation might compromise EA cytotoxicity, much as it is thought to compromise the cytotoxicity of HSP90 inhibitors (which also induce HSF1 [Zou et al., 1998]). We examined the impact of the HSF1 chemical enhancer BGP-15, currently under clinical evaluation for treating insulin-resistance disorders (Chung et al., 2008; Literáti-Nagy et al., 2009; Hargitai et al., 2003), on EA-induced cytotoxicity. To our surprise, addition of BGP-15 significantly increased EA cytotoxicity (Figure 3E, left panel). We have shown

that PKC θ induced insulin resistance in tumor cells, and Dai et al. (2007) demonstrated that HSF1 enforces glucose dependence in tumor cells. Thus, we hypothesized that the increased cytotoxicity obtained in vitro upon combination of BGP-15 and EA might result from the simultaneous occurrence of these two metabolic events. If this were the case, the cytotoxicity of an EA/BGP-15 drug combination should be augmented in cells exposed to low glucose. Indeed, as shown in Figure 3E (right panel), BGP-15 and EA, either administered as individual agents or in combination, displayed greater cytotoxicity when tumor cells were cultured in low glucose media.

EA Cytotoxicity Requires Expression of Both PKC θ and HSF1

Next, we asked whether HSF1 expression is necessary for EA-induced cytotoxicity. Using shRNA to knock down HSF1 (Figure S4A), we found that HSF1 expression, like PKC θ , is essential for cell sensitivity to EA (Figure 4A). Importantly, the synergistic effect obtained by combining BGP-15 and EA (see Figure 3E) also depended on HSF1 expression. To provide further support for our hypothesis that both PKC θ and HSF1 are necessary for EA cytotoxicity, we made use of the fact that HEK293 cells are insensitive to EA (see Table 1), express undetectable levels of endogenous PKC θ , and do not overexpress HSF1 (data not shown). We were able to induce EA sensitivity in HEK293 cells after transfection with both PKC θ and HSF1 but not after

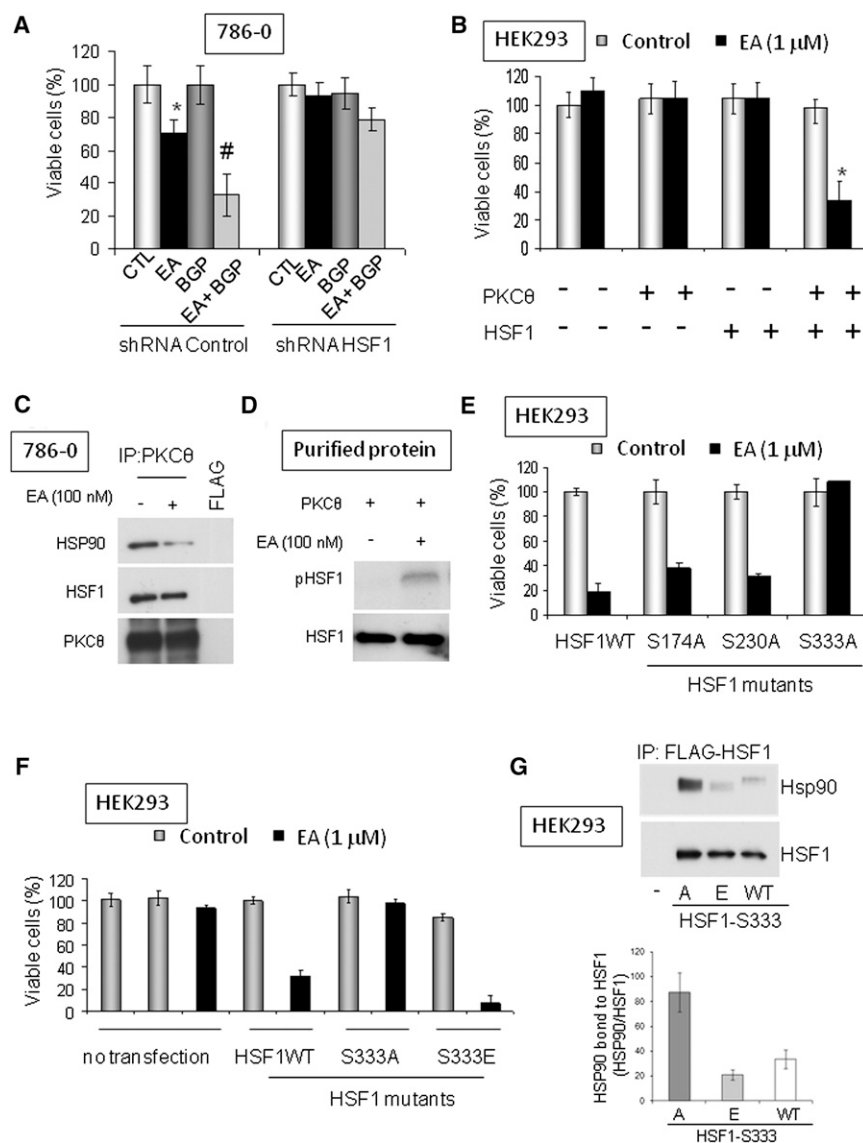


Figure 4. PKC θ and HSF1 Are Both Necessary for EA Cytotoxicity in Tumor Cells

(A) EA sensitivity of 786-0 cells to EA and EA/BGP-15 requires HSF1 expression. EA was used at 1 μ M and BGP-15 at 50 μ M (24 hr). HSF1 expression was decreased by transfection of HSF1-specific shRNA 24 hr prior to treatment. * p < 0.05 (compared to control); #, p < 0.05 (compared to EA-treated).

(B) HEK293 cells are not sensitive to EA. HSF1 and PKC θ overexpression confers EA sensitivity on HEK293 cells (EA treatment was for 24 hr at 1 μ M, commencing 24 hr after transfection). * p < 0.05 (compared to cotransfected control).

(C) Interaction of endogenous HSF1 and PKC θ in 786-0 cells was visualized by immunoprecipitation of endogenous PKC θ and blotting for associated HSF1. 786-0 cells grown in 6-well plates were lysed in TNEV buffer. The lysates were treated for 1 hr with EA (100 nM) or DMSO at 30°C before immunoprecipitation. HSP90 interaction with the PKC θ /HSF1 immunocomplex was reduced by EA treatment (left panel). The inputs for this experiment can be found in Figure S4C.

(D) EA stimulates PKC θ -mediated phosphorylation of purified HSF1 in vitro (50 ng of purified proteins; treatment for 30 min at 30°C).

(E) Identification of a putative PKC θ phosphorylation site on HSF1. HEK293 cells were transfected with PKC θ and either wild-type or point mutated HSF1 plasmids (see Figures S4E and S4F) and sensitivity to EA was assessed (treatment for 24 hr with 1 μ M EA).

(F) Effect of HSF1 S333 mutants on EA sensitivity of HEK293 cells overexpressing PKC θ . The phosphomimetic mutant HSF1-S333E supports EA cytotoxicity, whereas the nonphosphorylatable mutant HSF1-S333A does not (treatment for 24 hr with 1 μ M EA).

(G) Association of HSF1-S333A, HSF1-S333E, and wild-type HSF1 with HSP90. HEK293 cells were transiently transfected with Flag-tagged HSF1 plasmids as indicated. After 24 hr, Flag immunoprecipitates were subjected to SDS-PAGE, transferred to PVDF membrane, and immunoblotted for associated endogenous HSP90.

Anti-HSF1 antibody was also blotted to monitor the uniformity of HSF1 expression and efficiency of immunoprecipitation. The phosphomimetic mutant HSF1-S333E associates with endogenous HSP90 to a markedly lesser degree than does nonphosphorylatable HSF1-S333A; HSP90 association with wild-type HSF1 is shown for comparison. Band optical densities from two separate experiments were obtained by image analysis software and the HSP90 band density in each case was normalized to the respective HSF1 band density (graphical insert). The inputs for this experiment can be found in Figure S4H. Data are displayed as the mean \pm SD (see also Figure S4).

transfection with either construct alone (Figure 4B; see Figure S4B for inputs).

Extending our observation that PKC θ is necessary for HSF1 activation by EA (Figure 3D), we were able to detect the interaction of endogenous PKC θ and HSF1 in 786-0 cells (Figure 4C; see Figure S4C for inputs). In addition, we found that PKC θ phosphorylated HSF1 in vitro in the presence of EA (Figure 4D), and EA-induced serine phosphorylation of endogenous HSF1 in 786-0 cells was PKC θ -dependent (Figure S4D). Further, we observed that HSP90 was also a component of the HSF1/PKC θ complex but was dissociated after treatment with EA (Figure 4C).

Because dissociation from HSP90 is a prerequisite for HSF1 activation (Ankar and Sistonen, 2011; Zou et al., 1998), these

data suggest that PKC θ phosphorylation of HSF1 may promote this process. To identify a putative PKC θ phosphorylation site(s) on HSF1, we mutated several predicted PKC consensus phosphorylation sites (see Figure S4E), and we examined the ability of these HSF1 mutants to complement exogenous PKC θ in mediating EA cytotoxicity in HEK293 cells (Figure 4E; see Figure S4F for inputs). EA cytotoxicity was abrogated only when HSF1 serine 333 was mutated to alanine (S333A), implicating S333 as a potential PKC θ phosphorylation site. Supporting this possibility, we found that the phosphomimetic mutant HSF1-S333E, but not the nonphosphorylatable mutant HSF1-S333A, fully complemented PKC θ -dependent EA cytotoxicity (Figure 4F; see Figure S4G for inputs).

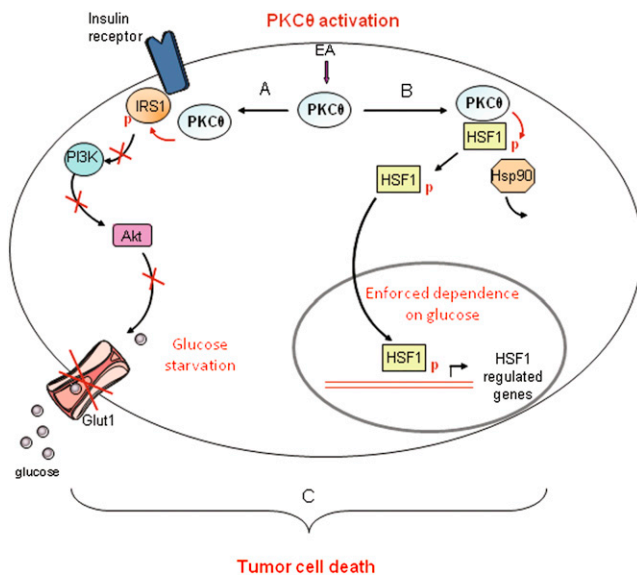


Figure 5. EA Proposed Mechanism of Action: Activation of PKC θ in Cells Expressing HSF1 Leads to Simultaneous Induction of Insulin Resistance and Glucose Dependence, Resulting in Metabolic Catastrophe

(A) EA-dependent activation of PKC θ stimulates an insulin-resistant phenotype via inhibitory phosphorylation of IRS1 and inhibition of AKT, limiting access of tumor cells to glucose.

(B) EA simultaneously stimulates PKC θ -mediated phosphorylation and activation of HSF1, a transcription factor that enforces tumor cell glucose dependence (Dai et al., 2007).

(C) By simultaneously inducing insulin resistance and glucose dependence, EA is synthetically lethal to glycolytic tumor cells.

Although the domain of HSF1 that interacts with HSP90 is not known, S333 is located within the regulatory domain of the transcription factor, a region rich in posttranslational modification sites and important for the stress inducibility of HSF1 (Anckar and Sistonen, 2011). Therefore, we examined whether S333 mutation to either alanine or glutamic acid affected HSF1 interaction with HSP90. FLAG-tagged HSF1 wild-type, S333A, and S333E plasmids were transiently transfected into HEK293 cells, and FLAG immunoprecipitates were probed for associated endogenous HSP90. Indeed, we found that HSF1-S333A associated with endogenous HSP90 to a markedly greater extent than did HSF1-S333E (Figure 4G; see Figure S4H for inputs). These data are consistent with the hypothesis that PKC θ -mediated phosphorylation of HSF1 S333 promotes dissociation from HSP90. Supporting this possibility, we found that HSF1-S333E was more efficiently activated (>2-fold) by heat shock when compared to HSF1-S333A (Figure S4I).

DISCUSSION

Survival of tumor cells depends on their ability to adapt to their environment. Because cellular transformation is associated with an increased dependence on glucose (Vander Heiden et al., 2009), tumor cells have reprogrammed their cellular signaling pathways to allow for increased glucose uptake. Indeed, positron emission tomography with 2-deoxy-2(18 F)-fluoro-D-

glucose, a nonmetabolizable glucose analog, is frequently used to distinguish tumors from adjacent normal tissues (Gambhir, 2002), and targeting glucose uptake and/or metabolism has been explored for its therapeutic potential in treating cancer, including VHL-deficient kidney cancer (Chan et al., 2011; Hamanaka and Chandel, 2012). The insulin pathway and the transcription factor HSF1 are two examples of evolutionarily conserved signaling networks that support and foster the glucose dependence of tumor cells (Barbieri et al., 2003; Pirkkala et al., 2001; Dai et al., 2007).

In this study, we have identified a unique strategy to create metabolic disaster in glucose-dependent tumor cells by selectively activating PKC θ with the natural product EA (schema illustrated in Figure 5). When examined in a panel of kidney-cancer-derived cell lines with unique genetic lesions distinct from VHL deficiency, EA cytotoxicity paralleled sensitivity to 2-deoxy-D-glucose (2-DG), itself an indicator of glucose dependence (see Table 1). In each case, correction of the unique genetic lesion in isogenic cell lines abrogated both EA sensitivity and 2-DG cytotoxicity. Nontumorigenic cell lines derived from normal kidney epithelium were resistant to both EA and 2-DG. Importantly, however, nontumorigenic HEK293 cells can be made sensitive to EA by exogenous expression of both PKC θ and HSF1.

Although the crystal structure of EA bound to PKC θ will be necessary to unambiguously identify its binding domain, competition binding experiments with the fluorescent phorbol ester SAPD suggest that EA binds within or adjacent to the C1 domain of PKC θ . Because EA is not able to compete with SAPD binding to PKC δ , and because EA is structurally dissimilar from either phorbol esters or DAG, it is likely that EA has binding requirements that are only met in PKC θ .

Because of the lack of selectivity of most PKC modulators, the unique role of PKC θ in cancer biology has remained unclear. Here, we have identified PKC θ as an important pharmacologic target in glucose-dependent tumor cells. Kim and collaborators first identified a link between PKC θ and insulin resistance when they demonstrated that PKC θ knockout mice were protected from developing fat-induced insulin resistance (Kim et al., 2004). We confirmed the association of PKC θ with insulin resistance in tumor cells by showing that selective activation of PKC θ disrupts insulin signaling to AKT and induces an insulin-resistant phenotype reminiscent of that caused in skeletal muscle by a high fat diet and observed in patients with type 2 diabetes (Samuel and Shulman, 2012).

We suspect that the lack of hyperglycemia in EA-treated mice is due to increased HSP70 levels because elevated HSP70 has been shown to enhance insulin sensitivity (Chung et al., 2008; Kavanagh et al., 2011). Because EA promoted increased HSP70 expression in tumor xenografts and in tumor cells in vitro, we examined the possible impact of EA on HSF1, a transcriptional regulator of HSP70 and a protein frequently upregulated in cancer (Whitesell and Lindquist, 2009; Santagata et al., 2011). As discussed earlier, HSF1 enhances tumor glucose dependence and the transcription factor, although not transforming on its own, is considered to be a critical contributor to tumor cell survival (Dai et al., 2007; Solimini et al., 2007). Recently, HSF1 has been reported to transcriptionally regulate a number of genes not involved in the heat shock response of

normal cells but which are commonly upregulated in cancer cells (Mendillo et al., 2012). Thus, inhibition of HSF1 is predicted to be of therapeutic value in cancer (Whitesell and Lindquist, 2009).

Unexpectedly, although EA stimulates HSF1 transcriptional activity, we found this to be a prerequisite for EA cytotoxicity. Thus, we propose that EA is synthetically lethal for tumor cells that simultaneously express PKC θ and are addicted to HSF1. PKC θ activates HSF1 by phosphorylating serine 333 in the stress responsive regulatory domain. Mutation of this residue to a non-phosphorylatable (S333A) or phosphomimetic (S333E) amino acid markedly affects the interaction of HSF1 with HSP90. Because dissociation of HSF1 from HSP90 is a prerequisite for HSF1 activation and nuclear translocation (Anckar and Sistonen, 2011), these data provide a mechanistic basis to explain PKC θ -dependent activation of HSF1 by EA. Importantly, EA sensitivity is strongly correlated with glucose dependence and is most pronounced when glucose availability is limiting.

In summary, our data show that PKC θ -mediated induction of insulin resistance occurring simultaneously with PKC θ -mediated HSF1 activation is responsible for EA cytotoxicity. PKC θ thus represents a unique molecular target for HSF1-addicted glycolytic tumors, and EA provides a template for designing effective PKC θ -activating drugs.

EXPERIMENTAL PROCEDURES

Cell Lines and Cell Culture

The sporadic VHL-deficient kidney tumor cell line 786-0 (Williams et al., 1978), the prostate cancer cell line PC3 (Kaighn et al., 1979), the breast cancer cell line SKBr3 (Fogh and Trempe, 1975), the normal kidney cell line HK2 (Ryan et al., 1994), and HEK293T, an embryonic kidney epithelial cell line (Pear et al., 1993), were all purchased from ATCC. UOK262, UOK262WT, UOK257, UOK257-2 (WT), and 786/VHL were established within the Urologic Oncology Branch. UOK262 is a kidney cancer cell line derived from a metastasis that is deficient in fumarate hydratase (FH) (Yang et al., 2010). UOK262WT was established by stably transfecting UOK262 with a functional FH gene (Tong et al., 2011) and is therefore considered to be "molecularly restored." UOK257 is a folliculin (FLCN)-deficient kidney tumor cell line derived from human renal carcinoma of an individual with Birt-Hogg-Dubé (BHD) syndrome and its molecularly restored counterpart UOK257-2 (WT) was established by stably transfecting UOK257 with FLCN (Yang et al., 2008; Hong et al., 2010). The stably VHL-transfected 786-0 (786/VHL) cell line has been described previously (Tong et al., 2011). Cells were cultured in Dulbecco's modified Eagle's medium (DMEM) high glucose without sodium pyruvate (Cellgro, Herndon, VA, USA) or in RPMI-1640 (PC3 only) supplemented with 10% fetal bovine serum (Invitrogen, Grand Island, NY, USA). Viability experiments were performed in serum-free media.

Reagents

EA was generously supplied by R. Akee of the Natural Products Support Group (Developmental Therapeutics Program, National Cancer Institute, Frederick National Laboratory, Frederick, MD, USA). Complete mini protease inhibitor cocktail tablets were purchased from Roche (Indianapolis, IN, USA). The siRNAs for PKC- α and - ζ were purchased from OriGene (Rockville, MD, USA). The siRNAs for PKC- θ , - δ , and - ϵ were from Santa Cruz Biotechnology (Santa Cruz, CA, USA). Purified HSF1, PKC- θ , - α , and - δ were purchased from EnzoLife Sciences (Farmingdale, NY, USA).

Prediction of EA Targets

Metadrag (Genego, Carlsbad, CA, USA) is a systems pharmacology platform using QSAR modeling to analyze and compare biological effects of small molecules. We used it to predict potential targets for EA (see a complete list of predicted targets in Table S1).

Nonradioactive PKC Kinase Assay

PKC kinase activity of cell lysates was measured using the pan-PKC activity assay from EnzoLife Sciences, following the manufacturer's recommendations. Briefly, cells were lysed in TNESV lysis buffer (50 mM Tris, 1% Nonidet P-40, 2 mM EDTA, 100 mM NaCl, and 2 mM Na₃VO₄). After 15 min of centrifugation (13, 200 rpm, 4°C), clarified supernatant was incubated with 10 μ M EA in the kinase buffer provided by the manufacturer (1 hr at 30°C with 10 μ M ATP). The reaction was stopped by emptying the wells prior to measuring the phosphorylation of a PKC substrate by spectrophotometry. PKC α , - δ , and - θ kinase assays were performed in a similar manner using 5 ng of purified PKC proteins instead of cell lysate (incubation for 1 hr at 30°C with 10 μ M ATP). Kinase activity was also assessed by incubating purified PKC θ (10 ng) with purified IRS1 (20 ng) in presence of increasing concentrations of EA (incubation for 1 hr at 30°C with 10 μ M ATP). The reaction was stopped by adding denaturing sample buffer, and phosphorylation of IRS1 on S1101 was assessed by immunoblot analysis.

Radioactive In Vitro Kinase Assay

Purified IRS1 (50 ng) or HSF1 (50 ng) was incubated with purified PKC θ (50 ng) in presence or absence of EA (100 nM). Reactions were initiated by the addition of 10 μ M nonradioactive ATP and 6 μ Ci (0.2 μ M) of [³²P]-ATP and incubated at 30°C for 30 min with periodic mixing. Proteins in the kinase reactions were separated by SDS-PAGE and transferred to PVDF membrane. Phosphorylation of IRS1 or HSF1 was assessed by radiography of PVDF membranes. IRS1 or HSF1 were immunoblotted to ensure equal loading.

Phorbol Ester Competition Binding Assay

The fluorescent phorbol ester sapintoxin D (SAPD, 2 μ M; Santa Cruz) (Taylor et al., 1981) was incubated with purified PKC proteins (5 ng) after preincubation for 20 min with EA (1 μ M) or DMSO. Fluorescence of SAPD is shifted from 455 to 420 nm when it is bound to PKC. Therefore, we monitored fluorescence emission at 420 nm to determine SAPD binding to PKC proteins (Das et al., 2004).

Glucose Uptake Assay

Glucose uptake was measured using a fluorescent nonmetabolizable D-glucose analog 2-[N-(7-nitrobenz-2-oxa-1,3-diazol-4-yl) amino]-2-deoxy-D-glucose (2-NBDG; Cayman Chemicals, Ann Arbor, MI) as previously described (O'Neil et al., 2005), with the following modifications. Five thousand cells were plated in black-well 96-well plates. After treatment as indicated (3 hr), cells were incubated for 20 min in KREB buffer containing 1g/l glucose in presence or absence of 20 μ M 2-NBDG. Cells were then washed three times for 5 min with PBS to remove all residual extracellular 2-NBDG. The amount of 2-NBDG imported into the cells was measured by assessing fluorescence at 488 nm. The Glut 1 inhibitor fasentin (50 μ M; Sigma-Aldrich, St. Louis, MO) was used as a positive control.

HSP70 Secretion

Plasma HSP70 in tumor-bearing mice was assessed using an ELISA kit purchased from EnzoLife Sciences and following the manufacturer's protocol. Blood was collected 4 hr after EA or vehicle (PBS/DMSO, 1/1) injection.

HSF1 Transcriptional Activity

Cellular HSF1 transcriptional activity was measured using a green fluorescent protein (GFP)-tag HSE promoter reporter (generously provided by Dr. Luke Whitesell, Whitehead Institute, Cambridge, MA, USA). Twenty-four hours prior to analysis, 5,000 786-0 cells were plated in 96-well black-view plates. While still in suspension, cells were transfected with the reporter plasmid (1 μ g DNA) using lipofectamine LTX (Invitrogen) and following the manufacturer's protocol. To avoid potential interference of the phenol red from the media with the GFP reading, phenol red-free DMEM (high glucose and without sodium pyruvate) was used instead of regular DMEM. The following day, 786-0 cells were treated as described with EA 6 hr prior to measure the amount of GFP produced using a spectrophotometer (488 nm). For HSF1 silencing experiments, 786-0 cells were transfected with 14 μ g of shRNA to HSF1 in 6-well plates using lipofectamine LTX (Invitrogen) 2 days prior to plating into 96-well black-view plates. Nuclear translocation of HSF1 was visualized by immunofluorescence. Three thousand 786-0 cells were plated in 2-well

chamber-slides (Nunc/Sigma-Aldrich) and treated for 1 hr with EA (1 μ M) before fixation with 4% paraformaldehyde. Cells were blocked 1 hr with BSA (3%) and permeabilized with Triton (0.5%). HSF1 antibody was incubated overnight at 4°C in a humidified atmosphere. After three washes with TBST buffer, slides were incubated 1 hr with secondary antibody coupled to Alexa455, washed, and mounted. DAPI (Cell Signaling Technology, Danvers, MA, USA) was used to visualize cell nuclei. Pictures were taken with a confocal microscope (Zeiss NLO510).

Xenograft Tumor Studies

Animal experiments were carried out following the ethical guidelines of the National Cancer Institute and using an animal protocol approved by the National Institutes of Health Animal Care Facility. Ten million 786-0 or one million PC3 cells were implanted subcutaneously on the left flanks of twenty 7-week-old female nude (Nu/Nu) mice (strain code 088; Charles River, Wilmington, MA, USA). After 1–4 weeks (depending on the cell line), tumors reached an average volume of 100–150 mm³. Tumor take for both 786-0 and PC3 xenografts was 100%; however, to maintain homogenous group sizes, only 16 mice out of the 20 were used. Mice were then randomly separated in two groups of eight mice with comparable tumor volumes and treated six times a week (daily except Sunday) intraperitoneally with either EA at 5 mg/kg or vehicle (PBS/DMSO, 1/1). Food and water were available ad libitum. Tumors were measured throughout the duration of the experiment using calipers and tumor volumes were estimated using the formula ($l \times w^2$)/2. At the end of the experiment, blood was collected, and tumors were surgically excised and frozen for further analysis. Animal experiments were performed twice with eight animals per group each time.

Statistics

Unless specified, all values are expressed as the mean \pm standard error. Values were compared using the Student-Newman-Keul's test. $p < 0.05$ was considered significant.

SUPPLEMENTAL INFORMATION

Supplemental Information includes one table, four figures, and Supplemental Experimental Procedures and can be found with this article online at <http://dx.doi.org/10.1016/j.ccr.2012.12.007>.

ACKNOWLEDGMENTS

We thank Drs. S. Calderwood (Harvard University, Cambridge, MA) and L. Whitesell (Whitehead Institute, Cambridge, MA) for generously providing reagents. We thank Dr. P.L. Nagy (N-Gene Research Laboratories, Budapest, Hungary) for generously providing BGP-15. We thank Drs. N. Kedei and P. Blumberg (National Cancer Institute, Bethesda, MD) and P. Csermely (Semmelweis University, Budapest, Hungary) for helpful discussions. This research was supported with funds provided by the Intramural Research Program of the National Cancer Institute.

Received: June 4, 2012

Revised: October 19, 2012

Accepted: December 18, 2012

Published: January 24, 2013

REFERENCES

- Anckar, J., and Sistonen, L. (2011). Regulation of HSF1 function in the heat stress response: implications in aging and disease. *Annu. Rev. Biochem.* 80, 1089–1115.
- Barbieri, M., Bonafé, M., Franceschi, C., and Paolisso, G. (2003). Insulin/IGF-I-signaling pathway: an evolutionarily conserved mechanism of longevity from yeast to humans. *Am. J. Physiol. Endocrinol. Metab.* 285, E1064–E1071.
- Chan, D.A., Sutphin, P.D., Nguyen, P., Turcotte, S., Lai, E.W., Banh, A., Reynolds, G.E., Chi, J.T., Wu, J., Solow-Cordero, D.E., et al. (2011). Targeting GLUT1 and the Warburg effect in renal cell carcinoma by chemical synthetic lethality. *Sci. Transl. Med.* 3, 94ra70.
- Chung, J., Nguyen, A.K., Henstridge, D.C., Holmes, A.G., Chan, M.H., Mesa, J.L., Lancaster, G.I., Southgate, R.J., Bruce, C.R., Duffy, S.J., et al. (2008). HSP72 protects against obesity-induced insulin resistance. *Proc. Natl. Acad. Sci. USA* 105, 1739–1744.
- Dai, C., Whitesell, L., Rogers, A.B., and Lindquist, S. (2007). Heat shock factor 1 is a powerful multifaceted modifier of carcinogenesis. *Cell* 130, 1005–1018.
- Das, J., Addona, G.H., Sandberg, W.S., Husain, S.S., Stehle, T., and Miller, K.W. (2004). Identification of a general anesthetic binding site in the diacylglycerol-binding domain of protein kinase C δ . *J. Biol. Chem.* 279, 37964–37972.
- Fogh, J., and Trempe, G. (1975). Human tumor cells in vitro (New York: Plenum Publishing), pp. 115–141.
- Gallagher, E.J., and LeRoith, D. (2011). Minireview: IGF, Insulin, and Cancer. *Endocrinology* 152, 2546–2551.
- Gambhir, S.S. (2002). Molecular imaging of cancer with positron emission tomography. *Nat. Rev. Cancer* 2, 683–693.
- Griffin, M.E., Marcucci, M.J., Cline, G.W., Bell, K., Barucci, N., Lee, D., Goodyear, L.J., Kraegen, E.W., White, M.F., and Shulman, G.I. (1999). Free fatty acid-induced insulin resistance is associated with activation of protein kinase C θ and alterations in the insulin signaling cascade. *Diabetes* 48, 1270–1274.
- Griner, E.M., and Kazanietz, M.G. (2007). Protein kinase C and other diacylglycerol effectors in cancer. *Nat. Rev. Cancer* 7, 281–294.
- Hamanaka, R.B., and Chandel, N.S. (2012). Targeting glucose metabolism for cancer therapy. *J. Exp. Med.* 209, 211–215.
- Hargitai, J., Lewis, H., Boros, I., Rácz, T., Fiser, A., Kurucz, I., Benjamin, I., Vigh, L., Péntes, Z., Csermely, P., and Latchman, D.S. (2003). Bimoclomol, a heat shock protein co-inducer, acts by the prolonged activation of heat shock factor-1. *Biochem. Biophys. Res. Commun.* 307, 689–695.
- Hong, S.B., Oh, H., Valera, V.A., Stull, J., Ngo, D.T., Baba, M., Merino, M.J., Linehan, W.M., and Schmidt, L.S. (2010). Tumor suppressor FLCN inhibits tumorigenesis of a FLCN-null renal cancer cell line and regulates expression of key molecules in TGF- β signaling. *Mol. Cancer* 9, 160.
- Kaighn, M.E., Narayan, K.S., Ohnuki, Y., Lechner, J.F., and Jones, L.W. (1979). Establishment and characterization of a human prostatic carcinoma cell line (PC-3). *Invest. Urol.* 17, 16–23.
- Kavanagh, K., Flynn, D.M., Jenkins, K.A., Zhang, L., and Wagner, J.D. (2011). Restoring HSP70 deficiencies improves glucose tolerance in diabetic monkeys. *Am. J. Physiol. Endocrinol. Metab.* 300, E894–E901.
- Kim, J.K., Fillmore, J.J., Sunshine, M.J., Albrecht, B., Higashimori, T., Kim, D.W., Liu, Z.X., Soos, T.J., Cline, G.W., O'Brien, W.R., et al. (2004). PKC- θ knockout mice are protected from fat-induced insulin resistance. *J. Clin. Invest.* 114, 823–827.
- Leto, D., and Saltiel, A.R. (2012). Regulation of glucose transport by insulin: traffic control of GLUT4. *Nat. Rev. Mol. Cell Biol.* 13, 383–396.
- Li, Y., Soos, T.J., Li, X., Wu, J., Degennaro, M., Sun, X., Littman, D.R., Birnbaum, M.J., and Polakiewicz, R.D. (2004). Protein kinase C θ inhibits insulin signaling by phosphorylating IRS1 at Ser(1101). *J. Biol. Chem.* 279, 45304–45307.
- Literáti-Nagy, B., Kulcsár, E., Literáti-Nagy, Z., Buday, B., Péterfai, E., Horváth, T., Tory, K., Kolonics, A., Fleming, A., Mandl, J., and Korányi, L. (2009). Improvement of insulin sensitivity by a novel drug, BGP-15, in insulin-resistant patients: a proof of concept randomized double-blind clinical trial. *Horm. Metab. Res.* 41, 374–380.
- Luo, J.H., and Weinstein, I.B. (1993). Calcium-dependent activation of protein kinase C. The role of the C2 domain in divalent cation selectivity. *J. Biol. Chem.* 268, 23580–23584.
- Marsland, B.J., and Kopf, M. (2008). T-cell fate and function: PKC- θ and beyond. *Trends Immunol.* 29, 179–185.
- Mendillo, M.L., Santagata, S., Koeva, M., Bell, G.W., Hu, R., Tamimi, R.M., Fraenkel, E., Ince, T.A., Whitesell, L., and Lindquist, S. (2012). HSF1 drives a transcriptional program distinct from heat shock to support highly malignant human cancers. *Cell* 150, 549–562.

- Min, J.N., Huang, L., Zimonjic, D.B., Moskophidis, D., and Mivechi, N.F. (2007). Selective suppression of lymphomas by functional loss of Hsf1 in a p53-deficient mouse model for spontaneous tumors. *Oncogene* 26, 5086–5097.
- Nelson, T.J., Sun, M.K., Hongpaisan, J., and Alkon, D.L. (2008). Insulin, PKC signaling pathways and synaptic remodeling during memory storage and neuronal repair. *Eur. J. Pharmacol.* 585, 76–87.
- O'Neil, R.G., Wu, L., and Mullani, N. (2005). Uptake of a fluorescent deoxyglucose analog (2-NBDG) in tumor cells. *Mol. Imaging Biol.* 7, 388–392.
- Pear, W.S., Nolan, G.P., Scott, M.L., and Baltimore, D. (1993). Production of high-titer helper-free retroviruses by transient transfection. *Proc. Natl. Acad. Sci. USA* 90, 8392–8396.
- Pirkkala, L., Nykänen, P., and Sistonen, L. (2001). Roles of the heat shock transcription factors in regulation of the heat shock response and beyond. *FASEB J.* 15, 1118–1131.
- Ratnayake, R., Covell, D., Ransom, T.T., Gustafson, K.R., and Beutler, J.A. (2009). Englerin A, a selective inhibitor of renal cancer cell growth, from *Phyllanthus engleri*. *Org. Lett.* 11, 57–60.
- Ryan, M.J., Johnson, G., Kirk, J., Fuerstenberg, S.M., Zager, R.A., and Torok-Storb, B. (1994). HK-2: an immortalized proximal tubule epithelial cell line from normal adult human kidney. *Kidney Int.* 45, 48–57.
- Samuel, V.T., and Shulman, G.I. (2012). Mechanisms for insulin resistance: common threads and missing links. *Cell* 148, 852–871.
- Santagata, S., Hu, R., Lin, N.U., Mendillo, M.L., Collins, L.C., Hankinson, S.E., Schnitt, S.J., Whitesell, L., Tamimi, R.M., Lindquist, S., and Ince, T.A. (2011). High levels of nuclear heat-shock factor 1 (HSF1) are associated with poor prognosis in breast cancer. *Proc. Natl. Acad. Sci. USA* 108, 18378–18383.
- Solimini, N.L., Luo, J., and Elledge, S.J. (2007). Non-oncogene addiction and the stress phenotype of cancer cells. *Cell* 130, 986–988.
- Taylor, S.E., Gafur, M.A., Choudhury, A.K., and Evans, F.J. (1981). Sapintoxin A, a new biologically active nitrogen containing phorbol ester. *Experientia* 37, 681–682.
- Tong, W.H., Sourbier, C., Kovtunovych, G., Jeong, S.Y., Vira, M., Ghosh, M., Romero, V.V., Sougrat, R., Vaulont, S., Viollet, B., et al. (2011). The glycolytic shift in fumarate-hydratase-deficient kidney cancer lowers AMPK levels, increases anabolic propensities and lowers cellular iron levels. *Cancer Cell* 20, 315–327.
- Trepel, J., Mollapour, M., Giaccone, G., and Neckers, L. (2010). Targeting the dynamic HSP90 complex in cancer. *Nat. Rev. Cancer* 10, 537–549.
- Vander Heiden, M.G., Cantley, L.C., and Thompson, C.B. (2009). Understanding the Warburg effect: the metabolic requirements of cell proliferation. *Science* 324, 1029–1033.
- Whitesell, L., and Lindquist, S. (2009). Inhibiting the transcription factor HSF1 as an anticancer strategy. *Expert Opin. Ther. Targets* 13, 469–478.
- Williams, R.D., Elliott, A.Y., Stein, N., and Fraley, E.E. (1978). In vitro cultivation of human renal cell cancer. II. Characterization of cell lines. *In Vitro* 14, 779–786.
- Yang, Y., Padilla-Nash, H.M., Vira, M.A., Abu-Asab, M.S., Val, D., Worrell, R., Tsokos, M., Merino, M.J., Pavlovich, C.P., Ried, T., et al. (2008). The UOK 257 cell line: a novel model for studies of the human Birt-Hogg-Dubé gene pathway. *Cancer Genet. Cytogenet.* 180, 100–109.
- Yang, Y., Valera, V.A., Padilla-Nash, H.M., Sourbier, C., Vocke, C.D., Vira, M.A., Abu-Asab, M.S., Bratslavsky, G., Tsokos, M., Merino, M.J., et al. (2010). UOK 262 cell line, fumarate hydratase deficient (FH-/FH-) hereditary leiomyomatosis renal cell carcinoma: in vitro and in vivo model of an aberrant energy metabolic pathway in human cancer. *Cancer Genet. Cytogenet.* 196, 45–55.
- Zou, J., Guo, Y., Guettouche, T., Smith, D.F., and Voellmy, R. (1998). Repression of heat shock transcription factor HSF1 activation by HSP90 (HSP90 complex) that forms a stress-sensitive complex with HSF1. *Cell* 94, 471–480.

LKB1 Inactivation Dictates Therapeutic Response of Non-Small Cell Lung Cancer to the Metabolism Drug Phenformin

David B. Shackelford,^{1,4,5,*} Evan Abt,^{4,5} Laurie Gerken,¹ Debbie S. Vasquez,¹ Atsuko Seki,³ Mathias Leblanc,¹ Liu Wei,⁴ Michael C. Fishbein,³ Johannes Czernin,⁴ Paul S. Mischel,^{3,4,6} and Reuben J. Shaw^{1,2,*}

¹Molecular and Cell Biology Laboratory

²Howard Hughes Medical Institute

Dulbecco Center for Cancer Research, The Salk Institute for Biological Studies, La Jolla, CA 92037, USA

³Department of Pathology and Laboratory Medicine

⁴Molecular and Medical Pharmacology

⁵Pulmonary and Critical Care Medicine

David Geffen UCLA School of Medicine, Los Angeles, CA 90095, USA

⁶Present address: Laboratory of Molecular Pathology, Ludwig Institute for Cancer Research, University of California at San Diego, La Jolla, CA 92093, USA

*Correspondence: dshackelford@mednet.ucla.edu (D.B.S.), shaw@salk.edu (R.J.S.)

<http://dx.doi.org/10.1016/j.ccr.2012.12.008>

SUMMARY

The LKB1 (also called STK11) tumor suppressor is mutationally inactivated in ~20% of non-small cell lung cancers (NSCLC). LKB1 is the major upstream kinase activating the energy-sensing kinase AMPK, making LKB1-deficient cells unable to appropriately sense metabolic stress. We tested the therapeutic potential of metabolic drugs in NSCLC and identified phenformin, a mitochondrial inhibitor and analog of the diabetes therapeutic metformin, as selectively inducing apoptosis in *LKB1*-deficient NSCLC cells. Therapeutic trials in *Kras*-dependent mouse models of NSCLC revealed that tumors with *Kras* and *Lkb1* mutations, but not those with *Kras* and *p53* mutations, showed selective response to phenformin as a single agent, resulting in prolonged survival. This study suggests phenformin as a cancer metabolism-based therapeutic to selectively target LKB1-deficient tumors.

INTRODUCTION

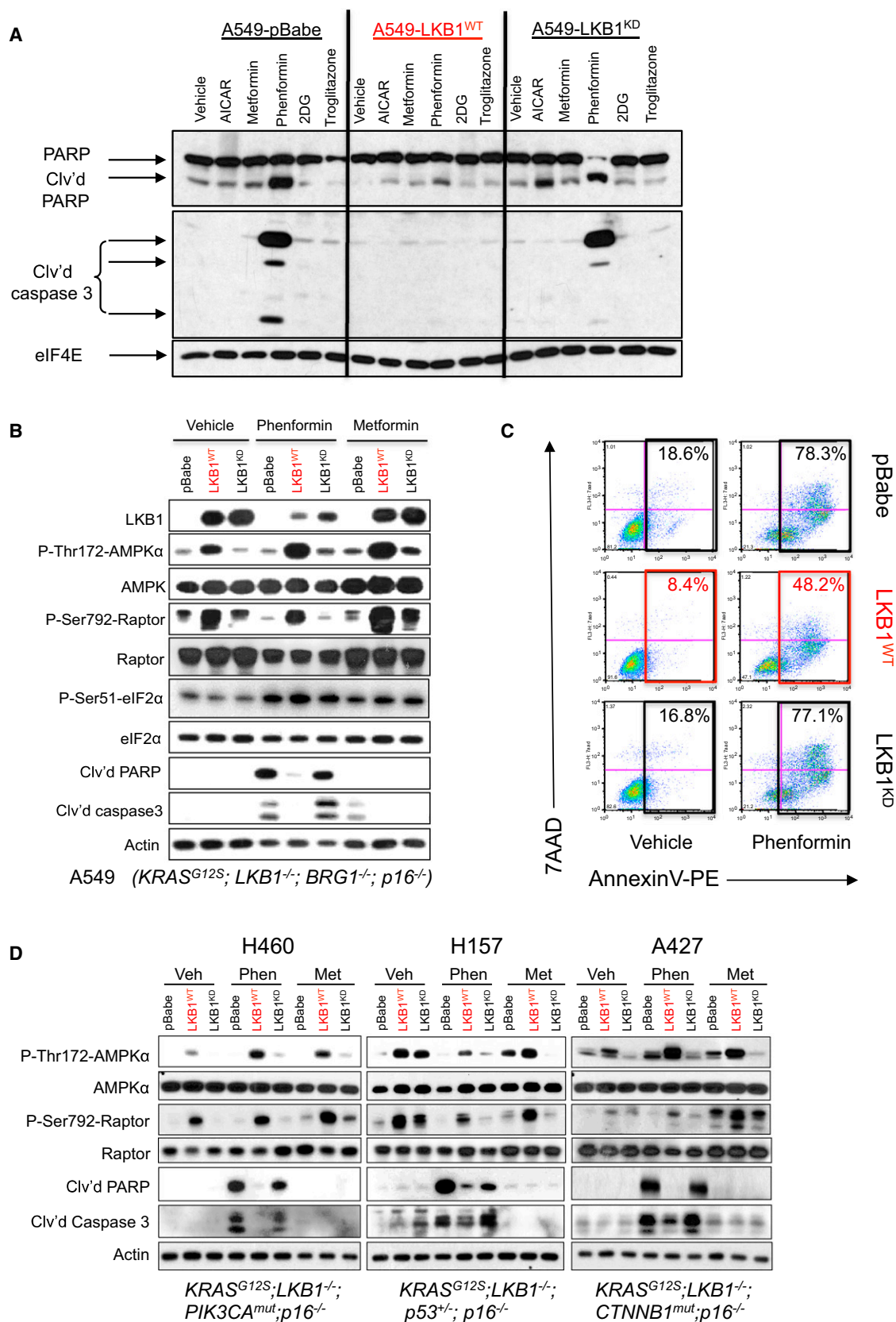
The gene encoding the serine/threonine kinase LKB1 was identified originally as the tumor suppressor gene responsible for the inherited cancer disorder Peutz-Jeghers syndrome (Hemminki et al., 1998). *LKB1* is also the second most commonly mutated tumor suppressor in sporadic human lung cancer (after *TP53*), particularly in multiple subtypes of NSCLC (Sanchez-Cespedes et al., 2002). *LKB1* is mutated in at least 15%–30% of NSCLCs, but the true frequency might be even higher because of difficulties in detecting inactivating lesions (Ding et al., 2008; Gill et al., 2011; Ji et al., 2007). Roughly half of the NSCLC tumors with *LKB1* mutation also bear activating *KRAS* mutations, and current

estimates suggest that 7%–10% of all NSCLC are comutated for *KRAS* and *LKB1* (Ding et al., 2008; The Cancer Genome Atlas). Studies in genetically engineered mouse models have shown that simultaneous activation of *Kras*^{G12D} and biallelic deletion of *Lkb1* in the lung dramatically increases tumor burden and metastasis (Carretero et al., 2010; Chen et al., 2012; Ji et al., 2007).

Biochemical and genetic analyses in worms, flies, and mice have shown that LKB1 is the major kinase phosphorylating the AMP-activated protein kinase (AMPK) under conditions of energy stress across metazoans (Hardie et al., 2012). AMPK is a highly conserved energy sensor and modulator of cell growth and metabolism that is activated under conditions of low intracellular ATP. Activated AMPK regulates cell growth at least in

Significance

Targeted therapeutics are making significant advances in subsets of NSCLC bearing activated oncogenic targets, such as *EGFR* and *ALK*. More prevalent in NSCLC are mutations in the *KRAS* oncogene coincident with mutations in the *LKB1* or *p53* tumor suppressor genes. Currently, there are limited options for *LKB1* mutant tumors. Here, we define the hypersensitivity of *LKB1*-defective cells to metabolic stress and test the therapeutic use of phenformin, a mitochondrial inhibitor and a former type 2 diabetes drug, in mouse models of NSCLC. Phenformin as a single agent reduced tumor burden and prolonged survival in *Kras*;*Lkb1* compound mutant mice but not *Kras*;*p53* mice. These findings suggest phenformin or related agents may find clinical utility to treat NSCLC bearing *LKB1* mutations.



(legend continued on next page)

part through inhibition of mTORC1 signaling achieved through dual phosphorylation of TSC2 (Inoki et al., 2003) and Raptor (Gwinn et al., 2008). AMPK is also hypothesized to maintain energy homeostasis in part by targeting defective mitochondria for autophagy (Egan et al., 2011) and control of fatty acid metabolism (Jeon et al., 2012).

The diabetes therapeutic biguanide compounds metformin and phenformin have been shown to inhibit complex I of the mitochondria (Dykens et al., 2008; El-Mir et al., 2000; Owen et al., 2000), resulting in increases in intracellular AMP and ADP that bind to the gamma regulatory subunit of AMPK and trigger LKB1-dependent phosphorylation of AMPK (Hawley et al., 2010). Consistent with activation of a low energy checkpoint, metformin treatment has been found to reduce tumor growth in xenograft, transgenic, and carcinogen-induced mouse cancer models (Algire et al., 2011; Anisimov et al., 2005; Buzzai et al., 2007; Memmott et al., 2010). Epidemiological studies revealed that diabetic patients taking metformin show a statistically significant reduced tumor incidence (Dowling et al., 2012; Evans et al., 2005). Given the extensive knowledge on the safety and use of metformin, there is increasing interest in using metformin as an anticancer agent (Taubes, 2012). Phenformin is a 50-fold more potent inhibitor of mitochondrial complex I than metformin (Dykens et al., 2008; Owen et al., 2000). Moreover, uptake of metformin, but not phenformin, into tissue appears to require the expression of Organic Cation Transporter 1 (OCT1), which is highly expressed in hepatocytes but not elsewhere (Shu et al., 2007). Consistent with greater potency and broader tissue bioavailability, phenformin delayed tumor progression in a *Pten*^{+/-} spontaneous lymphoma mouse model to a much greater extent than metformin (Huang et al., 2008).

In most settings metabolic stress induces a cytostatic growth arrest, dependent in part on AMPK. However, in cells lacking a functional LKB1 pathway, metabolic stress has been demonstrated to result in rapid apoptosis as the cells are unable to sense the energy stress and activate mechanisms to restore energy homeostasis (Shaw et al., 2004). Similar effects are seen in autophagy-defective cells that are unable to restore metabolism under low nutrient conditions (Jin et al., 2007). Here, we directly examine the hypothesis that LKB1-deficient lung tumors may be targeted with metabolic drugs.

RESULTS

Phenformin Selectively Induces Apoptosis in LKB1-Deficient NSCLC Cell Lines

We previously reported that nontransformed murine embryonic fibroblasts and HeLa cervical carcinoma cells deficient of

LKB1 exhibit increased apoptosis in response to metabolic stresses, including glucose deprivation and the AMP mimetic AICAR (Shaw et al., 2004). However, whether tumor cells undergo growth arrest or apoptosis following a particular cellular insult is dependent in part on the full constellation of oncogenic mutations present in the cell. We sought to determine whether NSCLC cell lines bearing KRAS mutations and lacking LKB1 would show enhanced rates of apoptosis following metabolic stress treatments compared to isogenic lines in which wild-type LKB1 had been restored.

We performed our initial studies using the KRAS mutant and LKB1-deficient NSCLC cell line A549 and derivatives with retrovirally introduced stable expression of wild-type LKB1 cDNA (LKB1^{WT}), a kinase-inactive LKB1 cDNA (LKB1^{KD}), or an empty vector (pBABE). These cells were treated with a variety of drugs with established roles in causing metabolic stress: metformin, phenformin, the cell permeable AMP-mimetic AICAR, the glycolysis inhibitor 2-deoxyglucose, or the thiazolidinedione compound troglitazone that acts as a mitochondrial inhibitor in addition to effects on PPAR γ (Hardie et al., 2012). Immunoblotting for cleaved caspase 3 and cleaved PARP as markers of apoptosis induction, we observed that, of the agents tested, only phenformin induced apoptosis in the cells lacking functional LKB1 (Figure 1A). Although both biguanides lowered ATP production in A549 cells (Figure S1A available online), phenformin reduced cellular ATP more, consistent with previous studies (Owen et al., 2000; Dykens et al., 2008). The ATP-lowering effect of both drugs was modestly blunted when wild-type LKB1 was present, consistent with the current model that AMPK acts to restore ATP levels and with previous findings in wild-type and *Lkb1*-deficient myocytes (Sakamoto et al., 2005). Consistent with a greater impact on ATP levels, phenformin but not metformin induced apoptosis in A549 cells lacking functional LKB1 by multiple measures: cleaved PARP and caspase 3 immunoblot (Figure 1B), activated caspase 3/7 luminescence assay (Figure S1B), and flow cytometry measuring AnnexinV and 7AAD staining (Figure 1C).

As human daily doses of metformin routinely run between 500 and 1,000 mg, and phenformin was given in the range of 50 to 100 mg previously when used clinically, we performed a direct comparison of metformin to phenformin at ratios of 1:1 and 10:1 in time course experiments in isogenic A549 cell lines. At early time points (8 or 12 hr) metformin at 2 or 20 mM or phenformin at 2 mM similarly induced AMPK signaling as shown by increased P-AMPK and P-Raptor levels (Figure S1C). However, only phenformin induced higher levels of cellular stress, triggering induction of P-Ser51 eIF2 α and its downstream target CHOP, and markers of apoptosis at later times (Figures 1B and

Figure 1. Phenformin Selectively Induces Apoptosis in LKB1^{-/-} NSCLC Tumor Cells

(A) A549 human NSCLC cells expressing the pBabe vector (A549-pBabe), full-length LKB1 (A549-LKB1^{WT}), or kinase-dead LKB1 (A549-LKB1^{KD}) were treated with vehicle (DMEM), AICAR (2 mM), metformin (20 mM), phenformin (2 mM), 2DG (10 mM), or troglitazone (25 μ M) for 48 hr. Lysates were immunoblotted with the indicated antibodies.

(B) A549 isogenic cell lines were treated for 24 hr with vehicle (DMEM), 2 mM phenformin, or 20 mM metformin. Lysates were immunoblotted with the indicated antibodies.

(C) Fluorescence-activated cell sorting (FACS) on cells stained with AnnexinV-PE and 7AAD following 48 hr treatment with vehicle or 2 mM phenformin.

(D) H460, H157, or A427 cell lines expressing the pBabe vector (pBabe), full-length WT LKB1 (LKB1^{WT}), or kinase-dead LKB1 (LKB1^{KD}) were treated for 24 hr with vehicle (DMEM), 2 mM phenformin, or 20 mM metformin. Lysates were immunoblotted with the indicated antibodies. Cancer gene driver mutations found in these cell lines listed under each.

See also Figure S1.

S1C). eIF2 α phosphorylation and upregulation of CHOP is observed in response to a diverse set of cellular stresses, including the unfolded protein response, nutrient deprivation, and mitochondrial stress (Muaddi et al., 2010; Ye et al., 2010; Chae et al., 2012). This suggests that although AMPK activation is a rapid and sensitive sensor of ATP loss, its signal plateaus and does not continue to increase with greater ATP loss, when additional stress sensing pathways like eIF2 α kinases may be engaged. Note that LKB1 did not impact P-eIF2 α or CHOP levels (Figures 1B and S1C), indicating that eIF2 α signaling is behaving here as an AMPK-independent pathway.

To examine how widely the sensitivity of cell lines to apoptosis by phenformin treatment is dictated by LKB1, we tested a panel of NSCLC lines that all had KRAS and LKB1 mutations, but each contained additional unique mutations. Isogenic derivatives of each cell line expressing wild-type or kinase-dead LKB1 were established and examined for sensitivity to phenformin or metformin. Despite each cell line containing different additional mutations, their sensitivity to undergo apoptosis following phenformin treatment was dictated by the LKB1 genotype in all cases (Figures 1D and S1B). Protection from phenformin-induced apoptosis was also observed with LKB1-reconstituted NSCLC and cervical cell lines H838 and HeLa, respectively, that are deficient for LKB1 but wild-type for KRAS (Figure S1B). Taken altogether, these data indicate that LKB1 dictates the sensitivity of a variety of cancer cell lines to phenformin-induced metabolic catastrophe regardless of the other tumor mutations present.

Developing Genetically Engineered Mouse Models of NSCLC that Can Be Monitored by Bioluminescence Longitudinally

Though a handful of studies have begun examining metabolic drugs in xenograft models, of particular concern is that subcutaneous placing a mass of tumor cells into an nonvascularized environment and without appropriate basement membrane attachment will itself result in severe metabolic stress and AMPK activation (Jeon et al., 2012; Laderoute et al., 2006), thus altering the very pathways being tested here for their impact on therapeutic outcome. To better model LKB1-deficient tumors, we took advantage of the well-characterized adenoviral cre-induced NSCLC models initiated by a conditionally activated *K-ras* oncogene (Lox-Stop-Lox-*Kras*^{G12D}, hereafter called *Kras*), combined with mice bearing floxed alleles of *p53* or *Lkb1* (Farago et al., 2012). As previously reported (Chen et al., 2012; Ji et al., 2007), when *p53* deficiency or *Lkb1* deficiency is combined with *Kras* activation, there is a dramatic increase in tumor burden leading to metastasis and earlier death, 10–12 weeks post-cre administration in both *Kras*;*Lkb1*^{L/L} and *Kras*;*p53*^{L/L} mice compared to 25+ weeks in *Kras* mice. To facilitate noninvasive imaging of tumor burden in longitudinal studies on these mice following therapeutic intervention, we crossed *Kras*, *Kras*;*Lkb1*^{L/L}, or *Kras*;*p53*^{L/L} mice with a ROSA26 lox-stop-lox luciferase allele (hereafter called *Luc*) (Safran et al., 2003) to generate *Kras*;*Luc* (*K_{Luc}*), *Kras*;*Lkb1*^{L/L};*Luc* (*KL_{Luc}*), or *Kras*;*p53*^{L/L};*Luc* (*KP_{Luc}*) mice. We bred these genotypes into the FVB background whose white coat allowed for noninvasive bioluminescent luciferase imaging without fur removal (Figures S2A–S2C). On the FVB genetic background, *KL_{Luc}* and *KP_{Luc}* mice exhibited comparable extents of tumor burden and similar latency.

We demonstrated that the bioluminescence output from the ROSA26-encoded luciferase was proportional to tumor burden (see the Supplemental Experimental Procedures). Analyzing lung tumor progression in *K_{Luc}*, *KL_{Luc}*, and *KP_{Luc}* mice, we detected bioluminescence as early as 4 weeks in *KL_{Luc}* and *KP_{Luc}* mice and confirmed the presence of adenomas by hematoxylin and eosin (H&E) staining (Figures 2A–2D; Figures S2A–S2C). At 6 weeks, tumors in the *KL_{Luc}* and *KP_{Luc}* mice began to change from adenomatous features to a more malignant tumor phenotype typical of carcinomas (Figure 2D). The most common histologic pattern in both *KL_{Luc}* and *KP_{Luc}* mice were high-grade invasive papillary adenocarcinoma. Squamous cell and adeno-squamous carcinoma were commonly observed tumor subtypes in *KL_{Luc}* mice, as previously noted (Ji et al., 2007). Interestingly, *KL_{Luc}* mice also displayed severe mucinous bronchiolar-epithelial adenocarcinoma (mBEAC) and bronchial mucinous papillary lesions, which were rarely seen in *K_{Luc}* or *KP_{Luc}* mice (Figure S2D). Of note, *LKB1* is frequently mutated in NSCLC patients with mucinous bronchiolar adenocarcinoma (Osoegawa et al., 2011).

Next, we characterized AMPK and mTORC1 signaling in *K_{Luc}*, *KL_{Luc}*, and *KP_{Luc}* lung tumors by immunohistochemical staining for P-AMPK and P-4E-BP1 (Figure 2E). Notably, the *KL_{Luc}* tumors contained the highest degree of P-4E-BP1, consistent with mTORC1 being particularly hyperactive in LKB1-deficient tumors. *Lkb1* deletion in the *Kras* mutant tumors was also accompanied by near-complete loss of P-AMPK as seen in many other tissues previously (Figure 2E).

Phenformin Activates the AMPK Signaling Pathway in *K_{Luc}* and *KP_{Luc}* Lung Nodules

To further examine their prospects as anticancer agents, we compared the bioavailability of metformin and phenformin in mouse lung tissue. Phenformin is a more lipophilic molecule compared to metformin (Figure S3A) and, unlike metformin requiring OCT1 for cell entry (Shu et al., 2007), readily permeates cells and tissues (Hawley et al., 2010; Huang et al., 2008). We performed intraperitoneal (i.p.) injections of vehicle, metformin, or phenformin on wild-type mice and isolated lung tissue at 1, 4, and 8 hr postinjection. Immunoblot analysis showed a weaker activation of the AMPK signaling pathway by metformin that only was observed at the 1 hr time point, unlike phenformin, which showed a robust activation at 4 hr postinjection (Figure 3A). However, mice bearing lung tumors did not tolerate daily i.p. injections over multiple weeks, and therefore phenformin was administered through the drinking water of mice fed ad libitum, as previously described (Appleyard et al., 2012; Huang et al., 2008). Quantitative analysis of P-AMPK staining in *KP_{Luc}* lung tumors from mice treated for 2 weeks showed greater activation of AMPK with phenformin than metformin (Figures S3B and S3C). As expected, no induction of P-AMPK was ever seen in *KL_{Luc}* tumors. Measurement of metformin and phenformin in blood plasma of mice by mass spectrometry revealed that levels of both were steady over days when administered via drinking water (Figure S3D).

Immunoblot analysis of snap-frozen *K_{Luc}*, *KL_{Luc}*, and *KP_{Luc}* lung tumor nodules revealed that tumors from *K_{Luc}* and *KP_{Luc}* mice treated with phenformin had higher levels of AMPK activation compared to vehicle treated mice, whereas *KL_{Luc}* lung tumors showed a lack of AMPK signaling as expected (Figure 3B).

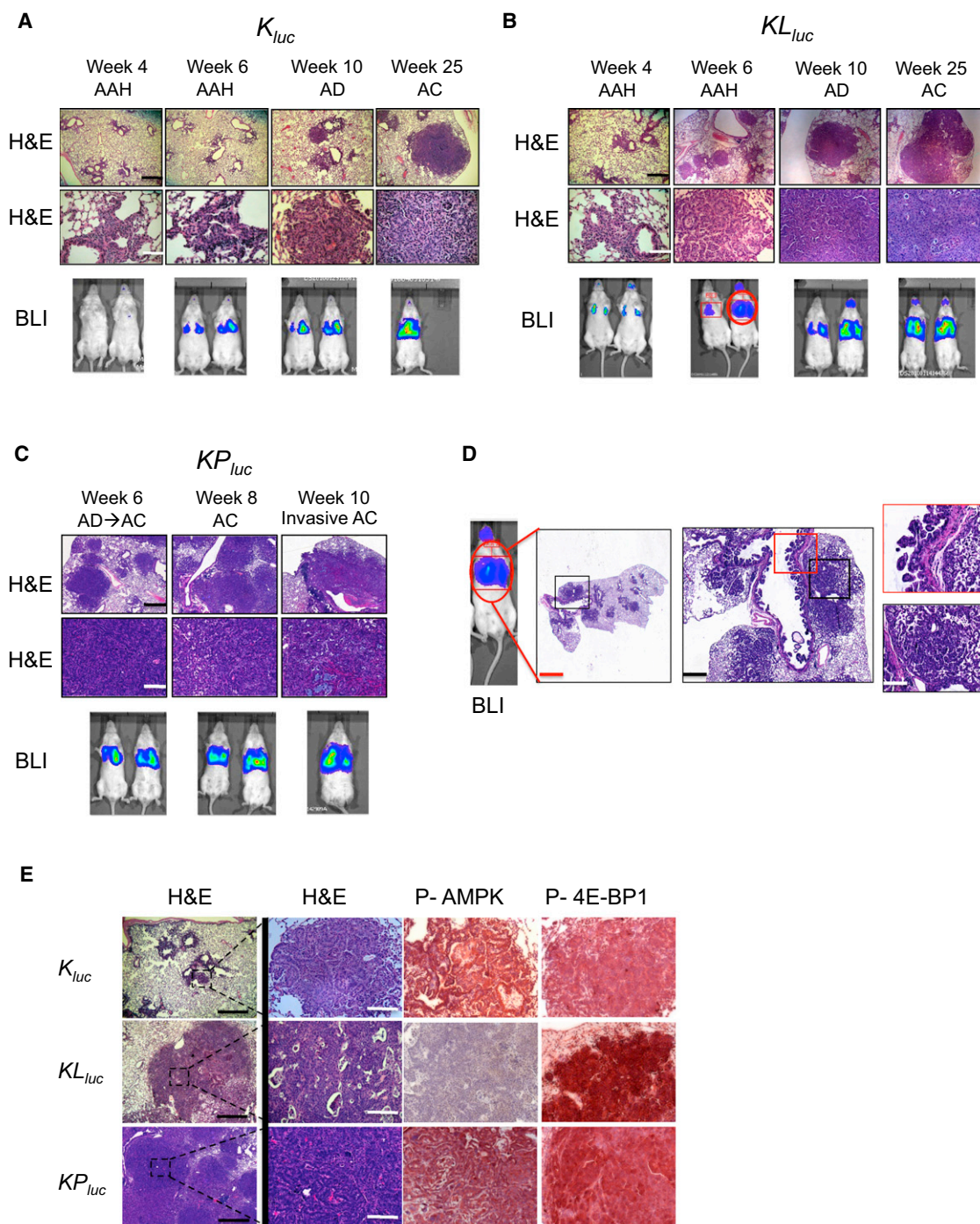


Figure 2. Time Course of Tumor Progression in K_{Luc} , KL_{Luc} , and KP_{Luc} Lung Tumor Models

(A–C) Tumor progression in K_{Luc} (A), KL_{Luc} (B), and KP_{Luc} (C) murine lung tumor measured by H&E staining or bioluminescence (bottom panel) at the indicated time points. Scale bars (black) = 300 μ m. Scale bars (white) = 100 μ m. Mice shown are representative of 10–12 mice per genotype.

(D) Detailed analysis of H&E-stained lung tumors from a KL_{Luc} mouse (red circled mouse from the bottom of B) at 6 weeks post-AdCre administration. Scale bars (red) = 1 mm, (black) = 500 μ m, and (white) = 100 μ m.

(E) Immunohistochemical analysis of representative lung tumors from K_{Luc} , KL_{Luc} , and KP_{Luc} mice 10 weeks post-AdCre administration. Sections were stained with H&E or the indicated antibodies. Scale bars (black) = 500 μ m. Scale bars (white) = 100 μ m.

See also Figure S2.

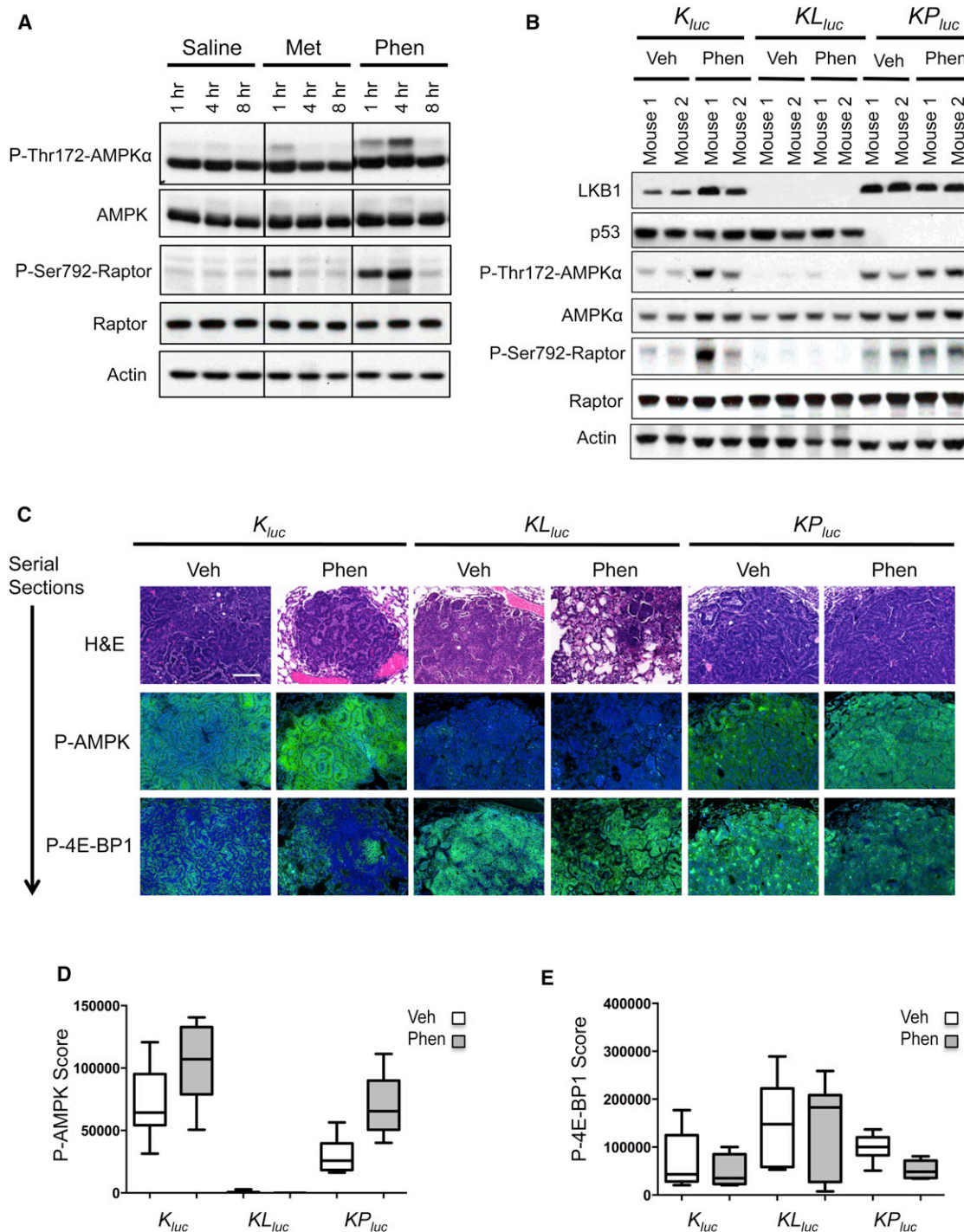


Figure 3. Phenformin Treatment Activates AMPK Pathway in K-Ras-Driven Lung Tumors In Vivo

(A) Lung tissue lysates from wild-type FVB mice following i.p. injection of saline (0.9%), metformin (300 mg/kg), or phenformin (150 mg/kg) and immunoblotted with the indicated antibodies.

(B) Lysates of lung tumor nodules from K_{Luc} , KL_{Luc} , and KP_{Luc} mice treated with vehicle (water) or phenformin via 5 days ad lib feeding were immunoblotted with the indicated antibodies.

(C) Representative images of K_{Luc} , KL_{Luc} , and KP_{Luc} lung tumor sections stained with hematoxylin and eosin (H&E), P-AMPK, or P-4E-BP1. P-AMPK or P-4E-BP1 positively stained cells (in green) and nuclei (in blue). Scale bar = 100 μ m.

(D and E) Box plots representing the mean P-AMPK (D) or P-4E-BP1 (E) signal from K_{Luc} , KL_{Luc} , and KP_{Luc} lung tumors treated with vehicle or phenformin. n = 6 mice analyzed per treatment group in each genotype (K_{Luc} , KL_{Luc} , and KP_{Luc}) treatment group.

All data are represented as the mean \pm SEM.

See also Figure S3.

Normal lung lysates from wild-type FVB mice given phenformin ad libitum for 2 weeks showed an increase in AMPK signaling and lowered mTORC1 signaling, when compared to the vehicle treated mice (Figure S3E). Phenformin also increased levels of P-eIF2 α and its target BiP/Grp78 in normal lung as well as in lung tumors (Figures S3E and S3F) (the CHOP antibody afore used recognized human but not mouse CHOP). There was no observed difference in IGF-IR/IR or Akt signaling between the vehicle- or phenformin-treated mice. Analysis of the AMPK activation in lung tumors by quantitative immunohistochemistry following phenformin treatment paralleled the results observed by immunoblotting (Figures 3C and 3D), and phenformin was observed to modestly reduce the mTORC1 substrate P-4E-BP1 levels in all genotypes (Figures 3C and 3E).

Lkb1^{-/-} Lung Tumors Reveal Higher Levels of Apoptosis and Reduced Tumor Burden following Phenformin Treatment

Having established that phenformin had greater bioavailability and was capable of more potently inducing energy stress in tumors than metformin, we next tested phenformin as a single-agent therapeutic in the *K_{luc}*, *KL_{luc}*, and *KP_{luc}* mice. Following tumor induction, we performed bioluminescent imaging (BLI) to monitor tumor growth and sorted mice into equal groups according to their BLI value to normalize the cohorts receiving vehicle or phenformin (Figures S4A–S4C). We first tested phenformin as a chemotherapeutic by initiating treatment 6 weeks postadenoviral cre delivery for the *KP_{luc}* and *KL_{luc}* mice and 9 weeks postadenoviral cre delivery in the *K_{luc}* mice (Figure S4D) in order to target aggressively growing tumors transitioning from benign to malignant tumors (Figures 2A–2C). After 3 weeks of treatment, BLI imaging revealed modestly reduced tumor burden in mice of all genotypes receiving phenformin, but the only statistically significant decrease was in the *KL_{luc}* lung tumors (Figures 4A and 4B).

To better quantify tumor burden in mice, we combined BLI with quantitative histological analysis. H&E-stained lungs were imaged with morphometric software to quantify the surface area composed of tumor as opposed to normal tissue of representative cross-sections of each lung lobe for each mouse was determined (Figures S4E and S4F). Importantly, tumor burden determined by histological analysis correlated closely with BLI. *KL_{luc}* mice showed significant reductions in lung tumor area (Figures 4C and 4D), while modest reductions in tumor burden were also seen in both *K_{luc}* and *KP_{luc}* mice. Normalization of the tumor burden for each tumor genotype, performed by calculating the ratio of phen:veh tumor mass, showed the largest decrease in tumor burden for the *KL_{luc}* mice as compared to *K_{luc}* and *KP_{luc}* mice (Figure S4G). In addition, we observed no change in rate of metastasis following phenformin treatment in any of our therapeutic trials. These results demonstrate phenformin as a single agent selectively attenuates *Lkb1*-deficient lung tumor growth in vivo.

We next analyzed apoptosis and tumor proliferation in the lung tumors by TUNEL and Ki67 staining, respectively. Phenformin treatment modestly reduced Ki67 index in *KL_{luc}* tumors but not *K_{luc}* and *KP_{luc}* tumors (Figures 4E and 4F), and TUNEL staining revealed that *KL_{luc}* lung tumors had the highest levels of apoptotic tumor cells following phenformin (Figures 4E and

4G). Interestingly, *KL_{luc}* lung tumors also had higher basal levels of apoptosis compared to *KP_{luc}* and *K_{luc}* tumors, perhaps reflecting the prosurvival role of LKB1 in restoring energy homeostasis under conditions of metabolic stress, which may spontaneously arise in the context of a tumor.

Phenformin Induced a Significant Increase in Survival and Therapeutic Response in *KL_{luc}* Mice following Long-Term Treatment

Given the response of late-stage *KL_{luc}* lung tumors to phenformin treatment, we decided to treat earlier stage lung tumors in *KL_{luc}* and *KP_{luc}* mice. To better mimic the human clinical use of biguanides, we used oral gavage (o.p.) to deliver daily the maximum tolerated dose of 100 mg/kg phenformin starting at 3 weeks posttumor induction (Figure S5A). As expected, delivery of phenformin by this method resulted in AMPK pathway activation in *KP_{luc}* but not *KL_{luc}* tumor nodules (Figures S5B and S5C). Mass spectrometry on phenformin in blood plasma following o.p. delivery demonstrated a rapid uptake of phenformin followed by a steady decrease in blood plasma over 24 hr (Figure S5D). Importantly, these FVB mice are on a chow diet and nondiabetic, and the dose of phenformin used following 6 weeks of daily administration did not significantly impact blood plasma insulin levels, glucose levels, or lead to increased blood lactate levels as compared to vehicle-treated mice (Figures S5E–S5H).

The loss of LKB1 function in tumors predicts increased glycolytic metabolism and ¹⁸F-fluoro-2-deoxyglucose positron emission tomography (FDG-PET) avidity as shown in gastrointestinal polyps from *Lkb1^{+/-}* mice (Shackelford et al., 2009) and in NSCLC in mice and humans (Chen et al., 2012). Therefore, we explored the use of FDG-PET as a surrogate endstage biomarker in combination with microCT (μ CT) imaging to longitudinally monitor tumor progression and response in *KL_{luc}* and *KP_{luc}* mice following phenformin treatment. *KL_{luc}* and *KP_{luc}* mice were given baseline FDG-PET and μ CT scans, which were scored by a radiologist blinded to the identities of the mice. Mice in both groups were determined to be negative for tumors by both PET and CT scans and were randomly sorted into treatment groups (Figure 5C).

When phenformin was administered by o.p. for an extended time, it significantly increased survival in *KL_{luc}* mice compared to *KP_{luc}* mice (Figures 5A and 5B). Phenformin treatment resulted in delayed tumor progression in *KL_{luc}* but not *KP_{luc}* mice as shown by μ CT measurements of lung tumor volume over time for individual mice in the study (Figures 5C–5E, S5J, and S5K). At 4 and 6 weeks of treatment, average lung tumor size was significantly reduced in *KL_{luc}* mice (Figure 5D). There was a trend toward smaller tumors in the *KP_{luc}* mice but did not reach statistical significance (Figure 5E). However, at endstage, there was the presence of large, advanced solid tumors of the vehicle and phenformin groups in both *KL_{luc}* and *KP_{luc}* tumor genotypes (Figure S5I). The ¹⁸FDG uptake into tumors was quantified by the standardized uptake value (SUVmax) at 4 and 6 weeks of treatment. The SUVmax for phenformin-treated *KL_{luc}* lung tumors was significantly reduced compared to vehicle ones (Figure 5F). No difference was seen in the SUVmax for the *KP_{luc}* mice at these same time points (Figure 5G). These data suggest a therapeutic response in *KL_{luc}* lung tumors following phenformin treatment. However, the SUVmax values in endstage tumors were

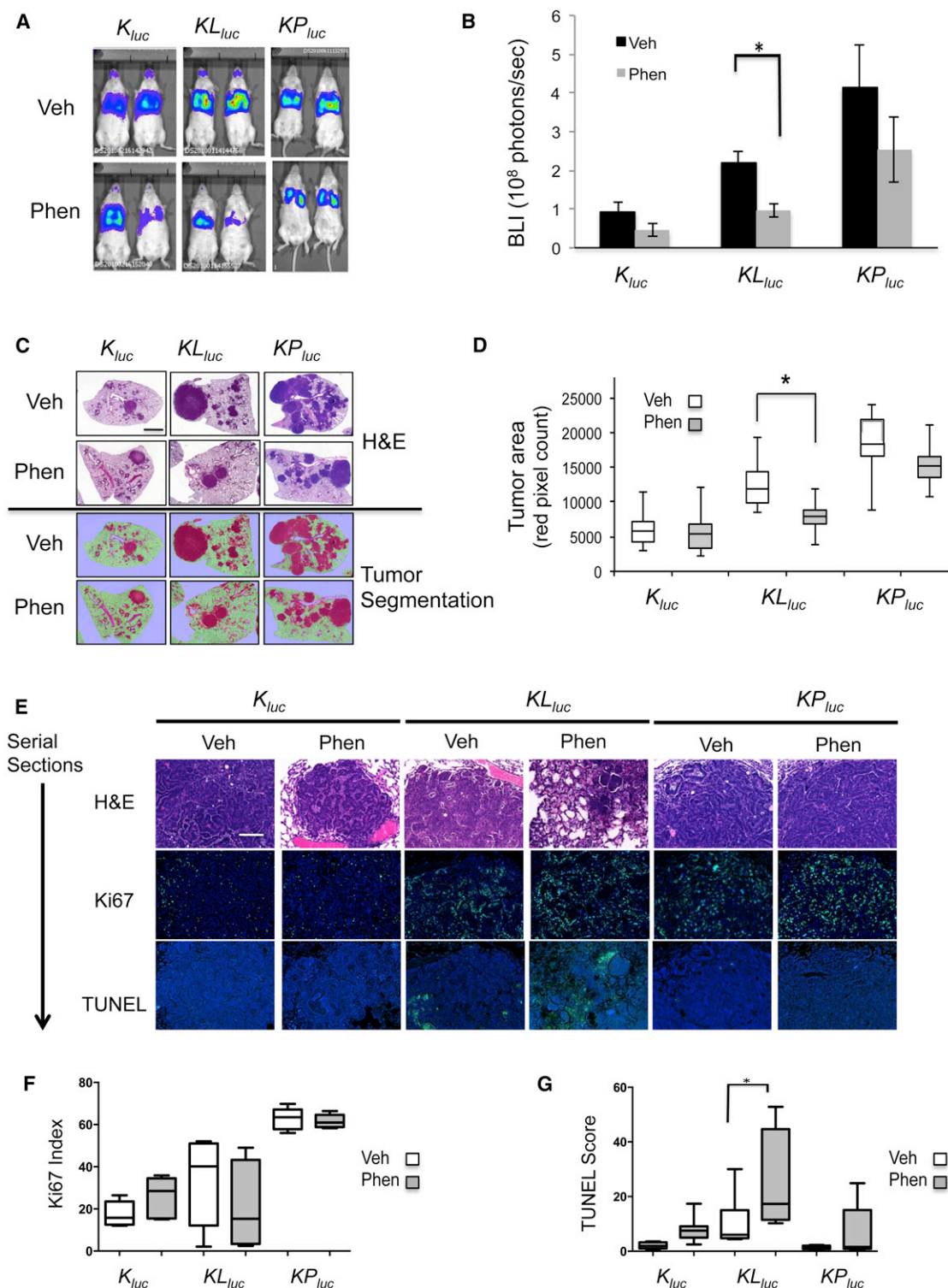


Figure 4. Phenformin Preferentially Inhibits LKB1-Deficient Lung Tumors In Vivo

(A) Representative ventral view images of bioluminescence from K_{luc} , KL_{luc} , and KP_{luc} mice. Bioluminescence imaging (BLI) performed on K_{luc} (veh, n = 11; phen, n = 12 mice), KL_{luc} (veh, n = 10; phen, n = 10 mice), and KP_{luc} (veh, n = 7; phen, n = 7 mice) following 3 weeks of treatment with vehicle (water) or phenformin via ad lib feeding.

(B) Average BLI for each treatment group of the K_{luc} , KL_{luc} , and KP_{luc} mice at 3 weeks treatment.

(C) Representative images of tumor burden in K_{luc} , KL_{luc} , and KP_{luc} mice as shown by H&E-stained lung sections (top panel) or the same images tissue segmented and pseudocolored with Inform software (bottom panel). Scale bar = 1 mm.

(legend continued on next page)

increased in both KL_{luc} and KP_{luc} mice (Figures S5L and S5M), suggesting the emergence of phenformin-resistant tumors in KL_{luc} mice (Figures S5J and S5L).

Histopathological analysis of 6 week o.p. phenformin-treated lungs revealed that KL_{luc} but not KP_{luc} lung tumors had large regions of necrosis, which was absent in the vehicle-treated controls (Figure 6A; Figure S6A). Further analysis of KL_{luc} lung sections revealed an 8-fold increase in necrotic tumor areas as shown by the presence of necrotic bodies with ghost cells (Figures 6B and 6F). Staining of KL_{luc} and KP_{luc} tumors for cleaved caspase 3 revealed a significant increase in tumor cell apoptosis in both KL_{luc} and KP_{luc} lung tumors following phenformin (Figures 6C, 6G, S6A, and S6B) but no difference in Ki67 indices in either genotype following phenformin treatment (Figures 6D, 6H, S6A, and S6C). Elevated P-AMPK levels were observed in both tumor and lung parenchyma of phenformin-treated KP_{luc} mice (Figure S6D), further reflecting that this dosing regimen was capable of inducing energy stress in these different lung cell populations. Strikingly, the abundant mucinous bronchiolar-epithelial adenocarcinoma (mBEAC), which occluded much of the upper airways in KL_{luc} mice, showed a 2-fold decrease in surface area in mice receiving phenformin compared to the vehicle group (Figures 6E and 6I). Altogether, these results indicate that phenformin as a single agent induces a tumor response in both KL_{luc} and KP_{luc} lung tumors with *Lkb1*-deficient tumors showing the most robust overall therapeutic response to phenformin.

Mitochondrial Defects May Sensitize LKB1-Deficient NSCLC Tumor Cells to Phenformin

To examine the molecular mechanism behind the selective induction of apoptosis in LKB1-deficient lung cancer cells, we analyzed signals downstream of its main target AMPK. Recently, we demonstrated that AMPK phosphorylates and activates the autophagy kinase ULK1, which is required for mitophagy and cell survival under starvation conditions (Egan et al., 2011). We previously observed an accumulation of mitochondria with defective mitochondrial membrane potential ($\Delta\psi$) in *Ampk*- and *Ulk1*-KO fibroblasts and hepatocytes (Egan et al., 2011), similar to that observed in *Lkb1*-KO hematopoietic stem cells (Nakada et al., 2010), so we examined here whether ULK1 and mitochondrial homeostasis might be disrupted in LKB1 mutant NSCLC cells. A549 cells reconstituted with functional LKB1 showed AMPK activation and its phosphorylation of endogenous ULK1 on Ser555 following phenformin treatment, paralleling phosphorylation of Raptor, another AMPK substrate (Figure 7A). Phenformin treatment also resulted in a decrease in levels of the p62/Sqstm1 protein only in the wild-type LKB1-reconstituted cells, indicative of efficient autophagy reliant on LKB1 function (Figure 7A). Importantly, p62 levels were not reduced by metformin here, perhaps reflecting the lower level of AMPK signaling from

metformin as compared to phenformin. Expression of functional LKB1 in LKB1-deficient H157 and H838 cells also restored their P-Ser555 ULK1 signal, indicating this is a general defect in LKB1-deficient NSCLC cell lines (Figure S7A). As observed previously in AMPK- and ULK1-defective fibroblasts and hepatocytes, here A549, H157, and H838 NSCLC cells defective for LKB1 function exhibited increased mitochondrial content as assayed by flow cytometry for mitotracker red staining (Figure 7B and S7B), suggesting that reconstitution of wild-type LKB1 into these LKB1-deficient NSCLC cell lines may actively induce functional mitophagy. A549-pBabe and A549-LKB1^{KD} cells had impaired $\Delta\psi$, reflecting impaired mitochondrial membrane integrity, as exhibited by the failure of JC-1 dye to accumulate in the mitochondrial membrane when compared to A549-LKB1^{WT} cells (red to green ratio of JC-1 staining in Figure 7C). Following treatment with phenformin, LKB1-deficient tumor cells showed a complete loss of mitochondrial membrane potential, whereas expression of functional LKB1 fully prevented this loss. In contrast, treatment with the mitochondrial uncoupler CCCP induced loss of $\Delta\psi$ in all cell lines, though LKB1-reconstituted cells still retained the most mitochondrial membrane potential (Figure 7C). As one measure of functionality of the mitochondria in these cell lines, we examined oxygen consumption as a direct measurement of mitochondrial respiration. Consistent with mitochondrial defects, A549-pBabe and A549-LKB1^{KD} cells had a lower basal rate of oxygen consumption rate (OCR) than the A549^{WT} cells (Figures 7D and S7C). Treatment of these cells with either phenformin or rotenone resulted in inhibition of mitochondrial respiration as shown by an acute drop OCR in levels (Figures S7C and S7D). OCR levels tracked inversely with mitotracker red staining here, consistent with the idea that the accumulated mitochondria in the LKB1-deficient cells are respiration defective.

Mitochondrial Complex I inhibition has been reported to induce reactive oxygen species (ROS) similar to that seen with Complex III inhibition (Hirst et al., 2008; Kushnareva et al., 2002). Thus, we next examined the release of mitochondrial reactive oxygen species (mtROS) following the treatment with phenformin, metformin, or the complex III inhibitor antimycin A and found that phenformin was a more potent inducer of mtROS than metformin (Figure S7E). Staining of A549-pBabe and A549-LKB1^{KD} cells showed modest elevations in mtROS compared to A549-LKB1^{WT} cells, both basally and following phenformin treatment (Figure 7E). To examine whether the doses of phenformin used in our therapeutic study were effective enough to induce LKB1-dependent effects on mitophagy, we performed western blot analysis of lung tumor nodules from mice with and without phenformin treatment for 5 days and discovered reduced phosphorylation of ULK1 and an accumulation of the mitophagy regulator Parkin in KL_{luc} but not K_{luc} , or KP_{luc} lung tumors (Figure 7F). These results suggest defects of the AMPK-ULK1 signaling

(D) Box plots representing the mean tumor burden following 3 weeks of treatment. Tumor burden was calculated by averaging the red pseudocolored tumor area from H&E-stained whole lung sections shown in (C) bottom panel.

(E) Representative images of H&E-, Ki67-, or TUNEL-stained K_{luc} , KL_{luc} , and KP_{luc} lung tumor sections. Ki67 or TUNEL positively stained cells (in green) and nuclei (in blue). Scale bar = 100 μ m.

(F and G) Box plots representing the mean Ki67 (F) and TUNEL scores (G) from K_{luc} , KL_{luc} , and KP_{luc} mice treated with vehicle or phenformin. (*) Statistical significance ($p < 0.05$) calculated using a nonparametric one-way ANOVA (Tukey test).

All data are represented as the mean \pm SEM. See also Figure S4.

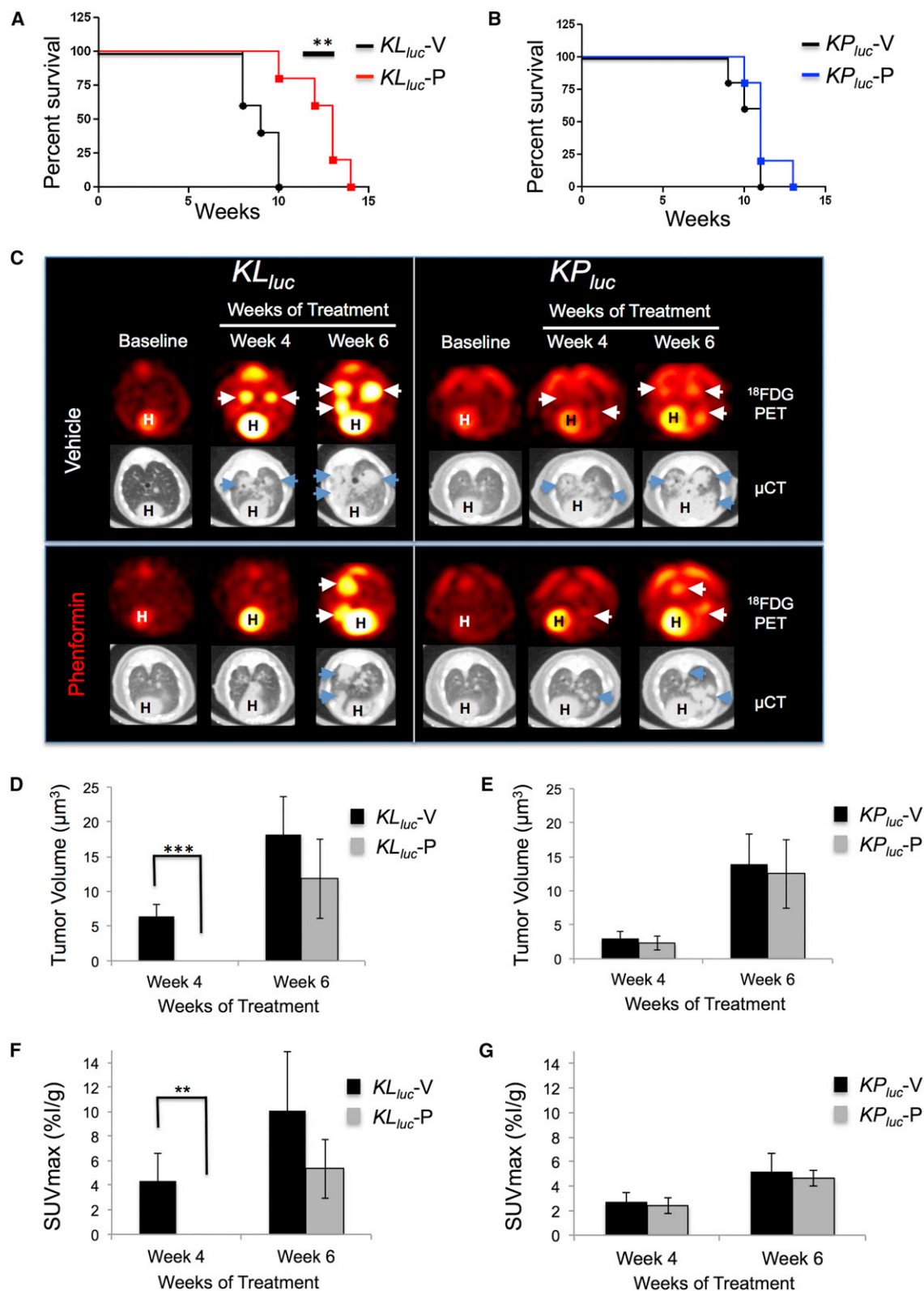


Figure 5. Phenformin Significantly Increased Overall Survival and Slowed Tumor Progression in KL_{luc} Mice Shown by ^{18}F FDG-PET and μ CT Imaging

(A and B) Kaplan-Meier survival curves for KL_{luc} mice (A) or KP_{luc} mice (B) treated with vehicle (n = 5) or phenformin (n = 5) for each tumor genotype, respectively, with a **p = 0.008 for KL_{luc} mice determined by Wilcoxon logrank test.

(legend continued on next page)

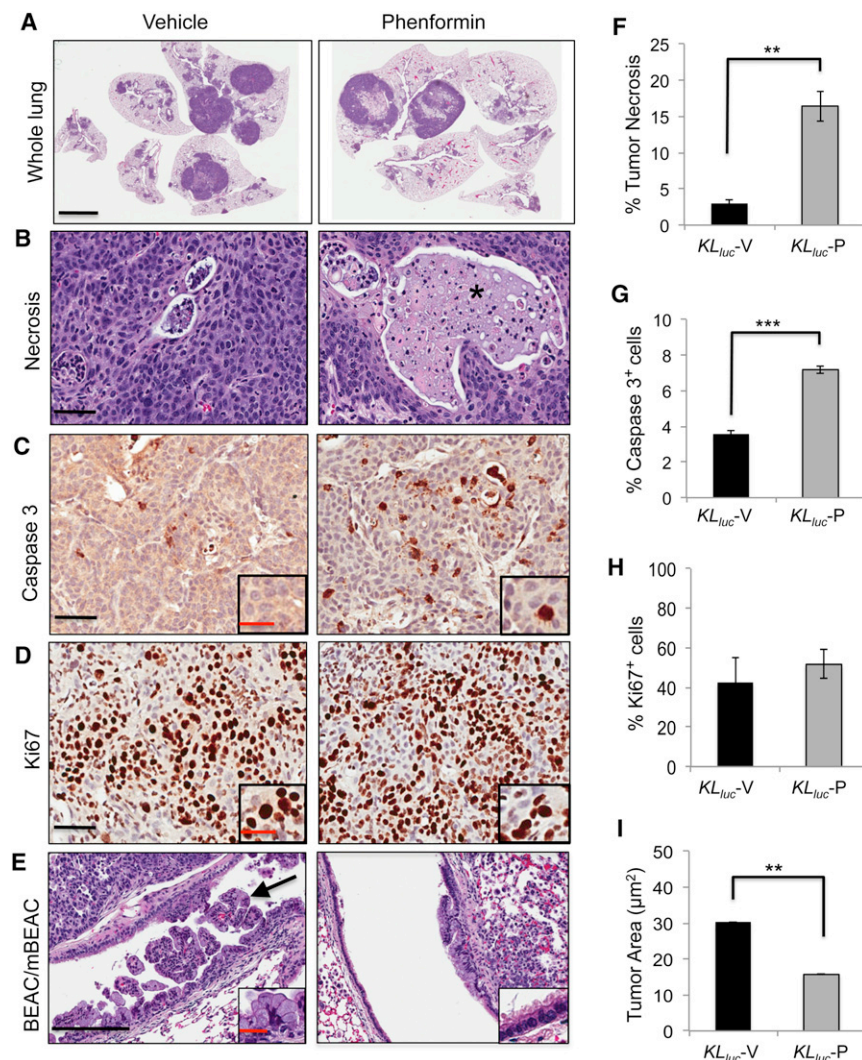


Figure 6. Phenformin Induces a Significant Therapeutic Response in *KL_{luc}* Lung Tumors

(A) Hematoxylin and eosin (H&E)-stained whole lung sections of *KL_{luc}* mice treated with vehicle (saline) or phenformin, scale bar = 4 mm.

(B–E) Representative images of lung tumors from *KL_{luc}* mice treated with vehicle (saline) or phenformin. (B) Tumor necrosis, scale bar = 50 μm. (C) Activated caspase 3, scale bar = 50 μm. Inset represents magnification of caspase-3-stained cells, scale bar = 25 μm. (D) Ki67 stain, scale bar = 50 μm. Inset represents magnification of Ki67-stained cells, scale bar = 25 μm. (E) Mixture of bronchiolar-epithelial adenocarcinoma (BEAC) and mucinous bronchiolar-epithelial adenocarcinoma (mBEAC) shown with arrow, scale bar = 200 μm. Inset represents magnification of mBEAC cells, scale bar = 50 μm.

(F) Mean percentage of necrotic tumor area in vehicle- and phenformin-treated *KL_{luc}* mice. **p = 0.002.

(G) Mean percentage of tumor cell apoptosis from vehicle- and phenformin-treated *KL_{luc}* mice. ***p < 0.0001.

(H) Ki67 index for vehicle- and phenformin-treated *KL_{luc}* mice.

(I) Total BEAC and mBEAC tumor area (μm²) in vehicle- and phenformin-treated *KL_{luc}* mice. **p < 0.006. n = 5 *KL_{luc}* mice per treatment group (vehicle or phenformin). Statistical analysis performed using an unpaired Student's t test.

All data are represented as the mean ± SEM. See also Figure S6.

pathway and mitophagy in vivo following loss of LKB1 (Figure 7G), which may help sensitize these tumors to the effects of phenformin on mitochondrial integrity.

DISCUSSION

In this study we have found that the diabetes drug phenformin shows selective and significant antitumor activity in genetically engineered mouse models of lung cancer bearing LKB1 mutations. Molecular targeted therapeutics hold great promise for the future of cancer treatment, but for the 15%–30% of NSCLC bearing inactivating mutations in *LKB1*, there has been little in the way of targeted agents to date. As loss of LKB1 results in

tumor model with *Kras* and *Lkb1* mutations similar to the one used here showed a minimal therapeutic effect (Liang et al., 2010), perhaps because of the multitude of pathways deregulated from LKB1 deficiency that can still fuel tumorigenesis even when mTORC1 is suppressed. Hyperactivation of Src family kinases was also discovered as a biochemical marker and potential therapeutic target in *Lkb1*-deficient lung tumors (Carretero et al., 2010). Combination of the Src inhibitor dasatinib with PI3K and MEK inhibitors in similar mouse lung tumor models showed a synergistic tumor response, though dasatinib as a single agent displayed a minimal effect (Carretero et al., 2010). The fact that phenformin induces therapeutic response as a single agent taken together with the success of dasatinib

(C) Representative images of micro-FDG-PET and CT scans of lungs from *KL_{luc}* and *KPluc* mice at baseline (pretreatment) or following 4 and 6 weeks treatment with vehicle or phenformin. Heart is labeled (H), and tumors are labeled with arrows (white or blue).

(D and E) Mean tumor volume measured by micro-CT at 4 and 6 weeks treatment for *KL_{luc}* (D) and *KPluc* (E) mice, respectively. ***p = 0.0009 for *KL_{luc}* mice as determined by Wilcoxon rank-sum test.

(F and G) Mean FDG-PET SUVmax measured at 4 and 6 weeks treatment for *KL_{luc}* (F) and *KPluc* mice (G), respectively. **p = 0.005 for *KL_{luc}* mice as determined by Wilcoxon rank-sum test. n = 5 mice per treatment group of each genotype.

All data are represented as the mean ± SEM. See also Figure S5.

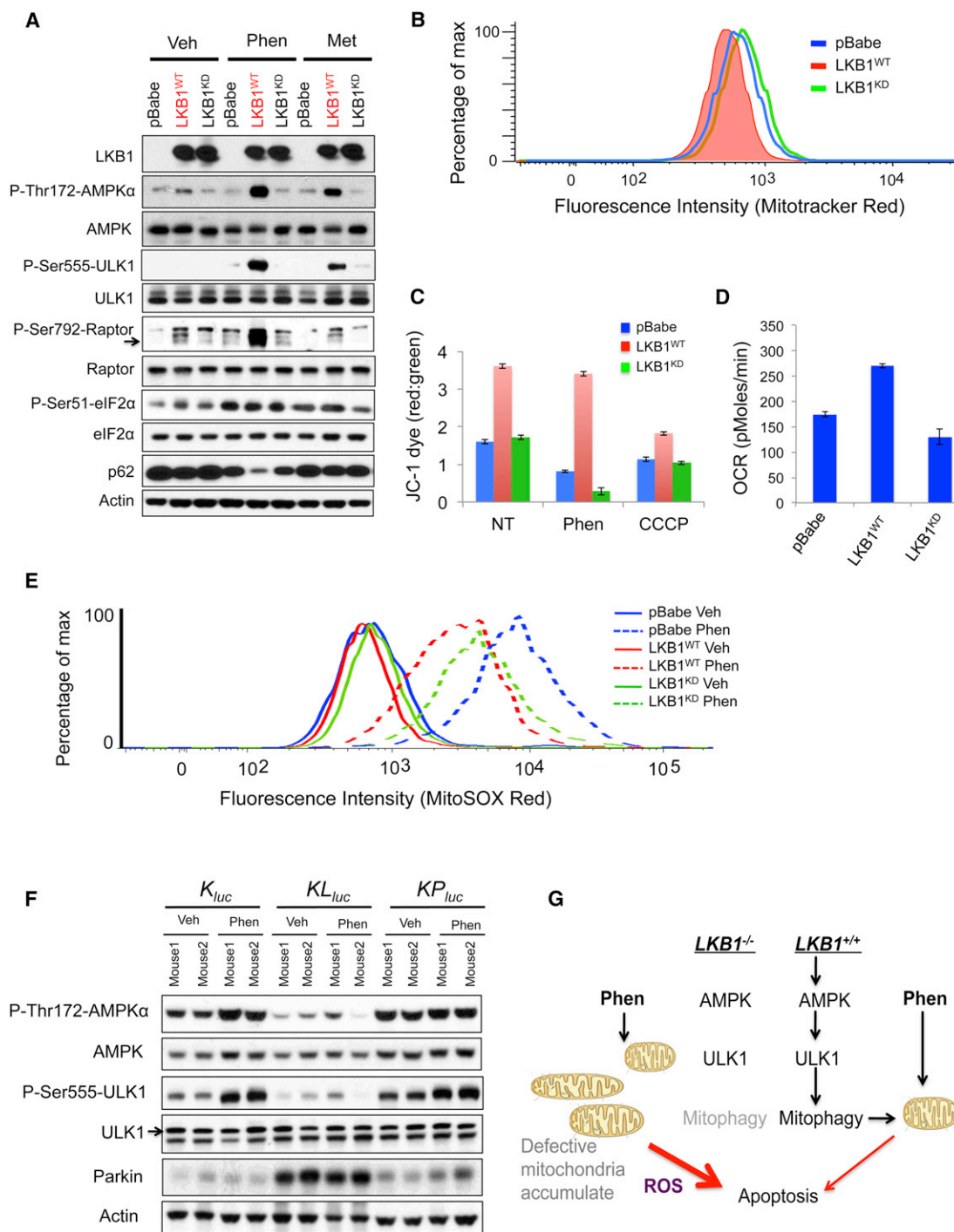


Figure 7. Mitochondrial Defects in *LKB1*^{-/-} NSCLC Confer Sensitivity to Phenformin

(A) Lysates from A549-pBabe, A549-LKB1^{WT}, and A549-LKB1^{KD} cells were treated with vehicle (DMEM), phenformin (2 mM), or metformin (20 mM) for 4 hr and immunoblotted with the indicated antibodies.

(B) FACS analysis of cells from (A) stained with Mitotracker Red.

(C) Cells from (A) stained with JC-1 dye following 4 hr of treatment with vehicle (DMEM), phenformin (2 mM), metformin (20 mM), or CCCP (100 μM). Mitochondrial membrane potential ($\Delta\psi$, red/green ratios) were measured by emission of red and green fluorescence using FACS.

(D) Oxygen consumption rate (OCR) of cells from (A).

(E) Cells from (A) were stained with MitoSOX Red following 16 hr of treatment with vehicle (DMEM) or phenformin (2 mM) and analyzed by FACS.

(F) Lung tumor lysates from *K_{Luc}*, *KL_{Luc}*, and *KP_{Luc}* mice treated 5 days with vehicle or phenformin ad lib feeding were immunoblotted with the indicated antibodies.

(G) Model illustrating mitochondrial defects and phenformin induced cell death in *LKB1*^{-/-}-deficient tumor cells.

All data are represented as the mean \pm SEM. See also Figure S7.

in combinations suggests that phenformin may also show greater success in defined combinations, which will be a focus for future investigations. Of relevance, a recent study treating the same three NSCLC models used here with a combination of standard-of-care docetaxel with MEK inhibitors revealed that *Kras*; *Lkb1* mutant tumors were selectively resistant to that combination, unlike *Kras* alone or *Kras*; *p53* mutant tumors (Chen et al., 2012). It is in the context of this body of work that selective sensitivity of *Kras*; *Lkb1* tumors to phenformin as a single agent in aggressive autochthonous models of lung cancer is so notable.

We have been interested in whether one could utilize metabolic stress-inducing compounds as anticancer agents for LKB1 mutant tumors in their autochthonous setting in the intact organism ever since we observed that LKB1-deficient cells were sensitive to apoptosis induced by metabolic stress in culture (Shaw et al., 2004). We focused our attention on the biguanide family of antidiabetes therapeutics for their ability to reduce intracellular ATP levels as a result of mitochondrial complex I inhibition. The absence of LKB1 signaling to AMPK means such cells will go for an extended time without activation of this sensor to restore ATP levels. We expect that mitochondrial damage and ATP loss also activate AMPK-independent stress sensing pathways, as we demonstrate here with multiple markers of the eIF2 α signaling pathway. These findings are consistent with previous reports of AMPK-independent effects of biguanides (Foretz et al., 2010; Kalender et al., 2010). Our results are also consistent with recent studies demonstrating that AMPK mediates cell survival following metabolic stress not only through effects on ATP restoration but also by restoring NADPH levels, which are needed to neutralize ROS that arise during these stresses (Jeon et al., 2012). Inhibition of mitochondria complex I has been shown to cause ROS induction (Hirst et al., 2008; Kushnareva et al., 2002), so the fact that phenformin is a potent complex I inhibitor may underlie its ROS generation, which LKB1-deficient cells are genetically incapable of neutralizing efficiently. Future studies will be needed to fully assess the contribution of ROS in the LKB1-sensitive apoptosis following phenformin.

The biguanide metformin is the most widely used type 2 diabetes therapeutic worldwide and more recently has become used in treating other insulin-resistant conditions, including polycystic ovary syndrome (PCOS) (Motta, 2008). Metformin garnered considerable attention as a potential anticancer agent once the connection between LKB1 and AMPK was discovered (Birsoy et al., 2012; Taubes, 2012). As AMPK activation can be growth suppressive, diabetics taking these agents daily for decades might have a lowered incidence of cancer because of chronic effects from AMPK-mediated suppression of mTORC1 and other progrowth pathways, depending on how effective and sustained the clinical doses of metformin are at activating AMPK in different tissues. In addition, a non-cell-autonomous mechanism for metformin's antitumor effects may be its ability to lower circulating blood glucose and insulin levels, which also contribute to cancer risk and incidence in some contexts (Pollak, 2010). A number of epidemiological studies have found that diabetics taking metformin exhibit lowered risk of overall cancer compared to those taking other forms of diabetes medication (Dowling et al., 2012; Pollak, 2012). Given these observations, over 50 different clinical trials investigating the use of

metformin in oncology are currently underway (<http://www.clinicaltrials.gov>). Whether phenformin would yield similar broad anticancer results, given that it also effectively lowers blood glucose and also more potently activates AMPK across a wide-variety of tissues, remains to be investigated. As phenformin has a 50-fold greater potency than metformin for mitochondrial complex I inhibition (Owen et al., 2000; Dykens et al., 2008), part of its therapeutic success in cancer models when compared to metformin may be due to the fact that at maximal tolerated doses in rodents and clinically utilized doses in humans, one achieves greater ATP loss and ROS induction with phenformin. However, another distinction between these two biguanides is a greater tissue bioavailability for phenformin, which may be due to the apparent reliance of metformin on a tissue-restricted cell-surface transporter, Oct1, to efficiently cross the plasma membrane, unlike the more lipophilic phenformin (Hawley et al., 2010). Phenformin was removed from clinical use for type 2 diabetes because of incidence of fatalities from lactic acidosis (Crofford, 1995; Owen et al., 2000), reported in 64 cases per 100,000 patients per year, with patients bearing compromised kidney function at greatest risk. However, phenformin or another biguanide analog may still find utility as anticancer agents as the dosing and shorter duration in cancer therapy would be quite different from its prior clinical use for diabetes. Patients could also be prescreened for kidney function and other biomarkers to reduce any risk of lactic acidosis. Based on our findings here and previous studies of metformin, it seems most likely that phenformin might have potential use for early-stage lung tumors or as an adjuvant therapy following resection of early-stage NSCLC tumors. Although phenformin is unlikely to be suitable as a single-agent therapy in advanced-stage disease, it may synergize with other modalities, which warrants future investigation. A critical need for future clinical studies will be developing biomarkers of metformin and phenformin action in human tissues using clinically achievable doses (Pollak, 2010). Our identification of phospho-Ser51 eIF2 α and its targets CHOP and BiP/Grp78 as AMPK-independent markers of phenformin-induced stress may prove valuable for such studies.

Whether *LKB1* deficiency confers sensitivity toward other agents that perturb ATP production via effects on mitochondria, glycolysis, or glutaminolysis also remains an interesting area for future targeted therapeutic development. Given the large percentage of sporadic lung, cervical, and endometrial cancers bearing *LKB1* mutations, identifying agents selectively targeting *LKB1* mutant tumors is a critical goal and one that seems particularly amenable to drugs targeting tumor metabolism.

EXPERIMENTAL PROCEDURES

Antibodies and Reagents

Antibodies from Cell Signaling Technologies (Danvers, MA, USA) used for immunoblots were diluted 1:1,000 and included LKB1 (D60C5) (#3047), phospho-AMPK Thr172 (#2531), total AMPK α 1/2 (#2532), phospho-Raptor Ser792 (#2083), total Raptor (#2280), phospho-ULK1 (ser555) (#5869), eIF4E (#9742), phospho-eIF2 α (ser51) (#3398), total eIF2 α (#9722), cleaved caspase 3 (#9664), PARP (#9542), cleaved PARP (Asp214) (#5625), cleaved PARP mouse-specific (Asp214) (#9544), phospho-S6 (ser255/236) (#4858), S6 (#2217), phospho-4E-BP1 (thr37/46) (#2855), 4E-BP1 (#9644), phospho-IGF-IR/IR (#3024), IGF-IR/IR (#3027), phospho-AKT (ser473) (#4060), AKT

(#9272), CHOP (#5554), and BiP/GRP78 (#3177). Total ULK1 (A7481 WB 1:1,000) and anti-actin (A5441 WB1:5000) were purchased from Sigma-Aldrich (St. Louis, MO, USA). The p53 (CM5) antibody was obtained from Vector Labs (Burlingame, CA, USA; VP-P956 WB 1:1,000). The p62 antibody was obtained from Progen (Heidelberg, Germany; #GP62-C). AICAR was obtained from Toronto Research Chemicals (North York, Ontario, Canada). Phenformin, Metformin, and 2-deoxyglucose (2DG) and Antimycin A (cat. no. A8674); were purchased from Sigma-Aldrich. CCCP was obtained from the Molecular Probes JC-1 dye kit (Carlsbad, CA, USA; cat. no. M34152).

Cell Culture

Cells were incubated at 37°C and maintained at 5% CO₂. A549, H460, A427, H838, and HeLa cell lines were obtained from ATCC, and H157 cells were a kind gift from Dr. John Minna. Cells were grown in Dulbecco's modified Eagle's medium (DMEM) or RPMI 1640 medium (GIBCO) plus 10% fetal bovine serum (Hyclone, Logan, UT, USA) and penicillin and streptomycin. Retroviral gene expression was performed as described previously (Gwinn et al., 2008). Briefly, for retroviral infection, the pBabe, pBabe-FLAG-LKB1, and pBabe-FLAG-LKB1-KD (Addgene #'s 1764, 8592, and 8593) constructs were transfected along with the amphi packaging plasmid into growing HEK293T cells. Viral supernatants were collected 48 hr after transfection, spun for 5 min at 3,000 rpm, and filtered, and target cells were infected in the presence of polybrene. Twenty-four hours later, cells were selected with puromycin. Cells were plated at a density of 1×10^5 per well in 6-well dishes and grown for 18 hr before treatment.

Mouse Therapeutic Trials

Lox-Stop-Lox Kras^{G12D} were obtained from Tyler Jacks at Massachusetts Institute of Technology (Jackson et al., 2005) and *p53^{lox/lox}* mice from the Mouse Models of Human Cancers Consortium (Jonkers et al., 2001). *Lkb1^{lox/lox}* mice are as previously reported (Shaw et al., 2005). *Rosa26-Lox-Stop-Lox-Luc* mice were obtained from Jackson Laboratories (Bar Harbor, ME, USA) courtesy of Bill Kaelin (Safran et al., 2003). Mice were inbred on an FVB background. Lung tumors were induced by intranasal inhalation of 5×10^6 plaque forming units adeno-Cre (purchased from University of Iowa adenoviral core) as previously described (Jackson et al., 2005). Mice that displayed with clinical signs of disease, such as labored breathing or severe weight loss, were euthanized and necropsied. The mean tumor latencies we observed were comparable to previous studies with the exception of *KPluc* mice, which developed large, aggressive lung tumors with the same latency of *KL_{luc}* mice (Jackson et al., 2005; Ji et al., 2007). In the experiments in Figure 4, mice were administered with vehicle (water), metformin, or phenformin (Toronto Research Corporation, Ontario, Canada) ad lib through their drinking water, and their daily intake of fluids were monitored. Fresh metformin (1.8 mg/ml) or phenformin (1.8 mg/ml) was administered every other day. Long-term treatments consisted of 3 weeks treatment (schematic in Figure S4D), and acute treatments lasted 5 days. For the intraperitoneal injections in Figure 4A, mice were given one injection of saline (0.9%), metformin (300 mg/kg), or phenformin (150 mg/kg) and euthanized at 1, 4, and 8 hr post-injection, and lung tissue was isolated. In the therapeutic trials in Figures 5 and 6 (schematized in Figure S5A), mice were administered phenformin (100 mg/kg/day) by o.p. once daily 6 days/week beginning at 3 weeks postdelivery of adenovirus expressing Cre. All experimental procedures performed on mice were approved by the Salk Institute and University of California at Los Angeles Institutional Animal Care and Use Committees.

Statistical Analysis Methods

Means were compared and p values determined by parametric or nonparametric ANOVA, and statistical test details and significance at $p < 0.05$ are indicated in the text and figure legends. Survival curves were computed using the Kaplan-Meier method. All statistical calculations were carried out using GraphPad Prism 5 software (San Diego, CA) or SAS 9.3 (SAS, Cary, NC). For analysis of SUVmax and tumor volume from FDG-PET and μ CT imaging, comparisons were made between vehicle (V) versus Phenformin (P) treatments at week 7 and week 9. Values that were below the level of detection, referred to as left-censored observations, were coded with "zero", although the actual value may be above zero but is usually lower than the lowest observed value.

SUPPLEMENTAL INFORMATION

Supplemental Information includes seven figures and Supplemental Experimental Procedures and can be found with this article online at <http://dx.doi.org/10.1016/j.ccr.2012.12.008>.

ACKNOWLEDGMENTS

D.B.S. performed all cell experiments and all mouse experiments with assistance from E.A., L.G., and D.S.V.; D.B.S. and R.J.S. designed the study, analyzed the data, and wrote the paper; M.L. is a board-certified veterinary pathologist; M.C.F. and A.S. are board-certified clinical pathologists who performed all pathological analysis; And P.S.M. contributed resources and critical feedback on the project. We thank Lawrence Pang and L.W., who performed PET and CT imaging on the mice and J.C. and Dr. Ken Herrmann, who reviewed PET and CT scans on the mice. We thank Anne Atkins in Ron Evans lab (Salk) for the high-performance liquid chromatography and mass spectrometry analysis of metformin and phenformin levels in blood. We thank Dr. Jeff Gornbein for statistical analysis and Laurent Vergnes, who performed the Seahorse experiments supported by grant S10RR026744. We thank UCLA's Translational Pathology Core Laboratory and Dr. Clara Magyar for assistance with the Aperio and Definiens software. We thank Dr. Steven M. Dubinett for critically reviewing the manuscript and providing feedback. D.B.S. was supported by a training grant (T32 CA009370) to the Salk Institute Center for Cancer Research and through generous support by the Adler Family Foundation, by the Ahmanson Translational Imaging Division at UCLA's School of Medicine, and by the National Center for Advancing Translational Sciences through UCLA CTSI grant numbers UL1TR000124 and KL2TR000122. R.J.S. is funded by the National Institutes of Health R01 DK080425 and P01CA120964 and an American Cancer Society Research Scholar Award (RSG-07-210-01-MGO). This was also supported in part through the Salk CCSG P30 CA014195 and the Samuel Waxman Cancer Research Foundation. We also thank the Leona M. and Harry B. Helmsley Charitable Trust for their generous support.

Received: May 16, 2011

Revised: October 7, 2012

Accepted: December 20, 2012

Published: January 17, 2013

REFERENCES

- Algire, C., Amrein, L., Bazile, M., David, S., Zakikhani, M., and Pollak, M. (2011). Diet and tumor LKB1 expression interact to determine sensitivity to anti-neoplastic effects of metformin in vivo. *Oncogene* 30, 1174–1182.
- Anisimov, V.N., Berstein, L.M., Egormin, P.A., Piskunova, T.S., Popovich, I.G., Zabezhinski, M.A., Kovalenko, I.G., Poroshina, T.E., Semchenko, A.V., Provinciali, M., et al. (2005). Effect of metformin on life span and on the development of spontaneous mammary tumors in HER-2/neu transgenic mice. *Exp. Gerontol* 40, 685–693.
- Appleyard, M.V., Murray, K.E., Coates, P.J., Wullschlegel, S., Bray, S.E., Kernohan, N.M., Fleming, S., Alessi, D.R., and Thompson, A.M. (2012). Phenformin as prophylaxis and therapy in breast cancer xenografts. *Br. J. Cancer* 106, 1117–1122.
- Birsoy, K., Sabatini, D.M., and Possemato, R. (2012). Untuning the tumor metabolic machine: Targeting cancer metabolism: a bedside lesson. *Nat. Med.* 18, 1022–1023.
- Buzzai, M., Jones, R.G., Amaravadi, R.K., Lum, J.J., DeBerardinis, R.J., Zhao, F., Viollet, B., and Thompson, C.B. (2007). Systemic treatment with the anti-diabetic drug metformin selectively impairs p53-deficient tumor cell growth. *Cancer Res.* 67, 6745–6752.
- Carretero, J., Shimamura, T., Rikova, K., Jackson, A.L., Wilkerson, M.D., Borgman, C.L., Buttarazzi, M.S., Sanofsky, B.A., McNamara, K.L., Brandstetter, K.A., et al. (2010). Integrative genomic and proteomic analyses identify targets for Lkb1-deficient metastatic lung tumors. *Cancer Cell* 17, 547–559.

- Chae, Y.C., Caino, M.C., Lisanti, S., Ghosh, J.C., Dohi, T., Danial, N.N., Villanueva, J., Ferrero, S., Vaira, V., Santambrogio, L., et al. (2012). Control of tumor bioenergetics and survival stress signaling by mitochondrial HSP90s. *Cancer Cell* 22, 331–344.
- Chen, Z., Cheng, K., Walton, Z., Wang, Y., Ebi, H., Shimamura, T., Liu, Y., Tupper, T., Ouyang, J., Li, J., et al. (2012). A murine lung cancer co-clinical trial identifies genetic modifiers of therapeutic response. *Nature* 483, 613–617.
- Crofford, O.B. (1995). Metformin. *N. Engl. J. Med.* 333, 588–589.
- Ding, L., Getz, G., Wheeler, D.A., Mardis, E.R., McLellan, M.D., Cibulskis, K., Sougnez, C., Greulich, H., Muzny, D.M., Morgan, M.B., et al. (2008). Somatic mutations affect key pathways in lung adenocarcinoma. *Nature* 455, 1069–1075.
- Dowling, R.J., Niraula, S., Stambolic, V., and Goodwin, P.J. (2012). Metformin in cancer: translational challenges. *J. Mol. Endocrinol.* 48, R31–R43.
- Dykens, J.A., Jamieson, J., Marroquin, L., Nadanaciva, S., Billis, P.A., and Will, Y. (2008). Biguanide-induced mitochondrial dysfunction yields increased lactate production and cytotoxicity of aerobically-poised HepG2 cells and human hepatocytes in vitro. *Toxicol. Appl. Pharmacol.* 233, 203–210.
- Egan, D.F., Shackelford, D.B., Mihaylova, M.M., Gelino, S., Kohnz, R.A., Mair, W., Vasquez, D.S., Joshi, A., Gwinn, D.M., Taylor, R., et al. (2011). Phosphorylation of ULK1 (hATG1) by AMP-activated protein kinase connects energy sensing to mitophagy. *Science* 331, 456–461.
- El-Mir, M.Y., Nogueira, V., Fontaine, E., Avéret, N., Rigoulet, M., and Leverve, X. (2000). Dimethylbiguanide inhibits cell respiration via an indirect effect targeted on the respiratory chain complex I. *J. Biol. Chem.* 275, 223–228.
- Evans, J.M., Donnelly, L.A., Emslie-Smith, A.M., Alessi, D.R., and Morris, A.D. (2005). Metformin and reduced risk of cancer in diabetic patients. *BMJ* 330, 1304–1305.
- Farago, A.F., Snyder, E.L., and Jacks, T. (2012). SnapShot: Lung cancer models. *Cell* 149, 246, 246 e241.
- Foretz, M., Hebrard, S., Leclerc, J., Zarrinpashneh, E., Soty, M., Mithieux, G., Sakamoto, K., Andreelli, F., and Viollet, B. (2010). Metformin inhibits hepatic gluconeogenesis in mice independently of the LKB1/AMPK pathway via a decrease in hepatic energy state. *J. Clin. Invest.* 120, 2355–2369.
- Gill, R.K., Yang, S.H., Meerzaman, D., Mechanic, L.E., Bowman, E.D., Jeon, H.S., Roy Chowdhuri, S., Shakoori, A., Dracheva, T., Hong, K.M., et al. (2011). Frequent homozygous deletion of the LKB1/STK11 gene in non-small cell lung cancer. *Oncogene* 30, 3784–3791.
- Gwinn, D.M., Shackelford, D.B., Egan, D.F., Mihaylova, M.M., Mery, A., Vasquez, D.S., Turk, B.E., and Shaw, R.J. (2008). AMPK phosphorylation of raptor mediates a metabolic checkpoint. *Mol. Cell* 30, 214–226.
- Hardie, D.G., Ross, F.A., and Hawley, S.A. (2012). AMPK: a nutrient and energy sensor that maintains energy homeostasis. *Nat. Rev. Mol. Cell Biol.* 13, 251–262.
- Hawley, S.A., Ross, F.A., Chevtzoff, C., Green, K.A., Evans, A., Fogarty, S., Towler, M.C., Brown, L.J., Ogunbayo, O.A., Evans, A.M., and Hardie, D.G. (2010). Use of cells expressing gamma subunit variants to identify diverse mechanisms of AMPK activation. *Cell Metab.* 11, 554–565.
- Hemminki, A., Markie, D., Tomlinson, I., Avizienyte, E., Roth, S., Loukola, A., Bignell, G., Warren, W., Aminoff, M., Höglund, P., et al. (1998). A serine/threonine kinase gene defective in Peutz-Jeghers syndrome. *Nature* 391, 184–187.
- Hirst, J., King, M.S., and Pryde, K.R. (2008). The production of reactive oxygen species by complex I. *Biochem. Soc. Trans.* 36, 976–980.
- Huang, X., Wulschleiger, S., Shpiro, N., McGuire, V.A., Sakamoto, K., Woods, Y.L., McBurnie, W., Fleming, S., and Alessi, D.R. (2008). Important role of the LKB1-AMPK pathway in suppressing tumorigenesis in PTEN-deficient mice. *Biochem. J.* 412, 211–221.
- Inoki, K., Zhu, T., and Guan, K.L. (2003). TSC2 mediates cellular energy response to control cell growth and survival. *Cell* 115, 577–590.
- Jackson, E.L., Olive, K.P., Tuveson, D.A., Bronson, R., Crowley, D., Brown, M., and Jacks, T. (2005). The differential effects of mutant p53 alleles on advanced murine lung cancer. *Cancer Res.* 65, 10280–10288.
- Jeon, S.M., Chandel, N.S., and Hay, N. (2012). AMPK regulates NADPH homeostasis to promote tumour cell survival during energy stress. *Nature* 485, 661–665.
- Ji, H., Ramsey, M.R., Hayes, D.N., Fan, C., McNamara, K., Kozlowski, P., Torrice, C., Wu, M.C., Shimamura, T., Perera, S.A., et al. (2007). LKB1 modulates lung cancer differentiation and metastasis. *Nature* 448, 807–810.
- Jin, S., DiPaola, R.S., Mathew, R., and White, E. (2007). Metabolic catastrophe as a means to cancer cell death. *J. Cell Sci.* 120, 379–383.
- Jonkers, J., Meuwissen, R., van der Gulden, H., Peterse, H., van der Valk, M., and Berns, A. (2001). Synergistic tumor suppressor activity of BRCA2 and p53 in a conditional mouse model for breast cancer. *Nat. Genet.* 29, 418–425.
- Kalender, A., Selvaraj, A., Kim, S.Y., Gulati, P., Brule, S., Viollet, B., Kemp, B.E., Bardeesy, N., Dennis, P., Schlager, J.J., et al. (2010). Metformin, independent of AMPK, inhibits mTORC1 in a rag GTPase-dependent manner. *Cell Metab.* 11, 390–401.
- Kushnareva, Y., Murphy, A.N., and Andreyev, A. (2002). Complex I-mediated reactive oxygen species generation: modulation by cytochrome c and NAD(P)⁺ oxidation reduction state. *Biochem. J.* 368, 545–553.
- Laderoute, K.R., Amin, K., Calaoagan, J.M., Knapp, M., Le, T., Orduna, J., Foretz, M., and Viollet, B. (2006). 5'-AMP-activated protein kinase (AMPK) is induced by low-oxygen and glucose deprivation conditions found in solid-tumor microenvironments. *Mol. Cell. Biol.* 26, 5336–5347.
- Liang, M.C., Ma, J., Chen, L., Kozlowski, P., Qin, W., Li, D., Goto, J., Shimamura, T., Hayes, D.N., Meyerson, M., et al. (2010). TSC1 loss synergizes with KRAS activation in lung cancer development in the mouse and confers rapamycin sensitivity. *Oncogene* 29, 1588–1597.
- Memmott, R.M., Mercado, J.R., Maier, C.R., Kawabata, S., Fox, S.D., and Dennis, P.A. (2010). Metformin prevents tobacco carcinogen-induced lung tumorigenesis. *Cancer Prev. Res. (Phila.)* 3, 1066–1076.
- Motta, D.A. (2008). Metformin in the treatment of polycystic ovary syndrome. *Curr. Pharm. Des.* 14, 2121–2125.
- Muaddi, H., Majumder, M., Peidis, P., Papadakis, A.I., Holcik, M., Scheuner, D., Kaufman, R.J., Hatzoglou, M., and Koromilas, A.E. (2010). Phosphorylation of eIF2 α at serine 51 is an important determinant of cell survival and adaptation to glucose deficiency. *Mol. Biol. Cell* 21, 3220–3231.
- Nakada, D., Saunders, T.L., and Morrison, S.J. (2010). Lkb1 regulates cell cycle and energy metabolism in haematopoietic stem cells. *Nature* 468, 653–658.
- Osoegawa, A., Kometani, T., Nosaki, K., Ondo, K., Hamatake, M., Hirai, F., Seto, T., Sugio, K., and Ichinose, Y. (2011). LKB1 mutations frequently detected in mucinous bronchioloalveolar carcinoma. *Jpn. J. Clin. Oncol.* 41, 1132–1137.
- Owen, M.R., Doran, E., and Halestrap, A.P. (2000). Evidence that metformin exerts its anti-diabetic effects through inhibition of complex 1 of the mitochondrial respiratory chain. *Biochem. J.* 348, 607–614.
- Pollak, M. (2010). Metformin and other biguanides in oncology: advancing the research agenda. *Cancer Prev. Res. (Phila.)* 3, 1060–1065.
- Pollak, M.N. (2012). Investigating metformin for cancer prevention and treatment: the end of the beginning. *Cancer Discov.* 2, 778–790.
- Safran, M., Kim, W.Y., Kung, A.L., Horner, J.W., DePinho, R.A., and Kaelin, W.G., Jr. (2003). Mouse reporter strain for noninvasive bioluminescent imaging of cells that have undergone Cre-mediated recombination. *Mol. Imaging* 2, 297–302.
- Sakamoto, K., McCarthy, A., Smith, D., Green, K.A., Grahame Hardie, D., Ashworth, A., and Alessi, D.R. (2005). Deficiency of LKB1 in skeletal muscle prevents AMPK activation and glucose uptake during contraction. *EMBO J.* 24, 1810–1820.
- Sanchez-Cespedes, M., Parrella, P., Esteller, M., Nomoto, S., Trink, B., Engles, J.M., Westra, W.H., Herman, J.G., and Sidransky, D. (2002). Inactivation of LKB1/STK11 is a common event in adenocarcinomas of the lung. *Cancer Res.* 62, 3659–3662.
- Shackelford, D.B., and Shaw, R.J. (2009). The LKB1-AMPK pathway: metabolism and growth control in tumour suppression. *Nat. Rev. Cancer* 9, 563–575.
- Shackelford, D.B., Vasquez, D.S., Corbett, J., Wu, S., Leblanc, M., Wu, C.L., Vera, D.R., and Shaw, R.J. (2009). mTOR and HIF-1 α -mediated tumor

metabolism in an LKB1 mouse model of Peutz-Jeghers syndrome. *Proc. Natl. Acad. Sci. USA* **106**, 11137–11142.

Shaw, R.J., Kosmatka, M., Bardeesy, N., Hurley, R.L., Witters, L.A., DePinho, R.A., and Cantley, L.C. (2004). The tumor suppressor LKB1 kinase directly activates AMP-activated kinase and regulates apoptosis in response to energy stress. *Proc. Natl. Acad. Sci. USA* **101**, 3329–3335.

Shaw, R.J., Lamia, K.A., Vasquez, D., Koo, S.H., Bardeesy, N., Depinho, R.A., Montminy, M., and Cantley, L.C. (2005). The kinase LKB1 mediates glucose homeostasis in liver and therapeutic effects of metformin. *Science* **310**, 1642–1646.

Shu, Y., Sheardown, S.A., Brown, C., Owen, R.P., Zhang, S., Castro, R.A., Ianculescu, A.G., Yue, L., Lo, J.C., Burchard, E.G., et al. (2007). Effect of genetic variation in the organic cation transporter 1 (OCT1) on metformin action. *J. Clin. Invest.* **117**, 1422–1431.

Taubes, G. (2012). Cancer research. Cancer prevention with a diabetes pill? *Science* **335**, 29.

Ye, J., Kumanova, M., Hart, L.S., Sloane, K., Zhang, H., De Panis, D.N., Bobrovnikova-Marjon, E., Diehl, J.A., Ron, D., and Koumenis, C. (2010). The GCN2-ATF4 pathway is critical for tumour cell survival and proliferation in response to nutrient deprivation. *EMBO J.* **29**, 2082–2096.

Modeling Clear Cell Sarcomagenesis in the Mouse: Cell of Origin Differentiation State Impacts Tumor Characteristics

Krystal M. Straessler,¹ Kevin B. Jones,² Hao Hu,⁴ Huifeng Jin,² Matt van de Rijn,⁵ and Mario R. Capecchi^{1,3,*}

¹Department of Human Genetics

²Department of Orthopaedics and Huntsman Cancer Institute Center for Children's Cancer Research

³Howard Hughes Medical Institute

University of Utah School of Medicine, Salt Lake City, UT 84112, USA

⁴Department of Epidemiology, The University of Texas M.D. Anderson Cancer Center, Houston, TX 77030, USA

⁵Department of Pathology, Stanford University Medical Center, Palo Alto, CA 94305

*Correspondence: mario.capecchi@genetics.utah.edu

<http://dx.doi.org/10.1016/j.ccr.2012.12.019>

SUMMARY

Clear cell sarcoma (CCS) of tendons and aponeuroses is a deadly soft-tissue malignancy resembling melanoma, with a predilection for young adults. *EWS-ATF1*, the fusion product of a balanced chromosomal translocation between chromosomes 22 and 12, is considered the definitional feature of the tumor. Conditional expression of the *EWS-ATF1* human cDNA in the mouse generates CCS-like tumors with 100% penetrance. Tumors, developed through varied means of initiating expression of the fusion oncogene, model human CCS morphologically, immunohistochemically, and by genome-wide expression profiling. We also demonstrate that although fusion oncogene expression in later stages of differentiation can transform mesenchymal progenitor cells and generate tumors resembling CCS generally, expression in cells retaining stem cell markers permits the full melanoma-related phenotype.

INTRODUCTION

Clear cell sarcoma (CCS) is a soft-tissue neoplasm classically arising in the extremities of young adults near tendons and aponeuroses. Despite their often small size, these tumors have high rates of recurrence and metastasis following standard local therapy, portending a poor general prognosis. CCS was first identified in 1965 and then termed “malignant melanoma of the soft parts” because of its histologic appearance fitting with metastatic melanoma (Enzinger, 1965). In addition, CCS was later found to demonstrate melanocytic differentiation markers, including immunohistochemical positivity for M-MITF, S100B, MelanA, and HMB45 (Granter et al., 2001; Hocar et al., 2012). Until recently, the only means of differentiating CCS from the soft-tissue metastasis of a distant

melanoma was its clinical history (i.e., confirmed absence of any cutaneous melanomas).

In the last decade, recognition of the characteristic t(12;22) (q13;q12) chromosomal translocation and its resultant fusion oncogene *EWSR1-ATF1* (*EWS-ATF1*) has provided a means of defining CCS and distinguishing it from melanoma (Antonescu et al., 2002). Traditional cytogenetics, fluorescent in situ hybridization (FISH), and RT-PCR have all proven to be diagnostic tools capable of identifying this defining molecular feature of CCS (Wang et al., 2009). The type 1 fusion of *EWS-ATF1*, which includes exons one through eight of *EWSR1* and exons four through seven of *ATF1*, is the most common variant of the described translocation products (Wang et al., 2009).

The *EWS-ATF1* fusion protein contains the amino-terminal transcriptional activation domain of the *EWSR1* protein joined

Significance

CCS, a rare soft tissue malignancy typically arising in the extremities of young adults, closely resembles melanoma. *EWS-ATF1*, a fusion oncogene resulting from a t(12;22) chromosomal translocation, defines the neoplasm. Conditional expression of the human *EWS-ATF1* cDNA in the mouse demonstrates its profound transformational impact. Although a number of cell types can be rendered tumorigenic via expression of the fusion oncogene, the undifferentiated cells appear to enable the full melanoma-related phenotype. This model deciphers part of the enigma of the melanoma expression profile of CCS and explains the range of human tumors derived from this powerful translocation product. The mouse model should provide a robust platform for interrogating molecular mechanisms and developing more effective therapies for CCS.

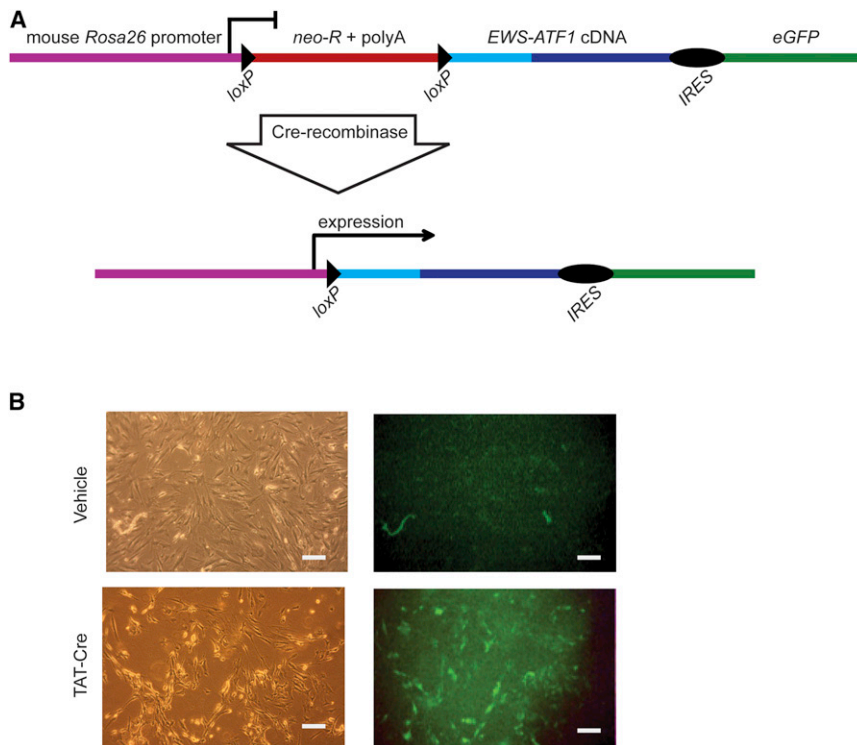


Figure 1. Conditional Expression of the Human Clear Cell Sarcoma Fusion Oncogene in the Mouse

(A) Schematic showing the cDNA of the type I variant of *EWS-ATF1* isolated from a human tumor and cloned into a vector designed for targeting into the mouse *Rosa26* locus. neo-R, neomycin resistance cassette; polyA, polyadenylation stop sequence; IRES, internal ribosome entry site; eGFP, enhanced green fluorescent protein. Cre-mediated recombination excises the stop sequence and initiates expression of the fusion oncogene and eGFP.

(B) Embryonic day 14.5 fibroblasts isolated from *Rosa26^{EA1}* heterozygous mice were exposed to TAT-Cre protein or vehicle control, and images were collected 24 hr later. The left two panels show light images of fibroblasts, whereas the right two panels show the GFP fluorescence. All scale bars are 50 μ m in length.

RESULTS

Generation of a Targeted Mouse Line Conditionally Expressing the *EWS-ATF1* Oncogene

To generate the *EWS-ATF1* cDNA, total RNA was isolated from human CCS

tumors, reverse transcribed, and screened by PCR to identify a type 1 *EWS-ATF1* fusion product. The integrity of the *EWS-ATF1* cDNA was confirmed by DNA sequencing. The *EWS-ATF1* cDNA was targeted to the ubiquitously expressed *Rosa26* locus (Mao et al., 1999). Linked to the *EWS-ATF1* cDNA via an internal ribosomal entry site (IRES) was the sequence encoding an enhanced green fluorescent protein (eGFP). To prevent transcription of the fusion gene and eGFP from the *Rosa26* promoter, a neomycin resistance cassette and poly-adenylation stop signal flanked by *loxP* sites was inserted between the promoter and the *EWS-ATF1*-IRES-eGFP sequence (Figure 1A). In the absence of Cre, neither the fusion gene product nor eGFP should be expressed. Temporal, spatial, and tissue-specific control of Cre presence is possible through a variety of techniques for its genetic or protein delivery. Mouse embryonic stem cells confirmed to bear the targeted allele were injected into blastocysts to generate chimeras that were then bred to generate progeny with a germline-transmissible conditional allele of *EWS-ATF1* (designated *Rosa26^{EA1}*).

The cell, or cells, of origin for CCS are not known. Traditionally, CCS tumors were characteristically identified near the tendons and aponeuroses of young adults but have also recently been identified in the gastrointestinal tract (Covinsky et al., 2005; D'Amico et al., 2012; Lyle et al., 2008) and dermis (Falconieri et al., 2012; Hantschke et al., 2010). The expression of melanocyte-specific markers in CCS tumors has been variably attributed to the effects of the cell of origin or the effects of aberrant *M-Mitf* expression, shown to be driven by *EWS-ATF1* in CCS cell lines (Davis et al., 2006). Using *EWS-ATF1* as a diagnostic marker led to the identification of CCSs that do not express melanocytic markers. Further, some histologically distinct neoplasms have also been associated with this fusion oncogene, including angiomatoid fibrous histiocytoma (Somers et al., 2005) and hyalinizing clear cell carcinoma of the salivary gland (Antonescu et al., 2011). The latter tumors do not express *M-Mitf* or other melanocytic markers.

To investigate the role that *EWS-ATF1* plays in clear cell sarcomagenesis and in tumorigenesis more broadly, we developed a mouse model that expresses the human *EWS-ATF1* fusion oncogene complementary DNA (cDNA) in a conditional fashion.

To confirm inducibility of the *EWS-ATF1* fusion gene and eGFP by Cre, embryonic fibroblasts were isolated from E14.5 mouse embryos heterozygous for the *Rosa26^{EA1}* allele and exposed in culture to purified TAT-Cre protein or vehicle buffer control. TAT-Cre is an engineered Cre protein containing a short peptide sequence derived from the human immunodeficiency virus that mediates efficient endocytic uptake and nuclear localization of the protein (Joshi et al., 2002). Recombination efficiency in vitro exceeds 95% as reported previously (Halder et al., 2009). Without exposure to TAT-Cre, mouse embryonic fibroblasts heterozygous for *Rosa26^{EA1}* demonstrated no green fluorescence. Twenty-four hours after exposure to TAT-Cre (5 μ M),

fibroblasts demonstrated strong green fluorescence, indicating successful recombination and expression of the fusion oncogene and eGFP. Temporal, spatial, and tissue-specific control of Cre presence is possible through a variety of techniques for its genetic or protein delivery. Mouse embryonic stem cells confirmed to bear the targeted allele were injected into blastocysts to generate chimeras that were then bred to generate progeny with a germline-transmissible conditional allele of *EWS-ATF1* (designated *Rosa26^{EA1}*).

cells began to express eGFP (Figure 1B), and the percentage of fluorescing cells increased thereafter. The expression of other sarcoma fusion oncogenes from the *Rosa26* locus has proven lethal for mouse embryonic fibroblasts (Haldar et al., 2007). Surprisingly, *EWS-ATF1*-expressing fibroblasts survived beyond the expected crisis and senescence of control fibroblasts that carried the *Rosa26^{EA1}* allele but were exposed to vehicle rather than TAT-Cre. Expression of *EWS-ATF1* remained strong in the embryonic fibroblasts activated by TAT-Cre, even following long-term passage (data not shown).

Generation of Tumors by In Vivo Exposure to TAT-Cre

Because expression of *EWS-ATF1* was so well tolerated in vitro, we investigated whether the *Rosa26^{EA1}* allele might be activated in vivo first by injecting TAT-Cre into mice heterozygous for the *Rosa26^{YFP}* allele. Mice receiving TAT-Cre show YFP expression within 24 hr of injection (Figure S1A available online). To look at this on a cellular level, mice heterozygous for *Rosa26^{mTomG}* reporter allele (Muzumdar et al., 2007) were also injected with TAT-Cre. All cells in mice bearing the *Rosa26^{mTomG}* allele express membrane-bound Tomato fluorescent protein prior to recombination with Cre but express a membrane-bound GFP after Cre-mediated excision of the *mTomato* coding sequence. A single subdermal injection of TAT-Cre resulted in dense GFP expression in the surrounding tissue (Figure S1B).

To determine the sufficiency of the *EWS-ATF1* fusion gene to drive clear cell sarcomagenesis in vivo, we injected TAT-Cre protein into the anterolateral soft tissues abutting the tibia and in the distal forelimbs of mice heterozygous for the *Rosa26^{EA1}* allele. *EWS-ATF1* transcripts were detectable by RT-PCR from tissues harvested within 24 hr of the TAT-Cre injection (Figure S1C). Every injection of TAT-Cre yielded a tumor (Figure 2A), tightly localized to the injection site. Control mice, including both uninjected littermates and littermates injected with saline and followed for 15 months, never formed tumors. All mouse tumors derived from the TAT-Cre-activated *Rosa26^{EA1}* allele demonstrated eGFP fluorescence (Figure 2A).

Noting an extremely brief latency to tumorigenesis, the ability to form tumors in a broad array of tissue locations, and the histological appearance of poly-clonality among the first rounds of TAT-Cre-induced tumors, we investigated whether the rapid growth of large tumors might result primarily from a large initial population of induced *EWS-ATF1*-expressing cells. To address this question, we injected limbs of mice heterozygous for the *Rosa26^{EA1}* allele with different concentrations of TAT-Cre and found that the latency to tumor formation correlated with the concentration of TAT-Cre administered (Figure 2B). Injecting 100 μ M of TAT-Cre resulted in visible tumors as quickly as 3 weeks postinjection, with 100% penetrance per injection site by 6 weeks. TAT-Cre at 2 μ M still produced tumors with full penetrance but required a longer latency with visible tumors observed after a period of 6 to 9 months. Although TAT-Cre concentration impacted latency to development of a visible tumor, it did not impact the observed rate of tumor growth following visible detection of any specific tumor. Tumors appearing early from concentrated TAT-Cre or after a longer latency from diluted TAT-Cre still grew at a similarly rapid rate after detection.

The tumors that formed following TAT-Cre injection into mice heterozygous for the *Rosa26^{EA1}* allele recapitulated human

CCS molecularly, with expression of the fusion oncogene and melanocytic markers *M-Mitf* and *Tyrosinase* (Figure 2C). Mouse tumors also matched human tumor histomorphology and immunohistochemical profile. In hematoxylin and eosin (H&E)-stained sections, the majority of murine tumors demonstrated nuclear features typical of primitive cell types, with prominent open chromatin patterns as well as abundant clear cytoplasm (the feature for which the tumor is named) (Figure 2D). Although some tumors had a pseudoencapsulated, pushing border with surrounding tissues, others demonstrated clear infiltration into adjacent tissue planes. A minority subset of tumors (20%) demonstrated spindle cell morphology, also observed in some human CCS cases (Figure 2D). Consistent with human CCS, the tumors demonstrated immunohistochemical positivity for melanocytic markers (M-MITF and S100B) and lacked staining for cytokeratins (Figure 2E).

Unbiased Expression of EWS-ATF1 Also Results in Tumorigenesis, Preferentially in Mesenchyme

Because tumors rapidly invaded surrounding tissues, dissections of the limbs did not clearly indicate from which tissues they arose. In a search for tissues incompatible with transformation, TAT-Cre was injected into subcutaneous adipose, dorsal paw peritendinous, periosteal, intramuscular, and mammary fat pad tissue compartments in mice between 3 weeks and 6 months of age. The latency to tumor appearance varied with age and injection site, but every injection in each of these tissue locations yielded completely penetrant tumorigenesis (Table S1). Each of these locations bears some cells of mesenchymal character, but whether these or neighboring cells actually gave rise to tumors remained unclear.

In order to broaden exposure to *EWS-ATF1* fusion protein across multiple cell types and developmental periods, we next utilized *Rosa26^{CreER}* to express Cre sporadically, in random cell types. Although efficient CreER-mediated recombination requires the presence of tamoxifen, a very low level of CreER-mediated recombination is observed even in the absence of tamoxifen (Haldar et al., 2009). Breeding mice bearing the *Rosa26^{CreER}* allele to mice bearing the *Rosa26^{EA1}* allele resulted in smaller litters than breeding *Rosa26^{EA1}* mice alone, fitting with the previously described early embryonic leakiness of this CreER and suggesting some developmental toxicity of early expression of *EWS-ATF1* (Figure 3A).

Among the *Rosa26^{CreER/EA1}* mice that survive embryogenesis, administration of tamoxifen prior to 3 weeks of age results in stunted growth (Figure 3B) and death by 12 weeks of age without detectable tumor formation. *Rosa26^{CreER/EA1}* mice receiving tamoxifen after 3 weeks of age form more tumors than those receiving no tamoxifen, but both of these groups demonstrate complete penetrance of tumor formation by 12 weeks of age (Figure 3C). The tumors arising in *Rosa26^{CreER/EA1}* mice were histologically similar to the murine TAT-Cre-induced tumors and human clear cell sarcoma (Figure 3D). Whether or not enhanced by later tamoxifen administration, tumors arose most often in the extremities, rib cage, and facial tissues of the *Rosa26^{CreER/EA1}* mice but were also less frequently found in the dermis, liver, and bone (Table S2). As following TAT-Cre induction, the preponderance of tumors arose in mesenchymal tissue compartments. A variety of mouse cells are permissive

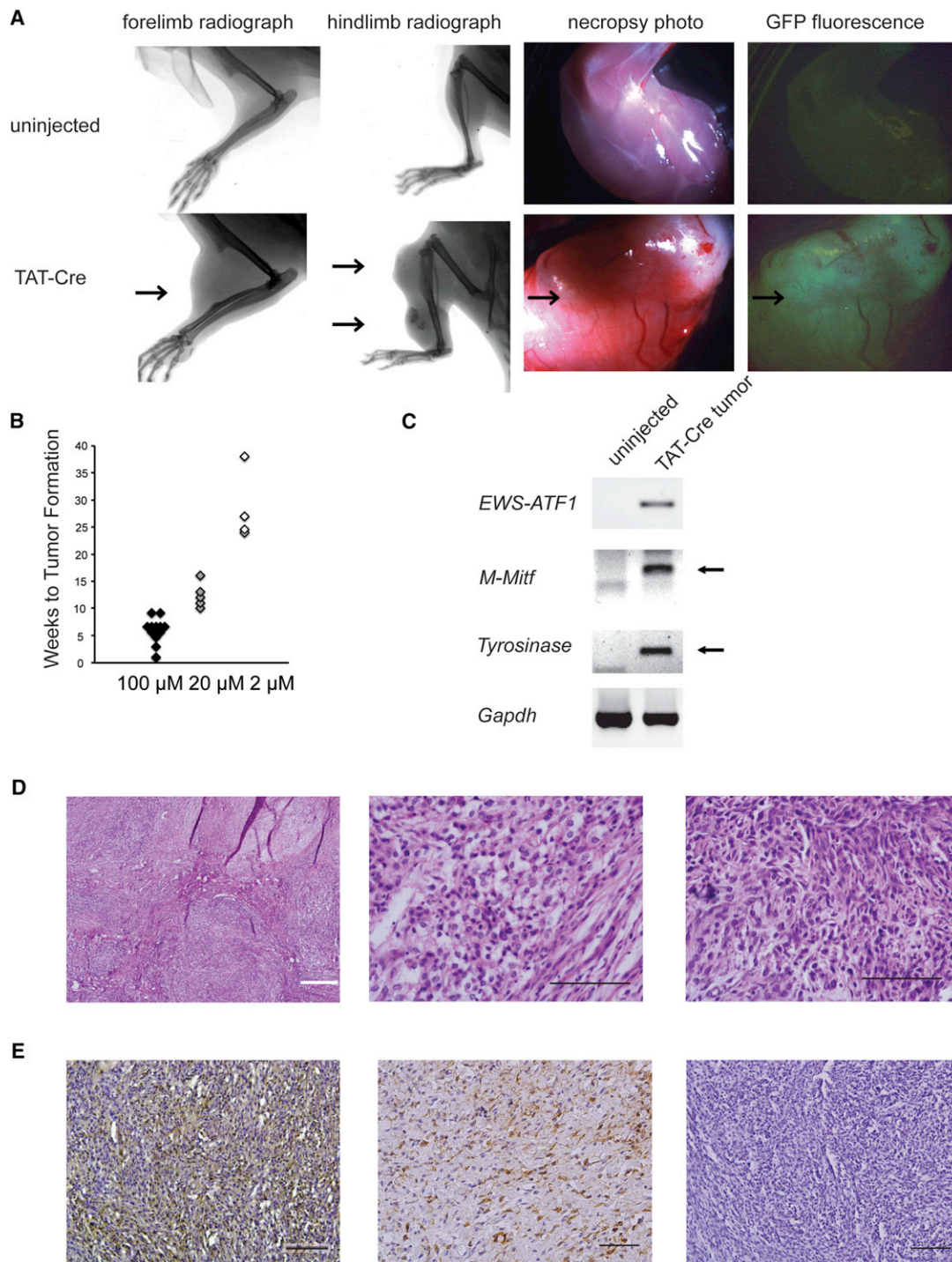


Figure 2. TAT-Cre-Initiated Expression of *EWS-ATF1* In Vivo Leads to Tumorigenesis

(A) Radiographs of limbs of *Rosa26^{EA1}* heterozygous mice without (top) or with (bottom) injection of TAT-Cre (left two columns). Necropsy light and GFP fluorescence photo of *Rosa26^{EA1}* limb without injection (top) or of tumor extracted from the TAT-Cre-injected *Rosa26^{EA1}* (bottom) (right two columns). Arrows point to individual tumors.

(B) Latency to visible tumor formation for *Rosa26^{EA1}* mice injected with 100, 10, and 2 μ M solutions of TAT-Cre.

(C) RT-PCR analysis of the indicated mRNAs from uninjected control tissues and TAT-Cre-induced tumors.

(D) Representative histology of TAT-Cre-induced tumors with H&E stain showing a multinodular tumor at low power (left), cells marked by round shape, clear cytoplasm and an open chromatin pattern at higher power (middle), and a tumor having a more spindled cell morphology (right).

(E) Immunohistochemical stains for M-MITF (left), S100B (middle), and cytokeratin 5 (right). All black scale bars are 100 μ m in length, and the white bar is 500 μ m. See also Figure S1 and Table S1.

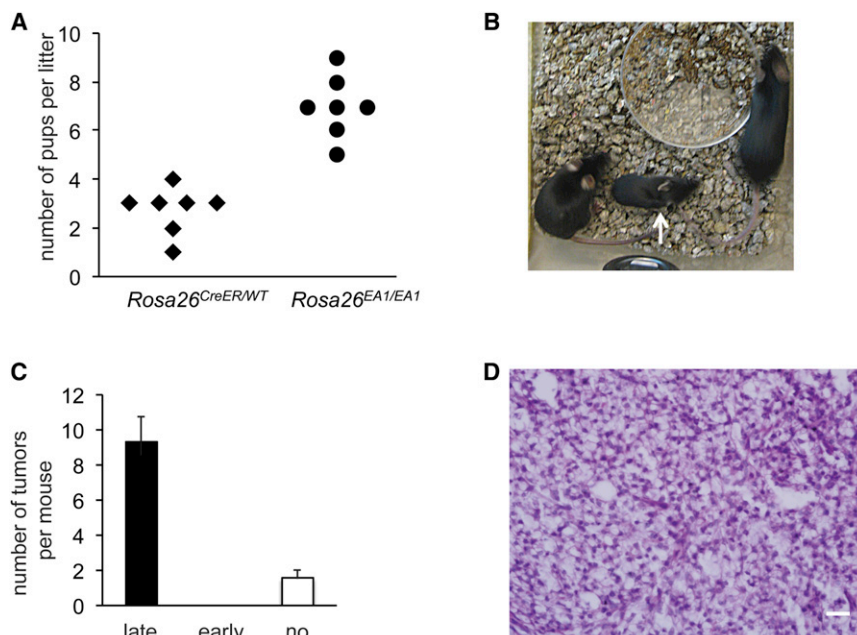


Figure 3. Early Expression of EWS-ATF1 in the Broad *Rosa26^{CreER}*-Lineage Renders Stunted Growth, but Later Expression Drives Tumorigenesis

(A) The number of pups per litter of mice heterozygous for the *Rosa26^{CreER}* allele crossed with mice homozygous for the *Rosa26^{EA1}* allele compared to that of *Rosa26^{EA1}/EA1* backcrossed controls.

(B) Photograph of a 7-week-old male *Rosa26^{EA1}/CreER* mouse injected with tamoxifen at 10 days (white arrow) and two uninjected female littermates of the same genotype.

(C) Chart of the number of tumors per mouse at 12 weeks age among *Rosa26^{EA1}/CreER* mice injected with tamoxifen after 3 weeks (late, n = 4), before 3 weeks (early, n = 3), or not at all (n = 5). Error bars denote standard deviation, t test $p < 0.05$.

(D) H&E-stained histopathology demonstrating the classic clear cell morphology apparent in a *Rosa26^{CreER}*-initiated tumor after late injection of tamoxifen. Scale bar is 20 μ m in length.

See also Table S2.

to *EWS-ATF1*-driven transformation, replicating the range of tumor tissue locations observed in molecularly defined human cases of CCS but preferentially arising in mesenchyme.

EWS-ATF1 Drives an Expression Signature of Transformation

Because the brief latency to tumorigenesis in both models suggested a powerful role for *EWS-ATF1* in driving transformation, we sought to define the expression signature shared by tumors from both means of inducing *EWS-ATF1* expression. To this end, we harvested tumors from each cohort as well as from control mesenchymal tissue, consisting of a portion of the thoracic cage, including cartilage, bone, skeletal muscle, and connective tissue, isolated total RNA from each, and performed Illumina sequencing. The samples generated an average of 24.4 ± 3.1 million reads, which aligned to $16,840 \pm 778$ genes at greater than or equal to 0.1 reads per kilobase per million (RPKM).

Clustering analysis demonstrated highly similar expression profiles among tumors induced by either TAT-Cre or *Rosa26^{CreER}*, both distinct from control tissues. An unsupervised hierarchical clustering of the samples according to the 200 most differentially expressed genes is shown in Figure 4A (gene lists in Tables S3, S4, and S5). DAVID analysis of the most significantly upregulated genes in the mouse tumors compared to control tissues highlighted several informative KEGG pathways, including cell-cycle control, cancer, p53, and extracellular matrix pathways (Huang da et al., 2009a, 2009b) (Figure 4B). These data provide insight into the transforming power of *EWS-ATF1*, with consistent alterations in gene expression profiling among different methods of activation.

Embryonic Expression of EWS-ATF1 in Mesenchymal Tissues and Predecessors Causes Lethality

Although experiments with TAT-Cre injections and *Rosa26^{CreER}*-initiated *EWS-ATF1* expression suggested that a variety of cell

types appear to support a program of transformation, they also suggested that the preferred clear cell sarcomagenesis tissue of origin is mesenchyme. As postnatal mesenchymal tissues derive from both neural crest and mesodermal origins, we investigated the identity of potential cells of origin by breeding mice bearing the *Rosa26^{EA1}* allele to mice bearing *Cre* expressed from promoters specific to these lineages. With regard to neural crest, mice bearing the *Rosa26^{EA1}* allele and *Wnt1-Cre* (Danielian et al., 1998) did not complete embryogenesis. Conditional *EWS-ATF1* activated by *Pax3-Cre* (Engleka et al., 2005), *Pax7-Cre* (Keller et al., 2004b), *Tie2-Cre* (Kisanuki et al., 2001), or *Prx1-Cre* (Durland et al., 2008; Logan et al., 2002), all expressed in mesoderm, also resulted in embryonic lethality.

At E13.5, the *Prx1-Cre* lineage demonstrated GFP fluorescence in *Prx1-Cre; Rosa26^{EA1}* mouse embryos, indicating expression of eGFP from the IRES on the *EWS-ATF1* transcript (Figure 5A). As late as E14.5 *Prx1-Cre; Rosa26^{EA1}* mouse embryos remained viable but demonstrated severe limb deformities (Figure 5A). It suggests that *EWS-ATF1* was toxic to these cells.

Pax7-Cre; Rosa26^{EA1} did not produce live progeny, but embryos were retrieved as late as E18.5. These embryos showed severe craniofacial deformation with no visible eGFP, which suggests that the lineage cannot survive expression of *EWS-ATF1* (Figure S2A).

Mice bearing the *Rosa26^{EA1}* allele and *Myf5-Cre*, which activated the fusion gene expression in myoblasts (Haldar et al., 2007), did not form tumors but demonstrated another phenotype in which *EWS-ATF1* was also apparently toxic to cells. These mice survived to birth and lived to approximately 3 months of age but were very small in size and severely myopathic, with eGFP expression detectable in the remaining muscle fibers (Figures S2B and S2C).

These data demonstrate that even though the expression of *EWS-ATF1* is tolerated better than the expression of other

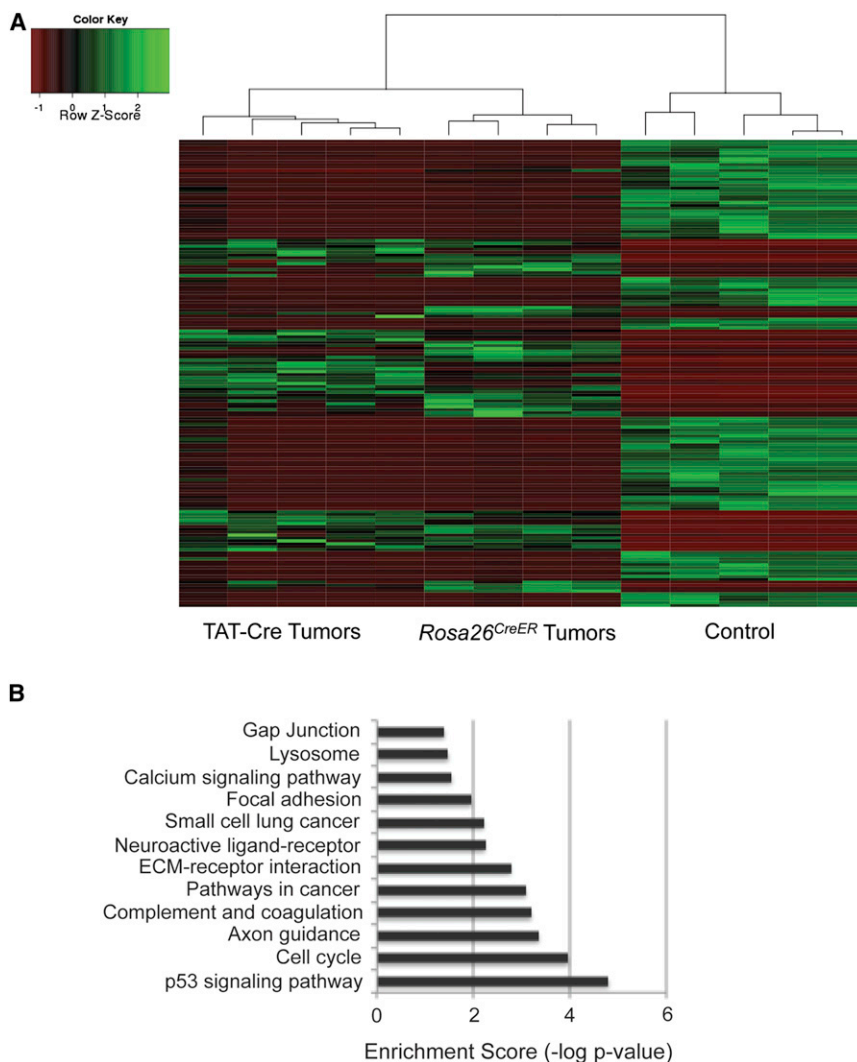


Figure 4. The Expression Signature of EWS-ATF1-Driven Tumors

(A) Heat map depicting the 200 most significantly ($p < 0.001$) differentially expressed genes between TAT-Cre- or Rosa26^{CreER}-initiated tumor and control tissue, as assessed by transcriptome sequencing.

(B) DAVID analysis of the most upregulated genes in tumors highlights Kegg pathways known to be involved in transformation.

See also Tables S3, S4, and S5.

developing mammalian limb and head (Durland et al., 2008), whereas *Prx1-CreERT2* expression is reported to be restricted postnatally to a smaller progenitor cell population in the same anatomic regions, still capable of osteochondrogenic differentiation (Kawanami et al., 2009).

Prx1-CreERT2;Rosa26^{EA1} mice developed tumors (Figure 5B) by 8 weeks posttamoxifen injection with 100% penetrance. Most of these tumors developed in the extremities and head, consistent with the expected anatomic distribution of *Prx1* postnatal expression. The tumors showed GFP fluorescence marking expression of the *EWS-ATF1-IRES-eGFP* transcript (Figure 5B). The *Prx1-CreERT2*-induced tumors appeared to arise from the periosteal/perichondrial layer as well as from within the musculature as judged by gross microscopy and histology (Figures 5B and 5C). The tumors induced in the *Prx1* lineage demonstrated either the clear cell morphology with lightly stained eosinophilic cytoplasm or spindle cell morphology, both closely resembling tumors induced by TAT-Cre.

Notably, some tumors induced by *Prx1-CreERT2* expressed M-MITF, but others did not (Figure 5D). CCS in humans often but not always expresses M-MITF (Granter et al., 2001). Thus, it appears that induction of *EWS-ATF1* expression with *Prx1-CreERT2* generated both subtypes of CCS.

EWS-ATF1 Expression in Postnatal Mesenchymal Stem Cells Generates CCSs with a More Consistent Phenotype

In order to interrogate possible cells of origin in the undifferentiated progenitor cell population that precedes *Prx1* expression postnatally, we bred mice bearing the Rosa26^{EA1} allele to mice bearing *Bmi1*^{CreERT2} (Sangiorgi and Capecchi, 2008). *Bmi1* is a general marker for stem cells and has been demonstrated to label intestinal, neural, epidermal, and hematopoietic stem cells (Claudinot et al., 2005; Leung et al., 2004; Park et al., 2003; Sangiorgi and Capecchi, 2008). A single peritoneal injection of tamoxifen into *Bmi1*^{CreERT2};Rosa26^{EA1} mice after 3 weeks of

sarcoma-related fusion oncogenes in mouse embryonic fibroblasts in vitro and many tissues in vivo when induced after weaning, it is of significant toxicity in specific tissue settings during development.

EWS-ATF1 Expression in Postnatal Mesenchymal Progenitors Generates Two CCS Tumor Types

Noting that early tamoxifen administration in Rosa26^{CreER/EA1} mice did not result in tumorigenesis but later administration did (Figure 3), we hypothesized that the toxicity prompted in the mesenchymal tissues embryonically might be avoided at later stages of development. In order to test this hypothesis, we bred mice bearing the Rosa26^{EA1} allele to mice bearing either *Pax7*^{CreERT2} (Murphy et al., 2011) or *Prx1-CreERT2* (Hasson et al., 2007), then administered tamoxifen after three weeks of age. By 12 months posttamoxifen, myopathy consistently developed in the *Pax7*^{CreERT2};Rosa26^{EA1} mice, but no tumors were observed (Figures S2D and S2E). The absence of tumor formation argues against muscle satellite cells being a potential cell of origin for EWS-ATF1-induced tumors. In the embryo, *Prx1-Cre* is widely expressed in the mesenchyme of the

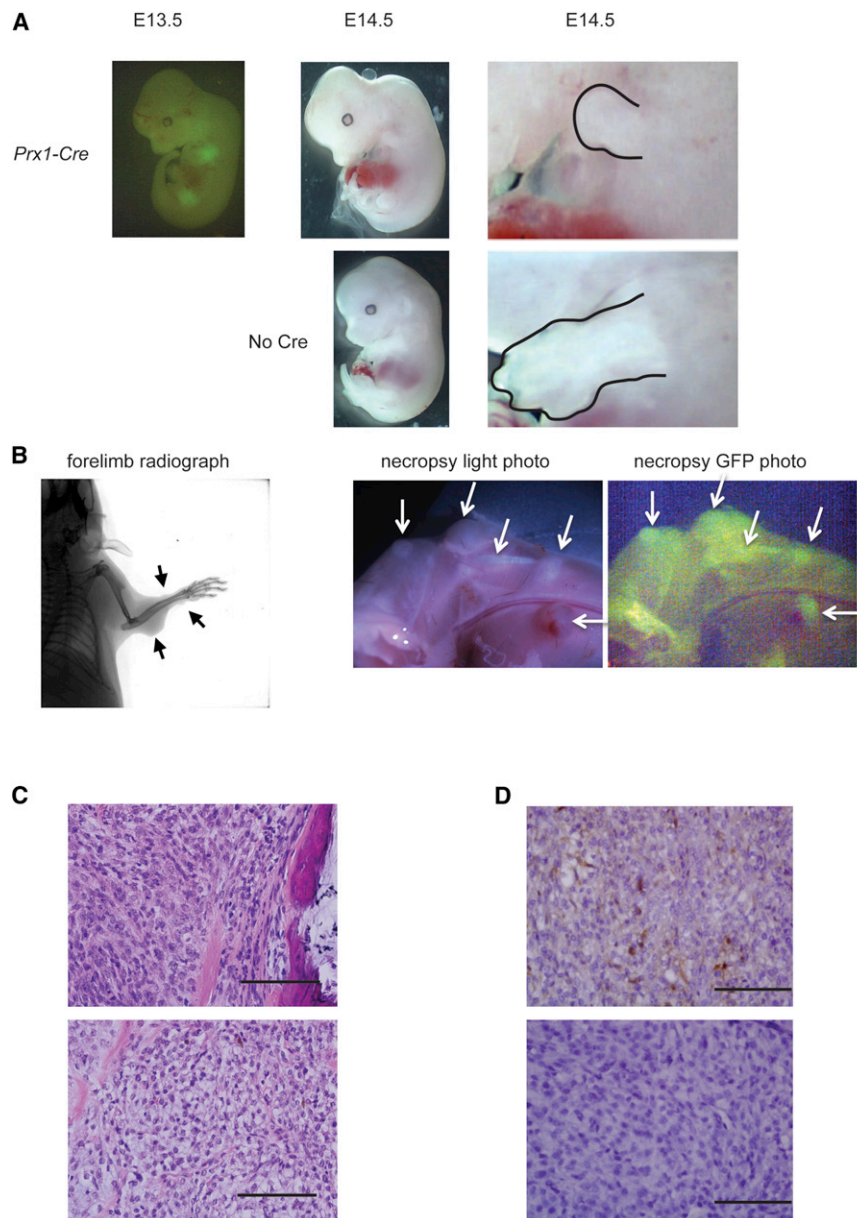


Figure 5. *EWS-ATF1* Drives Apoptosis in the Embryonic *Prx1*-Lineage and Tumorigenesis in the Postweaning *Prx1* Lineage

(A) GFP fluorescence image of *Prx1-Cre*; *Rosa26^{EA1}* embryos at embryonic day 13.5 (far left). *Prx1-Cre*; *Rosa26^{EA1}* at E14.5 (top middle), compared to littermate controls lacking *Prx1-Cre* (bottom middle); the limbs of mutant and control are enlarged to show difference in size (outlined in right panels).

(B) Radiograph of a *Prx1-CreERT2*; *Rosa26^{EA1}* mouse 8 weeks after a single tamoxifen injection at 4 weeks of age (left), gross necropsy photos with halogen light (middle) or GFP fluorescence (right) of *Prx1-CreERT2*; *Rosa26^{EA1}* limb 8 weeks posttamoxifen injection (arrows point to tumors).

(C) H&E-stained histopathology of *Prx1-CreERT2*; *Rosa26^{EA1}* tumor immediately adjacent to bone (upper) and tumor exhibiting classic clear cell sarcoma morphology (lower).

(D) Immunohistochemistry for M-MITF on *Prx1-CreERT2*; *Rosa26^{EA1}*-derived tumors. Scale bars are 100 μ m in length.

See also Figure S2.

age resulted in fully penetrant tumorigenesis. Every mouse developed tumors in the deeper mesenchymal tissues of the limb and trunk (Figure 6A). Some tumors formed completely within and surrounded by muscle (Figure 6B), similar to a subset of the *Prx1*-lineage tumors. A larger portion formed adjacent to bone, arising from the periosteum/perichondrium, also similar to several of the *Prx1*-lineage tumors (Figure 6B). The *Bmi1*-lineage tumors consistently matched the clear cell morphology and immunohistochemical profile of human CCS tumors, uniformly demonstrating M-MITF and S100B (Figures 6B and 6C).

Prior reports have suggested a role for *Bmi1* in mesenchymal stem cells based on depletion of the pool of osteochondroprogenitors in mice bearing homozygous disruption of *Bmi1* (Zhang et al., 2010). To follow up these studies and more fully characterize the *Bmi1* lineage in mesen-

chyme, mice bearing *Bmi1^{CreERT2}* were crossed to a robust reporter mouse expressing *tdTomato* conditionally from the *Rosa26* locus. *Bmi1^{CreER}*; *Rosa26^{tdTomato}* mice were injected with a single dose of tamoxifen at 6 weeks of age, and their limb tissues were harvested 1, 2, and 9 months postinjection for analysis.

We analyzed the early *Bmi1* lineage focused on the mesenchymal progenitor population within the bone marrow and endosteum. *Nestin* has recently been shown to be an accurate marker of the multipotent mesenchymal stem cell subpopulation in this location, whereas no specific markers are agreed upon in the periosteum (Méndez-Ferrer et al.,

2010). Colabeling experiments on tissue sections revealed the colocalization of the early *Bmi1* lineage marker to the *Nestin*-expressing cells, both at the endosteal surface in the bone marrow and in periosteum (Figure 6D), indicating that *Bmi1* is indeed expressed in this mesenchymal stem cell population. Lineage tracing experiments from tissues harvested 60 days and 9 months following tamoxifen administration revealed that *Bmi1*-expressing cells contribute to both osteoblast and chondrocyte lineages (Figure 6E), further affirming *Bmi1* as a marker of very early, stem-like cells in mesenchyme. The previously described *Prx1-CreERT2*-defined lineage marks a similar but smaller population of these differentiated mesenchymal cells (Kawanami et al., 2009). Using an antibody against *Prx1* to locate cells actively expressing the marker, we found a portion but not all of the cells in the *Bmi1^{CreER}*; *Rosa26^{tdTomato}* lineage expressed *Prx1*,

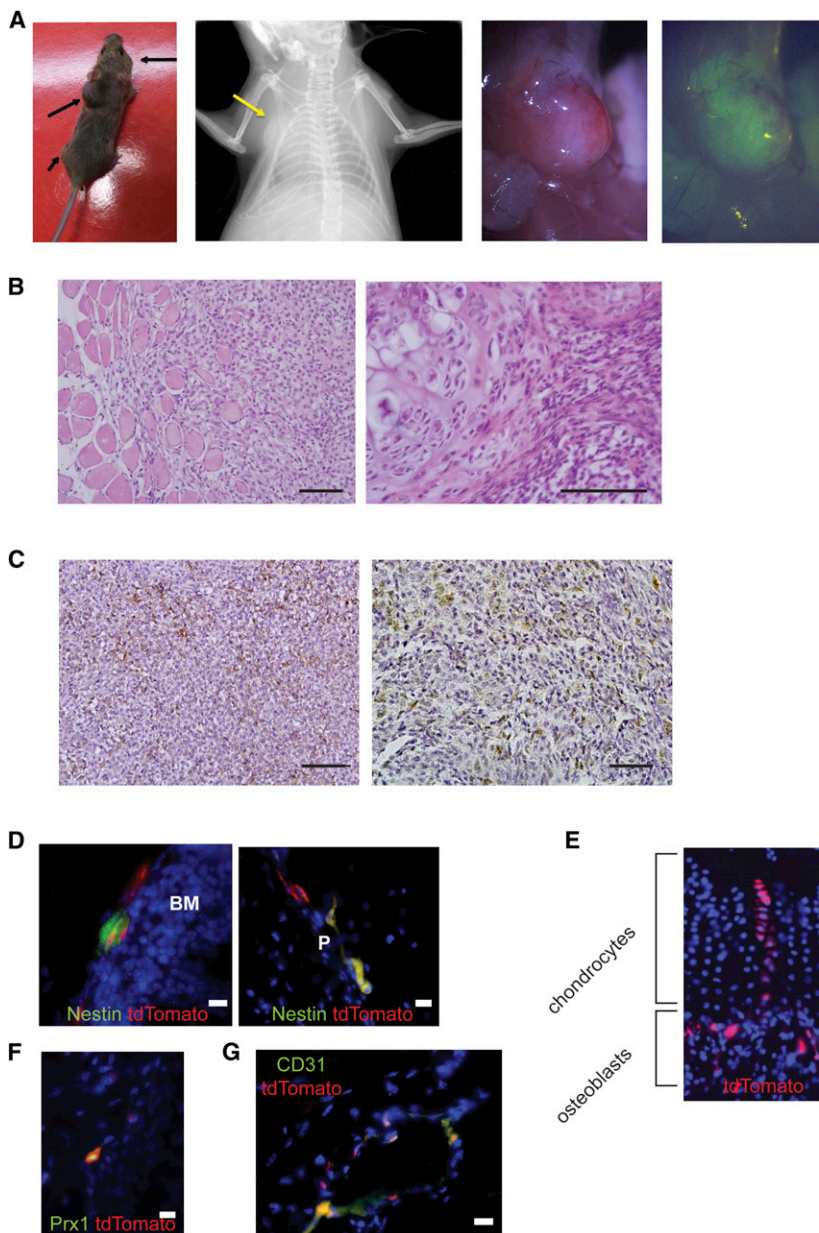


Figure 6. The *Bmi1* Lineage, Including Mesenchymal Stem Cells, Enables More Consistent Development of Clear Cell Sarcomas with Melanocytic Features

(A) Living image of *Bmi1*^{CreERT2};*Rosa26*^{EA1} mouse with black arrows indicating tumor formation (far left), radiograph (left), necropsy photo (right), and GFP fluorescence (far right) image of tumor formed in the chest wall (yellow arrow showing location of the tumor).

(B) H&E-stained histopathology of *Bmi1*^{CreERT2}-initiated tumors, including both intramuscular (left) and periosteal/perichondrial (right) tumors.

(C) Immunohistochemistry of *Bmi1*^{CreERT2}-initiated tumors stained for M-MITF (left) and S100B (right).

(D) Immunofluorescence for Nestin (green) and *Bmi1*^{CreERT2}-induced expression of tdTomato (red) in *Bmi1*^{CreERT2};*Rosa26*^{tdTomato} mice 30 days after injection of tamoxifen shown in the bone marrow BM (left) and periosteum P (right).

(E) *Bmi1*-lineage tracing from *Bmi1*^{CreERT2};*Rosa26*^{tdTomato} mouse at 60 days posttamoxifen demonstrates tdTomato fluorescence (red) in osteoblasts and chondrocytes.

(F) Immunofluorescence against Prx1 (green) and *Bmi1* lineage defined by tdTomato (red) in *Bmi1*^{CreERT2};*Rosa26*^{tdTomato} mice 30 days post-tamoxifen injection.

(G) Immunofluorescence against CD31 (green) and tdTomato *Bmi1*-lineage cells (red) at 60 days posttamoxifen. All scale bars are 100 μ m in length. See also Figure S3.

suggesting that differentiating cells from the *Bmi1* lineage express Prx1 (Figure 6F). Lineage tracing with *Prx1*-CreERT2 mice and immunofluorescence against Nestin confirmed that a subset of *Prx1*-lineage cells still express Nestin as well (Figure S3A).

Although mesenchymal stem cell and progenitor populations within and adjacent to the bone explain the location of some tumors arising in both the *Bmi1* and *Prx1* lineages, other tumors in both groups arose within the muscle compartments. Because it has previously been demonstrated that *Bmi1* is expressed in Pax7-positive satellite cells within muscle (Robson et al., 2011), it is possible that the intramuscular *Bmi1*-lineage tumors could arise from this cell population. However, we already discussed that *Pax7*^{CreERT2};*Rosa26*^{EA1} do not form tumors, arguing against the possibility that

different stages of differentiation, may serve as the originating cells of the CCS tumors that appear within the muscle compartments in these two groups.

Murine CCS Tumors Fit the Human CCS Expression Profile; Variations Appear to Reflect Different Cells of Origin

In order to determine the impact of these varied potential cells of origin on the resultant tumors, we performed RNA sequencing on a panel of mouse CCS tumors, induced by TAT-Cre, *Rosa26*^{CreER}, *Bmi1*^{CreERT2}, and *Prx1*-CreERT2. We simultaneously sequenced RNA from mouse synovial sarcomas and osteosarcomas, as well as control mesenchymal tissue. Using Spearman correlation as the distance metric and an average linkage, CCS from all induction methods clustered

satellite cells provide a potential cell of origin for CCS (Figures S2D and S2E).

Further analysis of the *Bmi1* lineage within the muscle compartments identified not only satellite cells but also CD31-expressing endothelial cells (Figure 6G). Lineage tracing with *Prx1*-CreERT2 mice identified CD31⁺ endothelial cells within its lineage as well (Figure S3B). A perivascular population of cells that has expressed both *Bmi1* and *Prx1*, perhaps at

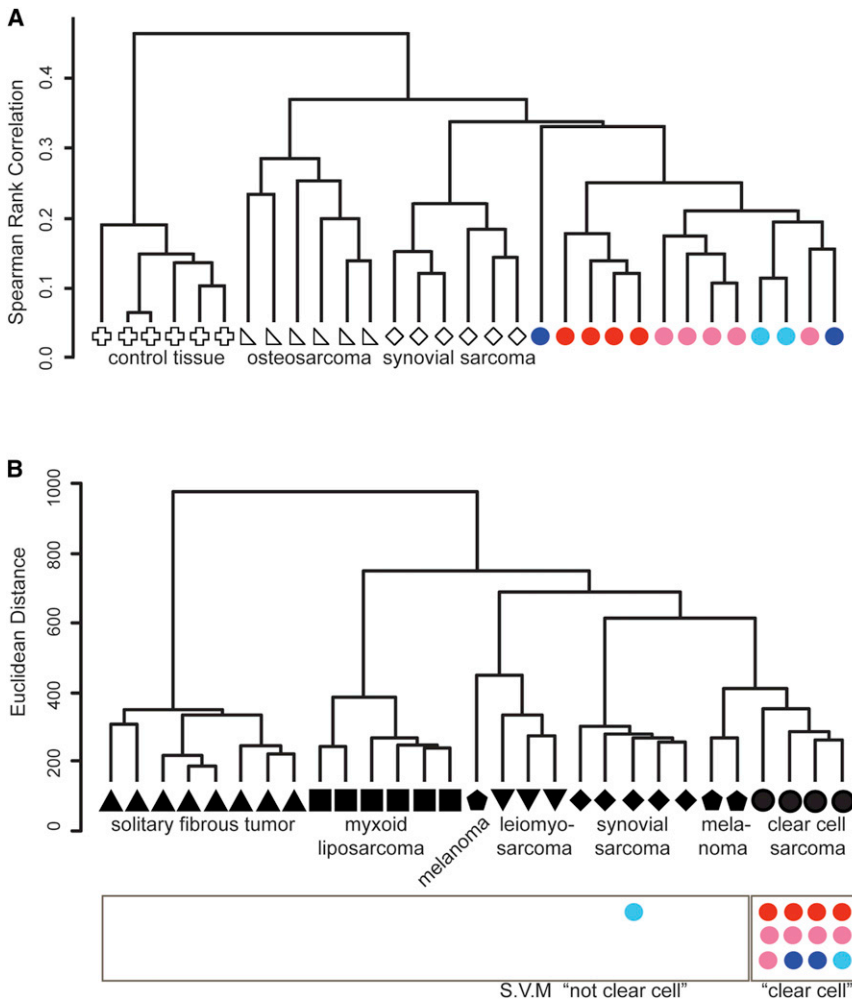


Figure 7. Tumors Derived from *EWS-ATF1* Expression in Different Cells of Origin Cluster Together According to Expression Profile and Fit Human Clear Cell Sarcoma Profiles

(A) Unsupervised hierarchical clustering of mouse samples by sequencing-defined transcriptional profiling, osteosarcomas (triangle), synovial sarcomas (diamond), *EWS-ATF1*-driven tumors by TAT-Cre (red circles), *Rosa26^{CreER}* (pink circles), *Bmi1^{CreERT2}* (dark blue circles), and *Prx1-CreERT2* (light blue circles) and control samples from chest-wall mesenchymal tissues (cross).

(B) Unsupervised hierarchical clustering of human tumors profiled by microarray and used to train the supervised machine-learning module, solitary fibrous tumor (triangle), myxoid liposarcoma (square), melanoma (pentagon), leiomyosarcoma (triangle), synovial sarcoma (diamond), and clear cell sarcoma (circle). The mouse *EWS-ATF1*-driven tumors are placed under the category of human tumors they most identified with on the supervised machine-learning module, TAT-Cre (red circles), *Rosa26^{CreER}* (pink circles), *Bmi1^{CreERT2}* (dark blue circles), and *Prx1-CreERT2* (light blue circles).

tumors were predicted to be human CCS, rather than one of the other tumor types (Figure 7B). As a control, zero of five RNA sequencing data sets from wild-type mouse mesenchymal tissue controls were identified as human CCS when input into the same SVM. These data confirm that mouse tumors derived from conditional expression of *EWS-ATF1* resemble the expression profile of

human CCS more closely than the other soft-tissue tumors or melanoma.

Notably, the one mouse CCS that did not cluster closely to the human CCS SVM prediction was a *Prx1-CreERT2*-initiated tumor that did not express *M-Mitf*. In contrast, another *Prx1-CreERT2*-initiated tumor that expressed *M-Mitf* did cluster with human clear cell sarcoma.

Further comparative analysis of the RNA-sequencing expression profiles of the two *Prx1*-lineage and the two *Bmi1*-lineage tumors, both sets from the same anatomic locations, identified a number of consistently differentially expressed genes. Three of the top ten genes more highly expressed in *Prx1-CreERT2*; *Rosa26^{EA1}* were *Crtf1*, which is present in osteoblasts and chondrocytes, along with *Saa1* and *Saa2*, which are upregulated in differentiated compared to undifferentiated mesenchymal stem cells (Clancy et al., 2003; Kovacevic et al., 2008).

To better evaluate the difference between the *Bmi1^{CreERT2}*; *Rosa26^{EA1}* and *Prx1-CreERT2*; *Rosa26^{EA1}* tumors, we performed RT-PCR on a panel of additional samples. This revealed that some *Prx1*-lineage tumors indeed expressed *M-Mitf* and *Tyrosinase* but not all (Figure 8A). All *Bmi1*-lineage tumors expressed these melanocytic markers. Interestingly, the *Prx1*-lineage tumor that did not express *Nestin* also did not express *M-Mitf* or

human CCS more closely than the other soft-tissue tumors or melanoma.

Notably, the one mouse CCS that did not cluster closely to the human CCS SVM prediction was a *Prx1-CreERT2*-initiated tumor that did not express *M-Mitf*. In contrast, another *Prx1-CreERT2*-initiated tumor that expressed *M-Mitf* did cluster with human clear cell sarcoma.

Further comparative analysis of the RNA-sequencing expression profiles of the two *Prx1*-lineage and the two *Bmi1*-lineage tumors, both sets from the same anatomic locations, identified a number of consistently differentially expressed genes. Three of the top ten genes more highly expressed in *Prx1-CreERT2*; *Rosa26^{EA1}* were *Crtf1*, which is present in osteoblasts and chondrocytes, along with *Saa1* and *Saa2*, which are upregulated in differentiated compared to undifferentiated mesenchymal stem cells (Clancy et al., 2003; Kovacevic et al., 2008).

To better evaluate the difference between the *Bmi1^{CreERT2}*; *Rosa26^{EA1}* and *Prx1-CreERT2*; *Rosa26^{EA1}* tumors, we performed RT-PCR on a panel of additional samples. This revealed that some *Prx1*-lineage tumors indeed expressed *M-Mitf* and *Tyrosinase* but not all (Figure 8A). All *Bmi1*-lineage tumors expressed these melanocytic markers. Interestingly, the *Prx1*-lineage tumor that did not express *Nestin* also did not express *M-Mitf* or

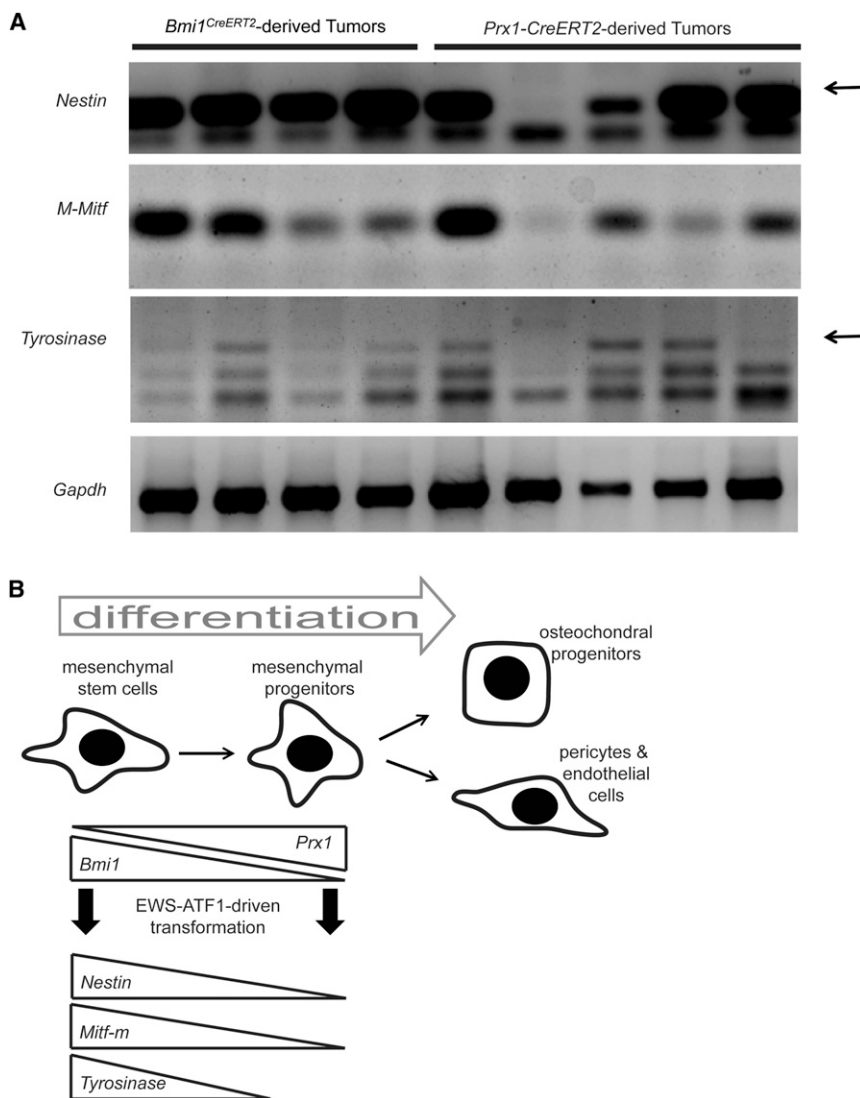


Figure 8. Tumors Arising from *EWS-ATF1* Expression Initiated in the *Prx1* or *Bmi1* Lineages Differ by Expression Profile

(A) RT-PCR analysis of the indicated transcripts on total RNA isolated from *Bmi1*- and *Prx1*-lineage tumors (arrow points to the correct band). (B) Working model of the impact of early differentiation within multipotent mesenchymal progenitors on the possibility of transdifferentiation to express melanocytic markers upon clear cell sarcomagenesis driven by *EWS-ATF1*.

Comparison of the two models highlights the brief latency to tumorigenesis following expression of *EWS-ATF1* initiated by *Rosa26*^{CreER}. The synovial sarcoma model develops tumors after a year, rather than within 3 months. Further, expression of *SS18-SSX2* in most cells, in vitro or in vivo, was toxic. The very rapid onset of visible tumors in the mouse CCS model relative to synovial sarcoma suggest that fewer additional hits may be required to foster progression of the tumor. This may represent a fundamental difference between the biology of the two fusion oncogenes, as all other aspects of the models are the same.

It has not escaped our notice that the extreme oncogenicity of *EWS-ATF1* in mice contrasts with the rare incidence of formally diagnosed CCS in humans. A potential explanation for this discrepancy is the possibility that *EWS-ATF1* involvement in human tumorigenesis remains underappreciated. t(12;22) (q13;q12) chromosomal translocation and resultant fusion oncogenes are identified only

Tyrosinase. An additional *Prx1*-lineage tumor failed to express *Tyrosinase* only. This may indicate that between the stem-like state of *Bmi1* expression and the progenitor state of *Prx1* expression *Nestin*, *M-Mitf*, and *Tyrosinase* are epigenetically silenced (Figure 8B).

DISCUSSION

A few mouse genetic models of translocation-associated sarcomas have been described over the last decade, including models of alveolar rhabdomyosarcoma expressing *PAX3-FKHR* (Keller et al., 2004a, 2004b; Keller and Capecchi, 2005), myxoid liposarcoma expressing *FUS-CHOP* (Pérez-Losada et al., 2000), and synovial sarcoma expressing *SS18-SSX2* (Haldar et al., 2007, 2008, 2009). The last of these used means of transcriptional control of the fusion oncogene similar to those used in the current study, with expression in *Cre/loxP* conditional fashion from the *Rosa26* locus. The model of synovial sarcoma also demonstrated fully penetrant tumorigenesis when initiated by *Rosa26*^{CreER} or *Myf5Cre* (Haldar et al., 2009).

when pursued in clinical tumors. The widening range of tumors recently found to bear *EWS-ATF1*, such as angiomatoid fibrous histiocytoma and clear cell carcinoma of the salivary gland (Antonescu et al., 2011; Chen et al., 2011; Mangham et al., 2010; Ren et al., 2009), suggests that more may yet be identified in the near future. Second, the observed toxicity to embryonic development in the mouse by the early expression of the *EWS-ATF1* fusion gene may greatly limit the acceptable time frame for the formation of the required t(12;22) chromosomal translocation in humans. Finally, not all balanced chromosomal translocations arise with equal frequency, and the formation of the t(12;22) translocation responsible for CCS may be the rate limiting step for this malignancy.

Different cells of origin impacted features of the tumors resulting from *EWS-ATF1* expression. Tumors from both the *Bmi1* and *Prx1* postnatal lineages developed in nearly identical anatomic locations (in the muscle and from the periosteal surface of bones) and fit the histologic appearance of human CCS, but the *Prx1*-lineage tumors did not consistently express the melanocytic markers *M-Mitf* and *Tyrosinase*. The

M-Mitf-expressing *Prx1*-lineage tumors fit the general expression signature of human CCS. Those not expressing *M-Mitf* did not. This observation may explain the fact that not all human CCSs clearly express melanoma markers. All four human tumors used for expression profiling were typical *M-Mitf*-expressing melanoma-like CCSs. Perhaps, the *Prx1*-induced mouse tumor that did not express *M-Mitf* might have fit better with a broader group of human CCSs.

Expression of *Nestin* has previously been reported in human CCS cell lines (Dimas et al., 2008). All *Bmi1*-lineage tumors expressed *Nestin* and the melanocytic markers, whereas variable *Nestin* expression in *Prx1*-lineage tumors predicted expression of the melanocytic markers. *Nestin* has previously been proven to be a marker of stemness in mesenchyme (Méndez-Ferrer et al., 2010) and to overlap with the *Bmi1* lineage and partly with the *Prx1* lineage. This evidence along with the colabeling experiments showing *Prx1* expression within the *Bmi1* lineage suggests that the differentiation steps between *Bmi1*-expressing cells and *Prx1*-expressing cells include a gradual loss of stemness. The epigenetic state may render the melanocytic markers unavailable for upregulation by ATF constitutive activation alone (Figure 8B).

Many have argued in the past about the origin of the melanocytic features of human CCS, variably attributing them to either cell of origin or transformation by *EWS-ATF1*, which also upregulates *M-Mitf*. Although we have not ruled out the possibility that melanocytes or their precursors might also offer sufficient cells of origin, the tumors we have induced in mesenchyme actually bolster both prior arguments. CCS transformation can enable transdifferentiation that includes melanocytic markers but only from certain cells of origin. Perhaps a cell's reprogrammability, even during aggressive transformation from expression of a powerful fusion oncogene, remains at least partly checked by its antecedent differentiation state.

This mouse model will enable additional dissection of the ATF pathway's impact on oncogenesis in vivo. Further, the model is ideally suited to preclinical testing of targeted therapies for this and other CCS pathways. Administration of TAT-Cre produces visible tumors within a few weeks and avoids any pleiotropic developmental effects from toxicity of the fusion oncogene expressed across an entire tissue. These tumors are well localized, offering a reasonable model for the study of metastasis. Unlike delivery of Cre with a virus, a single molecule of TAT-Cre cannot readily diffuse to a great distance or travel through the blood stream to a distant site and induce recombination, as at least two molecules of the TAT-Cre protein must enter any given cell to catalyze the recombination event (Joshi et al., 2002).

Because of the low frequency of sarcomas, the most critically scarce resource for developing more effective therapeutic strategies for these malignancies is patients themselves. It is not easy to assemble sufficient numbers of patients for carrying out subtype-specific sarcoma clinical trials. Therapeutic strategies must be optimized and prioritized in the preclinical arena before advancing to clinical trial. Authenticated mouse models could serve this purpose. Genomic sequencing and profiling has vastly increased the ability to test the authenticity of a mouse model's recapitulation of human malignancy. Once established as an excellent facsimile to the human cancer, a mouse model can

be used not only to interrogate cancer mechanisms and identify pertinent therapeutic targets but also as a platform for assessment of drug efficacy. Successful candidate therapeutic strategies could be then moved to human trials with greater assurance of success.

In summary, we have shown that the oncogenic fusion protein that characterizes CCS is sufficient to initiate CCS-like tumors in mice that recapitulate human CCS in terms of cell morphology, immunohistochemistry, and genome-wide expression. This fusion gene generates two distinguishable tumor types in mice that also reflect similar variance in morphology and tissue distribution seen in humans (i.e., principally falling in two classes: those that resemble melanomas because of the expression of *M-Mitf* and its target genes and those that do not). The apparent difference in cells of origin of these two potential subclasses described herein with mice may provide an explanation of why human CCS commonly, but inconsistently, displays the classical melanocytic features.

EXPERIMENTAL PROCEDURES

Targeted Mouse Line Production

Human *EWS-ATF1* cDNA was obtained by RT-PCR of total RNA from eight histologically and immunohistochemically confirmed clear cell sarcoma tumors. The total RNA was obtained as deidentified patient sample through an approved University of Utah Institutional Review Board Protocol. PCR was used to identify tumors that contained the type 1 *EWS-ATF1* fusion gene. After screening, the cDNA sample was used to amplify the entire fusion oncogene. The cDNA clone was subcloned into the *Rosa26UA* plasmid using *AscI* and *FseI* Sites. This plasmid contained the *Loxp-pgk-Neo-tPA-Loxp-AscI-FheI-IRES-EGFP* within the *Rosa26* homology arms, and the final targeting construct contained *Loxp-pgk-Neo-tPA-Loxp-EWS-ATF1-IRES-EGFP*. Genotyping protocol and further details on gene targeting used can be found in the Supplemental Experimental Procedures.

Animals, Radiograph, Tissue Preparation, and Immunohistochemistry

All mouse experiments were performed in accordance with humane practices, national and international regulations, and with the approval of the University of Utah Institutional Animal Care and Use committee. Radiographs were obtained postasphyxiation using a Carestream 4000 Pro-Fx instrument (Carestream Molecular Imaging, Woodbridge, CT, USA).

Mouse tumors were extracted after asphyxiation and were fixed overnight in 4% paraformaldehyde prior to embedding in paraffin. Immunostaining and tissue preparation along with antibodies used are described in the Supplemental Experimental Procedures.

Transcriptome Analysis

A portion of each tumor was snap frozen for delayed total RNA extraction using the QIAGEN RNeasy Mini kit (QIAGEN, Valencia, CA, USA). RT-PCR was performed with random hexamer primers to generate cDNAs, followed by PCR for specific transcripts (Supplemental Experimental Procedures).

For RNA sequencing, total RNA was prepared using an Illumina TruSeq RNA sample prep kit (Illumina, San Diego, CA, USA) and quality checked with an Agilent Bioanalyzer RNA 6000 chip (Agilent Technologies, Santa Clara, CA, USA). mRNAs were captured by oligodT magnetic beads and fragmented. Library quality was then checked by Nanodrop analysis (Thermo Scientific, Wilmington, DE, USA), qPCR quantitation using Illumina primers, and another bioanalyzer run. Sequencing was performed on an Illumina HiSeq 2000 machine (Illumina) using a 50-cycle single-end read. PhiX control library reads were added to each lane for quality assurance. Reads were then aligned with the mm9 mouse genome. Basic clusterings were performed using GeneSifter software (Geospiza, Seattle, WA, USA). Methods used to classify tumor type using RNA-seq data can be found in the Supplemental Experimental Procedures.

ACCESSION NUMBERS

The RNA-seq data have been deposited in NCBI's Gene Expression Omnibus (<http://www.ncbi.nlm.nih.gov/geo/>) and are accessible through the GEO series accession number GSE41293. Human microarray data have been deposited in NCBI's Gene Expression Omnibus and are accessible through the GEO series accession number GSE43045.

SUPPLEMENTAL INFORMATION

Supplemental Information includes three figures, five tables, and Supplemental Experimental Procedures and can be found with this article online at <http://dx.doi.org/10.1016/j.ccr.2012.12.019>.

ACKNOWLEDGMENTS

The authors gratefully acknowledge Matt Hockin (University of Utah, Salt Lake City, UT, USA) for producing the TAT-Cre, Allie Grossmann (University of Utah) for assistance with pathology analysis, Jay S. Wunder and Irene L. Andrulis (University of Toronto, Ontario, Canada) for providing the human CCS samples for isolation of the cDNA, and Brian Dalley and Brett Milash (University of Utah) for assistance with RNA sequencing and analysis. Research in the Capecchi lab is supported by the National Institute of Health. K.M.S. receives graduate student support from the Howard Hughes Med2Grad program. K.B.J. receives career development support from the National Cancer Institute (National Institutes of Health [NIH] K08CA138764K08). This work was partly supported by P30CA042014 from the National Cancer Institute. The content is solely the responsibility of the authors and does not necessarily represent the official views of the National Cancer Institute or the National Institutes of Health.

Received: September 20, 2012

Revised: November 13, 2012

Accepted: December 26, 2012

Published: February 11, 2013

REFERENCES

Antonescu, C.R., Tschernyavsky, S.J., Woodruff, J.M., Jungbluth, A.A., Brennan, M.F., and Ladanyi, M. (2002). Molecular diagnosis of clear cell sarcoma: detection of EWS-ATF1 and M-MITF transcripts and histopathological and ultrastructural analysis of 12 cases. *J. Mol. Diagn.* 4, 44–52.

Antonescu, C.R., Katabi, N., Zhang, L., Sung, Y.S., Seethala, R.R., Jordan, R.C., Perez-Ordoñez, B., Have, C., Asa, S.L., Leong, I.T., et al. (2011). EWSR1-ATF1 fusion is a novel and consistent finding in hyalinizing clear-cell carcinoma of salivary gland. *Genes Chromosomes Cancer* 50, 559–570.

Chen, G., Folpe, A.L., Colby, T.V., Sittampalam, K., Patey, M., Chen, M.G., and Chan, J.K. (2011). Angiomatoid fibrous histiocytoma: unusual sites and unusual morphology. *Mod. Pathol.* 24, 1560–1570.

Clancy, B.M., Johnson, J.D., Lambert, A.J., Rezvankhah, S., Wong, A., Resmini, C., Feldman, J.L., Leppanen, S., and Pittman, D.D. (2003). A gene expression profile for endochondral bone formation: oligonucleotide microarrays establish novel connections between known genes and BMP-2-induced bone formation in mouse quadriceps. *Bone* 33, 46–63.

Claudinot, S., Nicolas, M., Oshima, H., Rochat, A., and Barrandon, Y. (2005). Long-term renewal of hair follicles from clonogenic multipotent stem cells. *Proc. Natl. Acad. Sci. USA* 102, 14677–14682.

Covinsky, M., Gong, S., Rajaram, V., Perry, A., and Pfeifer, J. (2005). EWS-ATF1 fusion transcripts in gastrointestinal tumors previously diagnosed as malignant melanoma. *Hum. Pathol.* 36, 74–81.

D'Amico, F.E., Ruffolo, C., Romeo, S., Massani, M., Dei Tos, A.P., and Bassi, N. (2012). Clear cell sarcoma of the ileum: report of a case and review of the literature. *Int. J. Surg. Pathol.* 20, 401–406.

Danielian, P.S., Muccino, D., Rowitch, D.H., Michael, S.K., and McMahon, A.P. (1998). Modification of gene activity in mouse embryos in utero by a tamoxifen-inducible form of Cre recombinase. *Curr. Biol.* 8, 1323–1326.

Davis, I.J., Kim, J.J., Oszolak, F., Widlund, H.R., Rozenblatt-Rosen, O., Granter, S.R., Du, J., Fletcher, J.A., Denny, C.T., Lessnick, S.L., et al. (2006). Oncogenic MITF dysregulation in clear cell sarcoma: defining the MiT family of human cancers. *Cancer Cell* 9, 473–484.

Dimas, K., Tsimplouli, C., Anagnostopoulos, A.K., Mahaira, L., Iliopoulou, E., Perez, S., Vougas, K., and Tsangaris, G.T. (2008). The proteome profile of two cell lines and their xenografts isolated from a patient with clear cell sarcoma (soft tissue melanoma). *Cancer Genomics Proteomics* 5, 175–237.

Durland, J.L., Sferlazzo, M., Logan, M., and Burke, A.C. (2008). Visualizing the lateral somitic frontier in the Prx1Cre transgenic mouse. *J. Anat.* 212, 590–602.

Engleka, K.A., Gitler, A.D., Zhang, M., Zhou, D.D., High, F.A., and Epstein, J.A. (2005). Insertion of Cre into the Pax3 locus creates a new allele of Splotch and identifies unexpected Pax3 derivatives. *Dev. Biol.* 280, 396–406.

Enzinger, F.M. (1965). Clear-cell sarcoma of tendons and aponeuroses. An analysis of 21 cases. *Cancer* 18, 1163–1174.

Falconieri, G., Bacchi, C.E., and Luzar, B. (2012). Cutaneous clear cell sarcoma: report of three cases of a potentially underestimated mimicker of spindle cell melanoma. *Am. J. Dermatopathol.* 34, 619–625.

Fujimura, Y., Siddique, H., Lee, L., Rao, V.N., and Reddy, E.S. (2001). EWS-ATF-1 chimeric protein in soft tissue clear cell sarcoma associates with CREB-binding protein and interferes with p53-mediated trans-activation function. *Oncogene* 20, 6653–6659.

Granter, S.R., Weilbaecher, K.N., Quigley, C., Fletcher, C.D., and Fisher, D.E. (2001). Clear cell sarcoma shows immunoreactivity for microphthalmia transcription factor: further evidence for melanocytic differentiation. *Mod. Pathol.* 14, 6–9.

Haldar, M., Hancock, J.D., Coffin, C.M., Lessnick, S.L., and Capecchi, M.R. (2007). A conditional mouse model of synovial sarcoma: insights into a myogenic origin. *Cancer Cell* 11, 375–388.

Haldar, M., Randall, R.L., and Capecchi, M.R. (2008). Synovial sarcoma: from genetics to genetic-based animal modeling. *Clin. Orthop. Relat. Res.* 466, 2156–2167.

Haldar, M., Hedberg, M.L., Hockin, M.F., and Capecchi, M.R. (2009). A CreER-based random induction strategy for modeling translocation-associated sarcomas in mice. *Cancer Res.* 69, 3657–3664.

Hantschke, M., Mentzel, T., Rütten, A., Palmedo, G., Calonje, E., Lazar, A.J., and Kutzner, H. (2010). Cutaneous clear cell sarcoma: a clinicopathologic, immunohistochemical, and molecular analysis of 12 cases emphasizing its distinction from dermal melanoma. *Am. J. Surg. Pathol.* 34, 216–222.

Hasson, P., Del Buono, J., and Logan, M.P. (2007). Tbx5 is dispensable for forelimb outgrowth. *Development* 134, 85–92.

Hocar, O., Le Cesne, A., Berissi, S., Terrier, P., Bonvalot, S., Vanel, D., Auperin, A., Le Pechoux, C., Bui, B., Coindre, J.M., and Robert, C. (2012). Clear cell sarcoma (malignant melanoma) of soft parts: a clinicopathologic study of 52 cases. *Dermatol. Res. Pract.* 2012, 984096.

Huang da, W., Sherman, B.T., and Lempicki, R.A. (2009a). Bioinformatics enrichment tools: paths toward the comprehensive functional analysis of large gene lists. *Nucleic Acids Res.* 37, 1–13.

Huang da, W., Sherman, B.T., and Lempicki, R.A. (2009b). Systematic and integrative analysis of large gene lists using DAVID bioinformatics resources. *Nat. Protoc.* 4, 44–57.

Joshi, S.K., Hashimoto, K., and Koni, P.A. (2002). Induced DNA recombination by Cre recombinase protein transduction. *Genesis* 33, 48–54.

Kawanami, A., Matsushita, T., Chan, Y.Y., and Murakami, S. (2009). Mice expressing GFP and CreER in osteochondro progenitor cells in the perios-teum. *Biochem. Biophys. Res. Commun.* 386, 477–482.

Keller, C., and Capecchi, M.R. (2005). New genetic tactics to model alveolar rhabdomyosarcoma in the mouse. *Cancer Res.* 65, 7530–7532.

Keller, C., Arenkiel, B.R., Coffin, C.M., El-Bardeesy, N., DePinho, R.A., and Capecchi, M.R. (2004a). Alveolar rhabdomyosarcomas in conditional Pax3:Fkhr mice: cooperativity of Ink4a/ARF and Trp53 loss of function. *Genes Dev.* 18, 2614–2626.



- Keller, C., Hansen, M.S., Coffin, C.M., and Capecchi, M.R. (2004b). Pax3:Fkhr interferes with embryonic Pax3 and Pax7 function: implications for alveolar rhabdomyosarcoma cell of origin. *Genes Dev.* 18, 2608–2613.
- Kisanuki, Y.Y., Hammer, R.E., Miyazaki, J., Williams, S.C., Richardson, J.A., and Yanagisawa, M. (2001). Tie2-Cre transgenic mice: a new model for endothelial cell-lineage analysis in vivo. *Dev. Biol.* 230, 230–242.
- Kovacevic, A., Hammer, A., Stadelmeier, E., Windischhofer, W., Sundl, M., Ray, A., Schweighofer, N., Friedl, G., Windhager, R., Sattler, W., and Malle, E. (2008). Expression of serum amyloid A transcripts in human bone tissues, differentiated osteoblast-like stem cells and human osteosarcoma cell lines. *J. Cell. Biochem.* 103, 994–1004.
- Leung, C., Lingbeek, M., Shakhova, O., Liu, J., Tanger, E., Saremaslani, P., Van Lohuizen, M., and Marino, S. (2004). Bmi1 is essential for cerebellar development and is overexpressed in human medulloblastomas. *Nature* 428, 337–341.
- Logan, M., Martin, J.F., Nagy, A., Lobe, C., Olson, E.N., and Tabin, C.J. (2002). Expression of Cre Recombinase in the developing mouse limb bud driven by a Prx1 enhancer. *Genesis* 33, 77–80.
- Lyle, P.L., Amato, C.M., Fitzpatrick, J.E., and Robinson, W.A. (2008). Gastrointestinal melanoma or clear cell sarcoma? Molecular evaluation of 7 cases previously diagnosed as malignant melanoma. *Am. J. Surg. Pathol.* 32, 858–866.
- Mangham, D.C., Williams, A., Lalam, R.K., Brundler, M.A., Leahy, M.G., and Cool, W.P. (2010). Angiomatoid fibrous histiocytoma of bone: a calcifying sclerosing variant mimicking osteosarcoma. *Am. J. Surg. Pathol.* 34, 279–285.
- Mao, X., Fujiwara, Y., and Orkin, S.H. (1999). Improved reporter strain for monitoring Cre recombinase-mediated DNA excisions in mice. *Proc. Natl. Acad. Sci. USA* 96, 5037–5042.
- Méndez-Ferrer, S., Michurina, T.V., Ferraro, F., Mazloom, A.R., Macarthur, B.D., Lira, S.A., Scadden, D.T., Ma'ayan, A., Enikolopov, G.N., and Frenette, P.S. (2010). Mesenchymal and haematopoietic stem cells form a unique bone marrow niche. *Nature* 466, 829–834.
- Murphy, M.M., Lawson, J.A., Mathew, S.J., Hutcheson, D.A., and Kardon, G. (2011). Satellite cells, connective tissue fibroblasts and their interactions are crucial for muscle regeneration. *Development* 138, 3625–3637.
- Muzumdar, M.D., Tasic, B., Miyamichi, K., Li, L., and Luo, L. (2007). A global double-fluorescent Cre reporter mouse. *Genesis* 45, 593–605.
- Nielsen, T.O., West, R.B., Linn, S.C., Alter, O., Knowling, M.A., O'Connell, J.X., Zhu, S., Fero, M., Sherlock, G., Pollack, J.R., et al. (2002). Molecular characterisation of soft tissue tumours: a gene expression study. *Lancet* 359, 1301–1307.
- Park, I.K., Qian, D., Kiel, M., Becker, M.W., Pihalja, M., Weissman, I.L., Morrison, S.J., and Clarke, M.F. (2003). Bmi-1 is required for maintenance of adult self-renewing haematopoietic stem cells. *Nature* 423, 302–305.
- Pérez-Losada, J., Pintado, B., Gutiérrez-Adán, A., Flores, T., Bañares-González, B., del Campo, J.C., Martín-Martín, J.F., Battaner, E., and Sánchez-García, I. (2000). The chimeric FUS/TLS-CHOP fusion protein specifically induces liposarcomas in transgenic mice. *Oncogene* 19, 2413–2422.
- Ren, L., Guo, S.P., Zhou, X.G., and Chan, J.K. (2009). Angiomatoid fibrous histiocytoma: first report of primary pulmonary origin. *Am. J. Surg. Pathol.* 33, 1570–1574.
- Robson, L.G., Di Foggia, V., Radunovic, A., Bird, K., Zhang, X., and Marino, S. (2011). Bmi1 is expressed in postnatal myogenic satellite cells, controls their maintenance and plays an essential role in repeated muscle regeneration. *PLoS ONE* 6, e27116.
- Sangiorgi, E., and Capecchi, M.R. (2008). Bmi1 is expressed in vivo in intestinal stem cells. *Nat. Genet.* 40, 915–920.
- Somers, G.R., Viero, S., Nathan, P.C., Teshima, I., Pereira, C., and Zielenska, M. (2005). Association of the t(12;22)(q13;q12) EWS/ATF1 rearrangement with polyphenotypic round cell sarcoma of bone: a case report. *Am. J. Surg. Pathol.* 29, 1673–1679.
- Wang, W.L., Mayordomo, E., Zhang, W., Hernandez, V.S., Tuvin, D., Garcia, L., Lev, D.C., Lazar, A.J., and Lopez-Terrada, D. (2009). Detection and characterization of EWSR1/ATF1 and EWSR1/CREB1 chimeric transcripts in clear cell sarcoma (melanoma of soft parts). *Mod. Pathol.* 22, 1201–1209.
- Zhang, H.W., Ding, J., Jin, J.L., Guo, J., Liu, J.N., Karaplis, A., Goltzman, D., and Miao, D. (2010). Defects in mesenchymal stem cell self-renewal and cell fate determination lead to an osteopenic phenotype in Bmi-1 null mice. *J. Bone Miner. Res.* 25, 640–652.

Integrated Analyses Identify a Master MicroRNA Regulatory Network for the Mesenchymal Subtype in Serous Ovarian Cancer

Da Yang,^{1,11} Yan Sun,^{1,7,11} Limei Hu,^{1,11} Hong Zheng,^{8,11} Ping Ji,¹ Chad V. Pecot,⁶ Yanrui Zhao,⁸ Sheila Reynolds,⁹ Hanyin Cheng,^{1,12} Rajesha Rupaimoole,² David Cogdell,¹ Matti Nykter,¹⁰ Russell Broadus,¹ Cristian Rodriguez-Aguayo,⁴ Gabriel Lopez-Berestein,^{4,5} Jinsong Liu,¹ Ilya Shmulevich,⁹ Anil K. Sood,^{2,3,5,*} Kexin Chen,^{8,*} and Wei Zhang^{1,5,*}

¹Department of Pathology

²Department of Gynecologic Oncology and Reproductive Medicine

³Department of Cancer Biology

⁴Department of Experimental Therapeutics

⁵Center for RNAi and Non-Coding RNA

⁶Division of Cancer Medicine

The University of Texas MD Anderson Cancer Center, Houston, TX 77030, USA

⁷Department of Pathology

⁸Department of Epidemiology and Biostatistics

Tianjin Medical University Cancer Institute and Hospital, Tianjin 300060, China

⁹Institute for Systems Biology, Seattle, WA 98103, USA

¹⁰Tampere University of Technology, Tampere 33101, Finland

¹¹These authors contributed equally to this work

¹²Present address: Department of Cancer Biology, Kimmel Cancer Center, Thomas Jefferson University, Philadelphia, PA

*Correspondence: asood@mdanderson.org (A.K.S.), chenkexin@tjmu.edu.cn (K.C.), wzhang@mdanderson.org (W.Z.)

<http://dx.doi.org/10.1016/j.ccr.2012.12.020>

SUMMARY

Integrated genomic analyses revealed a miRNA-regulatory network that further defined a robust integrated mesenchymal subtype associated with poor overall survival in 459 cases of serous ovarian cancer (OvCa) from The Cancer Genome Atlas and 560 cases from independent cohorts. Eight key miRNAs, including miR-506, miR-141, and miR-200a, were predicted to regulate 89% of the targets in this network. Follow-up functional experiments illustrate that miR-506 augmented E-cadherin expression, inhibited cell migration and invasion, and prevented TGF β -induced epithelial-mesenchymal transition by targeting *SNAI2*, a transcriptional repressor of E-cadherin. In human OvCa, miR-506 expression was correlated with decreased *SNAI2* and *VIM*, elevated E-cadherin, and beneficial prognosis. Nanoparticle delivery of miR-506 in orthotopic OvCa mouse models led to E-cadherin induction and reduced tumor growth.

INTRODUCTION

Ovarian carcinoma (OvCa) is the most lethal gynecologic malignancy in the United States, with 22,280 new cases and 15,460 deaths estimated for 2012 (Siegel et al., 2012). The high rate of lethality from OvCa is primarily due to the advanced stage of disease at diagnosis. Early stage cancers can be cured in up

to 90% of patients with current therapies (Bast et al., 2009), but these rates drop substantially in patients with advanced disease. Approximately 30% of patients with advanced stage OvCa survive 5 years after initial diagnosis (Jemal et al., 2004).

Unlike cancers in other organ sites, OvCa can spread by direct invasion to adjacent organs or by transport throughout the peritoneal cavity via peritoneal fluid (Naora and Montell, 2005).

Significance

Ovarian cancer (OvCa) is one of the most lethal malignancies in women. Identification of molecular subtypes and corresponding molecular driver events is critical for the development of new therapies for patients with OvCa. Although accumulating evidence illustrates that epithelial-mesenchymal transition (EMT) plays an important role in OvCa progression, the driving molecular events are largely unknown. Our studies identified and validated miR-506, a key node in the microRNA regulatory network, as an EMT inhibitor in OvCa by targeting *SNAI2*. Nanoparticle delivery of miR-506 can suppress EMT and reduce tumor growth in orthotopic mouse models of OvCa, suggesting miR-506 may serve as a potential therapeutic tool for patients with OvCa.

Because of the diffuse nature of OvCa, surgery alone rarely leads to complete tumor resection. Postoperative platinum and taxane chemotherapy is required. Although 70% of patients with OvCa initially experience a response to therapy, most eventually die of disease recurrence (Bast et al., 2009; Jemal et al., 2004). A better understanding of the mechanisms involved in OvCa invasion and more effective therapeutic approaches are urgently needed.

Emerging evidence suggests that acquisition of invasiveness in OvCa cells is accompanied by the loss of epithelial features and the gain of a mesenchymal phenotype, a process known as epithelial-to-mesenchymal transition (EMT) (Cao et al., 2011; Rosanò et al., 2011). Tothill and colleagues investigated the gene expression profiles of 285 OvCa cases and reported that a mesenchymal subtype had relatively poor overall survival (Tothill et al., 2008). The recent publication by The Cancer Genome Atlas (TCGA) network recapitulated the mesenchymal subtype among close to 500 serous histological subtype of OvCa cases on the basis of transcriptome data (Cancer Genome Atlas Research Network, 2011). However, there was no correlation between the transcriptome mesenchymal subtype and overall survival in the TCGA data set. The driving molecular events behind the mesenchymal subtype in OvCa are poorly understood and need to be elucidated.

MiRNAs are a class of small noncoding RNA (~22 nt) that regulate gene expression by binding to the 3'-untranslated region (3'-UTR) of target genes triggering message RNA (mRNA) degradation or protein translation inhibition (Bagga et al., 2005). Almost 1,000 miRNAs have been identified in the human genome and are thought to regulate 30% of the transcriptome (Esquela-Kerscher and Slack, 2006). Most recently, several miRNAs, including miR-200 family members, have been found to regulate EMT by targeting E-cadherin repressors *ZEB1* and *ZEB2* (Gregory et al., 2008; Park et al., 2008).

In this study, we took an integrated approach and analyzed multidimensional data from 459 serous OvCa cases in TCGA to uncover the underlying molecular network of mesenchymal subtype of ovarian cancer.

RESULTS

Identification of TCGA Mesenchymal Signature Gene Sets Associated with DNA Copy Number Alterations, Promoter Methylation, and miRNA Expression

A consensus clustering analysis of expression data among serous OvCa cases led to the identification of four transcriptional subtypes: differentiated, immunoreactive, proliferative, and mesenchymal (Cancer Genome Atlas Research Network, 2011). These four subtypes (based solely on mRNA expression) were not significantly associated with survival differences (Cancer Genome Atlas Research Network, 2011). We hypothesized that integrating mRNA expression with associated alterations in genomic, epigenetic, and miRNA systems would allow us to identify molecular driver events and characterize clinically relevant subtypes.

The mRNA, miRNA, DNA copy number, and DNA methylation data on 459 clinical annotated OvCa cases were obtained from TCGA Data Portal (<http://tcga-data.nci.nih.gov/tcga/findarchives.htm>). We first identified 2,942 genes that were significantly overexpressed (FDR < 1%) in the mesenchymal

subtype relative to other TCGA-defined subtypes. Next, a multivariate linear regression model (see [Experimental Procedures](#)) was performed to search for genes whose expression was correlated with copy number alteration (CNA), DNA methylation, or associated miRNA expression. This analysis narrowed the list to 253 genes that were potentially regulated by these three genetic and epigenetic mechanisms. A set of 219 genes was predicted to be targeted by 19 miRNAs (Figure 1; see also [Table S1](#) available online). These miRNA-associated genes included EMT inducers *SNAI2* and *ZEB2*. The well-characterized mesenchymal regulators miR-141 and miR-200a were among the 19 identified miRNAs. The remaining two sets represent 26 CNA-associated and nine methylation-associated genes (Figure 1; [Table S1](#)). Twenty-three of the 26 CNA-associated genes, including *STAT3*, are located in chromosomal regions 19q13 and 17q11-q21, two regions reported to be frequently deleted in OvCa (Cancer Genome Atlas Research Network, 2011). The methylation-associated genes include *IL20RA*, which is frequently methylated in primary lung adenocarcinomas and lung cancer cell lines (Tessem et al., 2008).

MiRNA-Associated Genes Identified a Mesenchymal Subtype Associated with Poor Overall Survival

The above analysis showed that 259 of the 2,942 TCGA mesenchymal subtype-associated genes were correlated with CNA, methylation, or miRNA alterations. Most of these genes were members of a miRNA-mRNA regulatory network. We sought to determine whether the miRNA-associated gene set could be used to further characterize a mesenchymal subtype in OvCa. Consensus *K*-means clustering of 459 OvCa cases, based on 219 miRNA-associated genes, identified two clusters (Figure 2A), with clustering stability decreasing for larger *K* values (*K* = 2–6). Cluster 1, including 172 OvCa cases, formed a tight cluster, with higher expression of miRNA-associated genes. The majority of patients with cluster 1 OvCa (98%; 169 of 172 cases) had advanced stage (stages III and IV) disease ($p < 10^{-6}$, two-sided Fisher's exact test; Figure 2B; [Table S2](#)) and significantly shorter overall survival durations ($p = 0.02$, log-rank test; Figure 2B) than cluster 2 patients in whom miRNA-associated genes were consistently downregulated. Cluster 1 remained a predictor of poor patient overall survival (hazard ratio = 0.87, $p = 0.058$) on Cox multivariate analysis, after adjusting for patient age and tumor stage. When only CNA or methylation-associated gene sets were used, the groups were not clinically distinguishable (Figures S1B and S1F).

The clustering analysis based on the 219 miRNA-associated genes was then performed on three independent cohorts (Tothill, Bentink, and Bonome data sets; [Table 1](#)) with 246, 129, and 185 serous OvCa cases, respectively (Bentink et al., 2012; Bonome et al., 2008; Tothill et al., 2008). In all three data sets, the miRNA-associated genes characterized two distinct subtypes that were associated with overall survival (Figures 2C–2H; [Table S2](#)). This suggests the miRNA-associated genes robustly manifest a clinically relevant mesenchymal subtype in serous OvCa. We designated cluster 1 as the integrated mesenchymal subtype (iM) and cluster 2 as the integrated epithelial subtype (iE). An evaluation of hematoxylin and eosin (H&E)-stained tumor tissue sections from TCGA revealed that iE cases exhibited papillary

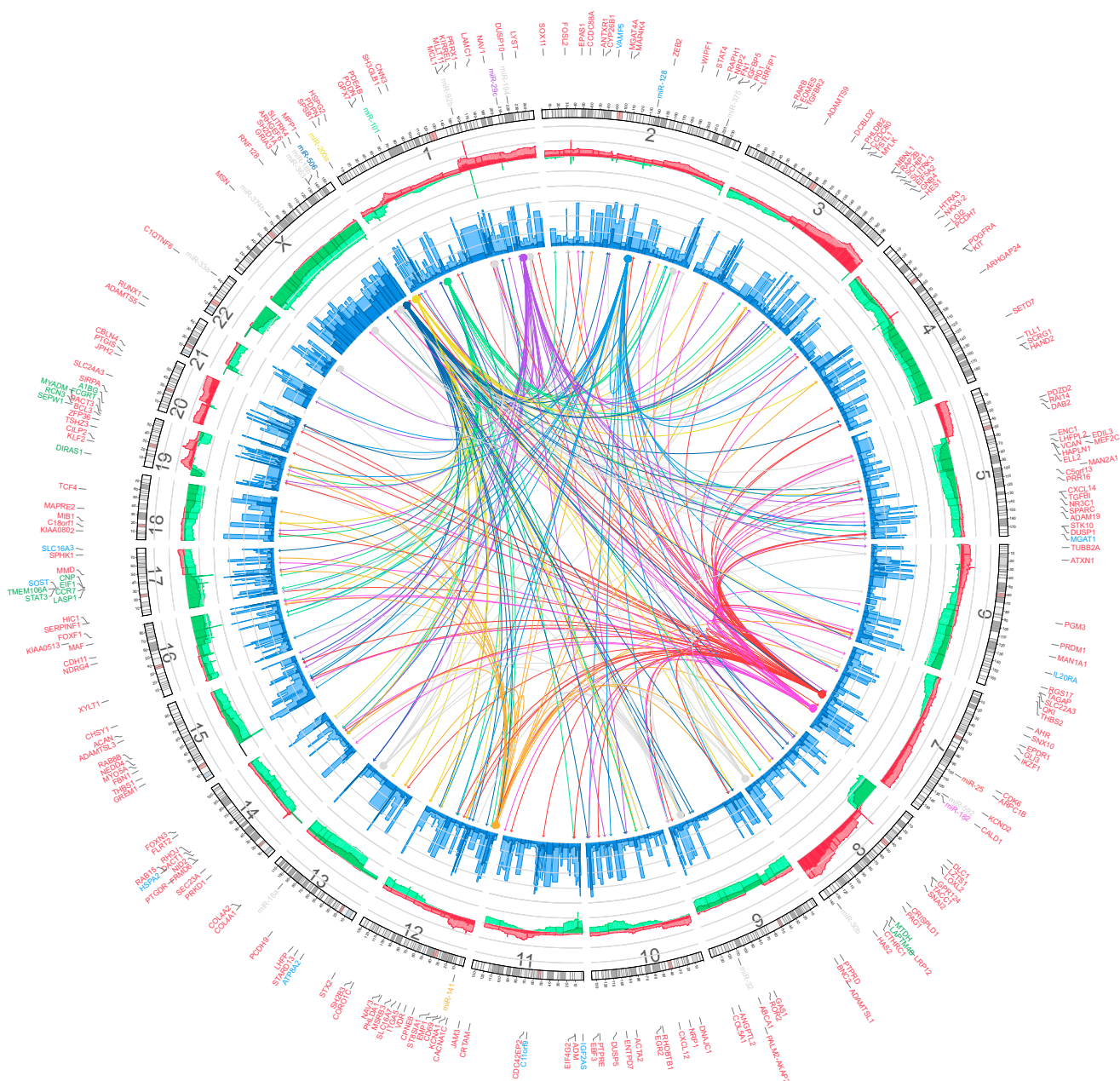


Figure 1. Integrated View of Mesenchymal Signature Genes Regulated by Copy Number, Methylation, and MiRNA

Integrated Circos plot shows mesenchymal signature genes regulated by copy number (CN), methylation, and miRNA. An ideogram of a normal karyotype is shown in the outer ring. The next outermost ring represents copy number as a function of genomic coordinates. (Red represents amplification and green represents deletion. Dark red and dark green indicate median CN values across all patients, and lighter red and green indicate the 25th and 75th percentiles. The vertical axis ranges from -1 to $+1$ on a \log_2 scale.) The next ring represents the amount of DNA methylation: dark blue indicates the median methylation beta value, and light blue indicates the 75th percentile. The vertical axis ranges from 0 to 1, and methylation data are averaged using variable-width bins along the genomic axis (25 CpG probes per bin). In the center of the figure, each arc indicates a predicted regulatory relationship between a miRNA (solid circle) and a gene (arrow). The colored arcs represent predicted regulation by the eight key miRNAs, whereas the gray arcs represent regulation by the remaining 11 miRNAs. Outside the ideogram, the miRNAs are colored the same as the corresponding arc. Outside the miRNA, labels are the miRNA-associated genes (red), CNA-associated genes (green), and methylation-associated genes (blue). Detailed information on each group of genes is listed in Table S1. See also Figure S1.

adenocarcinoma with frond-like projections on thin fibrovascular cores covered by typical cobblestone-like epithelial cells, resembling fallopian tube epithelium. In contrast, iM cases

lacked well-organized epithelial structures, and contained elongated tumor cells and weaker connections between tumor cells, resembling mesenchymal cells (Figure 2l).

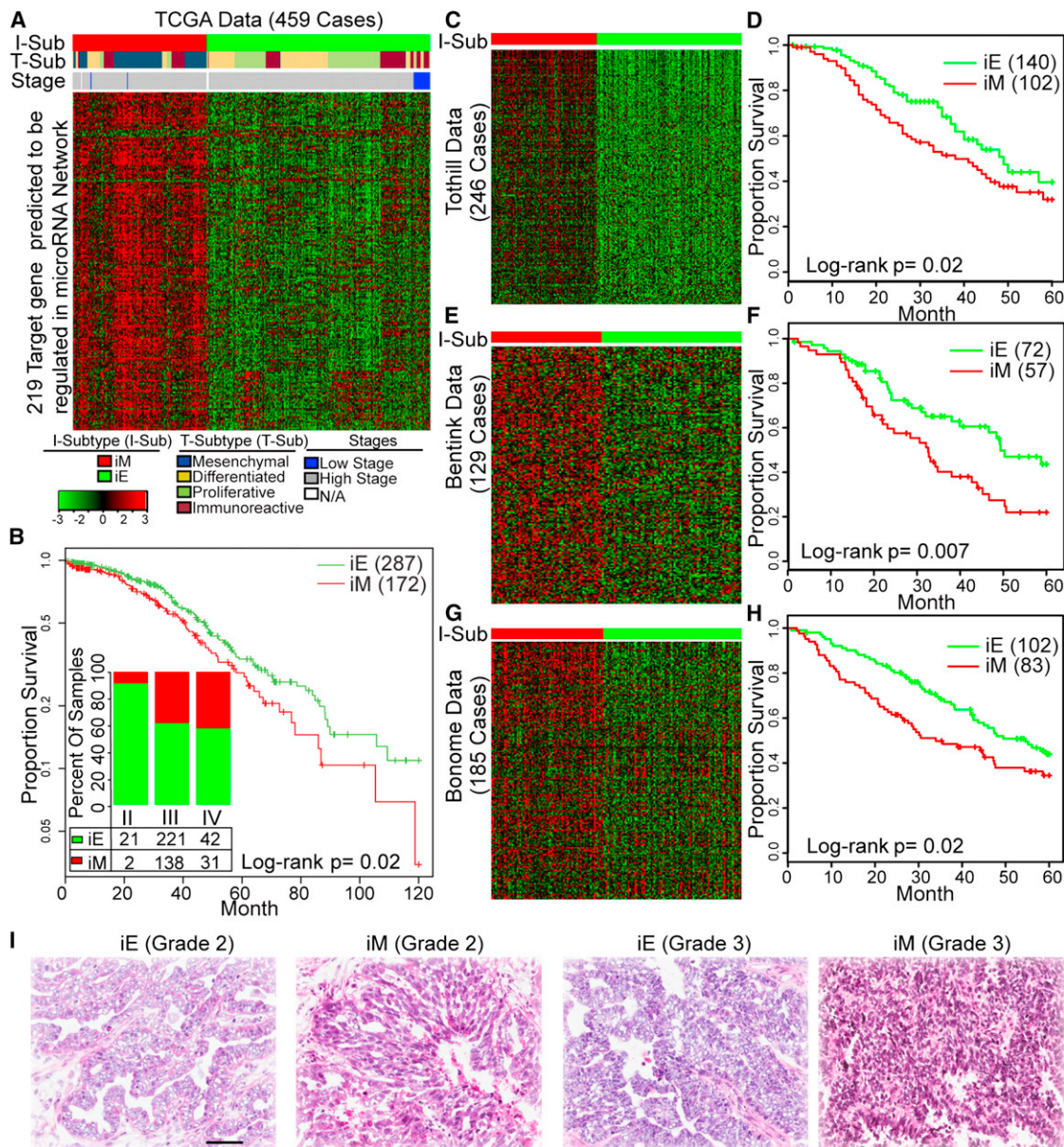


Figure 2. Consensus Clustering Based on 219 miRNA-Associated Genes Identified iM and iE Subtypes

(A, C, E, and G) Consensus K -means clustering ($K = 2$) identified two clusters based on the expression levels of 219 miRNA-associated mesenchymal genes in 459 TCGA cases (A), 246 Tothill cases (C), 129 Bentink cases (E), and 185 Bonome cases (G). The cases are stratified into iM and iE subtypes as shown by a color code at the top of the panel (integrated subtype [I-Sub]). Detailed subtype and clinical information is listed in Table S2. For (A), each sample is further labeled in the middle row of color bands for the TCGA transcriptional subtype (T-Sub).

(B, D, F, and H) Kaplan-Meier overall survival curves for the OvCa iM and iE subtypes in the TCGA (B), Tothill (D), Bentink (F), and Bonome cases (H) data sets. For (B), the y-axis is log scale and the inserted bar chart shows the distribution of tumor stages in the iM and iE subtypes in the TCGA data set. Cases are categorized by clinical stages. The number and percentage of tumors in the iM and iE clusters (red, iM; green, iE) are indicated for each stage. Numbers do not add up because of missing values.

(I) Representative H&E-stained images of iEs and iMs in grade 2 and 3 tumors from the TCGA data set. Scale bar represents 100 μ m.

See also Figure S2 and Table S2.

Compared with the four TCGA-identified transcriptional subtypes, the iM included nearly all (103 of 105; $p < 10^{-6}$, two-sided Fisher's exact test; Figure 2A) transcriptional mesenchymal subtype cases, as well as 69 cases from other TCGA-defined subtypes (12, 32, and 25 cases from the proliferative, immunoreactive, and differentiated subtypes, respectively;

Table S2). We evaluated the expression pattern of epithelial and mesenchymal markers (*CDH1* [*E-cadherin*], *FN1*, *VIM*, *SNAI1*, *SNAI2*, and *ZEB1*) in these 69 iM cases previously defined as other subtypes solely on the basis of mRNA

Table 1. Clinicopathologic Information of the OvCa Patient Cohorts

	TCGA	Tothill	Bonome	Bentink ^a	Tianjin	Bagnoli
Number	459	246	185	129	92	55
Age (SD)	60 (11)	60 (10)	62 (12)	61 (14)	55.5 (12)	56 (12)
Stage						
II	23	10	0	1	15	0
III	359	199	144	109	63	45
IV	73	21	41	19	7	10
Tumor Grade						
G2	57	88	40	NA	43	7
G3	392	145	144	NA	47	43
Surgical Outcome						
Optimal	289	131	90	98	50	24
Suboptimal	114	65	95	28	42	31
Vital Status						
Living	203	132	56	56	47	23
Deceased	251	110	129	73	45	32
Follow-Up						
Median (range)	31 (1–179)	28 (1–214)	38 (1–164)	31 (1–91)	25 (1–79)	36 (7–91)
Subtype						
iE	287	140	102	71	NA ^b	NA ^b
iM	172	102	83	58	NA ^b	NA ^b
Source	TCGA	GSE9891	GSE26712	MTAB386	TCH	GSE25204

Numbers do not add up because of missing information in some cases. NA, not applicable; TCH, Tianjin Cancer Hospital.

^aFor Bentink Data set, both mRNA and miRNA microarray data are available.

^bNo iM/iE subtype was assigned because only miRNA expression data are available.

expression data and found that they showed distinct expression patterns compared with the iE cases in the same transcriptional subtype (Figure S2A). For instance, in the immunoreactive subtype, 32 and 67 cases were assigned to the iM and iE subtypes, respectively. The expression of the mesenchymal markers *SNAI2* and *FN1* was significantly upregulated by more than 2-fold in the 32 iM cases compared with that in the 67 iE cases in the same immunoreactive subtype ($p < 10^{-6}$). Remarkably, we observed a significantly poorer overall survival ($p = 0.04$, log-rank test; Figure S2B) in the 32 iM cases than in the 67 iE cases. Similar trends were observed in the proliferative subtype (Figure S2C). We also assigned the iM/iE subtype classification for the transcriptional subtypes in the Tothill data set. The 13 iM cases and 32 iE cases in the Tothill “C2” subtype have enough sample size for us to compare the EMT marker expression and overall survival duration (Table S2). Similar to our comparison in TCGA data set, the iM cases showed significant overexpression in mesenchymal makers (Figure S2E) and shorter overall survival ($p = 0.05$, Figure S2F) than the iE cases in the same C2 subtype. The results suggested that iM/iE subtype could further classify transcriptional subtypes into clinically relevant groups in multiple data sets.

Key miRNAs' Regulatory Role in the iM OvCa Subtype

The finding that only 219 miRNA-associated genes characterized the poor prognostic mesenchymal subtype strongly suggested that the OvCa mesenchymal phenotype is likely governed by a miRNA regulatory network. Of the 19 miRNAs identi-

fied in our analysis, eight (miR-25, miR-506, miR-29c, miR-182, miR-128, miR-101, miR-141, and miR-200a) were predicted to regulate 89% (195 of 219) of the miRNA-associated genes (Figures 3A and 3B; Table S3). In addition to having binding sites in the 3'-UTRs of their predicted targets, these eight miRNA were also inversely correlated with the expression levels of their predicted targets ($FDR < 0.01$, based on linear regression model).

Our analysis showed that miR-141 and miR-200a regulated 22 and 24 genes (Table S3), respectively, including *ZEB2*. Both miR-141 and miR-200a belong to the miR-200 family, and miRNAs in this family have been demonstrated to prevent EMT by targeting *ZEB1* and *ZEB2* in multiple cancer types (Gregory et al., 2008; Park et al., 2008). Consistently, these two miRNAs were downregulated in the iM subtype ($p < 10^{-6}$, Wilcoxon rank-sum test; Figure 3C). Besides the miR-200 family, miR-128 was predicted to target 27 genes (Table S3), and was significantly downregulated in the iM subtype ($p < 10^{-3}$, Wilcoxon rank-sum test; Figure 3C; Table S4). Previous studies have also shown that miR-128 inhibits tumor cell migration and invasion in neuroblastoma (Evangelisti et al., 2009).

The three miRNAs predicted to regulate the largest number of targets are miR-25, miR-506, and miR-29c (regulating 49, 35, and 32 targets, respectively; Table S3). In nasopharyngeal carcinomas, miR-29c has been shown to inhibit metastasis by targeting *SPARC*, *LAMC1*, *COL4A1*, *COL4A2*, and other mesenchymal markers implicated in invasion and metastasis (Sengupta et al., 2008). These molecules were also predicted to be targets of miR-29c in our network (Figure 3A; Table S3). Among

the three miRNAs, miR-506 exhibited the most significant down-regulation in the iM subtype ($p < 2.2 \times 10^{-16}$, Wilcoxon rank-sum test; Figure S4A; Table S4). In addition, 35 mesenchymal signature genes, including the E-cadherin transcriptional repressor *SNAI2* (aka *SLUG*), were significantly inversely correlated with miR-506 expression in the 459 TCGA OvCa cases ($p = 1.24 \times 10^{-7}$ for *SNAI2*; Figures S4B and S4C).

miR-506 Promoted the Epithelial Phenotype In Vitro and Directly Targeted *SNAI2*

To determine whether forced expression of miR-506 can promote epithelial phenotype, we transfected SKOV3 cells with either miR-506 mimic (miR-506) or a scrambled negative microRNA control (miR-Ctrl). miR-506 overexpression significantly increased *CDH1* mRNA levels, while the mesenchymal markers *SNAI2* and *VIM* were downregulated by miR-506 (Figure 4A). Consistently, forced miR-506 expression also increased E-cadherin and markedly decreased *SNAI2* protein expression. Another mesenchymal marker, N-cadherin, was also downregulated by miR-506 (Figure 4B). These results suggest that cells with miR-506 overexpression gained an epithelial signature characterized by E-cadherin expression induction and mesenchymal marker suppression.

To further confirm these results, we performed immunofluorescence staining to directly visualize the effect of miR-506 on E-cadherin expression, localization, and cell morphology. As shown in Figure 4C, miR-506-transfected SKOV3 cells showed epithelial cell features, characterized by aggregated cells (Figure 4C, left panel); immunofluorescence staining revealed that E-cadherin protein was localized on the membrane at cell-cell junctions and formed a typical cobblestone structure, indicative of epithelial cells (Figure 4C). In addition, F-actin distribution was rearranged to a cortical pattern, which is another hallmark of the epithelial phenotype (Figure 4C). In contrast, the cells transfected with miR-Ctrl showed mesenchymal phenotype indicated by an absence of E-cadherin on the cell membrane and rearrangement of F-actin from a cortical to a stress-fiber pattern (Figure 4C). In addition, ectopic miR-506 expression decreased cell migration compared with miR-Ctrl transfected cells, as indicated by a wound-healing assay (Figure 4D). An invasion assay revealed similar results, in which miR-506 expression significantly decreased invaded cell numbers by more than 5-fold compared with in miR-Ctrl-transfected cells (Figure 4E).

E-cadherin is a critical protein that determines epithelial cell phenotype, and lack of E-cadherin is believed to be a driving event for EMT and cancer invasion and metastasis (Thiery et al., 2009). E-cadherin is regulated by a number of transcription factors, including the repressor *SNAI2* (Peinado et al., 2007). TargetScan predicted three miR-506 binding sites in the 3'-UTR of the *SNAI2* gene (Figure 4F). Our computational and functional study results provided evidence that miR-506 down-regulated *SNAI2* and upregulated E-cadherin. We performed luciferase reporter assay to examine whether miR-506 directly targeted *SNAI2*. We cloned the 3'-UTR of *SNAI2* into the pGL3-ctrl vector and generated pGL3-*SNAI2* constructs. Cotransfection of pGL3-*SNAI2* and miR-506 resulted in a 72.2% reduction in luciferase activity compared with that after cotransfection with miR-Ctrl, suggesting that miR-506 directly targets *SNAI2* (Figure 4F). To further confirm that miR-506

specifically regulates *SNAI2* through the predicted binding sites, we generated the control construct-pGL3-*SNAI2*-Mu, in which the miR-506 binding site sequences on the 3'-UTR of *SNAI2* were deleted. We then cotransfected this construct with miR-506 mimic or miR-Ctrl into cells. We observed that deletion of the miR-506 binding sites from the 3'-UTR of *SNAI2* abolished the effect of miR-506 on luciferase activity (Figure 4F). To determine whether miR-506's inhibition of EMT was mediated by *SNAI2*, we established SKOV3 cells overexpressing *SNAI2* from expression vector without the 3'-UTR (Figures S4D and S4E). As shown in Figure S4F, SKOV3 cells overexpressing *SNAI2* had decreased expression of E-cadherin protein and exhibited elongated mesenchymal cell morphology. In contrast, knockdown of *SNAI2* by three different siRNAs led to increased E-cadherin protein levels and typical cobblestone epithelial cell morphology (Figures S4G). Notably, overexpression of *SNAI2* abolished miR-506's induction of E-cadherin (Figure 4G). These results confirmed that miR-506 specifically targeted the 3'-UTR of *SNAI2* and thus inhibited *SNAI2* gene expression, leading to E-cadherin upregulation.

miR-506 Blocked Transforming Growth Factor β -Induced EMT In Vitro

Previous studies have established that transforming growth factor- β (TGF β) is a robust inducer of EMT in multiple cell types (Zhu et al., 2010). Consistent with these findings, our pathway analysis revealed that the TGF β pathway was significantly up-regulated in iM subtypes ($p < 10^{-6}$; Figure S5; Table S5). Consequently, we sought to determine whether miR-506 affected TGF β -induced EMT in OvCa cells. We treated OVCA420 and OVCA433 cells with TGF β after transfecting miR-506 or miR-Ctrl. In miR-Ctrl-transfected OVCA420 cells, TGF β treatment induced *SNAI2* by 6-fold and suppressed *CDH1* expression by 2-fold at the mRNA level ($p < 0.05$, Figure 5A). In contrast, miR-506 overexpression abolished TGF β -induced alterations of EMT markers (Figure 5A).

We next performed immunofluorescence staining to evaluate the morphologic changes in these cells. After TGF β treatment, OVCA420 cells transfected with miR-Ctrl underwent a morphologic change characterized by elongated cells, a marked spreading growth pattern together with an absence of E-cadherin on the cell membrane and strong F-actin stress fibers, suggesting augmented mesenchymal features compared with untreated cells (Figure 5B). In contrast, miR-506 transfection blocked the TGF β -induced mesenchymal phenotype, promoting an epithelial phenotype characterized by E-cadherin localization at cell-cell junctions and cortical F-actin staining (Figure 5B). Consistently, miR-506 treatment blocked TGF β -induced invasion (Figure 5C). Similar results were also observed in OVCA433 cells (Figures 5D–5F).

miR-506 Expression Was Associated with Increased E-Cadherin, Decreased *SNAI2* and *VIM*, and Longer Overall Survival Duration in Serous OvCa

While the TCGA database allowed us to evaluate the association between miR-506 and *CDH1* and *SNAI2* mRNA levels, protein level data were not available in this data set. To further investigate this proposed regulation in OvCa samples, we acquired a cohort of 92 clinically annotated serous OvCa tumor samples

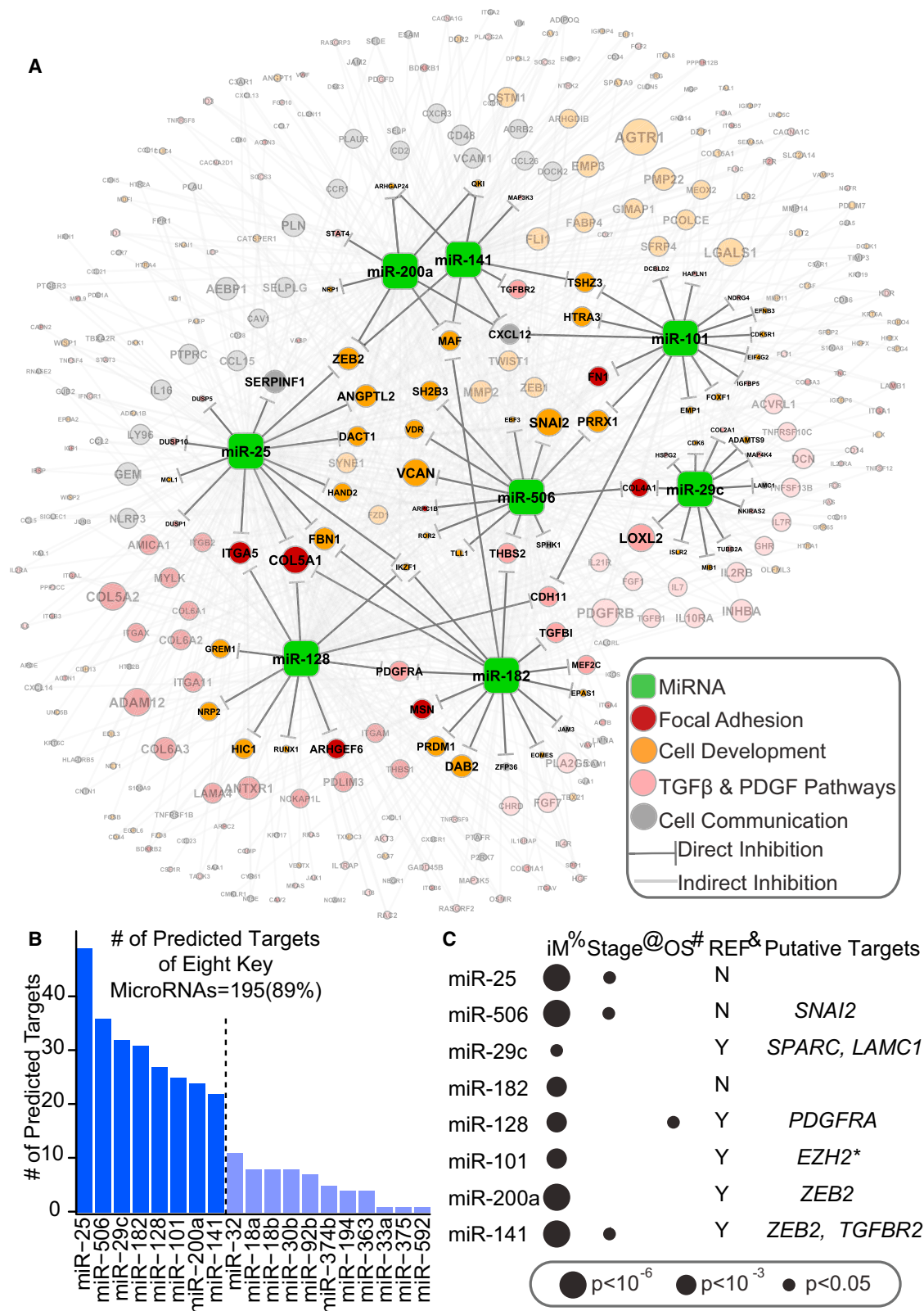


Figure 3. Core miRNA-Gene Network, Including Eight Key miRNAs and Their Targets

(A) The miRNA-gene network shows the relationships between eight key miRNAs and EMT signature genes they are predicted to regulate. The size of each gene node indicates the number of predicted targets; the colors indicate the annotated function of the gene. Only genes with GO and KEGG annotations are shown in this network.

(legend continued on next page)

from Tianjin Cancer Hospital (TCH). In this cohort, the median follow-up duration was 25 months (range, 1–79 months). Fifty-one percent of patients were alive at the last follow-up. The median overall survival duration of the cohort was similar to those in the TCGA and Tothill data sets. Detailed clinical information was described in Table S6. miR-506 was measured using real-time RT-PCR analysis in frozen tissues and miRNA in situ hybridization on tissue microarrays (TMAs) of formaldehyde-fixed, paraffin-embedded tissues from the same patients. Both methods revealed consistent results for miR-506 expression (Figures 6A and 6B). At the same time, we performed H&E and immunohistochemical staining for SNAI2, E-cadherin, and VIM on the TMAs. Consistent with our observations from TCGA samples, tumors with low miR-506 expression exhibited a more mesenchymal phenotype, with elongated tumor cells and weaker connections between tumor cells, whereas those with high miR-506 expression exhibited more epithelial characters, such as displaying a papillary structure with frond-like projections on thin fibrovascular cores covered by typical cobblestone-like epithelial cells (Figure 6A). Moreover, miR-506 expression was inversely correlated with SNAI2 and VIM protein expression ($p = 0.008$ and 0.03 , respectively) and positively correlated with E-cadherin protein expression ($p = 0.004$) (Figures 6A and 6B). Remarkably, high miR-506 expression was significantly correlated with longer overall survival in the univariate model (log-rank $p = 0.045$, Figure 6C) and multivariate model (hazard ratio = 0.72 , $p = 0.05$). In TCGA data, the patients with high miR-506 and low SNAI2 expression have significantly longer overall survival and progression free survival (Figures S4H and S4I) compared to those with low miR-506 and high SNAI2 expression. To further confirm miR-506's association with good prognosis in ovarian cancer, we obtained two miRNAs microarray data sets from GEO and ArrayExpress (Bentink Data set and Bagnoli Data set, Table 1) with 129 and 55 OvCa cases, respectively. In both data sets, miR-506 expression is significantly associated with longer progression-free survival (log-rank $p = 0.02$ and 0.0006 for Bentink and Bagnoli Data sets, respectively, Figures 6D and 6E).

Next, we sought to explore the mechanisms for the attenuated expression of miR-506 in patients with poor clinical outcome. Integrated analysis of copy number and miRNA expression data in TCGA showed miR-506 expression was not associated with copy number alterations. Interestingly, we performed a demethylation experiment by treating ovarian cancer cells with 5-azaC and found an induction of miR-506 (Figure S6A). To more directly evaluate the methylation status of the miR-506 promoter in serous OvCa patient tumors, we identified five CpG sites in the promoter region of miR-506 (Figure S6B). Although the TCGA methylation microarray does not contain the five sites that would allow us to directly evaluate the methylation status of the miR-506 promoter in the TCGA data, we performed quantitative pyrosequencing following sodium bisulfite treatment of

DNAs isolated from the ovarian cancer tissues in the Tianjin cohort. Our results showed that among the five methylation sites we interrogated, two displayed trends of negative correlation between methylation and miR-506 expression ($p = 0.06$ and 0.15 for sites 5 and 1, respectively, Figure S6C).

Systematic Delivery of miR506 Inhibited SNAI2 and VIM and Induced E-Cadherin expression in vivo

To further verify miR-506's role and to determine the therapeutic efficacy of miR-506, we established OvCa orthotopic mouse models using two serous OvCa cell lines (SKOV3-IP1 and HeyA8-IP1, see Experimental Procedures for details). These two sublines were generated from ascites developed in nu/nu mouse by administering an intraperitoneal injection of SKOV3 and HeyA8, as described previously (Xu et al., 1999). For both models, delivery of miR-506 incorporated in DOPC nanoliposomes (miR-506-DOPC) resulted in a significant reduction in the number of tumor nodules (75% reduction in HeyA8-IP1; $p = 0.009$ and 48% reduction in SKOV3-IP1; $p = 0.01$; Figures 7A and 7B) and tumor weight (78% reduction in HeyA8-IP1, $p = 0.004$; and 53% reduction in SKOV3-IP1, $p = 0.01$; Figure 7C) compared with miR-Ctrl. We further performed immunohistochemical staining of SNAI2, E-cadherin, and VIM in the tumors to determine whether systemic delivery of miR-506 affected the expression of these EMT markers. For each model, representative sections with the staining of SNAI2, E-cadherin, and VIM were shown (Figure 7D). Compared with miR-Ctrl, miR-506 treatment significantly suppressed SNAI2 (58% reduction in HeyA8-IP1 and 68% reduction in SKOV3-IP1 models; $p < 0.05$, Figure 7E) and VIM (30% reduction in both models; $p < 0.05$, Figure 7E), and significantly induced E-cadherin (200% induction in HeyA8-IP1 and 120% induction in SKOV3-IP1; $p < 0.05$, Figure 7E). These results showed that nanoparticle delivery of miR-506 may serve as a potential therapeutic intervention for OvCa.

DISCUSSION

Using integrated approaches, we uncovered a key miRNA-regulatory network that reproducibly defines the iM subtype robustly associated with poor overall survival of women with serous OvCa. Extensive functional studies characterized miR-506 as a potent EMT inhibitor and a potential therapeutic tool, which may have an impact on improving treatment for one of the most aggressive cancer types among women.

Genomic and molecular profiling has revealed that even within the same anatomical location and histological classification, cancer is heterogeneous (Ein-Dor et al., 2005). Efforts from systematic studies such as TCGA have allowed comprehensive molecular classification of cancer by integrated analyses of multidimensional data from a large cohort of clinical samples at both genomic and epigenetic levels (Noushmehr et al., 2010;

(B) A histogram reveals the number of predicted targets for each of the 19 miRNAs.

(C) The association between key miRNA expression and clinical information, as well as miRNAs' putative functional targets in terms of EMT inhibition. %, The significance of differential expression between iM and iE subtypes, as estimated by the Wilcoxon signed-rank test. Detailed information is listed in Table S4; @, the significance of miRNA expression's association with clinical stage, as estimated using Spearman's rank correlation coefficient; #, the significance of miRNA expression's association with overall survival (OS), as estimated using the Cox proportional hazards model; *, reported by (Carvalho et al., 2012).

See also Figure S3 and Table S3.

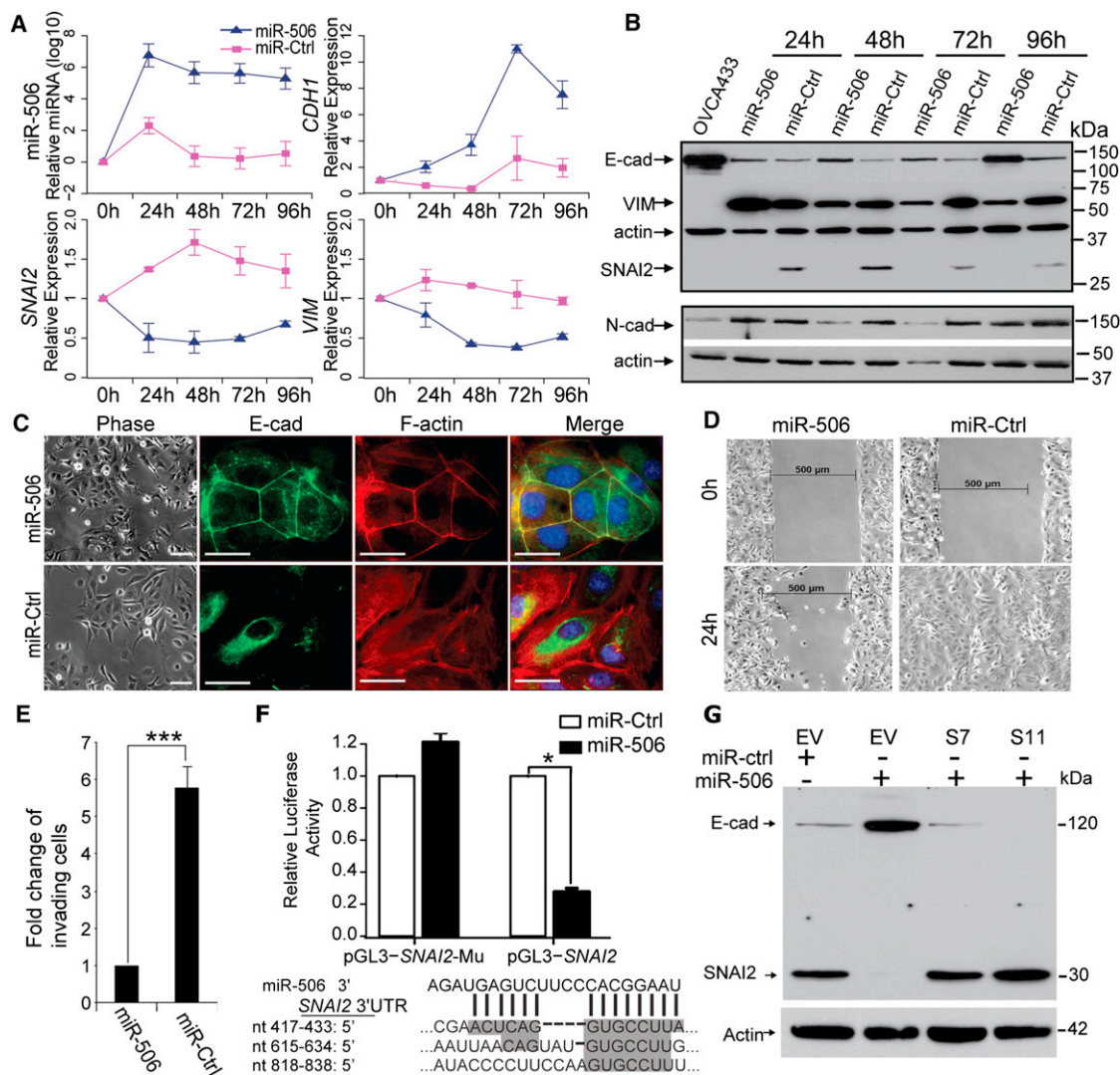


Figure 4. Overexpression of miR-506 in OvCa Cells Is Sufficient to Induce Epithelial Phenotype

(A) Changes in microRNA and mRNA levels in SKOV3 cells transfected with miR-506 or control miRNA (miR-Ctrl) as measured by real-time RT-PCR (TaqMan). Two independent time course experiments were performed; the average \pm standard error (indicated by the error bars) of the two experiments were shown.

(B) Western blotting analysis of epithelial and mesenchymal markers in SKOV3 cells transfected with miR-506 or control miRNA (miR-Ctrl) from the same transfection as in (A). OVCA433 cell lysate was used as the positive control for the epithelial marker E-cadherin. One mesenchymal marker, N-cadherin (N-cad), was measured on a different blot. Both blots were re-probed with actin to control for protein loading.

(C) Inverse phase microscopy (left panel) and E-cadherin and F-actin staining (right panels) of SKOV3 cells transfected with miR-506 or control miRNA (miR-Ctrl) for 72 hr. Cell nuclei were stained with DAPI. Scale bars represent 50 μ m.

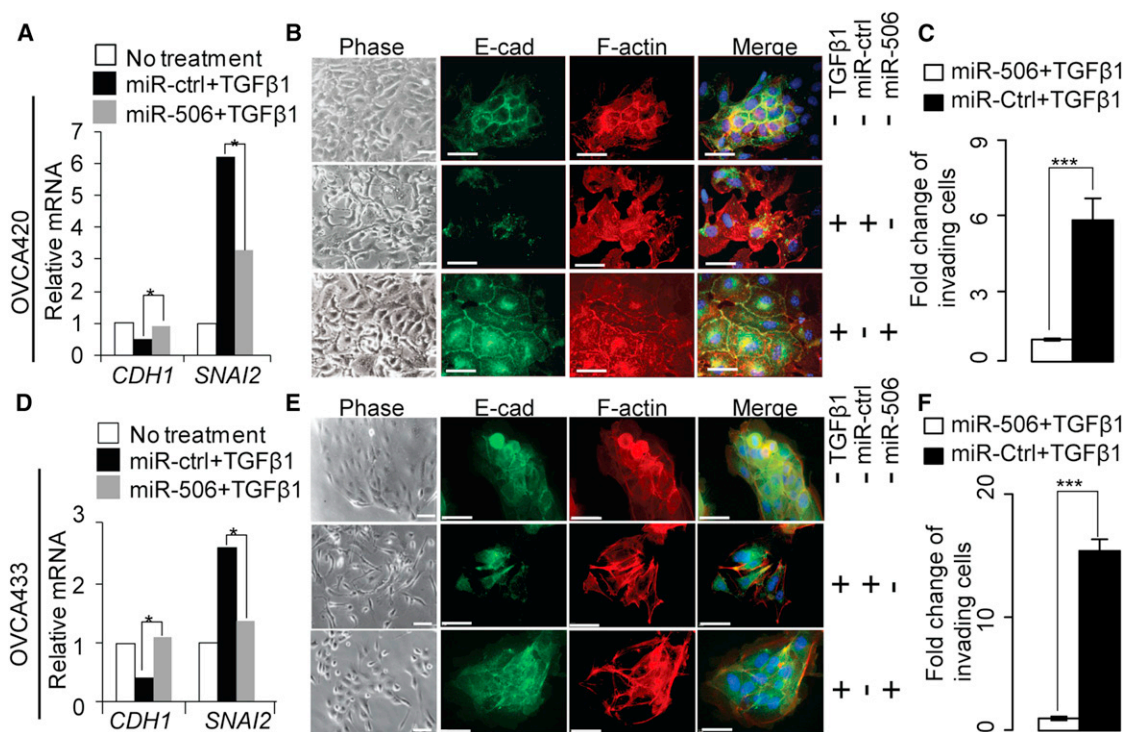
(D) Wound healing assay. Cells from the same transfection as in (C) were seeded into the μ -dish 35mm, high culture-insert and a wound was applied at 48 hr post-transfection.

(E) In vitro invasion assay. Cells from the same transfection as in (C) were seeded into triplicate mitrigel coated invasion chambers at 48 hr post-transfection and allowed to invade toward serum for 22 hr. The invading cell numbers on each filter were counted and data were plotted in fold change by defining the number from miR-506-transfected cells as 1. Error bars represent \pm SD.

(F) The relative luciferase activities were shown from three independent experiments (upper panel). The pGL3-SNAI2 reporter gene has the full length of SNAI2 3'-UTR cloned into pGL3- control vector. The pGL3-SNAI2-Mu vector has the three miR506 binding sites deleted and confirmed by sequencing. SKOV3 cells were transfected with pGL3-SNAI2 or pGL3-SNAI2-Mu, respectively, together with miR-506 mimics or mimic negative control. The three predicted binding sites of miR-506 were shown in the SNAI2 3'-UTR region (lower panel). Error bars represent \pm SD.

(G) Overexpression of SNAI2 from expression vector without 3'-UTR abrogates miR-506's induction of E-cadherin. Two SKOV3-SNAI2 stable clones (S7 and S11) and empty vector stable cells (EV) were transfected with miR-506. Whole cell lysate from each sample was collected at 72 hr post-transfection and subjected for western blot. For comparison, the levels of E-cadherin and SNAI2 in the EV cells transfected with mimic negative control (miR-ctrl) for 72 hr were shown.

See also Figure S4.



Yang et al., 2011). The current study shows that our integrated approach is a major step forward compared to the commonly used transcriptome-based approaches, which have resulted in inconsistent clinical associations from different data sets (Cancer Genome Atlas Research Network, 2011; Tothill et al., 2008). Specifically, integrated analysis of miRNAs and transcriptome further grouped the transcriptional subtypes into more clinically relevant iM and iE subtypes. The strength of this integrated approach is that it also reveals regulatory mechanisms associated with the subtypes. In particular, our integrated analysis of OvCa highlights the important role of a miRNA regulatory network consisting of eight key miRNAs for the mesenchymal subtype. MiR-141 and miR-200, among the eight key miRNAs, have been reported to be EMT regulators (Gregory et al., 2008; Park et al., 2008). Other key miRNAs, such as miR-29c, miR-101, and miR-128 have also been shown to regulate EMT-related processes (e.g., cell adhesion, cytoskeleton organization, and extracellular matrix molecular function) (Evangelisti et al., 2009; Varambally et al., 2008). We subsequently narrowed our focus on the function of miR-506 because it was the least studied among the miRNA network.

MiR-506 is located in Xq27.3, a chromosomal region associated with the “fragile X syndrome.” Female patients with fragile X syndrome suffer from primary ovarian insufficiency (Santoro et al., 2012). The region has also been identified as a high susceptibility locus in linkage studies of familial testicular germ cell tumors (Rapley et al., 2000). Downregulation of miR-506 has been observed in kidney cancer (Zhou et al., 2010) and chemical carcinogen-transformed lung cancer (Zhao et al., 2011), suggesting that miR-506 potentially plays a role in tumor suppression.

SNAI2 (also known as Slug) is one of the three zinc finger transcription factors of the Snail family, which in recent years has been shown to be a major regulator of EMT (Peinado et al., 2007). In experimental models of ovarian carcinoma, SNAI2 was shown to induce EMT by repressing E-cadherin, and to promote tumor growth and invasion (Kurrey et al., 2005). In addition, it was reported that treatment of cultured ovarian surface epithelium (OSE) by TGFβ induces an EMT-like process, characterized by the inability to form an epithelial barrier, with an increase in SNAI2 level and decrease of E-cadherin. However, TGFβ treatment did not increase expression in TWIST1 and

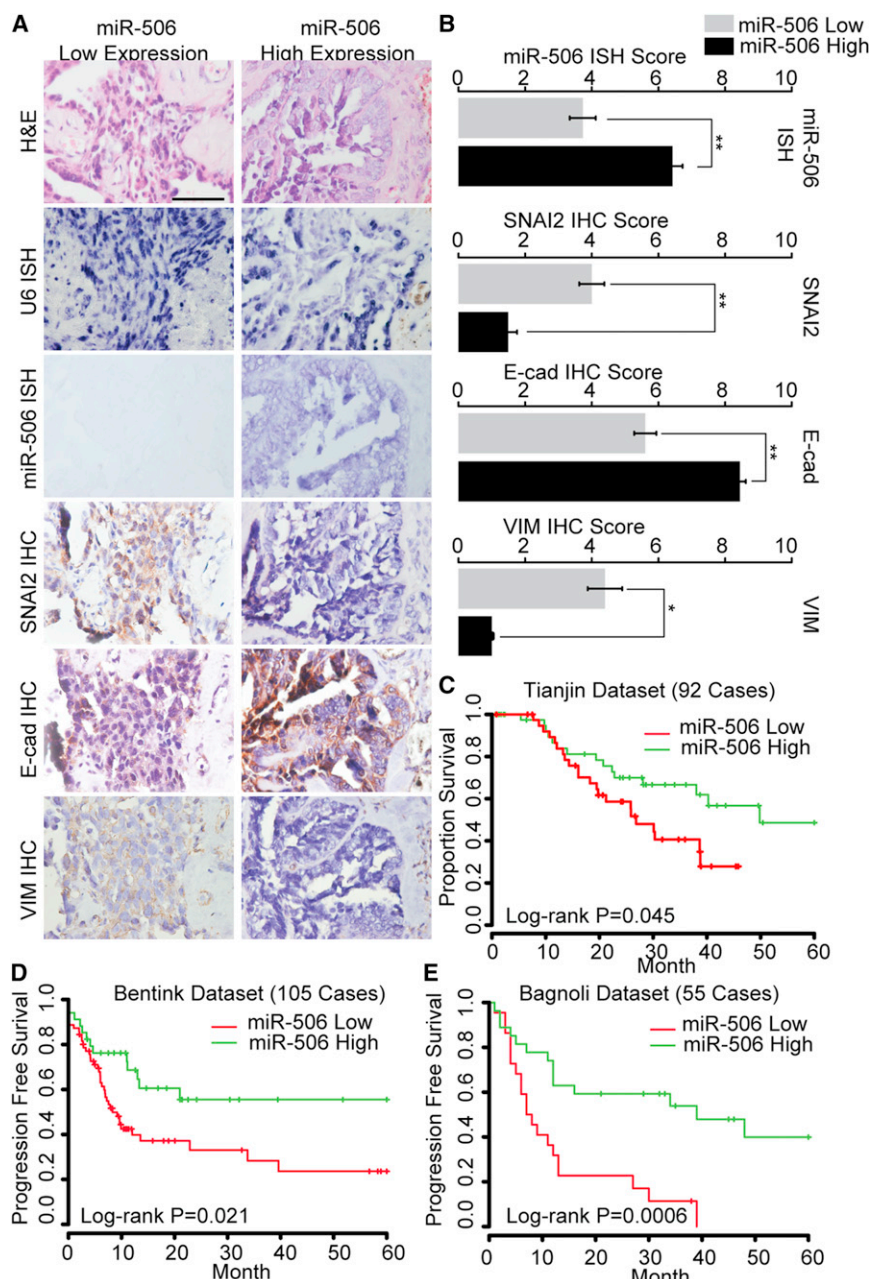


Figure 6. Correlation between miR-506 and SNAI2, E-cadherin, and VIM Expression and Prognosis in Multiple Serous OvCa Cohorts

(A) Representative images of in situ hybridization staining for U6 snRNA (positive control) and miR-506 and immunohistochemical staining for SNAI2, E-cadherin (E-cad), and vimentin (VIM) in low and high miR-506 expression cases. The low and high miR-506 expression was stratified by using average of miR-506 PCR expression as threshold. Scale bar represents 100 μ m.

(B) Bar charts show the association between miR-506 expression and SNAI2, E-cadherin, and VIM expression. The low and high miR-506 expression is based on average value of miR-506 PCR expression. The x-axes represent miR-506 expression, as measured by in situ hybridization, and SNAI2, E-cadherin (E-cad), and vimentin (VIM) expression, as indicated by immunohistochemical staining. Error bars represent \pm SD. * $p < 0.05$ ** $p < 0.01$.

(C) Kaplan-Meier overall survival curves in miR-506 low and high expression OvCa cases. The low and high miR-506 expression is based on average value of miR-506 PCR expression.

(D and E) Kaplan-Meier progression-free survival curves in miR-506 low and high expression (according to average of miR-506 expression) in 129 Bentinck cases (D) and 55 Bagnoli cases (E). See also Figure S6.

studies showed that other EMT inhibitory miRNAs including miR-200 are also subject to negative regulation by methylation. In lung cancer, epigenetically silenced miR-200-mediated EMT is likely an early event in carcinogen-induced transformation of human lung epithelial cells (Tellez et al., 2011). Further studies using larger sample sizes are needed to reveal the relationship between miR-506 methylation and miR-506 expression.

Besides indicating the function and mechanism of miR-506 in EMT, our study explored the potential therapeutic value of miR-506 for OvCa. Introduction of miRNAs in vitro is well known to be highly

ZEB1 (Zhu et al., 2010), suggesting that SNAI2 plays an essential role in ovarian EMT. In this study, we demonstrate that miR-506 is a potent inhibitor of the mesenchymal phenotype and TGF β -induced EMT by directly targeting SNAI2. We established the importance of the miR-506-SNAI2 axis by rescue experiment and the reverse correlation between miR-506 and SNAI2 expression in tumor samples from multiple patient cohorts.

Our observation suggests miR-506 is partially regulated by methylation. This is consistent with a recent large-scale screening of epigenetic regulated miRNAs in OvCa, which showed the Xq27.3 miRNA cluster (including miR-506) was regulated by epigenetic mechanisms (Zhang et al., 2008). Interestingly, recent

efficient. However, delivery of miRNAs in vivo is much more challenging (Garzon et al., 2010). Although the initial proof-of-principle studies using miRNAs as therapeutics took advantage of adenoviral-based (Esquela-Kerscher et al., 2008) and lentiviral-based (Trang et al., 2010) delivery vehicles, translation into clinical practice requires the development of safer delivery methods (Pecot et al., 2011; Rupaimoole et al., 2011). Packaging mature miRNAs into lipid-based nanoparticles (neutral or charged) that can be systemically or specifically delivered to the tumor microenvironment has been shown to successfully transfer miRNAs and therapeutically regulate their targets in the lung (Wiggins et al., 2010), pancreas (Pramanik et al., 2011), and prostate (Liu et al., 2011). In this study, we

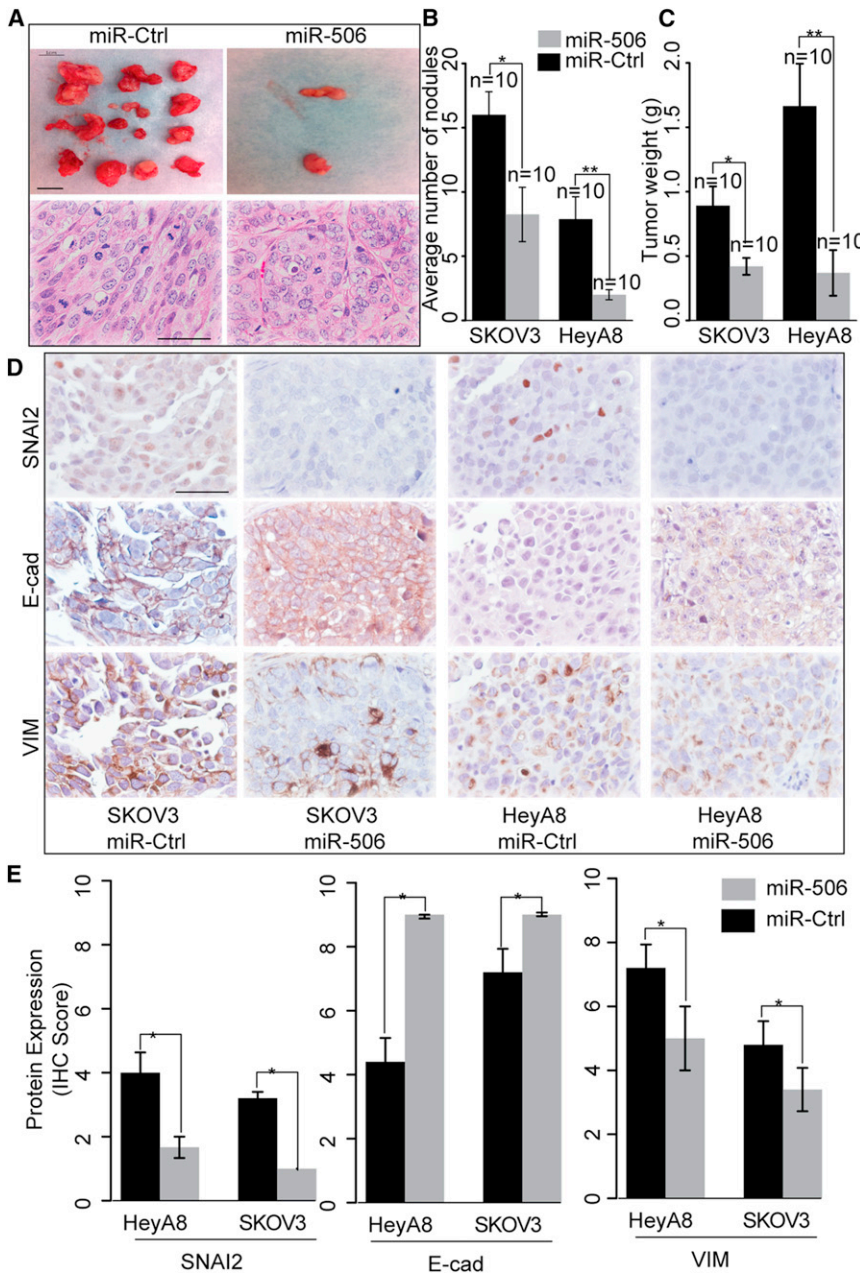


Figure 7. miR-506 Inhibits Tumor Progression in the Orthotopic Mouse Model of OvCa

(A) Representative images of tumor nodules and H&E staining of tumors in control miRNA- and miR-506-treated mice (HeyA8-ip1). Scale bar in the upper panel represent 1 cm. Scale bar in the lower panel represents 100 μ m. (B and C) Quantification of tumor weights (B) and tumor nodules (C) in control and miR-506 treated mice (n = 10 for each group) that were injected intraperitoneally with HeyA8-ip1 (HeyA8) and SKOV3-ip1 (SKOV3) ovarian cancer cells, respectively. Error bars represent \pm SD. (D) HeyA8-ip1 and SKOV3-ip1 tumor samples from control and miR-506 treated mice were stained for SNAI2, VIM and E-cad by immunohistochemistry. Scale bar represents 100 μ m. (E) Quantification of SNAI2, VIM and E-cad protein expression. Error bars represent standard errors. *p < 0.05. Error bars represent \pm SD.

one of the key miRNAs in the network, may represent an important strategy for the treatment of the most aggressive ovarian cancers.

EXPERIMENTAL PROCEDURES

Patients and Data Collection

Agilent Human Genome comparative genomic hybridization microarray 1x1M copy number data, Agilent 244K gene expression data, Agilent human miRNA microarray 8 \times 15K miRNA expression data, Illumina Infinium methylation data, and clinical information were obtained from the open-access and controlled-access tiers of the TCGA data portal, with NIH approval. Alignment of sample identifiers yielded 459 tumor cases, with all information available at the time of data retrieval from the TCGA. The Tothill, Bentink, Bonome, and Bagnoli data sets were downloaded from the Gene Expression Omnibus and ArrayExpression databases (Table 1). Frozen and paraffin-embedded tissues from 92 OvCa cases were collected from Tianjin Medical University Cancer Institute and Hospital, with approval of the institutional review board. Informed consent has been obtained from patients. All patients had been treated with a combination of surgery and platinum-based chemotherapy. The detailed clinical characteristics for each patient in the Tianjin cohort are listed in Table S6.

Identification of Integrated Mesenchymal Gene Signatures

A linear regression model was used to analyze the expression level of each mesenchymal signature gene. The associated gene copy number, promoter methylation probes, and miRNA expression level (see Supplemental Experimental Procedures) were chosen as regulatory factors for each gene and designated as independent variables in the regression model. For each regulatory factor in the model, a regression coefficient was estimated, reflecting its influence on gene expression. Sample labels were randomly permuted 1,000 times to generate a background distribution of regression coefficients, and a threshold was used (FDR = 0.01) to define the significant regulatory factors for each gene. A refined subset of mesenchymal signature genes was then selected according to two criteria: (1) each gene was significantly regulated by one or more factors on the basis of the regression model, and (2) the

illustrated that nanoparticle-delivery of miR-506 effectively suppressed tumor growth in two orthotopic ovarian cancer models. EMT of the resulting treated tumors was blocked based on the examination of EMT markers. Although we have not examined whether the delivery of miR-506 will sensitize ovarian cancers to chemotherapy in our preclinical model, a recent study demonstrated that an OvCa cell line that stably expresses miR-141 or miR-200a shows better response to chemotherapy in a subcutaneous xenograft OvCa mouse model (Mateescu et al., 2011). Future studies are needed to validate the clinical value of miR-506 in OvCa treatment.

In summary, our integrated analyses have identified a master microRNA regulatory network for the mesenchymal subtype in serous ovarian cancer. Nanoparticle delivery of the miR-506,

significant regulatory factor itself was also significantly altered ($FDR < 1\%$) between the mesenchymal subgroup and other subgroups. We termed this integrative analysis algorithm as MIRACLE (Master miRNA Analysis for Cancer moLecular subtypeE). The miRNA target information was from TargetScan (Lewis et al., 2003).

Statistical and Clustering Analysis

Student's *t* test, analysis of variance, chi-square, Wilcoxon rank-sum test, Fisher's exact test, Kaplan-Meier estimate, and Mantel-Cox survival analyses were performed using R 2.10.0. Significance was defined as $p < 0.05$. Benjamini-Hochberg multiple testing correction (Benjamini and Hochberg, 1995) was used to estimate the FDR when multiple testing correction was applied. Consensus clustering was performed as in previous studies (Noush-mehr et al., 2010; Verhaak et al., 2010). Increasing values of *K* (2 through 6, inclusive) were used to identify optimal segregation. For each *K*, 1,000 random iterations were performed to characterize the clusters.

Animals, Orthotopic In Vivo Model, and Tissue Processing

Forty female athymic nude mice were purchased from the National Cancer Institute, Frederick Cancer Research and Development Center (Frederick, MD) and were cared for according to guidelines set forth by the American Association for Accreditation of Laboratory Animal Care and the U.S. Public Health Service policy on Human Care and Use of Laboratory Animals. All mouse studies were approved and supervised by the MD Anderson Cancer Center Institutional Animal Care and Use Committee. All animals were 8–12 weeks of age at the time of injection. HeyA8-ip1 and SKOV3-ip1 cells were trypsinized, washed, and resuspended in Hanks' balanced salt solution (GIBCO, Carlsbad, CA) and injected into the peritoneal cavities of mice (HeyA8IP1 or SKOV3IP1: 1.0×10^6 cells/animal). Seven days after tumor cell injection, mice were randomly separated into two groups ($n = 10$ mice per group) and treated with miRNA incorporated in DOPC nanoliposomes (intraperitoneal administration)—control miRNA/DOPC or miR-506/DOPC for each cell line (see Supplemental Experimental Procedures for detailed method of liposomal preparation). Twice-weekly treatments continued for 4–6 weeks. All mice in the experiment were then killed and necropsied, and their tumors were harvested. Tumor weights, numbers, and locations were recorded. Mean mouse body weights were similar among groups, suggesting that feeding and drinking habits were not affected. Tumor tissue was snap frozen or fixed in formalin. H&E and immunohistochemical staining were performed on formalin-fixed, paraffin-embedded slides (see Supplemental Experimental Procedures).

SUPPLEMENTAL INFORMATION

Supplemental Information includes six figures, six tables, and Supplemental Experimental Procedures and can be found with this article online at <http://dx.doi.org/10.1016/j.ccr.2012.12.020>.

ACKNOWLEDGMENTS

We thank Drs. Xinna Zhang and George Calin for their assistance with miRNA in situ hybridization, Yingmei Wang and Jared Burks (Flow Cytometry & Cellular Imaging Core Facility) for technical assistance, Yuexin Liu for discussion, and Ms. Ann Sutton in the Department of Scientific Publications and Brittany Parker for editing this manuscript. This study was supported by a grant from the National Institutes of Health (U24CA143835) to I.S. and W.Z.; a grant from the Blanton-Davis Ovarian Cancer Research Program to W.Z.; an Ovarian Cancer SPORE grant (P50 CA083639), Ovarian Cancer Research Fund Program Project Development Grant, the Gilder Foundation and U54 CA151668 grant to A.K.S.; the Program for Changjiang Scholars and Innovative Research Team in University (IRT1076) in China and National Key Scientific and Technological Project (2011ZX09307-001-04) and Tianjin Science and Technology Committee Foundation grants (09ZCZDSF04700) to K.C.; and the Finnish Funding Agency for Technology and Innovation Finland Distinguished Professor Program to M.N.. The genomic studies were supported in part by the Cancer Genomics Core Laboratory and the National Institutes of Health through The University of Texas MD Anderson's Cancer Center Support Grant (CA016672). D.Y. is an Odyssey Fellow at MD Anderson Cancer

Center, and supported by The Diane Denson Tobola Fellowship in Ovarian Cancer Research fellowship and The Harold C. and Mary L. Daily Endowment Fund. Y.S. is supported by the National Natural Science Foundation of China (81201651), the Linda K. Manning Fellowship in Ovarian Cancer, and The A. Lavoy Moore Endowment Fund.

Received: January 23, 2011

Revised: November 8, 2011

Accepted: December 28, 2012

Published: February 11, 2013

REFERENCES

- Bagga, S., Bracht, J., Hunter, S., Massirer, K., Holtz, J., Eachus, R., and Pasquinelli, A.E. (2005). Regulation by let-7 and lin-4 miRNAs results in target mRNA degradation. *Cell* 122, 553–563.
- Bast, R.C., Jr., Hennessy, B., and Mills, G.B. (2009). The biology of ovarian cancer: new opportunities for translation. *Nat. Rev. Cancer* 9, 415–428.
- Benjamini, Y., and Hochberg, Y. (1995). Controlling the false discovery rate: a practical and powerful approach to multiple testing. *J. Roy. Statist. Soc. Ser. B* 57, 289–300.
- Bentink, S., Haibe-Kains, B., Risch, T., Fan, J.B., Hirsch, M.S., Holton, K., Rubio, R., April, C., Chen, J., Wickham-Garcia, E., et al. (2012). Angiogenic mRNA and microRNA gene expression signature predicts a novel subtype of serous ovarian cancer. *PLoS ONE* 7, e30269.
- Bonome, T., Levine, D.A., Shih, J., Randonovich, M., Pise-Masison, C.A., Bogomolny, F., Ozbun, L., Brady, J., Barrett, J.C., Boyd, J., and Birrer, M.J. (2008). A gene signature predicting for survival in suboptimally debulked patients with ovarian cancer. *Cancer Res.* 68, 5478–5486.
- Cancer Genome Atlas Research Network. (2011). Integrated genomic analyses of ovarian carcinoma. *Nature* 474, 609–615.
- Cao, L., Shao, M., Schilder, J., Guise, T., Mohammad, K.S., and Matei, D. (2011). Tissue transglutaminase links TGF-beta, epithelial to mesenchymal transition and a stem cell phenotype in ovarian cancer. *Oncogene* 31, 2521–2534.
- Carvalho, J., van Grieken, N.C., Pereira, P.M., Sousa, S., Tijssen, M., Buffart, T.E., Diosdado, B., Grabsch, H., Santos, M.A., Meijer, G., et al. (2012). Lack of microRNA-101 causes E-cadherin functional deregulation through EZH2 up-regulation in intestinal gastric cancer. *J. Pathol.* 228, 31–44.
- Ein-Dor, L., Kela, I., Getz, G., Givol, D., and Domany, E. (2005). Outcome signature genes in breast cancer: is there a unique set? *Bioinformatics* 21, 171–178.
- Esquela-Kerscher, A., and Slack, F.J. (2006). Oncomirs - microRNAs with a role in cancer. *Nat. Rev. Cancer* 6, 259–269.
- Esquela-Kerscher, A., Trang, P., Wiggins, J.F., Patrawala, L., Cheng, A., Ford, L., Weidhaas, J.B., Brown, D., Bader, A.G., and Slack, F.J. (2008). The let-7 microRNA reduces tumor growth in mouse models of lung cancer. *Cell Cycle* 7, 759–764.
- Evangelisti, C., Florian, M.C., Massimi, I., Dominici, C., Giannini, G., Galardi, S., Buè, M.C., Massalini, S., McDowell, H.P., Messi, E., et al. (2009). MiR-128 up-regulation inhibits Reelin and DCX expression and reduces neuroblastoma cell motility and invasiveness. *FASEB J.* 23, 4276–4287.
- Garzon, R., Marcucci, G., and Croce, C.M. (2010). Targeting microRNAs in cancer: rationale, strategies and challenges. *Nat. Rev. Drug Discov.* 9, 775–789.
- Gregory, P.A., Bert, A.G., Paterson, E.L., Barry, S.C., Tsykin, A., Farshid, G., Vadas, M.A., Khew-Goodall, Y., and Goodall, G.J. (2008). The miR-200 family and miR-205 regulate epithelial to mesenchymal transition by targeting ZEB1 and SIP1. *Nat. Cell Biol.* 10, 593–601.
- Jemal, A., Tiwari, R.C., Murray, T., Samuels, A., Ward, E., Feuer, E.J., and Thun, M.J.; American Cancer Society. (2004). Cancer statistics, 2004. *CA Cancer J. Clin.* 54, 8–29.
- Kurrey, N.K., K, A., and Bapat, S.A. (2005). Snail and Slug are major determinants of ovarian cancer invasiveness at the transcription level. *Gynecol. Oncol.* 97, 155–165.

- Lewis, B.P., Shih, I.H., Jones-Rhoades, M.W., Bartel, D.P., and Burge, C.B. (2003). Prediction of mammalian microRNA targets. *Cell* 115, 787–798.
- Liu, C., Kelnar, K., Liu, B., Chen, X., Calhoun-Davis, T., Li, H., Patrawala, L., Yan, H., Jeter, C., Honorio, S., et al. (2011). The microRNA miR-34a inhibits prostate cancer stem cells and metastasis by directly repressing CD44. *Nat. Med.* 17, 211–215.
- Mateescu, B., Batista, L., Cardon, M., Gruosso, T., de Feraudy, Y., Mariani, O., Nicolas, A., Meyniel, J.P., Cottu, P., Sastre-Garau, X., and Mechta-Grigoriou, F. (2011). miR-141 and miR-200a act on ovarian tumorigenesis by controlling oxidative stress response. *Nat. Med.* 17, 1627–1635.
- Naora, H., and Montell, D.J. (2005). Ovarian cancer metastasis: integrating insights from disparate model organisms. *Nat. Rev. Cancer* 5, 355–366.
- Noushmehr, H., Weisenberger, D.J., Diefes, K., Phillips, H.S., Pujara, K., Berman, B.P., Pan, F., Pelloski, C.E., Sulman, E.P., Bhat, K.P., et al.; Cancer Genome Atlas Research Network. (2010). Identification of a CpG island methylator phenotype that defines a distinct subgroup of glioma. *Cancer Cell* 17, 510–522.
- Park, S.M., Gaur, A.B., Lengyel, E., and Peter, M.E. (2008). The miR-200 family determines the epithelial phenotype of cancer cells by targeting the E-cadherin repressors ZEB1 and ZEB2. *Genes Dev.* 22, 894–907.
- Pecot, C.V., Calin, G.A., Coleman, R.L., Lopez-Berestein, G., and Sood, A.K. (2011). RNA interference in the clinic: challenges and future directions. *Nat. Rev. Cancer* 11, 59–67.
- Peinado, H., Olmeda, D., and Cano, A. (2007). Snail, Zeb and bHLH factors in tumour progression: an alliance against the epithelial phenotype? *Nat. Rev. Cancer* 7, 415–428.
- Pramanik, D., Campbell, N.R., Karikari, C., Chivukula, R., Kent, O.A., Mendell, J.T., and Maitra, A. (2011). Restitution of tumor suppressor microRNAs using a systemic nanovector inhibits pancreatic cancer growth in mice. *Mol. Cancer Ther.* 10, 1470–1480.
- Rapley, E.A., Crockford, G.P., Teare, D., Biggs, P., Seal, S., Barfoot, R., Edwards, S., Hamoudi, R., Heimdal, K., Fossâ, S.D., et al. (2000). Localization to Xq27 of a susceptibility gene for testicular germ-cell tumours. *Nat. Genet.* 24, 197–200.
- Rosanò, L., Cianfrocca, R., Spinella, F., Di Castro, V., Nicotra, M.R., Lucidi, A., Ferrandina, G., Natali, P.G., and Bagnato, A. (2011). Acquisition of chemoresistance and EMT phenotype is linked with activation of the endothelin A receptor pathway in ovarian carcinoma cells. *Clin. Cancer Res.* 17, 2350–2360.
- Rupaimoole, R., Han, H.D., Lopez-Berestein, G., and Sood, A.K. (2011). MicroRNA therapeutics: principles, expectations, and challenges. *Chin J Cancer* 30, 368–370.
- Santoro, M.R., Bray, S.M., and Warren, S.T. (2012). Molecular mechanisms of fragile X syndrome: a twenty-year perspective. *Annu. Rev. Pathol.* 7, 219–245.
- Sengupta, S., den Boon, J.A., Chen, I.H., Newton, M.A., Stanhope, S.A., Cheng, Y.J., Chen, C.J., Hildesheim, A., Sugden, B., and Ahlquist, P. (2008). MicroRNA 29c is down-regulated in nasopharyngeal carcinomas, up-regulating mRNAs encoding extracellular matrix proteins. *Proc. Natl. Acad. Sci. USA* 105, 5874–5878.
- Siegel, R., DeSantis, C., Virgo, K., Stein, K., Mariotto, A., Smith, T., Cooper, D., Gansler, T., Lerro, C., Fedewa, S., et al. (2012). Cancer treatment and survivorship statistics, 2012. *CA Cancer J. Clin.* 62, 220–241.
- Tellez, C.S., Juri, D.E., Do, K., Bernauer, A.M., Thomas, C.L., Damiani, L.A., Tessema, M., Leng, S., and Belinsky, S.A. (2011). EMT and stem cell-like properties associated with miR-205 and miR-200 epigenetic silencing are early manifestations during carcinogen-induced transformation of human lung epithelial cells. *Cancer Res.* 71, 3087–3097.
- Tessema, M., Willink, R., Do, K., Yu, Y.Y., Yu, W., Machida, E.O., Brock, M., Van Neste, L., Stidley, C.A., Baylin, S.B., and Belinsky, S.A. (2008). Promoter methylation of genes in and around the candidate lung cancer susceptibility locus 6q23–25. *Cancer Res.* 68, 1707–1714.
- Thiery, J.P., Acloque, H., Huang, R.Y., and Nieto, M.A. (2009). Epithelial-mesenchymal transitions in development and disease. *Cell* 139, 871–890.
- Tothill, R.W., Tinker, A.V., George, J., Brown, R., Fox, S.B., Lade, S., Johnson, D.S., Trivett, M.K., Etemadmoghadam, D., Locandro, B., et al.; Australian Ovarian Cancer Study Group (2008). Novel molecular subtypes of serous and endometrioid ovarian cancer linked to clinical outcome. *Clin. Cancer Res.* 14, 5198–5208.
- Trang, P., Medina, P.P., Wiggins, J.F., Ruffino, L., Kelnar, K., Omotola, M., Homer, R., Brown, D., Bader, A.G., Weidhaas, J.B., and Slack, F.J. (2010). Regression of murine lung tumors by the let-7 microRNA. *Oncogene* 29, 1580–1587.
- Varambally, S., Cao, Q., Mani, R.S., Shankar, S., Wang, X., Ateeq, B., Laxman, B., Cao, X., Jing, X., Ramnarayanan, K., et al. (2008). Genomic loss of microRNA-101 leads to overexpression of histone methyltransferase EZH2 in cancer. *Science* 322, 1695–1699.
- Verhaak, R.G., Hoadley, K.A., Purdom, E., Wang, V., Qi, Y., Wilkerson, M.D., Miller, C.R., Ding, L., Golub, T., Mesirov, J.P., et al.; Cancer Genome Atlas Research Network. (2010). Integrated genomic analysis identifies clinically relevant subtypes of glioblastoma characterized by abnormalities in PDGFRA, IDH1, EGFR, and NF1. *Cancer Cell* 17, 98–110.
- Wiggins, J.F., Ruffino, L., Kelnar, K., Omotola, M., Patrawala, L., Brown, D., and Bader, A.G. (2010). Development of a lung cancer therapeutic based on the tumor suppressor microRNA-34. *Cancer Res.* 70, 5923–5930.
- Xu, L., Xie, K., Mukaida, N., Matsushima, K., and Fidler, I.J. (1999). Hypoxia-induced elevation in interleukin-8 expression by human ovarian carcinoma cells. *Cancer Res.* 59, 5822–5829.
- Yang, D., Khan, S., Sun, Y., Hess, K., Shmulevich, I., Sood, A.K., and Zhang, W. (2011). Association of BRCA1 and BRCA2 mutations with survival, chemotherapy sensitivity, and gene mutator phenotype in patients with ovarian cancer. *JAMA* 306, 1557–1565.
- Zhang, L., Volinia, S., Bonome, T., Calin, G.A., Greshock, J., Yang, N., Liu, C.G., Giannakakis, A., Alexiou, P., Hasegawa, K., et al. (2008). Genomic and epigenetic alterations deregulate microRNA expression in human epithelial ovarian cancer. *Proc. Natl. Acad. Sci. USA* 105, 7004–7009.
- Zhao, Y., Liu, H., Li, Y., Wu, J., Greenlee, A.R., Yang, C., and Jiang, Y. (2011). The role of miR-506 in transformed 16HBE cells induced by anti-benzo[a]pyrene-trans-7,8-dihydrodiol-9,10-epoxide. *Toxicol. Lett.* 205, 320–326.
- Zhou, L., Chen, J., Li, Z., Li, X., Hu, X., Huang, Y., Zhao, X., Liang, C., Wang, Y., Sun, L., et al. (2010). Integrated profiling of microRNAs and mRNAs: microRNAs located on Xq27.3 associate with clear cell renal cell carcinoma. *PLoS ONE* 5, e15224.
- Zhu, Y., Nilsson, M., and Sundfeldt, K. (2010). Phenotypic plasticity of the ovarian surface epithelium: TGF-beta 1 induction of epithelial to mesenchymal transition (EMT) in vitro. *Endocrinology* 151, 5497–5505.

Integrative Genomic Analyses Reveal an Androgen-Driven Somatic Alteration Landscape in Early-Onset Prostate Cancer

Joachim Weischenfeldt,^{1,14} Ronald Simon,^{2,14} Lars Feuerbach,^{4,14} Karin Schlangen,^{8,14} Dieter Weichenhan,^{5,14} Sarah Minner,^{2,14} Daniela Wuttig,^{6,14} Hans-Jörg Warnatz,⁸ Henning Stehr,⁸ Tobias Rausch,¹ Natalie Jäger,⁴ Lei Gu,⁵ Olga Bogatyrova,⁵ Adrian M. Stütz,¹ Rainer Claus,⁵ Jürgen Eils,⁴ Roland Eils,^{4,12} Clarissa Gerhäuser,⁵ Po-Hsien Huang,⁵ Barbara Hutter,⁴ Rolf Kabbe,⁴ Christian Lawrenz,⁴ Sylwester Radomski,⁴ Cynthia C. Bartholomae,⁷ Maria Fälth,⁶ Stephan Gade,⁶ Manfred Schmidt,⁷ Nina Amschler,² Thomas Haß,² Rami Galal,² Jovisa Gjoni,² Ruprecht Kuner,⁶ Constance Baer,⁵ Sawinee Masser,² Christof von Kalle,⁷ Thomas Zichner,¹ Vladimir Benes,¹³ Benjamin Raeder,¹ Malte Mader,⁹ Vyacheslav Amstislavskiy,⁸ Meryem Avci,⁷ Hans Lehrach,⁸ Dmitri Parkhomchuk,⁸ Marc Sultan,⁸ Lia Burkhardt,² Markus Graefen,³ Hartwig Huland,³ Martina Kluth,² Antje Krohn,² Hüseyin Sirma,² Laura Stumm,² Stefan Steurer,² Katharina Grupp,² Holger Sülthmann,^{6,15} Guido Sauter,^{2,15} Christoph Plass,^{5,15} Benedikt Brors,^{4,15} Marie-Laure Yaspo,^{8,15} Jan O. Korbel,^{1,10,15,*} and Thorsten Schlömm^{3,11,15}

¹Genome Biology Unit, European Molecular Biology Laboratory (EMBL), Meyerhofstr. 1, 69117 Heidelberg, Germany

²Institute of Pathology

³Martini-Clinic, Prostate Cancer Center

University Medical Center Hamburg-Eppendorf, Martinistr. 52, 20246 Hamburg, Germany

⁴Division of Theoretical Bioinformatics

⁵Division of Epigenomics and Cancer Risk Factors

German Cancer Research Center, Im Neuenheimer Feld 280, 69120 Heidelberg, Germany

⁶Working Group Cancer Genome Research

⁷Division of Translational Oncology

German Cancer Research Center and National Center of Tumor Diseases, Im Neuenheimer Feld 460, 69120 Heidelberg, Germany

⁸Department of Vertebrate Genomics, Max Planck Institute for Molecular Genetics, Ihnestr. 63, 14195 Berlin, Germany

⁹Hamburg University, Centre for Bioinformatics, Bundesstr. 43, 20146 Hamburg, Germany

¹⁰European Bioinformatics Institute, Wellcome Trust Genome Campus, Hinxton, Cambridge, CB10 1SD, UK

¹¹Department of Urology, Section for Translational Prostate Cancer Research, University Medical Center Hamburg-Eppendorf, Martinistr. 52, 20246 Hamburg, Germany

¹²Institute of Pharmacy and Molecular Biotechnology, and Bioquant Center, University of Heidelberg, Im Neuenheimer Feld 267, 69120 Heidelberg, Germany

¹³Genomics Core facility, European Molecular Biology Laboratory (EMBL), Meyerhofstr. 1, 69117 Heidelberg, Germany

¹⁴These authors contributed equally to this work

¹⁵These authors contributed equally to this work as senior authors

*Correspondence: jan.korbel@embl.de

<http://dx.doi.org/10.1016/j.ccr.2013.01.002>

SUMMARY

Early-onset prostate cancer (EO-PCA) represents the earliest clinical manifestation of prostate cancer. To compare the genomic alteration landscapes of EO-PCA with “classical” (elderly-onset) PCA, we performed deep sequencing-based genomics analyses in 11 tumors diagnosed at young age, and pursued comparative assessments with seven elderly-onset PCA genomes. Remarkable age-related differences in structural rearrangement (SR) formation became evident, suggesting distinct disease pathomechanisms. Whereas

Significance

It is presently unknown whether genetic or mechanistic differences distinguish “classical” elderly-onset PCA from EO-PCA. Using integrative high-throughput sequencing approaches, combined with validations in a large-scale patient cohort, we show that EO-PCA formation involves a characteristic pathomechanism associated with the specific emergence of androgen-driven SRs. By comparison, elderly-onset PCAs accumulate nonandrogen-associated SRs, indicating that a different tumor formation mechanism is operating in these. This work reveals a striking age-dependent SR associated disease mechanism in a common human cancer, and presents a significant advancement in understanding age-dependencies of PCA initiation and progression, with implications for clinical management. The genomics data from our consortium further provide a valuable compendium of massively-parallel DNA sequencing data in EO-PCA.

EO-PCAs harbored a prevalence of balanced SRs, with a specific abundance of androgen-regulated ETS gene fusions including *TMPRSS2:ERG*, elderly-onset PCAs displayed primarily non-androgen-associated SRs. Data from a validation cohort of > 10,000 patients showed age-dependent androgen receptor levels and a prevalence of SRs affecting androgen-regulated genes, further substantiating the activity of a characteristic “androgen-type” pathomechanism in EO-PCA.

INTRODUCTION

Prostate cancer (PCA) is the most common cancer in Western countries and the second most lethal cancer in men (Siegel et al., 2012). The incidence of PCA increases with age, with a median age at diagnosis of ~70 years (Grönberg, 2003). Due to relatively slow disease progression when compared to life expectancy, patients with PCA do not always require definite therapy, with active surveillance representing an established treatment option (Heidenreich et al., 2011). A relevant subset of PCA, however, is diagnosed early in life, referred to as early-onset PCA (EO-PCA), with ~2% of all tumors detected in men 50 years of age or younger (Figure 1). EO-PCAs are of substantial clinical relevance, requiring obligatory definite treatment (Heidenreich et al., 2011). This is due to the high life expectancy of these young patients, with a higher risk of dying of disease (Albertsen et al., 2005; Parker et al., 2006), although there are also studies showing a more pronounced risk of rapid death in EO-PCA (Lin et al., 2009b; Ryan et al., 2007) compared to the “classical” cases of PCA diagnosed in 60- to 80-year-old men (herein referred to as “elderly-onset PCA”).

Initial genomics surveys focused on classical, elderly-onset PCA have revealed a substantial diversity in somatic single nucleotide variants (SNVs) (Berger et al., 2011; Kumar et al., 2011), and identified recurrent SRs, including oncogene-activating gene fusion events (Berger et al., 2011; Bastus et al., 2010; Lin et al., 2009a; Mani et al., 2009; Taylor et al., 2010; Tomlins et al., 2005) in elderly-onset PCAs. Despite the recent progress in identifying molecular drivers of PCA with massively-parallel sequencing of cancer genomes (Berger et al., 2011) and exomes (Kumar et al., 2011; Barbieri et al., 2012; Grasso et al., 2012), so far no study has generated whole-genome sequencing data of EO-PCAs. Hence, it has therefore remained unclear whether EO-PCA is characterized by a distinctive spectrum of driver mutations or a specific pathomechanism. A better understanding of genomic alterations associated with EO-PCA will facilitate the understanding of molecular defects leading to early disease onset and foster the development of new diagnostic, prognostic, therapeutic, and prevention strategies.

On behalf of the International Cancer Genome Consortium (ICGC) project on Early-Onset Prostate Cancer (<http://www.icgc.org>), we carried out integrated genomic analyses, including whole-genome, transcriptome, and DNA methylome sequencing (Campbell et al., 2008) in 11 patients with EO-PCA. We used these genomics data, together with a large-scale tissue microarray (Schlomm et al., 2008) (TMA)-based validation platform, to pinpoint molecular features linked with early disease occurrence.

RESULTS

Integrative High-Throughput Sequencing and Variant Calling

Tumor and paired control tissue samples (lymphocytes) were obtained from all 11 patients with EO-PCA who provided informed consent. The patient mean age at surgery was 47 years, tumor Gleason grades ranged from 3+4 to 5+4, and tumor stages from pT2c to pT3b (Table 1). Our multitiered genomics approach (see Experimental Procedures) involved ~30- to 40-fold whole-genome sequencing (Table 2; Figure S1A available online) of tumor and control samples, with two sequencing libraries per sample displaying complementary paired read insert sizes (ie, ~200 bp paired-end, and ~4.5 kb mate-pair inserts) (Ley et al., 2008). We furthermore carried out transcriptome sequencing (RNA-seq) (Sultan et al., 2008) of each tumor in comparison to a normal prostate tissue control, using two complementary library generation approaches geared toward assessing mRNAs and MicroRNAs (miRNAs). In addition, we identified altered DNA methylation patterns by performing an enrichment of methylated DNA fragments with an Fc-coupled MBD2 protein (Gebhard et al., 2006) followed by massively parallel sequencing (Figures S1B and S1C; see Experimental Procedures).

Following the mapping of DNA reads onto the human reference assembly we applied complementary computational approaches for the detection of somatic genome alterations (see Experimental Procedures). We identified SNVs, as well as short deletions and insertions (short InDels) by directly evaluating read alignments onto the reference genome assembly (Li and Durbin, 2009; DePristo et al., 2011). Furthermore, we detected large-scale somatic structural rearrangements (SRs) by evaluating the relative depth-of-coverage of DNA reads along chromosomes, by scanning DNA reads for split or clipped read alignments, and by identifying read-pairs that abnormally mapped onto the reference (Xi et al., 2011).

Altogether, we identified 931–5,696 somatic SNVs per patient (Tables 2 and S1; Figure S1A), with the C > T nucleotide transition being the most common substitution (42.6% ± 5.6%), similar to what has been observed in elderly-onset PCAs (Berger et al., 2011; Kumar et al., 2011). On average, 16 nonsynonymous somatic SNVs fell into protein-coding genes (range 3–55), affecting altogether 175 genes. We further detected six nonsynonymous rare germline SNVs with a second somatic mutational event, leading to compound heterozygosity (Table S1; Supplemental Experimental Procedures). A low number (four) of high-confidence somatic InDels of ≤50 bp in size was identified (Table S2). By comparison, we detected a considerably larger number—20–90 per EO-PCA genome (average, 45)—of somatic SRs (Tables 2 and S2; Figures 2A and S2A). These somatic variants included copy-number alterations (average, 23), and

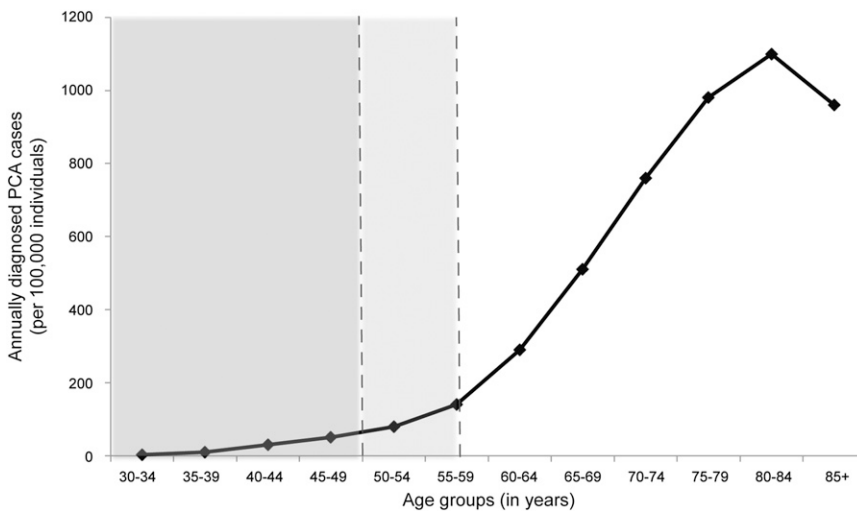


Figure 1. The Age Distribution in Elderly-Onset PCA and EO-PCA

Dark and light areas depict patients younger than 50 years (EO-PCA) and patients between 50 and 60 years old, respectively (reproduced from epidemiologic data; Grönberg, 2003).

also a relatively large number of balanced rearrangements (average, 22), most of which were translocations. PCR followed by capillary sequencing verified 85 of 95 (89%) SNVs, all four short somatic InDels, and 50 of 53 (94%) of the SRs (Table S3).

Computational Inference and Characterization of Candidate Driver Somatic Alterations

To assess the functional relevance of these somatic alterations, we first analyzed gene-altering events in detail. Because a relevant portion of the somatic alterations identified may constitute passenger alterations (Stratton et al., 2009), we performed integrative analyses to infer candidate driver alterations in our EO-PCA samples. This involved using our somatic SNV and SR data to identify genes recurrently altered across samples, and applying a “two-hit hypothesis” approach for the identification of candidate tumor suppressor genes (Knudson, 1971), by probing for genes for which both alleles were affected by genetic

mechanisms of inactivation (see Experimental Procedures). Our search strategy resulted in the identification of 23 genes that were disrupted or mutated in at least two additional PCA patient cohorts (Barbieri et al., 2012; Berger et al., 2011; Grasso et al., 2012). We further inferred 76 genes harboring two genomic hits, a list comprising several previously described tumor suppressors including

CDH1, *TP53*, *PTEN*, and *NCOR2*, many of which also showed promoter hypermethylation in samples not carrying the respective genetic lesion (Table S4).

NCOR2, a transcriptional corepressor interacting with the androgen receptor (AR), was previously reported as mutated in PCA (Taylor et al., 2010). In addition to biallelic genetic alterations affecting *NCOR2* in one tumor (EOPC-06), we observed homozygous loss of an *NCOR2* regulator in another tumor (EOPC-04) in conjunction with *NCOR2* downregulation. We further identified high levels of DNA methylation of the *NCOR2* promoter in association with *NCOR2* downregulation in a third tumor (EOPC-01). The clinical relevance of *NCOR2* deletions was evaluated with our large-scale TMA resource (Schlomm et al., 2008) revealing *NCOR2* deletions in 3.2% (163/5100) PCAs, and showing significant association with biochemical disease recurrence ($p = 0.039$, Likelihood ratio test; Figure S2B).

A pronounced diversity of inactivating genetic mechanisms was also observed for *PTEN*, in agreement with a recent study of elderly-onset PCAs (Reid et al., 2012). Namely, *PTEN* was disrupted by a translocation in sample EOPC-05, also harboring a large (55 Mb) deletion removing the other *PTEN* allele, with our transcriptome data showing a pronounced *PTEN* downregulation (Figure 2B). Analysis in a large patient cohort revealed a high frequency of homozygous *PTEN* losses involving such combinations of disruptive events, which are linked with biochemical disease recurrence (Figures S2C–S2J). The additional finding of multiple upregulated *PTEN*-targeting miRNAs (Figures S2K–S2O; Tables S5, S6, and S7) indicates the involvement of different mechanisms of *PTEN* inactivation in PCA.

An Abundance of Gene-Fusing Rearrangements, Including such Leading to ETS Fusion Genes, in EO-PCA

The striking abundance of balanced SRs in our EO-PCA samples—with approximately half of all SRs being balanced (a higher number than that recently reported [$<30\%$] in elderly-onset PCAs; Berger et al., 2011)—prompted us to investigate in further detail the formation of gene-fusing rearrangements, because fusion gene formation is frequently associated with balanced SR formation (Rubin et al., 2011; Tomlins et al., 2005). Indeed, we could identify a relatively large number

Table 1. Summary of Clinical Data for the 11 Patients with EO-PCA

Patient ID	Age at Surgery (years)	pT Stage	pN Stage	Gleason Score	Preoperative PSA (ng/ml)	Family History of PCA ^a
EOPC-01	45	pT3a	pN0	3+4	30.0	no
EOPC-02	51	pT2c	pN0	3+4	23.8	NA
EOPC-03	46	pT3a	pN0	5+4	12.0	no
EOPC-04	51	pT3b	pN1	4+3	72.0	no
EOPC-05	50	pT3a	NX	3+4	5.0	no
EOPC-06	38	pT3b	pN1	3+4	18.2	NA
EOPC-07	49	pT2c	pN0	3+4	5.4	yes
EOPC-08	44	pT2c	pN0	3+4	7.8	yes
EOPC-09	48	pT2c	pN0	3+4	5.1	no
EOPC-010	46	pT2c	NX	3+4	6.0	no
EOPC-011	48	pT2c	pN0	3+4	4.8	yes

All patients were diagnosed <50 years. All patients are of German ancestry. PSA, prostate-specific antigen; NA, not applicable.

^aAt least one first-degree relative with PCA.

Table 2. Sequence Data and Somatic Genome Alterations in 11 EO-PCAs

Patient ID	EOPC-01	EOPC-02	EOPC-03	EOPC-04	EOPC-05	EOPC-06	EOPC-07	EOPC-08	EOPC-09	EOPC-010	EOPC-011
Bp (paired) (tumor/blood)	179/165	110/135	245/99	112/230	105/102	141/135	104/100	139/102	110/134	151/148	104/102
Sequence coverage	42×/44×	30×/26×	69×/30×	32×/65×	31×/30×	41×/40×	31×/30×	29×/31×	33×/40×	46×/44×	31×/30×
PE physical coverage	30×/33×	21×/24×	75×/28×	30×/76×	29×/28×	38×/36×	29×/27×	38×/29×	27×/33×	40×/39×	27×/27×
MP physical coverage	14×/17×	15×/15×	16×/16×	16×/11×	17×/15×	16×/18×	13×/17×	17×/20×	18×/18×	17×/17×	18×/18×
mRNA-Seq reads (million reads/Gb)	18/14	9/7	10/7	10/8	13/11	14/11	13/10	12/10	16/13	14/10	13/10
miRNA-Seq in M reads (total/mapped to miRNAs)	NA	NA	NA	NA	144/ 19	66/ 16	71/ 26	82/ 12	74/9	74/ 11	92/ 24
Methylome reads in M (total/mapped)	67/21	89/23	75/20	85/24	62/16	119/22	143/30	115/24	169/32	128/27	88/21
Somatic SNVs	5,696	3,747	4,529	2,430	1,475	1,277	1,404	931	985	1,536	1,567
Mutations per Mb	2.0	1.3	1.6	0.8	0.5	0.4	0.5	0.3	0.3	0.5	0.5
Nonsilent coding SNVs	55	11	40	21	6	8	9	6	3	10	6
Nonsilent InDels	1	1	0	0	0	0	1	1	0	0	0
Somatic Dels (genes/Mb)	1452/235	442/101	671/124	598/84	1,043/194	2,283/347	961/153	524/91	481/93	771/144	566/125
Somatic Dups (genes/Mb)	138/18.8	1/0.0	4/1.0	45/6.7	0/0.0	21/2.2	1/0.6	7/1.5	15/ 2.3	1/0.0	42/ 9.7
Translocation (coding/noncoding breaks)	15/11	12/8	14/4	32/40	27/27	38/20	14/4	11/1	21/5	11/1	26/18
Inversions (coding/noncoding breaks)	3/1	2/8	1/1	11/7	2/4	10/4	2/10	2/0	21/7	3/3	10/6
Estimated tumor purity (%)	50	40	37	55	45	47	60	61	44	50	51

Production centers—sample acquisition and nucleic acid isolation: Martini Clinic, Prostate Cancer Center, and Institute of Pathology, University Clinic Hamburg-Eppendorf (UKE); paired-end (PE) whole-genome sequencing: Max Planck Institute for Molecular Genetics (MPIMG), German Cancer Research Center (DKFZ), and European Molecular Biology Laboratory (EMBL); long-range paired-end, or mate-pair (MP), genomic sequencing: EMBL; transcriptome sequencing: MPIMG; miRNA sequencing: DKFZ; methylome sequencing: DKFZ. NA, not available.

See also [Figure S1](#) and [Table S1](#).

(ie, 139) of gene-fusing rearrangements (12 per sample) in the 11 EO-PCA samples, 109 of which resulted from balanced SRs (mostly translocations). While many of these gene-fusing events were out-of-frame and likely correspond to passenger events, most in-frame fusion genes received additional support from mRNA-seq reads mapping directly over the junction point of the fusion, or by the striking overexpression of the 3' fusion partner ([Table S2](#)), suggesting their possible biologic relevance.

Fusion genes supported by marked expression upregulation included the prototypical ETS gene family-associated fusion genes *TMPRSS2:ERG* and *SLC45A3:ERG* ([Tomlins et al., 2005, 2007](#)). Furthermore, we observed evidence for 17 rare (nonrecurrent) previously undescribed in-frame gene fusion events ([Table S2](#)). These included *SNURF:ETV1*, which evidently was formed in conjunction with a complex rearrangement event

(closed chain; [Berger et al., 2011](#)) involving an androgen-regulated 5'-end fusion gene partner (*SNURF*) that, based on our mRNA-Seq data, led to marked overexpression of an *ETV1* open reading frame with previously demonstrated oncogenic activity ([Tomlins et al., 2007](#)) ([Figures 2C](#) and [S2P–S2T](#)). We also identified 17 fusion gene transcripts that were exclusively discovered in our mRNA-seq data, ie, events missed by our DNA sequencing-based SR detection pipeline (see [Supplemental Experimental Procedures](#)).

Early-Onset Prostate Cancers Harbor a Distinctive Landscape of Genetic Rearrangements

The conspicuous frequency of gene-fusing SRs in EO-PCA prompted us to perform a more detailed comparison between the genomic landscapes of young and elderly patients, by

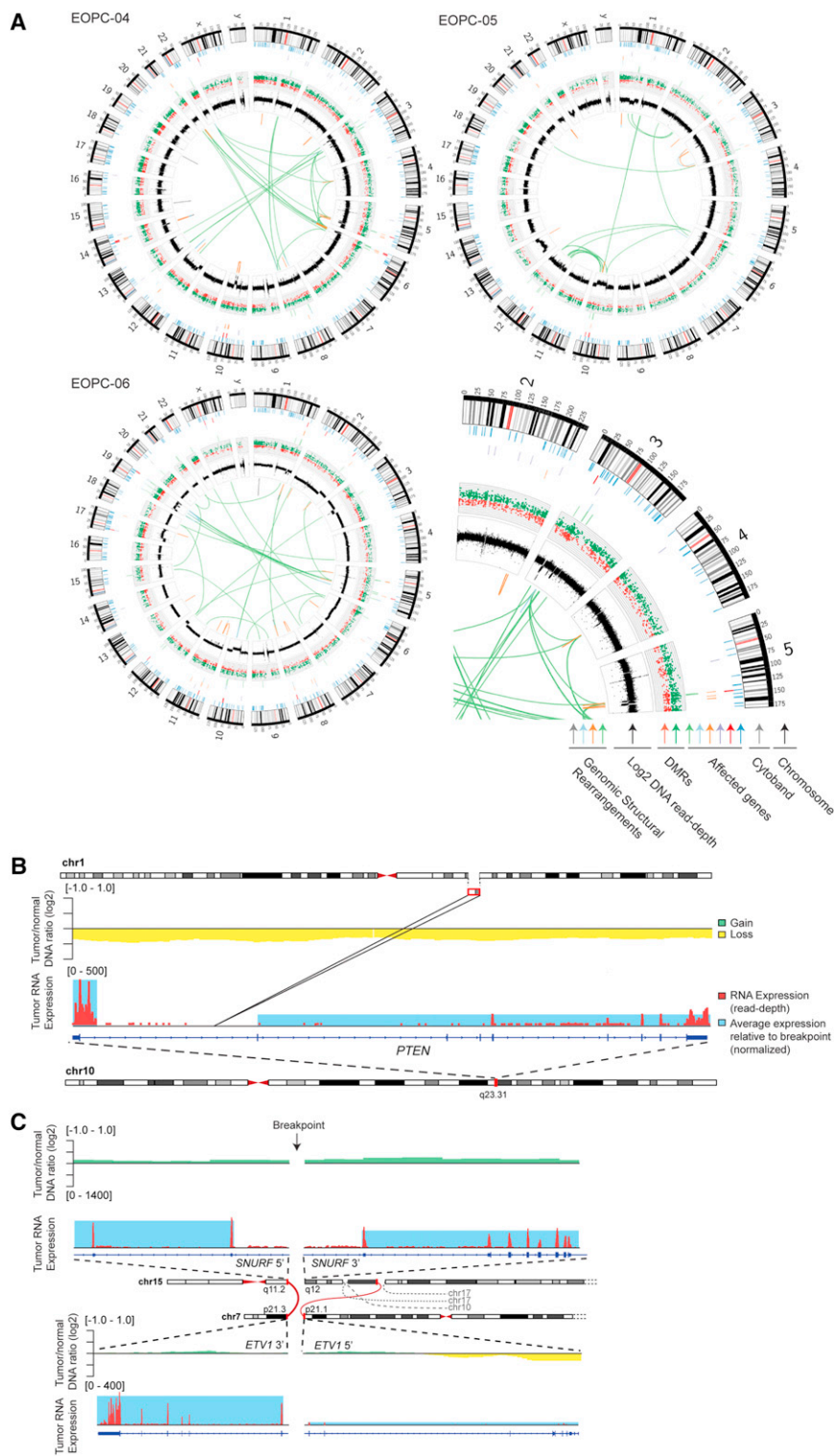


Figure 2. Genomes of EO-PCA Revealed by High-Throughput Sequencing

(A) Circos plots, depicting genomic and epigenomic somatic aberrations in three EO-PCA patients (all 11 EO-PCA genomes are displayed in Figure S2A). Displayed features from outer to inner ring include chromosomes (black) with cytobands (gray) in the first ring; lines in second ring refer to genes, with colors highlighting CancerCensus genes (Futreal et al., 2004) (blue), biallelic inactivated genes (red), nonsynonymous SNVs (purple), inferred gene-disrupting deletions (orange), gene-disrupting inversions (light blue) and gene-disrupting translocations (light green); squares in third ring refer to hypermethylated (dark green) and hypomethylated DMRs (light red); the fourth ring displays somatic inferred copy-number gains and losses as read-depth plots; the innermost shows translocations (green), deletions (orange), inversions (light blue), and duplications (gray).

(B) Biallelic inactivation of *PTEN* by combined loss-of-heterozygosity and a disruptive t(1;10) translocation in EOPC-05. RNA expression values are depicted up- and downstream of the breakpoint, along with the inferred copy-number profile of the tumor sample relative to germline control (\log_2 DNA read-depth ratio), with losses indicated in yellow and gains in green. Gene expression values are displayed in terms of the RNA-seq read-depth (red) and averaged RPKM (light blue) values upstream and downstream of the insertion event.

(C) Rearrangements leading to the identified *SNURF:ETV1* fusion in EOPC-03, comprising up to intron 2 of *SNURF* at the 5'-end, and continuing from intron 4 of *ETV1* at the 3'-end.

See also Figure S2 and Tables S2, S3, S4, S5, S6, and S7).

comparing genetic alterations identified in our samples with the recently published whole-genomes of seven elderly-onset ("classical") PCAs, with a mean age at diagnosis of 65 years (Berger et al., 2011). Relative to the total number of somatic rearrangements, EO-PCAs indeed displayed a significantly

higher portion of SRs leading to gene-fusing events (25% in EO-PCA versus 10% in the elderly; ie, 2.5-fold enrichment with $p = 0.001$; Welch's two-sample t test; Figure 3A). This was despite an overall lower number of SRs in EO-PCA compared to elderly-onset PCA genomes (average 45 versus 108 rearrangements, respectively; $p = 0.038$, Welch's two-sample t test; Figure 3B), a trend that we also confirmed upon reanalysis of the raw DNA sequence read data from Berger et al. using our computational SV detection pipeline (see Supplemental Experimental Procedures).

By comparison, when assessing somatic SNVs, we observed no significant difference between EO-PCAs and elderly-onset PCAs in terms of genome-wide (or protein-coding sequence-wide) SNV counts (Table S1). Hence, despite marked differences evident at the level of SRs, no such differences appeared to exist at the level of SNVs.

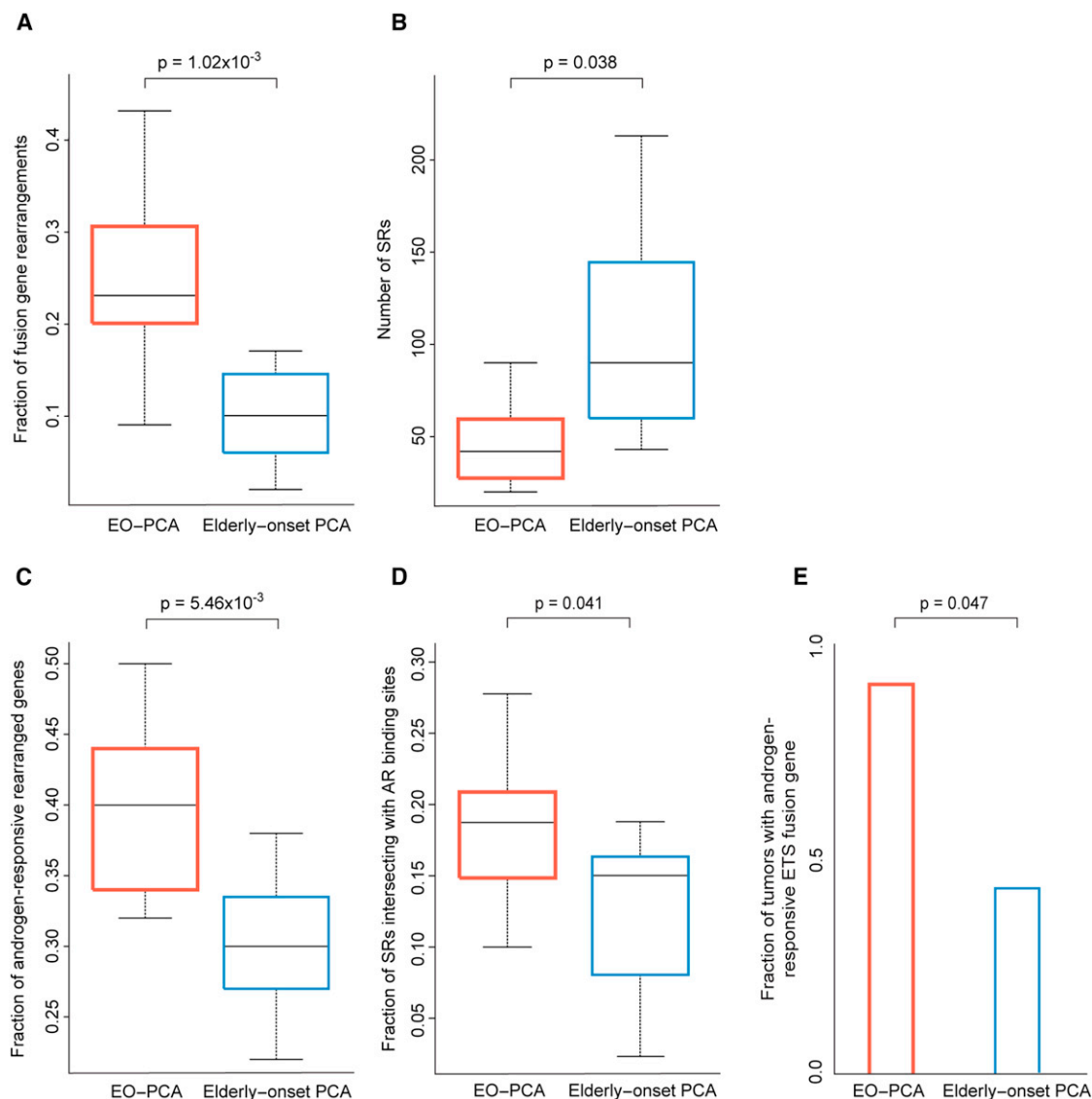


Figure 3. Whole-Genome Sequencing-Based Analyses Reveal that EO-PCAs Harbor a Markedly Different SR Landscape than Elderly-Onset PCAs

(A) Proportion of SRs leading to gene fusions. These analyses considered all breakpoints affecting Refseq gene models.

(B) SRs identified per sample.

(C) Fraction of gene rearrangements affecting androgen-regulated genes.

(D) Fraction of SRs intersecting high-confidence androgen-receptor binding sites (ARBS) using a 50-kb search window.

(E) Portion of tumors harboring ETS fusion genes.

Welch's two-sample t test was used to compute p values in (A)–(D). Boxplots display the 25th to 75th percentiles (boxes), medians (lines), and 1.5 times the interquartile range (whiskers).

See also [Table S2](#).

Early-Onset Prostate Cancers Harbor an Androgen-Driven Somatic Genome Alteration Landscape

Because gene-fusing events in PCA can be mediated directly upon activation of the AR (Mani et al., 2009), facilitating gene fusion events that involve androgen-regulated genes bound by the AR (Rubin et al., 2011), we hypothesized that the observed differences in the somatic SR spectrum of EO-PCA versus elderly-onset PCA may have resulted from the differential usage of an AR-dependent SR formation mechanism driving

specific DNA rearrangements. To test this hypothesis, we first generated a catalog of genes under androgen-regulation, by measuring differential expression before and after dihydrotestosterone-stimulation of LNCaP cells using gene expression microarrays (see [Supplemental Experimental Procedures](#) and [Table S2](#)). Strikingly, we observed a significantly higher fraction of gene rearrangements affecting androgen-driven genes—in which a break occurred in a gene differentially expressed upon dihydrotestosterone-stimulation—in EO-PCA compared to

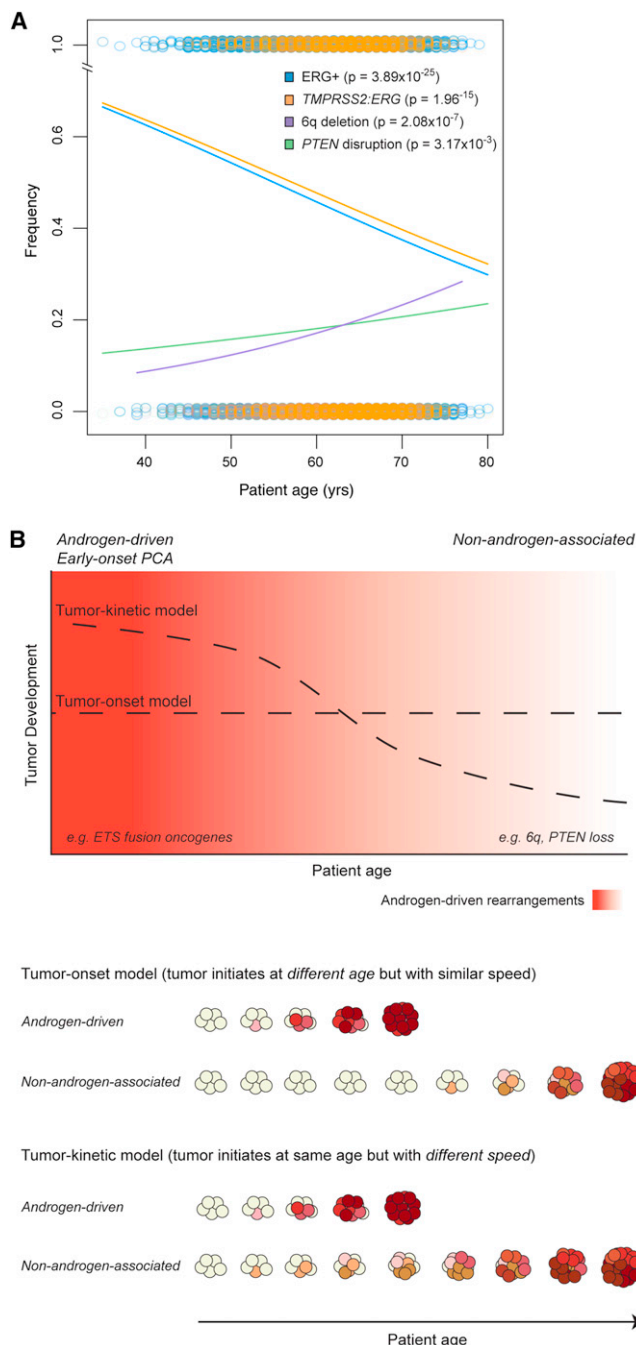


Figure 4. TMA Verifies Distinct Age Spectra of Androgen-Dependent and -Independent Progression Types

(A) Large-scale TMA analyses depict age relationships of the androgen-driven ETS-fusion protein $TMPRSS2:ERG$ in EO-PCA, and of nonandrogen-associated rearrangements in elderly-onset PCA. Frequency of assessed protein (rings) and binomial logistic regressions (lines) depict ERG overexpression (blue; $n = 9,567$), $TMPRSS2:ERG$ fusion gene presence (orange; $n = 6,071$), chromosome 6q deletion (purple; $n = 3,493$), and $PTEN$ deletion/disruption (green; $n = 5,374$) as a function of patient age (age at diagnosis ranging between 36 and 80 years). ERG overexpression was detected by immunohistochemistry, and genomic rearrangements by FISH. P values are based on binomial logistic regression.

(B) Proposed tumor progression models for androgen-type PCAs. See also Figure S3.

elderly-onset PCA (Figure 3C; $p < 0.01$; Welch's two-sample t test). In further support of these findings, we observed a statistical enrichment of AR signaling and WNT signaling (which interacts with AR signaling in PCA; Yang et al., 2006) pathways among genes involved in gene fusion events in EO-PCAs, but not in elderly-onset PCAs (see Experimental Procedures and Table S2). These findings indicate a prevalence of EO-PCA to acquire specific, androgen-driven, somatic genome alterations.

AR binding to nuclear DNA can facilitate genomic rearrangements through recruitment of topoisomerase 2B (TOP2B), leading to DNA double strand break formation within or nearby transcriptional hubs, joining different sections of the genome that upon breakage may reconnect to lead to intra- or inter-chromosomal SRs (Haffner et al., 2010; Lin et al., 2009a). Hence, we followed the assumption that if androgen drives the formation of SRs characteristically arising in EO-PCA, we would observe a relative enrichment of genomic AR binding sites near the breakpoints of SRs in EO-PCA relative to elderly-onset PCA. High-confidence binding sites of the AR were recently mapped in LNCaP cells by chromatin immunoprecipitation followed by massively parallel sequencing (ChIP-Seq), upon androgen stimulation (Urbanucci et al., 2012). Indeed, when relating these ChIP-Seq data to our SR data, we observed a marked enrichment of SRs intersecting with AR binding sites (Urbanucci et al., 2012) in EO-PCA compared to elderly-onset PCA (Figure 3D; $p < 0.05$, Welch's two sample t test). These results are consistent with the chromosomal looping by the AR bound to its cognate binding sites specifically facilitating SRs in EO-PCA in an androgen-driven manner.

ETS Fusion Genes Are a Hallmark of Early-Onset Prostate Cancer

We next assessed the status of ETS family oncogene containing fusion genes, with ETS fusions representing prototypic PCA driver gene rearrangements mediated by androgen stimulation and the AR (reviewed in Rubin et al., 2011). Even though the number of sequenced PCA genomes is presently small, comparison of the ETS rearrangement status in 11 EO-PCAs versus the seven elderly-onset PCAs published by Berger and coworkers already revealed statistically significant differences, with 10 of 11 (~90%) EO-PCAs, but only three of seven (~40%) elderly-onset PCAs harboring such androgen-driven ETS rearrangements (Figure 3E; $p = 0.047$; two-sided Fisher's exact test). Notably, the abundance of ETS fusions in EO-PCA was further supported by our reanalysis of data published by Barbieri et al., a study in which four of five patients ≤ 50 years harbored $TMPRSS2:ERG$ -fusions, compared to 54 of 107 patients > 50 years (Barbieri et al., 2012).

To verify the specific abundance of androgen-driven SRs in EO-PCA in a larger patient cohort, we made use of our TMA resource, covering thousands of patients (Figure 4A). We used a surrogate for assessing androgen-driven ETS gene fusion events, by applying a break-apart FISH probe for evaluating the presence of the prototypical androgen-driven $TMPRSS2:ERG$ fusion gene (Lin et al., 2009a; see Experimental Procedures) in patients with a disease age-of-onset of 36–80 years. Indeed, the TMA analyses verified the continuous and significant relative increase of the ETS gene fusion $TMPRSS2:ERG$ ($p < 2 \times 10^{-15}$, logistic regression) in patients with early disease onset, hence

further strengthening our finding based on whole-genome sequencing of an abundance of androgen-driven alterations in EO-PCA (Figures 4A and S3). Because *ERG* gene fusions may involve androgen-regulated genes other than *TMPRSS2*, we additionally measured *ERG* protein expression by immunohistochemistry (IHC), an analysis that further substantiated the marked overexpression of *ERG* ($p < 4 \times 10^{-25}$, logistic regression) in young versus elderly patients (Figures 4A and S3).

Nonandrogen-Associated Structural Rearrangements Frequently Accumulate in Elderly-Onset Prostate Cancer

Because SRs affecting androgen-regulated genes are markedly enriched in EO-PCAs, whereas elderly-onset PCAs show an overall higher load of SRs (Figure 3), we screened several additional recurrent SRs (Sun et al., 2007) for a relationship with patient age at diagnosis, including those that do not involve androgen-regulated genes. To this end, we performed extensive FISH analyses, targeting the chromosome 6q15 region (Liu et al., 2007b), the *PTEN* locus (Krohn et al., 2012), the *CHD1* locus (Huang et al., 2012), and *NCOR2*. Our data showed a significant increase of 6q15, *PTEN*, and *CHD1* genomic breaks, all of which are not considered to be androgen-regulated, in elderly patients (Figures 4A and S3)—findings that were independent of tumor stage or Gleason grade (see also Table S2, which presents data from detailed assessments of *PTEN* and *ERG*). These results show that nonandrogen-associated SRs accumulate in elderly-onset PCA. As a consequence, elderly-onset PCAs acquire high loads of SRs, most of which correspond to copy-number unbalanced alterations.

By comparison, deletions of *NCOR2* were significantly associated with young age (Figure S3). Because *NCOR2* is an AR corepressor (Hodgson et al., 2005; Godoy et al., 2012), deletions of this gene are predicted to lead to increased AR levels and in turn may contribute to androgen-driven rearrangements in young patients.

Increased Levels of Androgen or Its Receptor May Explain the Early Disease Onset in Androgen-Driven PCAs

The high abundance of androgen-driven genetic alterations in EO-PCA suggests a relevance of those alterations for the timing and initiation of tumorigenesis in the cells of the prostate. Specifically, the preponderance of androgen-driven SRs in young patients may intuitively be explained by a particularly early development of tumors occurring in young patients (tumor-onset model; Figure 4B). Alternatively, particularly rapid growth kinetics of androgen-driven tumors may also explain the observed age relationship (tumor-kinetic model; Figure 4B).

Because the initiation of tumorigenesis in the prostate cannot be confidently ascertained in humans—with PCAs initiating years or decades before being diagnosed (Knudsen and Vasioukhin, 2010)—we sought to evaluate the possible role of tumor kinetics in the abundance of androgen-driven genetic alterations in EO-PCA. We therefore employed IHC to measure cancer cell proliferation using the Ki67 labeling index (LI) as a marker (Bubendorf et al., 1996). Importantly, while growth kinetics differed markedly between tumor grades (Figure 5A), there were no observable differences between the growth kinetics of

androgen-driven (using *ERG* positivity as a proxy) versus nonandrogen-associated (*ERG*-negative) tumors (Figure 5A). Furthermore, there was no correlation between cancer cell proliferation and age at diagnosis ($R^2 \sim 0$; $p = 0.44$, Spearman's rank correlation). Hence, we can practically exclude a role of growth kinetics in facilitating androgen-driven cancer occurrence in young patients. Furthermore, the overall similar aggressive potential of androgen-driven (*ERG*-positive) tumors versus nonandrogen-associated (*ERG*-negative) tumors is consistent with tumor growth kinetics playing no marked role in generating the herein observed age-associated SR spectra (Figure S4A). Hence, we conclude that differences in the age-of-initiation of tumors harboring androgen-driven SRs versus those not showing an abundance of such SRs must have resulted in the characteristic somatic DNA alteration landscapes of EO-PCA versus elderly-onset PCA (Figure 4B).

Androgen Receptor Levels Are Elevated in Early-Onset Prostate Cancer

Our findings hence point toward a crucial role of androgen and AR activation in shaping the genomic landscape of PCAs, and driving tumor initiation, motivating further in vivo analyses. While it is impossible to estimate testosterone levels retrospectively in patients during cancer initiation and evolution, patterns of AR activity can be studied in tumor samples by measuring AR protein expression (as a surrogate) in tumor samples at diagnosis (Lee and Chang, 2003). We pursued AR expression analysis using IHC, relating AR levels to patient age and *ERG* status. Importantly, our data revealed both a significantly increased AR level in young patients (Figures 5B and 5C) and a significant positive correlation of AR levels with *ERG* rearrangements ($p < 4 \times 10^{-8}$ and $p < 2 \times 10^{-12}$, respectively; Figure 5C; see also Figures 5B–5D, S4B, and S4C). Hence, high AR expression levels are associated with *ERG* rearrangements and young age, indicating an age-dependent activity of AR in PCA. *ERG*, when highly expressed, was shown to lead to an inhibition of AR expression in PCA cell lines (Yu et al., 2010), which makes an inverse scenario in which *ERG* rearrangements result in high AR levels exceedingly unlikely. Hence, our data indicate a key role of androgen, and the AR, in mediating age-dependent genomic alterations characteristically observed in EO-PCA.

DISCUSSION

PCA is typically characterized by a prolonged clinical course with an estimated disease onset one to two decades prior to clinical diagnosis (Lilja et al., 2007). Our genomics data based on massively parallel DNA sequencing, comprising the largest number of PCA whole-genomes sequenced to date, show that most EO-PCAs involve an androgen-driven pathomechanism characterized by a marked absolute and relative abundance of DNA structural alterations involving androgen-regulated genes (“androgen-type prostate cancer”). Our data are consistent with a role of tumor onset, rather than tumor growth kinetics, in driving the early occurrence of androgen-type PCA.

It is tempting to speculate that this early development of androgen-type PCA may be driven by a particularly strong AR activation, eg, by high testosterone levels, associated with young patient age. It has previously been established that

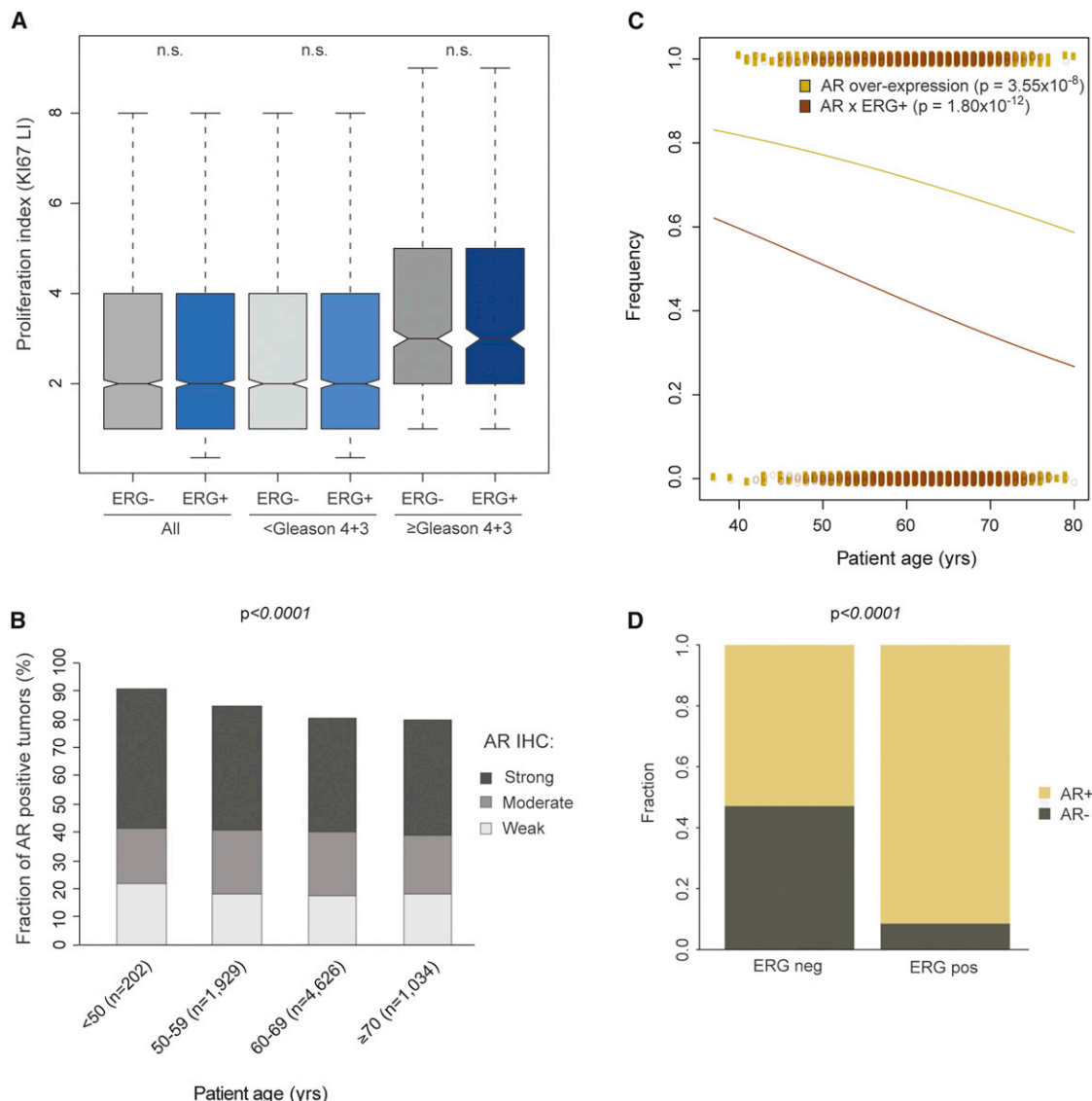


Figure 5. EO-PCA Is Associated with High AR levels

(A) Proliferation rates, measured by KI67 IHC staining, for high- and low-grade PCAs, and specifically for ERG positive (proxy for androgen-driven; $n = 2,888$) and ERG-negative tumors (proxy for nonandrogen-associated; $n = 3,095$). Low, Gleason grade $< 4+3$; High, Gleason grade $\geq 4+3$; KI67 Labeling Index, LI.

(B) Age-relationship of AR overexpression, detected as strong, moderate, or weak expression based on judgment of IHC staining intensity by an experienced pathologist (see [Supplemental Experimental Procedures](#)).

(C) Age-related interaction between AR overexpression and ERG rearranged tumors. Logistic regression of tumors with AR overexpression (yellow line, $n = 4,668$; $p = 3.55 \times 10^{-8}$), and tumors with both AR and ERG overexpression (AR \times ERG; frequency of tumors displaying both ERG and AR overexpression, red line, $n = 4,172$; $p = 1.80 \times 10^{-12}$; logistic regression).

(D) AR overexpression in ERG-positive and ERG-negative tumors ($n = 4,172$; p values based on Fisher's exact test). Boxplots in (A) display the 25th to 75th percentiles (boxes), medians (lines), and 1.5 times the interquartile range (whiskers). Notches show the 95% confidence interval of the median. n.s., not significant.

See also [Figure S4](#).

average serum testosterone levels in healthy men continuously decrease with age (Liu et al., 2007a; Mohr et al., 2005; [Figure S4B](#)) in a manner that remarkably parallels our observed age-associated decrease of ERG positivity in PCA. Furthermore, in vitro-data have demonstrated that the formation of ERG rearrangements can be induced by serum androgen levels in prostate epithelial cells (Lin et al., 2009a; Mani et al., 2009)

through a mechanism involving inter- or intra-chromosomal transcriptional hubs with co-recruitment of *TOP2B*, resulting in SR-inducing DNA double-strand breaks (Haffner et al., 2010; Lin et al., 2009a). Increased AR levels in young patients, which we established by in vivo measurements at diagnosis, provide further support to a crucial role of androgen in EO-PCA. In addition, the strong link seen between AR expression and

positive ERG status across all age groups, including patients older than 70 years suggests that high AR expression, and hence activity, may result in androgen-type PCA, with androgen-driven SRs irrespective of patient age.

Importantly, our finding of a specific pathomechanism driving EO-PCA may be of relevance for a tailored clinical management. Androgen-mediated rearrangements cause a complex androgen-associated modulation of transcriptional patterns and cellular pathways (Brase et al., 2011), with potential consequences for disease progression and response to androgen-ablative treatment in EO-PCA. Furthermore, cancer screening by detection of androgen-mediated rearrangements, eg, from biopsies, circulating tumor cells, or free circulating DNA, may be particularly effective in young men.

With over 200 PCA samples having already been subjected to exome sequencing (Barbieri et al., 2012; Grasso et al., 2012; Kumar et al., 2011), the identification of previously uncharacterized recurrent somatic SNVs affecting protein-coding regions is becoming exceedingly challenging. At the same time, approaches for clinical validation are becoming increasingly relevant. In this regard, our study shows the utility of evaluating genetic findings on large-scale TMAs containing thousands of samples. Moreover, our study emphasizes the power of whole-genomic sequencing, revealing information on mechanisms of SR formation by ascertaining genetic variants beyond those detectable by exome sequencing. Our genome-based findings on SR formation in conjunction with large-scale FISH and IHC-based assessment of ERG and AR enabled us to find a remarkable missing link in the relationship of the AR, somatic genome alterations, and PCA subtypes. In summary, our findings demonstrate striking age-dependent differences in the mechanistic landscapes of structural genomic alterations in a common cancer.

EXPERIMENTAL PROCEDURES

Patients

Informed consent and an ethical vote (institutional reviewing board) were obtained according to the current ICGC guidelines (see <http://www.icgc.org>). The patients did not receive any neo-adjuvant radiotherapy, androgen deprivation therapy, or chemotherapy prior to the surgical removal of tumor tissue. Tumor samples and one normal prostate control were frozen at -20°C and subsequently stored at -80°C .

DNA Library Preparation and Sequencing

DNA library preparation and whole-genome sequencing was performed on Illumina sequencers as described recently (Rausch et al., 2012a) with the raw length of the reads displaying a median of 101 bp for short paired-end insert-size libraries and 36 bp for large insert-size mate-pair libraries, and a median insert-size of the sequenced libraries of 155–206 bp (short insert-size paired-end), and 4,265–5,350 bp (large insert-size mate-pairs).

DNA Read Mapping and Sequence Variant Calling

Reads were aligned to the hg19 assembly of the human reference genome using the proprietary ELAND2 tool from Illumina, as well as the BWA tool (Li and Durbin, 2009). Post-processing of the aligned reads included merging of lane-level data and removal of duplicate read-pairs using Picard tools (<http://picard.sourceforge.net>). Only uniquely aligned reads were considered for downstream mutation analysis. Aligned reads were converted to the SAM/BAM format using SAMtools (Li et al., 2009), before initiating a set of complementary variant calling algorithms. We applied three distinct computational pipelines for SNV discovery, and subsequently kept SNV calls if

they were identified by at least two out of the three pipelines (Details and parameters are in the Supplemental Experimental Procedures). InDels were called using the Genome Analysis Toolkit (GATK) (DePristo et al., 2011) and SAMtools (Li et al., 2009) mpileup. Consensus InDels were manually inspected to identify potential misalignments. SRs ~ 200 bp to megabases in size were detected using the DELLY tool (Rausch et al., 2012b), as previously described (Rausch et al., 2012a), employing discordantly mapping read-pairs, split-read analysis (using an approach comparable to the soft-clipping functionality of CREST; Wang et al., 2011), as well as sequencing depth-of-coverage (for further details, see Supplemental Experimental Procedures). PCR verification and Sanger sequencing of sequence variants was performed as previously described (Rausch et al., 2012a). The False Discovery Rate (FDR) was obtained for randomly picked SNVs with a minor allele frequency (MAF) greater than 0.15 (to enable capillary sequencing-based data interpretation). We further validated a number of SNVs below 0.15 MAF (marked in gray in Table S3; see also Figure S1A).

mRNA Library Sequencing and Analysis

Strand-specific mRNA sequencing libraries were prepared from 10 μg of total RNA as recently described (Parkhomchuk et al., 2009). However, instead of shearing the cDNA, we fragmented the RNA PolyA⁺ fraction. The following modifications were implemented: the purified polyA⁺ RNA fraction was fragmented at 70°C for 5 min using RNA fragmentation reagents (Ambion, Cat. no. AM8740) and following the manufacturer instructions; the first strand synthesis was performed with random hexamers (dN)6 primers. Sequencing was carried out with 2×51 cycles on the Illumina HiSeq2000 instrument (further details are in the Supplemental Experimental Procedures). Reads were aligned to the hg19 genome assembly using BWA (0.5.9-r16) (Li and Durbin, 2009). For calculation of fusion gene expression values, RNA-seq-derived average exon RPKM values were extracted 5' and 3' to the breakpoint and a relative expression ratio was calculated after normalizing to the respective exon RPKM of the normal control. The minimum exon expression value was set to 1 RPKM. Further details are in the Supplemental Experimental Procedures.

Small RNA Sequencing and Analysis

Small RNAs (mainly miRNAs) up to 40 nt were size-fractionated on a polyacrylamide gel from up to 5 μg mRNA-depleted, DNase-treated (RNase-free DNase I, QIAGEN, Hilden, Germany) RNA. Small RNA libraries were prepared using the NEBNext Small RNA Sample Prep Set (NEB, Frankfurt/M., Germany) as described by the manufacturer, with some modifications (see Supplemental Experimental Procedures for details). Amplicons of ~ 90 –100 bp were sequenced on an Illumina HiSeq2000 instrument (read length: 50 bp) and mapped to the reference using the miRDeep2 package (Friedländer et al., 2012).

DNA Methylation Sequencing and Analysis

MCIp for enrichment of highly methylated DNA was performed as described previously (Gebhard et al., 2006) (see Supplemental Experimental Procedures for details). For deep-sequencing library preparation with highly methylated DNA, the NebNext chemistry (New England Biolabs, Ipswich, MA, USA) and barcoded adaptors compatible with the SOLiD sequencing platform were used. Single-end 50 bp reads were generated using the SOLiD 4 next-generation sequencing platform (Applied Biosystems, Life Technologies Corporation, Carlsbad, CA, USA). Mapped (software BFAST; Homer et al., 2009) and quality controlled reads were used to identify DMRs between tumor and normal (further details in the Supplemental Experimental Procedures).

Biallelic Inactivation Inference and Pathway Analysis

We scanned for genes inactivated in a biallelic fashion by extracting loci with two overlapping events, ie, germline or somatic homozygous nonsynonymous SNVs or an exon-disrupting deletion overlapping a second gene-disrupting aberration such as an SNV, deletion, inversion, or translocation. Genes within deletions were additionally required to have read-depth support. With estimated raw SNV allele frequencies ranging from 0.15 to 0.4, raw SV allele frequencies estimated to range from 0.20 to 0.45 and estimated tumor purities of ~ 0.5 , the vast majority of intersecting events (eg, a deletion overlapping a mutation, or gene disruption) occurred on different alleles in the same cell

Cancer Cell

Androgen-Driven Early-Onset Prostate Cancer

population (rather than representing subclonal events affecting different cell subpopulations). For carrying out the pathway enrichment analysis, fusion genes were extracted and analyzed by Genomatrix Genome Analyzer with standard parameters. The *p* values were adjusted for multiple-testing by controlling the FDR according to Benjamini and Hochberg.

PCA Tissue Microarray Resource

Details on the PCA prognosis TMA (earlier described in Schlörm et al., 2008) used for FISH and IHC analyses are in the Supplemental Experimental Procedures.

ERG Immunohistochemistry Analysis

ERG IHC using antibody ERG (clone EPR3864, dilution 1:450, Epitomics) was performed as previously described (Minner et al., 2011). See Supplemental Experimental Procedures for further details.

FISH Analysis

FISH analysis was performed as previously described before (Minner et al., 2011). Details on probes are in the Supplemental Experimental Procedures.

TMA Statistical Analysis

Logistic regression analyses were performed using the generalized linear model glm package in R. Statistical significance and fitness of the models were verified with the Wald test and likelihood ratio test.

ACCESSION NUMBERS

The European Genome-phenome archive database (hosted at the EBI) accession number for the short-read sequencing data reported in this paper is EGAS00001000258.

SUPPLEMENTAL INFORMATION

Supplemental Information includes four figures, seven tables, and Supplemental Experimental Procedures and can be found with this article online at <http://dx.doi.org/10.1016/j.ccr.2013.01.002>.

ACKNOWLEDGMENTS

We thank Anke Renter, Marion Bähr, Oliver Mücke, Andreas Schlattl, Anne Stranghöner, Christina Koop, Bettina Haase, and Dinko Pavlinic for assistance with experiments and Megumi Ohnishi-Seebacher for helpful comments. This project was supported by the German Federal Ministry of Education and Science in the program for medical genome research (FKZ: 01KU1001A, -B, -C, and -D). P.H. was supported by a stipend from the Alexander von Humboldt Foundation, and J.K. was additionally supported by the European Commission (Health-F2-2010-260791). The authors acknowledge assistance provided by sequencing and high-performance computational analysis centers at the Max Planck Institute for Molecular Genetics, German Cancer Research Center, and European Molecular Biology Laboratory.

Received: May 10, 2012

Revised: August 16, 2012

Accepted: January 3, 2013

Published: February 11, 2013

REFERENCES

Albertsen, P.C., Hanley, J.A., and Fine, J. (2005). 20-year outcomes following conservative management of clinically localized prostate cancer. *JAMA* 293, 2095–2101.

Barbieri, C.E., Baca, S.C., Lawrence, M.S., Demichelis, F., Blattner, M., Theurillat, J.P., White, T.A., Stojanov, P., Van Allen, E., Stransky, N., et al. (2012). Exome sequencing identifies recurrent SPOP, FOXA1 and MED12 mutations in prostate cancer. *Nat. Genet.* 44, 685–689.

Bastus, N.C., Boyd, L.K., Mao, X., Stankiewicz, E., Kudahetti, S.C., Oliver, R.T.D., Berney, D.M., and Lu, Y.J. (2010). Androgen-induced TMPRSS2:ERG fusion in nonmalignant prostate epithelial cells. *Cancer Res.* 70, 9544–9548.

Berger, M.F., Lawrence, M.S., Demichelis, F., Drier, Y., Cibulskis, K., Sivachenko, A.Y., Sboner, A., Esquivela, R., Pflueger, D., Sougnez, C., et al. (2011). The genomic complexity of primary human prostate cancer. *Nature* 470, 214–220.

Brase, J.C., Johannes, M., Mannsperger, H., Fälth, M., Metzger, J., Kacprzyk, L.A., Andrasiuk, T., Gade, S., Meister, M., Sirma, H., et al. (2011). TMPRSS2-ERG -specific transcriptional modulation is associated with prostate cancer biomarkers and TGF- β signaling. *BMC Cancer* 11, 507.

Bubendorf, L., Sauter, G., Moch, H., Schmid, H.P., Gasser, T.C., Jordan, P., and Mihatsch, M.J. (1996). Ki67 labelling index: an independent predictor of progression in prostate cancer treated by radical prostatectomy. *J. Pathol.* 178, 437–441.

Campbell, P.J., Stephens, P.J., Pleasance, E.D., O'Meara, S., Li, H., Santarius, T., Stebbings, L.A., Leroy, C., Edkins, S., Hardy, C., et al. (2008). Identification of somatically acquired rearrangements in cancer using genome-wide massively parallel paired-end sequencing. *Nat. Genet.* 40, 722–729.

DePristo, M.A., Banks, E., Poplin, R., Garimella, K.V., Maguire, J.R., Hartl, C., Philippakis, A.A., del Angel, G., Rivas, M.A., Hanna, M., et al. (2011). A framework for variation discovery and genotyping using next-generation DNA sequencing data. *Nat. Genet.* 43, 491–498.

Friedländer, M.R., Mackowiak, S.D., Li, N., Chen, W., and Rajewsky, N. (2012). miRDeep2 accurately identifies known and hundreds of novel microRNA genes in seven animal clades. *Nucleic Acids Res.* 40, 37–52.

Futreal, P.A., Coin, L., Marshall, M., Down, T., Hubbard, T., Wooster, R., Rahman, N., and Stratton, M.R. (2004). A census of human cancer genes. *Nat. Rev. Cancer* 4, 177–183.

Gebhard, C., Schwarzfischer, L., Pham, T.H., Schilling, E., Klug, M., Andreesen, R., and Rehli, M. (2006). Genome-wide profiling of CpG methylation identifies novel targets of aberrant hypermethylation in myeloid leukemia. *Cancer Res.* 66, 6118–6128.

Godoy, A.S., Sotomayor, P.C., Villagran, M., Yacoub, R., Montecinos, V.P., McNerney, E.M., Moser, M., Foster, B.A., and Onate, S.A. (2012). Altered corepressor SMRT expression and recruitment to target genes as a mechanism that change the response to androgens in prostate cancer progression. *Biochem. Biophys. Res. Commun.* 423, 564–570.

Grasso, C.S., Wu, Y.M., Robinson, D.R., Cao, X., Dhanasekaran, S.M., Khan, A.P., Quist, M.J., Jing, X., Lonigro, R.J., Brenner, J.C., et al. (2012). The mutational landscape of lethal castration-resistant prostate cancer. *Nature* 487, 239–243.

Grönberg, H. (2003). Prostate cancer epidemiology. *Lancet* 361, 859–864.

Haffner, M.C., Aryee, M.J., Toubaji, A., Esopi, D.M., Albadini, R., Gurel, B., Isaacs, W.B., Bova, G.S., Liu, W., Xu, J., et al. (2010). Androgen-induced TOP2B-mediated double-strand breaks and prostate cancer gene rearrangements. *Nat. Genet.* 42, 668–675.

Heidenreich, A., Bellmunt, J., Bolla, M., Joniau, S., Mason, M., Matveev, V., Mottet, N., Schmid, H.P., van der Kwast, T., Wiegel, T., and Zattoni, F.; European Association of Urology. (2011). EAU guidelines on prostate cancer. Part 1: screening, diagnosis, and treatment of clinically localised disease. *Eur. Urol.* 59, 61–71.

Hodgson, M.C., Astapova, I., Cheng, S., Lee, L.J., Verhoeven, M.C., Choi, E., Balk, S.P., and Hollenberg, A.N. (2005). The androgen receptor recruits nuclear receptor CoRepressor (N-CoR) in the presence of mifepristone via its N and C termini revealing a novel molecular mechanism for androgen receptor antagonists. *J. Biol. Chem.* 280, 6511–6519.

Homer, N., Merriman, B., and Nelson, S.F. (2009). BFAS: an alignment tool for large scale genome resequencing. *PLoS ONE* 4, e7767.

Huang, S., Gulzar, Z.G., Salari, K., Lapointe, J., Brooks, J.D., and Pollack, J.R. (2012). Recurrent deletion of CHD1 in prostate cancer with relevance to cell invasiveness. *Oncogene* 31, 4164–4170.

- Knudsen, B.S., and Vasioukhin, V. (2010). Mechanisms of prostate cancer initiation and progression. *Adv. Cancer Res.* 109, 1–50.
- Knudson, A.G.J., Jr. (1971). Mutation and cancer: statistical study of retinoblastoma. *Proc. Natl. Acad. Sci. USA* 68, 820–823.
- Krohn, A., Diedler, T., Burkhardt, L., Mayer, P.S., De Silva, C., Meyer-Kornblum, M., Kötschau, D., Tennstedt, P., Huang, J., Gerhäuser, C., et al. (2012). Genomic deletion of PTEN is associated with tumor progression and early PSA recurrence in ERG fusion-positive and fusion-negative prostate cancer. *Am. J. Pathol.* 181, 401–412.
- Kumar, A., White, T.A., MacKenzie, A.P., Clegg, N., Lee, C., Dumpit, R.F., Coleman, I., Ng, S.B., Salipante, S.J., Rieder, M.J., et al. (2011). Exome sequencing identifies a spectrum of mutation frequencies in advanced and lethal prostate cancers. *Proc Natl Acad Sci. USA* 108, 17087–17092.
- Lee, D.K., and Chang, C. (2003). Endocrine mechanisms of disease: Expression and degradation of androgen receptor: mechanism and clinical implication. *J. Clin. Endocrinol. Metab.* 88, 4043–4054.
- Ley, T.J., Mardis, E.R., Ding, L., Fulton, B., McLellan, M.D., Chen, K., Dooling, D., Dunford-Shore, B.H., McGrath, S., Hickenbotham, M., et al. (2008). DNA sequencing of a cytogenetically normal acute myeloid leukaemia genome. *Nature* 456, 66–72.
- Li, H., and Durbin, R. (2009). Fast and accurate short read alignment with Burrows-Wheeler transform. *Bioinformatics* 25, 1754–1760.
- Li, H., Handsaker, B., Wysoker, A., Fennell, T., Ruan, J., Homer, N., Marth, G., Abecasis, G., and Durbin, R.; 1000 Genome Project Data Processing Subgroup. (2009). The Sequence Alignment/Map format and SAMtools. *Bioinformatics* 25, 2078–2079.
- Lilja, H., Ulmert, D., Björk, T., Becker, C., Serio, A.M., Nilsson, J.A., Abrahamsson, P.A., Vickers, A.J., and Berglund, G. (2007). Long-term prediction of prostate cancer up to 25 years before diagnosis of prostate cancer using prostate kallikreins measured at age 44 to 50 years. *J. Clin. Oncol.* 25, 431–436.
- Lin, C., Yang, L., Tanasa, B., Hutt, K., Ju, B.G., Ohgi, K., Zhang, J., Rose, D.W., Fu, X.D., Glass, C.K., and Rosenfeld, M.G. (2009a). Nuclear receptor-induced chromosomal proximity and DNA breaks underlie specific translocations in cancer. *Cell* 139, 1069–1083.
- Lin, D.W., Porter, M., and Montgomery, B. (2009b). Treatment and survival outcomes in young men diagnosed with prostate cancer: a Population-based Cohort Study. *Cancer* 115, 2863–2871.
- Liu, P.Y., Beilin, J., Meier, C., Nguyen, T.V., Center, J.R., Leedman, P.J., Seibel, M.J., Eisman, J.A., and Handelsman, D.J. (2007a). Age-related changes in serum testosterone and sex hormone binding globulin in Australian men: longitudinal analyses of two geographically separate regional cohorts. *J. Clin. Endocrinol. Metab.* 92, 3599–3603.
- Liu, W., Chang, B.L., Cramer, S., Koty, P.P., Li, T., Sun, J., Turner, A.R., Von Kap-Herr, C., Bobby, P., Rao, J., et al. (2007b). Deletion of a small consensus region at 6q15, including the MAP3K7 gene, is significantly associated with high-grade prostate cancers. *Clin. Cancer Res.* 13, 5028–5033.
- Mani, R.S., Tomlins, S.A., Callahan, K., Ghosh, A., Nyati, M.K., Varambally, S., Palanisamy, N., and Chinnaiyan, A.M. (2009). Induced chromosomal proximity and gene fusions in prostate cancer. *Science* 326, 1230.
- Minner, S., Enodien, M., Sirma, H., Luebke, A.M., Krohn, A., Mayer, P.S., Simon, R., Tennstedt, P., Müller, J., Scholz, L., et al. (2011). ERG status is unrelated to PSA recurrence in radically operated prostate cancer in the absence of antihormonal therapy. *Clin. Cancer Res.* 17, 5878–5888.
- Mohr, B.A., Guay, A.T., O'Donnell, A.B., and McKinlay, J.B. (2005). Normal, bound and nonbound testosterone levels in normally ageing men: results from the Massachusetts Male Ageing Study. *Clin. Endocrinol. (Oxf.)* 62, 64–73.
- Parker, C., Muston, D., Melia, J., Moss, S., and Dearnaley, D. (2006). A model of the natural history of screen-detected prostate cancer, and the effect of radical treatment on overall survival. *Br. J. Cancer* 94, 1361–1368.
- Parkhomchuk, D., Borodina, T., Amstislavskiy, V., Banaru, M., Hallen, L., Krobitsch, S., Lehrach, H., and Soldatov, A. (2009). Transcriptome analysis by strand-specific sequencing of complementary DNA. *Nucleic Acids Res.* 37, e123.
- Rausch, T., Jones, D.T., Zapatka, M., Stütz, A.M., Zichner, T., Weischenfeldt, J., Jäger, N., Remke, M., Shih, D., Northcott, P.A., et al. (2012a). Genome sequencing of pediatric medulloblastoma links catastrophic DNA rearrangements with TP53 mutations. *Cell* 148, 59–71.
- Rausch, T., Zichner, T., Schlattl, A., Stütz, A.M., Benes, V., and Korbel, J.O. (2012b). DELLY: structural variant discovery by integrated paired-end and split-read analysis. *Bioinformatics* 28, i333–i339.
- Reid, A.H., Attard, G., Brewer, D., Miranda, S., Riisnaes, R., Clark, J., Hylands, L., Merson, S., Vergis, R., Jameson, C., et al. (2012). Novel, gross chromosomal alterations involving PTEN cooperate with allelic loss in prostate cancer. *Mod. Pathol.* 25, 902–910.
- Rubin, M.A., Maher, C.A., and Chinnaiyan, A.M. (2011). Common gene rearrangements in prostate cancer. *J. Clin. Oncol.* 29, 3659–3668.
- Ryan, C.J., Elkin, E.P., Cowan, J., and Carroll, P.R. (2007). Initial treatment patterns and outcome of contemporary prostate cancer patients with bone metastases at initial presentation: data from CaPSURE. *Cancer* 110, 81–86.
- Schlomm, T., Iwers, L., Kirstein, P., Jessen, B., Köllermann, J., Minner, S., Passow-Drolet, A., Mirlacher, M., Milde-Langosch, K., Graefen, M., et al. (2008). Clinical significance of p53 alterations in surgically treated prostate cancers. *Mod. Pathol.* 21, 1371–1378.
- Siegel, R., Naishadham, D., and Jemal, A. (2012). Cancer statistics, 2012. *CA Cancer J. Clin.* 62, 10–29.
- Stratton, M.R., Campbell, P.J., and Futreal, P.A. (2009). The cancer genome. *Nature* 458, 719–724.
- Sultan, M., Schulz, M.H., Richard, H., Magen, A., Klingenhoff, A., Scherf, M., Seifert, M., Borodina, T., Soldatov, A., Parkhomchuk, D., et al. (2008). A global view of gene activity and alternative splicing by deep sequencing of the human transcriptome. *Science* 321, 956–960.
- Sun, J., Liu, W., Adams, T.S., Sun, J., Li, X., Turner, A.R., Chang, B., Kim, J.W., Zheng, S.L., Isaacs, W.B., et al. (2007). DNA copy number alterations in prostate cancers: a combined analysis of published CGH studies. *Prostate* 67, 692–700.
- Taylor, B.S., Schultz, N., Hieronymus, H., Gopalan, A., Xiao, Y., Carver, B.S., Arora, V.K., Kaushik, P., Cerami, E., Reva, B., et al. (2010). Integrative genomic profiling of human prostate cancer. *Cancer Cell* 18, 11–22.
- Tomlins, S.A., Rhodes, D.R., Perner, S., Dhanasekaran, S.M., Mehra, R., Sun, X.-W., Varambally, S., Cao, X., Tchinda, J., Kuefer, R., et al. (2005). Recurrent fusion of TMPRSS2 and ETS transcription factor genes in prostate cancer. *Science* 310, 644–648.
- Tomlins, S.A., Laxman, B., Dhanasekaran, S.M., Helgeson, B.E., Cao, X., Morris, D.S., Menon, A., Jing, X., Cao, Q., Han, B., et al. (2007). Distinct classes of chromosomal rearrangements create oncogenic ETS gene fusions in prostate cancer. *Nature* 448, 595–599.
- Urbanucci, A., Sahu, B., Seppälä, J., Larjo, A., Latonen, L.M., Waltering, K.K., Tammela, T.L., Vessella, R.L., Lähdesmäki, H., Jänne, O.A., and Visakorpi, T. (2012). Overexpression of androgen receptor enhances the binding of the receptor to the chromatin in prostate cancer. *Oncogene* 31, 2153–2163.
- Wang, J., Mullighan, C.G., Easton, J., Roberts, S., Heatley, S.L., Ma, J., Rusch, M.C., Chen, K., Harris, C.C., Ding, L., et al. (2011). CREST maps somatic structural variation in cancer genomes with base-pair resolution. *Nat. Methods* 8, 652–654.
- Xi, R., Hadjipanayis, A.G., Luquette, L.J., Kim, T.M., Lee, E., Zhang, J., Johnson, M.D., Muzny, D.M., Wheeler, D.A., Gibbs, R.A., et al. (2011). Copy number variation detection in whole-genome sequencing data using the Bayesian information criterion. *Proc. Natl. Acad. Sci. USA* 108, E1128–E1136.
- Yang, X., Chen, M.W., Terry, S., Vacherot, F., Bemis, D.L., Capodice, J., Kitajewski, J., de la Taille, A., Benson, M.C., Guo, Y., and Buttyan, R. (2006). Complex regulation of human androgen receptor expression by Wnt signaling in prostate cancer cells. *Oncogene* 25, 3436–3444.
- Yu, J., Yu, J., Mani, R.S., Cao, Q., Brenner, C.J., Cao, X., Wang, X., Wu, L., Li, J., Hu, M., et al. (2010). An integrated network of androgen receptor, polycomb, and TMPRSS2-ERG gene fusions in prostate cancer progression. *Cancer Cell* 17, 443–454.

Endothelial Cells Promote the Colorectal Cancer Stem Cell Phenotype through a Soluble Form of Jagged-1

Jia Lu,¹ Xiangcang Ye,¹ Fan Fan,¹ Ling Xia,¹ Rajat Bhattacharya,¹ Seth Bellister,² Federico Tozzi,² Eric Sceusi,² Yunfei Zhou,¹ Isamu Tachibana,¹ Dipen M. Maru,³ David H. Hawke,³ Janusz Rak,⁶ Sendurai A. Mani,⁴ Patrick Zweidler-McKay,⁵ and Lee M. Ellis^{1,2,*}

¹Department of Cancer Biology

²Department of Surgical Oncology

³Department of Pathology

⁴Department of Translational Molecular Pathology

⁵Department of Pediatrics

The University of Texas M.D. Anderson Cancer Center, Houston, TX 77030, USA

⁶Montreal Children's Hospital Research Institute, McGill University, Montreal, Quebec H3Z 2Z3, Canada

*Correspondence: lellis@mdanderson.org

<http://dx.doi.org/10.1016/j.ccr.2012.12.021>

SUMMARY

We report a paracrine effect whereby endothelial cells (ECs) promote the cancer stem cell (CSC) phenotype of human colorectal cancer (CRC) cells. We showed that, without direct cell-cell contact, ECs secrete factors that promoted the CSC phenotype in CRC cells via Notch activation. In human CRC specimens, CD133 and Notch intracellular domain-positive CRC cells colocalized in perivascular regions. An EC-derived, soluble form of Jagged-1, via ADAM17 proteolytic activity, led to Notch activation in CRC cells in a paracrine manner; these effects were blocked by immunodepletion of Jagged-1 in EC-conditioned medium or blockade of ADAM17 activity. Collectively, ECs play an active role in promoting Notch signaling and the CSC phenotype by secreting soluble Jagged-1.

INTRODUCTION

Colorectal cancer (CRC) is the second-leading cause of cancer death in the United States, with ~50,000 patients dying each year as a result of metastatic disease that is refractory to systemic therapy (American Cancer Society, 2010; Davies and Goldberg, 2008, 2011). Although there are now six Food and Drug Administration approved drugs for the treatment of metastatic CRC, median overall survival remains less than 2 years (Davies and Goldberg, 2011). Targeted therapies, including anti-angiogenic therapies, have not dramatically improved clinical outcomes of patients with metastatic CRC (Saltz et al., 2008). A better understanding of the biology of CRC is imperative for the development of more effective therapeutic approaches that can benefit patients with CRC.

There is evidence for the existence of cancer stem cells (CSCs) in CRC (Barker et al., 2009; Du et al., 2008; Huang et al., 2009; O'Brien et al., 2007; Ricci-Vitiani et al., 2007). Because of the intrinsic stem cell-like properties of CSCs, this subpopulation of tumor cells is believed to not only initiate and sustain tumor growth but also mediate chemoresistance (Al-Hajj, 2007; Wicha et al., 2006). Notably, a number of studies suggest that CSCs exist in a state of flux and the CSC phenotype can be enhanced by microenvironmental influences (Butler et al., 2010a; Rosen and Jordan, 2009). Therefore, the development of CSC- and/or microenvironment-targeting strategies that could eliminate the CSC population is critical for improving the clinical outcomes of patients with CRC.

Several groups have reported that tumor progenitor cells reside in perivascular niches in certain types of cancers (Butler

Significance

We found that endothelial cell (EC)-derived soluble factors enhance the cancer stem cell (CSC) phenotype and chemoresistance of colorectal cancer (CRC) cells. This suggests that ECs in the tumor microenvironment are more than simply conduits for blood flow—they also actively secrete factors that promote tumor cell survival and growth. We further defined a soluble, ADAM17-cleaved form of Jagged-1 in EC-conditioned medium that activates Notch signaling and promotes the CSC phenotype in CRC cells. Identification of this mechanism, by which the tumor microenvironment can promote the CSC phenotype, should provide the foundation for more refined targeted therapies for the treatment of both early- and late-stage malignancies.

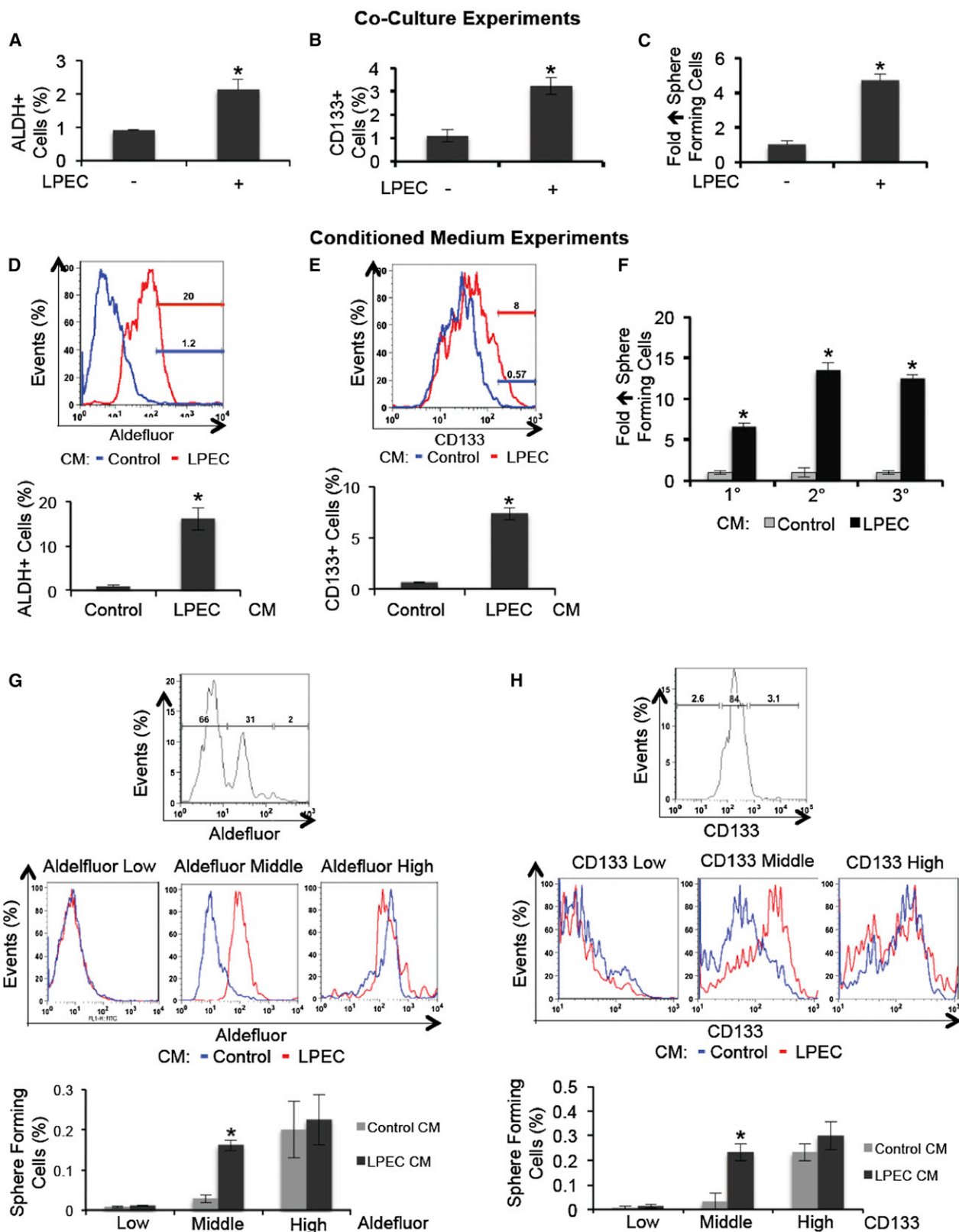


Figure 1. Endothelial Cells Promote the CSC Phenotype in CRC Cells In Vitro

(A) Freshly isolated xenografted human CRC (xhCRC) cells were cocultured with freshly isolated human liver parenchyma endothelial cells (LPECs), and the Aldefluor-positive xhCRC cell population was determined.

(legend continued on next page)

et al., 2010a; Calabrese et al., 2007; Krishnamurthy et al., 2010). Whether perivascular niches of CSCs exist in other solid tumors, including CRCs, is yet unclear. More importantly, how ECs function to establish and maintain tumor-initiating-cell niches remains to be further elucidated. Understanding the mechanisms by which ECs promote the CSC phenotype will provide the foundation for the development of novel and refined CSC-targeting approaches. The purpose of this study was to understand the role of ECs in mediating the CSC phenotype of CRC cells and the mechanism by which this occurs.

RESULTS

Coculture with ECs Promotes the Cancer Stem Cell Phenotype of CRC Cells

In order to understand tumor-EC cross-talk, and particularly the potential role of ECs in promoting the CSC phenotype of CRC cells, we first conducted a coculture experiment. We used freshly isolated human CRC cells from surgical specimens after establishing a first passage xenograft in mice (xhCRC) to expand the number of cells. We also used freshly isolated liver parenchyma ECs (LPECs) labeled with GFP-Luc or mCherry in tissue culture. After coculture for three days, xhCRC cells were isolated by fluorescence-activated cell sorting (FACS) and were analyzed for potential enrichment of the population with CSC characteristics. As shown in Figure 1A, coculture with LPECs increased the fraction of xhCRC cells that were Aldefluor positive, a population presumably enriched for CSCs (Huang et al., 2009). Similarly, coculture of LPECs with CRC cells increased the percentage of cells that were CD133 positive (Figure 1B). Coculture with LPECs also increased the percentage of xhCRC cells with in vitro sphere-forming ability (4-fold; $p < 0.05$; Figure 1C). Collectively, these data suggest that ECs could promote the CSC phenotype of cocultured CRC cells ex vivo. Similar results were also obtained from in vitro experiments with the established human CRC cell line HCT116 and immortalized human umbilical vein endothelial cell line RF24 (Figures S1A and S1B available online).

Endothelial Cell-Conditioned Medium Promotes the Cancer Stem Cell Phenotype of CRC Cells

To determine whether the effect observed above required direct cell-cell contact or whether it is mediated by soluble factors secreted by ECs, we cultured freshly isolated human CRC (hCRC) cells in conditioned medium obtained from freshly isolated LPECs, or control medium (MEM containing 1% FBS);

after exposure to the CM, hCRC cells were analyzed for the CSC phenotype. Compared to control medium, LPEC CM enriched the Aldefluor-positive hCRC cell population by 16-fold (Figure 1D) and enriched the CD133-positive hCRC cell population by 7-fold (Figure 1E), after 72 hr treatment. In addition, LPEC CM treatment also increased sphere-forming capability of hCRC cells by over 6-fold (Figure 1F). Upon serial passaging, hCRC cells treated with LPEC CM demonstrated significantly greater capability (10–15-fold increase) to form secondary and tertiary tumor spheres (Figure 1F). We were able to obtain similar results from established CRC cell lines (HCT116 and HT29) treated with CM collected from established endothelial cell lines (RF24 and HDMECs) or LPECs (Figures S1C and S1D). As important controls, CM obtained from freshly isolated human CRC cells, established CRC cell lines (HCT116 and HT29), or fibroblasts were not able to significantly enrich the CSC population in CRC cells (data not shown). Taken together, these data suggest that EC-derived soluble factor(s) can promote the CSC phenotype of CRC cells in a paracrine manner.

We next sought to understand whether ECs promote the colorectal CSC phenotype either by converting a subset of CRC cells into CSCs or by expanding the CSC population. We sorted xhCRC cells by the Aldefluor assay and treated Aldefluor-high, -middle, and -low fractions with LPEC CM in parallel; the Aldefluor assay was repeated and sphere forming assay was performed to determine which ALDH population could be enriched for CSCs by EC CM. Interestingly, we found that the CSC population enrichment only occurred in the Aldefluor-middle population, but not in Aldefluor-high (presumably CSCs) or -low populations (presumably terminally differentiated cells) (Figure 1G). Similar results were obtained using another colorectal CSC marker, CD133, as the readout (Figure 1H). These data suggest that the EC CM-mediated promotion of the CSC phenotype is primarily achieved in nonstem CRC cells that retain cellular plasticity. We also assessed levels of intestinal differentiation marker expression using quantitative reverse transcription polymerase chain reaction (q-RT-PCR) and found that LPEC CM treatment significantly reduced the expression of Keratin 20 (*KRT20*) by 8-fold in hCRC cells (Figure S1E). In addition, we tested the expression levels of additional differentiation markers, ANPEP and PRSS7, and found that their expression levels, although easily detectable by qRT-PCR in cells treated with control CM, were not detectable in the LPEC CM treated group. These findings indicate that LPEC CM promotes the colorectal CSC phenotype by inducing dedifferentiation in a subset of nonstem CRC cells.

(B) Freshly isolated xhCRC cells were cocultured with freshly isolated LPECs, and the CD133-positive xhCRC cell population was determined.

(C) Freshly isolated xhCRC cells were cocultured with freshly isolated LPECs, and the xhCRC sphere-forming assay was performed.

(D) Freshly isolated human CRC (hCRC) cells were treated with LPEC-derived conditioned medium (CM), and the Aldefluor-positive cell population was determined.

(E) Freshly isolated human CRC (hCRC) cells were treated with LPEC-derived conditioned medium (CM), and the CD133-positive cell population was determined.

(F) Sphere-forming capability in 1st, 2nd, and 3rd cultures of freshly isolated hCRC cells treated with LPEC CM.

(G) xhCRC cells were FAC-sorted by the Aldefluor assay into high, middle, and low cell populations (upper panel). The Aldefluor-high, -middle, and -low cell populations were treated with LPEC CM in parallel; the Aldefluor assay was then repeated (middle panel) and sphere forming assay was performed (lower panel) to determine which ALDH fraction could be enriched for CSCs by EC CM.

(H) xhCRC cells were FAC-sorted for high, middle, and low CD133 expression (upper panel). The CD133-high, -middle, and -low fractions were treated with LPEC CM in parallel; the flow cytometry analysis on CD133 was then repeated (middle panel) and sphere forming assay was performed (lower panel) to determine which CD133 fraction could be enriched for CSCs by EC CM.

* $p < 0.05$, mean \pm SEM. See also Figure S1.

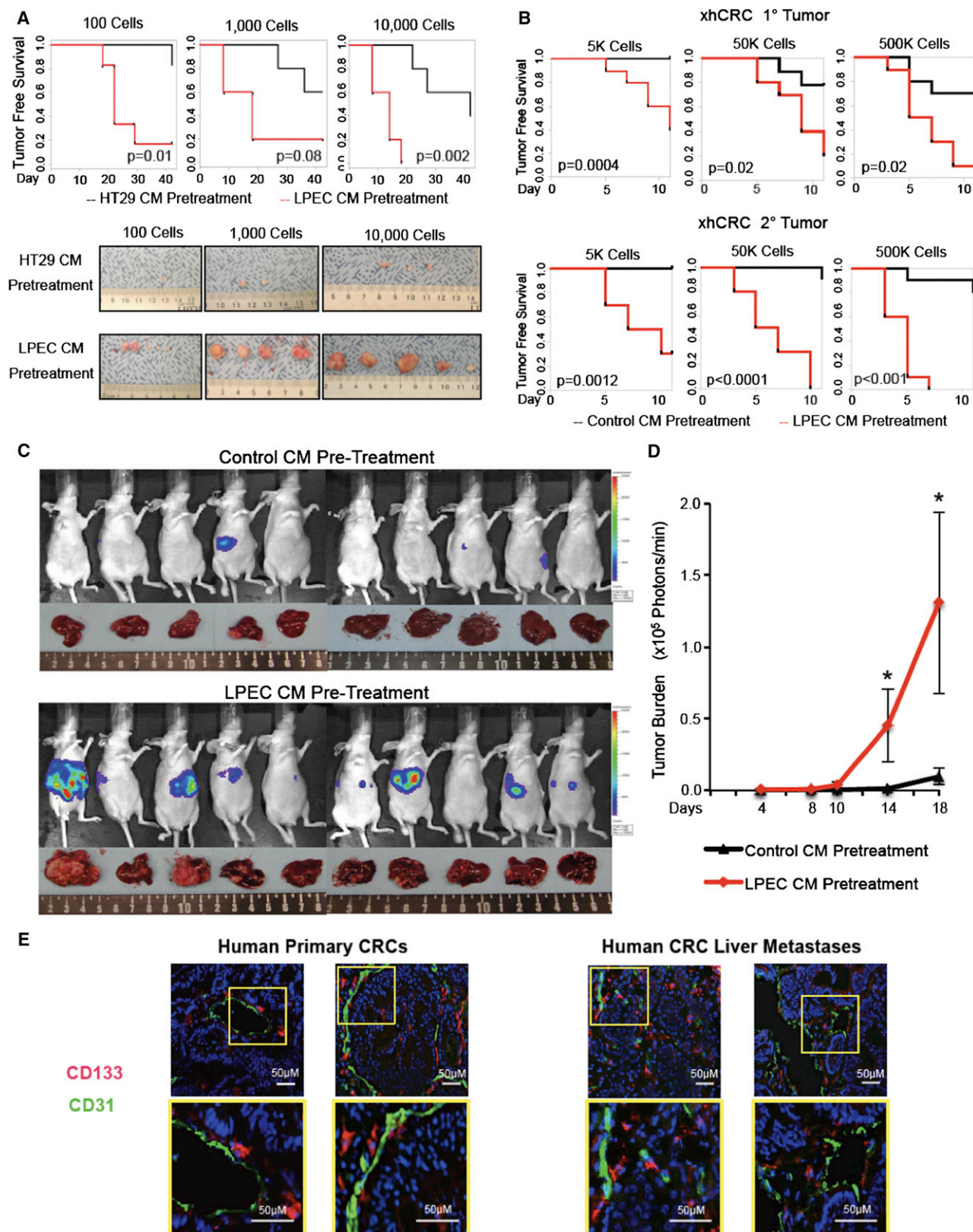


Figure 2. Endothelial Cells Promote the CSC Phenotype of CRC Cells In Vivo

(A) In vivo tumorigenicity assay with limited dilution using HT29 cells pretreated with control CM or LPEC CM.

(legend continued on next page)

Endothelial Cell-Conditioned Medium Promotes Tumorigenicity and Metastasis of CRC Cells In Vivo

A critical experiment for determining the CSC phenotype is the in vivo tumorigenicity assay by serial dilution (Clarke et al., 2006). Therefore, we sought to validate our in vitro findings by using an in vivo model. To this end, CRC cells pretreated with either EC CM or control CM were serially diluted and injected subcutaneously into mice, and tumorigenicity was determined. LPEC CM-pretreated HT29 cells led to earlier tumor formation, as well as greater tumor incidence and growth, compared with control (HT29 CM pretreated) cells (Figure 2A). Similar results were obtained when we compared the effect of RF24 CM on HCT116 tumorigenicity (data not shown). We further extended our study using serial passaging of cells in xenograft experiments with freshly isolated xenografted hCRC (xhCRC) cells, combined with limited dilution, and found that xhCRC cells pretreated with LPEC CM demonstrated significantly increased tumorigenicity compared with those pretreated with control medium, in both primary and secondary xenografts (Figure 2B).

We also investigated the effect of EC CM on the metastatic potential of CRC cells. First we employed a tail vein injection experiment, and found that, compared to control (HCT116 CM treated) cells, RF24 CM-treated HCT116 CRC cells formed significantly more metastases (Figures S2A and S2B). We then used a splenic injection model to induce liver metastasis, the most common site of CRC metastasis. Compared with xhCRC cells treated with control medium, xhCRC cells treated with LPEC CM demonstrated an increased incidence of liver metastasis (nine of ten in the LPEC CM pretreatment group, compared with three of ten in the control group; $p < 0.05$) (Figure 2C) and a significantly increased tumor burden, as demonstrated by an increase in luciferase activity (Figure 2D) and a 57% increase in liver weight (photographs in Figure 2C) (Figure S2C; $p < 0.05$). Collectively, these data demonstrated that EC-derived soluble factor(s) promote the metastatic potential of CRC cells injected in the spleen.

CD133-Positive CRC Cells Are Located Adjacent to ECs in Human Surgical Specimens

Having established that ECs secrete soluble factors to enrich CRC cells with CSC phenotype, we sought to determine whether CRC cells that express the CSC marker CD133 are located in the perivascular regions in human CRC surgical specimens. Immunofluorescent staining for CD133 and CD31 (endothelial cell marker) was carried out in primary colon cancer specimens and chemotherapy-naïve human CRC liver metastases. CD133 staining identified CRC cells that were located in proximity to CD31-positive ECs (Figure 2E). Further staining confirmed that these CD133-positive cells were not pericytes or stroma cells because CD133 staining did not costain with desmin (a pericyte marker) (Figure S2D), nor did they costain with smooth muscle actin (a marker of stroma and pericytes), CD3 (a marker of

T cells and lymphocytes), CD68 (a marker of monocytes and macrophages), or myeloperoxidase (a marker of myeloid cells) (Figures S2E–S2H). In addition, we costained with antibodies to CD133 and EPCAM (an epithelial marker) and demonstrated colocalization of these markers (Figure S2I). Cumulatively, these immune-staining data show that, in clinical specimens, the CD133-positive cells are epithelial but not stromal in origin. These data showed that colorectal CSCs are located adjacent to tumor vasculature, and this is consistent with our preclinical data that ECs can mediate the colorectal CSC phenotype.

Endothelial Cell-Conditioned Medium Promotes Chemoresistance of CRC Cells

Preclinical studies suggest that CSCs possess intrinsic properties that mediate their resistance to chemotherapy (Al-Hajj, 2007; Dallas et al., 2009; Wicha et al., 2006). We therefore hypothesized that CRC cells pretreated with EC CM would exhibit resistance to chemotherapeutic agents. To test this hypothesis, HCT116 CRC cells were exposed to oxaliplatin (2 μ M) or 5-fluorouracil (5-FU, 2 μ g/ml) in RF24 CM or control medium for 96 hr; chemosensitivity was determined by MTT assay. Compared with cells that were pretreated with control medium, HCT116 cultured in RF24 CM demonstrated a significantly higher survival rate after oxaliplatin or 5-FU treatment (~3 fold) (Figure 3A). Similarly, LPEC CM treatment for 72 hr led to chemoresistance of xhCRC cells (Figure 3C). To further validate the chemoprotective effect of EC CM on tumor cells, chemotherapy-induced apoptosis in HCT116 cells was assessed after the cells were treated with chemotherapy while cultured in EC CM or control HCT116 CM for 48 hr. Annexin V staining demonstrated a significant decrease of apoptotic events in the HCT116 cells treated with oxaliplatin or 5-FU while cultured in LPEC CM (28% to 6% with oxaliplatin treatment, and 43% to 15% with 5-FU treatment, respectively; data not shown). Western blot analysis showed lower levels of cleaved poly ADP-ribose polymerase (PARP) and cleaved Caspase 3 in HCT116 cells treated with oxaliplatin or 5-FU while cultured in RF24 CM compared to control CM (Figure 3B). Similar results were observed in xhCRC treated with 5-FU while cultured in LPEC CM (Figure 3D).

Endothelial Cell-Conditioned Medium Activates the Notch Pathway in CRC Cells In Vitro

To understand the underlying mechanism by which EC CM promotes the CSC phenotype of CRC cells, we sought to examine the activation of canonical CSC pathways such as Notch (Katoh and Katoh, 2007), Wnt/beta-catenin (Vermeulen et al., 2010), and Sonic hedgehog (Saif and Chu, 2010) in CRC cells treated with EC CM. To this end, we infected HT29 cells with a lentivirus containing a Hes-1 promoter-driven reporter (Jarriault et al., 1995), TCF reporter, or a Gli reporter (Lingala et al., 2009), and treated the cells with LPEC CM or control

(B) In vivo tumorigenicity assay with limited dilution combined with serial transplantation using freshly isolated xhCRC cells pretreated with control CM or LPEC CM. (C and D) Hepatic metastatic incidence and burden of xhCRC cells pretreated with control CM or LPEC CM in a splenic injection model (* $p < 0.05$, mean \pm SEM). (E) Representative immunofluorescent staining of CD133 and CD31 in human primary CRC surgical specimens (left panel), and human CRC liver metastases (right panel). The highlighted regions in the upper panels are enlarged in the lower panels. See also Figure S2.

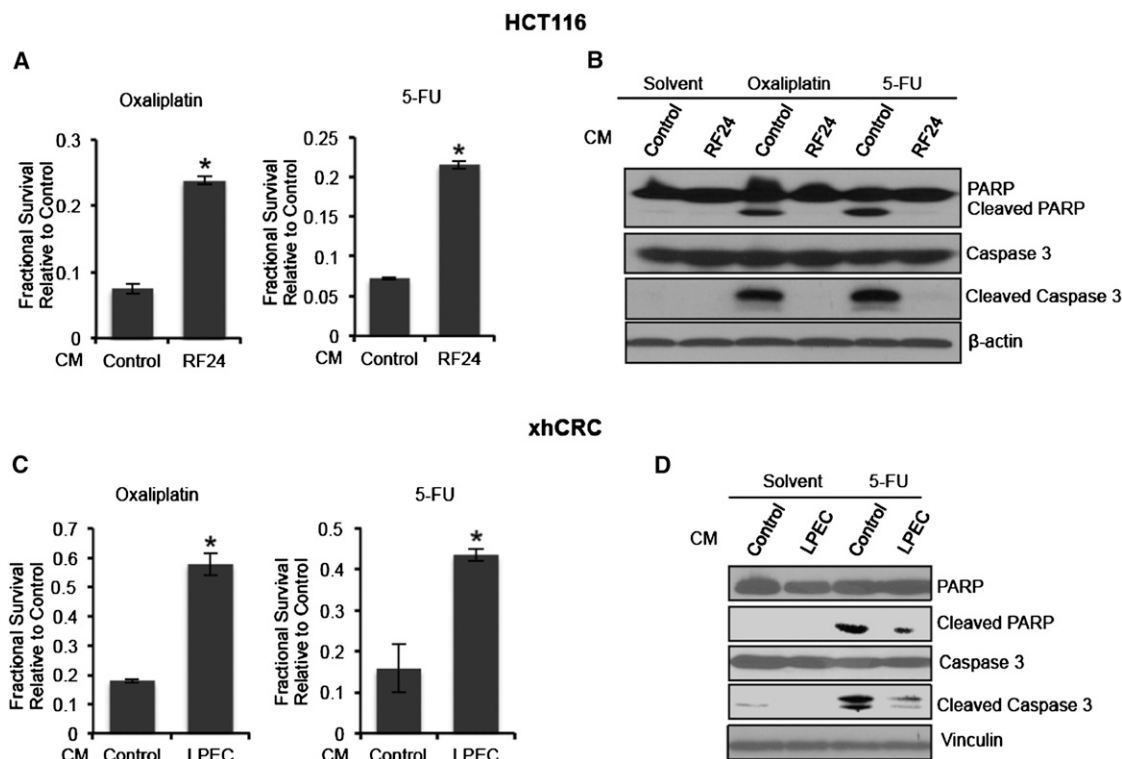


Figure 3. Endothelial Cell-Conditioned Medium Promotes Chemoresistance of Colorectal Cancer Cells

(A) HCT116 cells treated with oxaliplatin or 5-FU in control CM or RF24 CM (MTT assay).

(B) Western blot analysis of the expression of proapoptotic markers in HCT116 cells treated with oxaliplatin or 5-FU in control CM or RF24 CM.

(C) xhCRC cells treated with oxaliplatin or 5-FU in control CM or LPEC CM (MTT assay).

(D) Western blot analysis of the expression of proapoptotic markers in xhCRC cells treated with 5-FU in control CM or LPEC CM.

* $p < 0.05$, mean \pm SEM.

CM. LPEC CM treatment led to significantly increased activity of the Hes-1 reporter but not the Gli or TCF reporter (Figure 4A). Using the identical luciferase reporter assays, we also observed increased Hes-1 promoter activity in xhCRC cells treated with LPEC CM (Figure 4B) and HCT116 cells treated with RF24 CM (Figure S3A). In addition, we found that following EC CM treatment, protein levels of Notch intracellular domain (NICD) and Hes-1 in CRC cells were significantly increased (Figures 4C, S3B, and S3C). These data suggest that EC CM activates Notch signaling in CRC cells.

To determine whether Notch activation is indeed responsible for the promotion of the colorectal CSC phenotype by EC CM, gamma secretase inhibitor X (GSI), which inhibits the liberation of NICD, was added to RF24 CM during treatment of the CRC cells. GSI treatment blocked EC CM-induced Notch signaling activation and CSC enrichment, as demonstrated by the suppression of both NICD upregulation and Aldefluor-positive cell population increase (Figures S3D and S3E).

CRC Cells Adjacent to ECs in Human Specimens Demonstrate Activation of Notch Signaling

Having established that ECs secrete soluble factors to activate Notch signaling, we sought to determine whether CRC cells located in perivascular regions in human tumor samples displayed Notch activation. Immunofluorescent staining for NICD

and CD31 was carried out in human CRC surgical specimens. We found that tumor cells expressing NICD were predominantly located in the perivascular region (Figure 4D). These NICD-positive cells are not pericytes because NICD staining does not overlap with desmin staining (Figure S3F). Furthermore, coimmunofluorescent staining of CD133 and NICD highlighted the colocalization of CD133-positive and NICD-positive CRC cells in the perivascular niches (Figure 4E).

ECs Secrete a Soluble Form of Jagged-1 to Promote the CSC Phenotype in CRC Cells

Because the Notch signaling pathway in CRC cells was activated by soluble factors in EC CM, we sought to identify the molecules that activate Notch signaling. Although Notch activation is thought to occur exclusively via a juxtacrine mechanism, some studies reported the presence of soluble Notch ligands with variable effects on Notch signaling (Hukriede and Fleming, 1997; Nickoloff et al., 2002; Sun and Artavanis-Tsakonas, 1997). In contrast to the classic view of Notch activation, our studies suggested the presence of a soluble Notch ligand that was an activator of Notch signaling. Therefore, we examined the presence of the known Notch-1 ligands DLL4 and Jagged-1 in EC CM using western blot analysis. Our results showed that DLL4 was not differentially secreted by CRC cells and ECs, but a significantly greater amount of Jagged-1 was

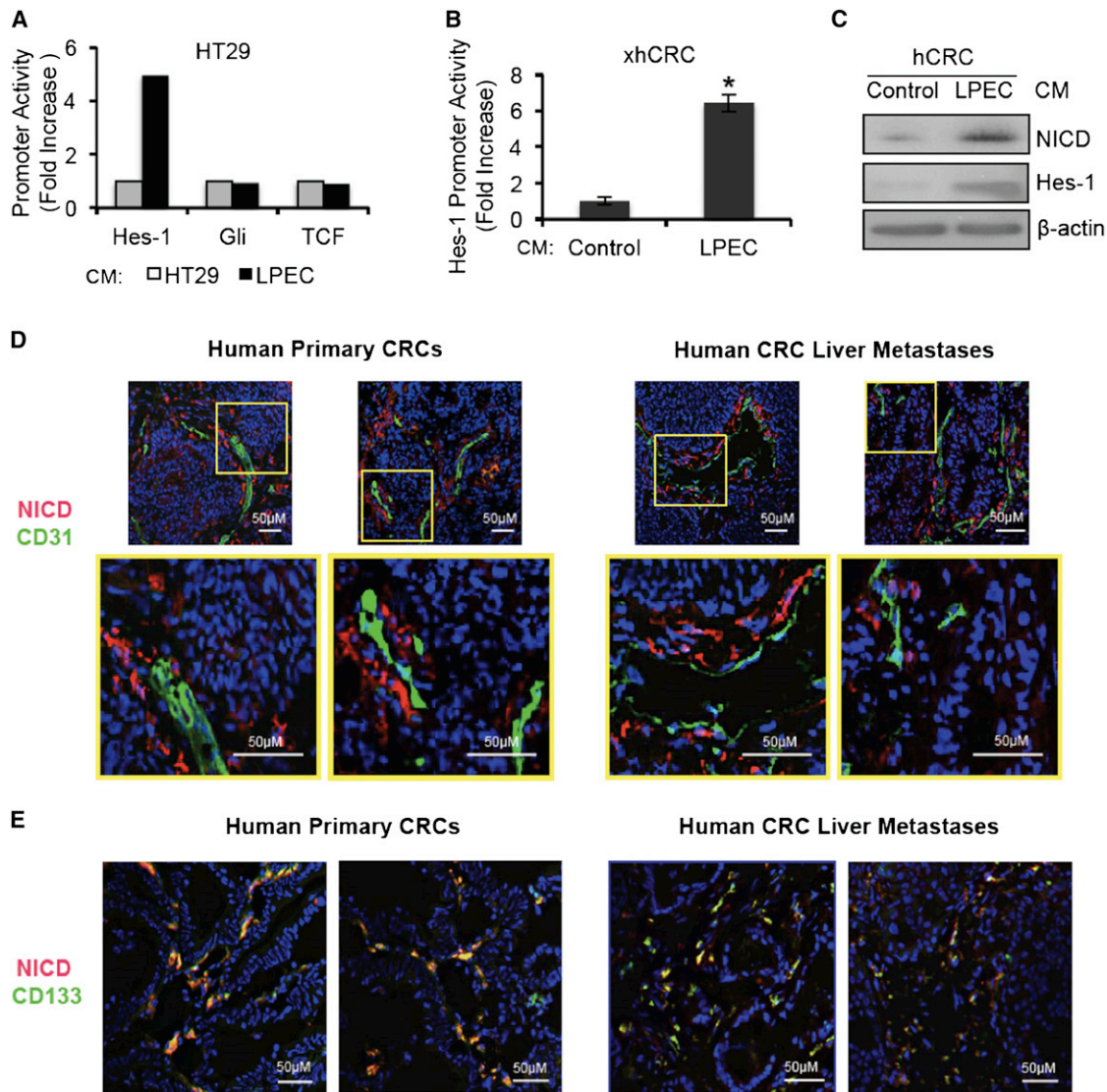


Figure 4. Endothelial Cells Activate Notch Signaling in Neighboring Colorectal Cancer Cells

(A) Promoter activity of Hes-1, Gli, and TCF in HT29 cells after treatment with control Hes or LPEC CM.

(B) Hes-1 promoter activity in freshly isolated xhCRC cells treated with control CM or LPEC CM (* $p < 0.05$, mean \pm SEM).

(C) NICD and Hes-1 expression in freshly isolated hCRC cells treated with control CM or LPEC CM.

(D) Representative immunofluorescent staining for NICD and CD31 in human primary CRCs (left panel) and CRC liver metastases (right panel). The highlighted regions in the upper panels are enlarged in the lower panels.

(E) Representative immunofluorescent staining of NICD and CD133 in primary CRCs (left panel) and CRC liver metastases (right panel).

See also Figure S3.

detected (using an N terminus antibody) in LPEC and RF24 CM compared to that in HT29 and HCT116 CM (Figures 5A and S4A). Because Notch-activating Jagged-1 is usually membrane bound, we sought to determine whether the Jagged-1 in EC CM was associated with microvesicles. Even after depletion of microvesicles, Jagged-1 could still be detected in the RF24 CM supernatant (Figure S4B), suggesting that the Jagged-1 found in EC CM is not anchored on microvesicles.

To determine whether this soluble form of Jagged-1 is responsible for the EC-mediated paracrine or angiocrine activation of Notch signaling in neighboring cancer cells, we first used small

interfering RNA (siRNA) to knock down Jagged-1 expression in LPEC cells and decrease secretion of soluble Jagged-1 in LPEC CM (Figure 5B). CM collected from Jagged-1 siRNA- or control (scrambled) siRNA-transfected LPECs were applied to HT29 cells for 72 hr, and activation of Notch signaling pathway and the CSC phenotypes were then assessed. Depletion of Jagged-1 in LPEC CM by siRNA blocked the EC CM-mediated activation of Notch signaling in HT29 cells, as demonstrated by the decreased expression of NICD and Hes-1, compared with that in controls (Figure 5C). Furthermore, depletion of Jagged-1 in LPEC CM also blocked its effect on promotion of the CSC

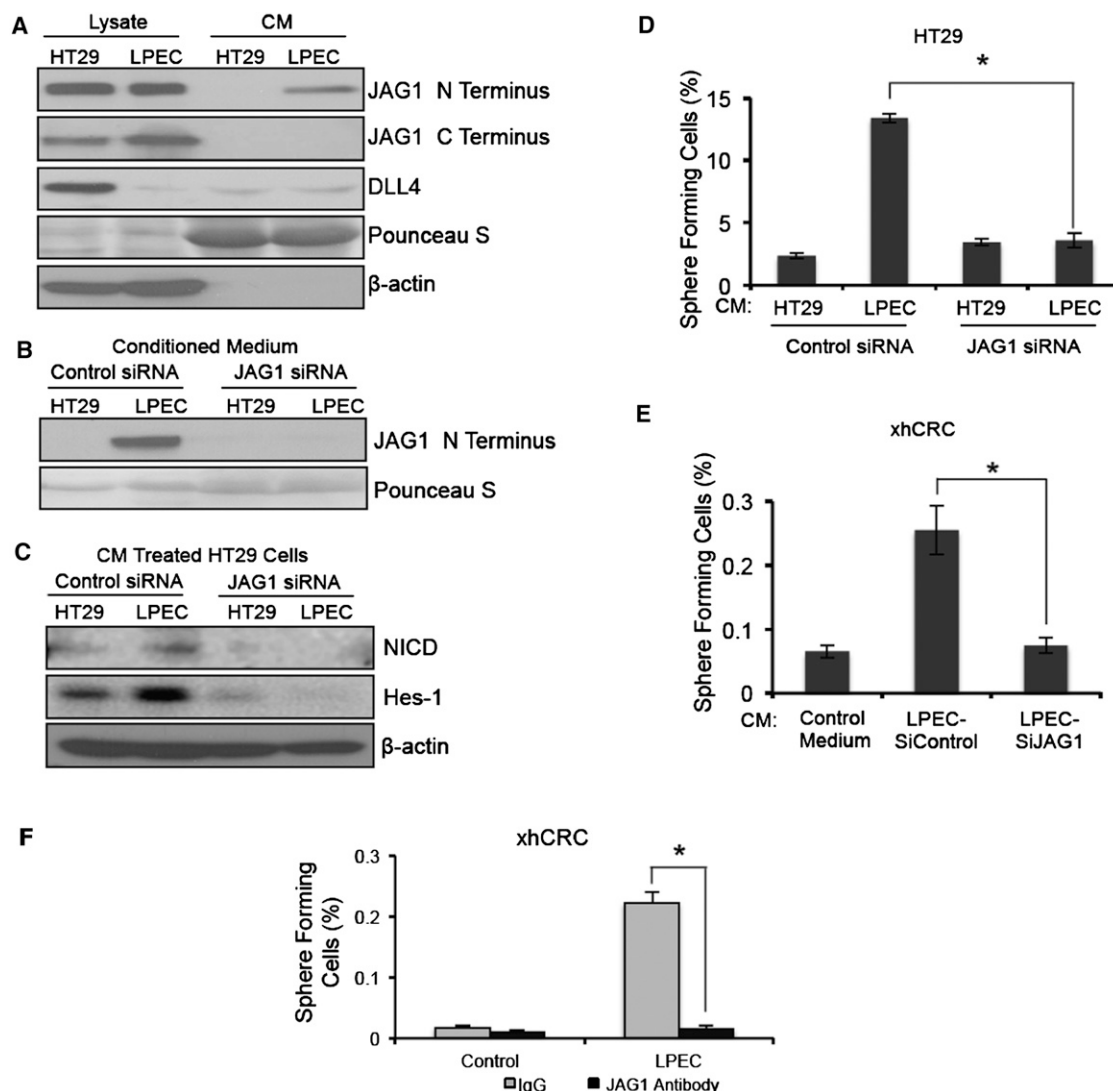


Figure 5. Endothelial Cells Secrete a Soluble Form of Jagged-1 to Promote the CSC Phenotype in Colorectal Cancer Cells

(A) Western blot analysis of HT29 and LPEC cell lysates and conditioned medium utilizing antibodies to the N terminus and C terminus regions of Jagged-1 (JAG1). Western blotting for DLL4 was also performed.

(B) Detection of soluble Jagged-1 in the conditioned medium from HT29 cells and LPECs after siRNA-mediated Jagged-1 knockdown.

(C) NICD and Hes-1 expression in HT29 cells after treatment with control CM or LPEC CM with decreased Jagged-1 levels by siRNA knockdown.

(D) Sphere-forming assay of HT29 cells exposed to control CM or LPEC CM with decreased Jagged-1 levels by siRNA knockdown.

(E) Sphere-forming assay of freshly isolated xhCRC cells exposed to control CM or LPEC CM with decreased Jagged-1 levels by siRNA knockdown.

(F) Sphere-forming assay of freshly isolated xhCRC cells exposed to the LPEC CM that is Jagged-1 depleted by immunoprecipitation.

* $p < 0.05$, mean \pm SEM. See also Figure S4.

phenotype in HT29 cells and xhCRC cells, as demonstrated by blockade of sphere-forming ability (Figures 5D and 5E). Similarly, depletion of Jagged-1 in RF24 CM by siRNA (Figure S4C) blocked the activation of Notch signaling (Figure S4D) and blocked enrichment of the Aldefluor-positive cells and increase of sphere-forming ability (Figures S4E and S4F).

We also used an immunoprecipitation-based approach to deplete Jagged-1 in EC CM to determine whether Jagged-1 was responsible for promoting the CSC phenotype. Following depletion of soluble Jagged-1 in EC CM by an antibody recognizing the N terminus of Jagged-1 (Figure S4G), the EC CM

was no longer able to enrich for cells with sphere-forming capability in xhCRC cells and HCT116 cells (Figures 5F and S4H). In a follow-up study, we added a Jagged-1 neutralizing antibody directly to the LPEC CM, and it blocked the enrichment of the sphere forming population in freshly isolated xhCRC cells (data not shown).

We obtained additional confirmation that the soluble form of Jagged-1 secreted by ECs is indeed the major factor that activates Notch signaling and promotes the CSC phenotype in neighboring CRC cells. First, we fractionated LPEC CM using size exclusion-fast protein liquid chromatography and

determined the fractions with Notch activation activity using a Hes-1 promoter driven luciferase reporter assay. As is shown in Figure 6A, we identified a single bioactive peak covering the fractions 32–34 that induced Notch signaling. Simultaneously, we examined the presence of soluble Jagged-1 in the various fractions by western blotting, and found that the soluble Jagged-1 containing fractions corresponded directly to the fractions (32–34) that activated the Hes-1 reporter (Figure 6A). Second, we immunoprecipitated Jagged-1 from EC CM and ran the IP sample in a polyacrylamide gel electrophoresis (PAGE) gel. After staining with Coomassie blue, we observed a single band representing Jagged-1 (data not shown). Next, we ran both native and denatured LPEC CM protein samples on a nondenaturing PAGE gel, and blotted for Jagged-1 by western blotting. As shown in Figure S5A, the soluble form of Jagged-1 secreted by ECs is not stably associated with other proteins. These data indicate that the soluble form of Jagged-1 that we identified is the Notch activating molecule in EC CM.

The EC-Secreted Soluble Form of Jagged-1 Is a C-Terminally Truncated Protein

In CRC and EC cell lysates, intact Jagged-1 could be detected by both Jagged-1 N terminus-specific and C terminus-specific antibodies. However, soluble Jagged-1 in EC CM could only be detected by the N terminus-specific antibody (Figures 5A and S4A). After deglycosylation, the molecular weight of soluble Jagged-1 in CM was ~15–20 kDa smaller than that of full-length Jagged-1 (Figure S5B). These results suggest that this soluble Jagged-1 is a C-terminally truncated form.

In order to gain insights into whether this C-terminally truncated form of soluble Jagged-1 is relevant in human CRCs, we stained human CRC specimens using an antibody against either N-terminal or C-terminal Jagged-1; we simultaneously stained tissue sections with an antibody against the endothelial cell marker CD31. As shown in Figure S5C, staining with the C-terminal Jagged-1 antibody, which only reacts with full-length Jagged-1, largely overlaps with CD31 staining. In contrast, the N-terminal Jagged-1 antibody, which recognizes both full-length and soluble Jagged-1, not only costains CD31-positive ECs, but also strongly stains areas that are adjacent to ECs. These data support the existence of soluble Jagged-1 in human CRCs.

We then sought to determine the nature of the soluble Jagged-1 protein enriched in the EC CM. First, we asked whether soluble Jagged-1 was a product of alternative splicing. We performed semiquantitative RT-PCR to detect Jagged-1 splicing variants in CRC cells and ECs and excluded this possibility because these two types of cells expressed equal levels of the alternatively spliced Jagged-1 mRNA (Figure S5D). We then hypothesized that a posttranslational event leads to the generation of this soluble Jagged-1. When we transfected full-length Jagged-1 cDNA into LPEC cells, an increase of soluble Jagged-1 secretion in its CM was observed (data not shown). Compared with the CM of mock-transfected LPECs, CM collected from LPECs with Jagged-1 overexpression could further promote the CSC phenotype of HT29 cells, as demonstrated by a further enrichment of the Aldefluor-positive cell population (data not shown). We then treated LPECs and RF24 cells with a protease inhibitor cocktail and found that broad-spectrum inhibition of protease activity resulted in reduction of

the soluble Jagged-1 generation (Figure S5E), suggesting that EC-secreted soluble Jagged-1 is a product derived from protease cleavage of full-length Jagged-1. Taken together, these results suggest that ECs are capable of posttranslational modifications that lead to the production of this soluble form of Jagged-1.

Proteomic Analysis of Soluble Jagged-1

In order to further define the structure of the soluble Jagged-1 protein, we employed a mass spectrometry-based strategy. Briefly, we isolated the Jagged-1 proteins from LPEC CM via immunoprecipitation using an N-terminal antibody and subjected them to deglycosylation followed by proteolytic digestion. Mass spectrometry identified multiple peptides consistent with the Jagged-1 amino acid sequence (Figure 6B), confirming the identity of soluble Jagged-1 protein in the EC CM. In addition, we identified a peptide “KRDGNSSLIAVAE” bearing only one Lys-N site, indicating that the possible C terminus of soluble Jagged-1 was at amino acid E1054. The identical proposed C-terminal peptide was also found in protein samples isolated by immunoprecipitation of N-terminal Jagged-1 from CM of a second endothelial cell line, RF24, indicating that this EC-secreted soluble form of Jagged-1 might be truncated at amino acid 1054 (Figure 6B).

ADAM17 Cleaves Jagged-1 on ECs to Produce the Soluble Form Jagged-1

A recent study reported that the protease ADAM17 could mediate Jagged-1 shedding (Parr-Sturgess et al., 2010); however, the investigators did not describe the specific cleavage site or the function of this cleaved product. Interestingly, by analyzing the protein sequences flanking E1054 of Jagged-1 (Figure 6B), we found that VAEV is a plausible recognition motif for the protease ADAM17, which may cleave the protein between E1054 and V1055 (Caescu et al., 2009). Therefore, we hypothesized that ADAM17 is the protease that cleaves Jagged-1 in ECs to generate the soluble form of the protein. To test our hypothesis, we first synthesized a peptide consisting of aa 1047–1061 (SLIAVAEVRVQRRP) of Jagged-1 and subjected it to ADAM17 cleavage followed by mass spectrometry analysis. After ADAM17 cleavage, a 906.56 Da peptide was identified and determined to be VRVQRRP (Figure 6C, middle panel); this cleavage was inhibited by TAPI-2, an inhibitor of ADAM17 (Figure 6C, right panel). These data confirm that ADAM17 specifically cleaves Jagged-1 between residues E1054 and V1055.

We next cotransfected full-length human Jagged-1 and ADAM17 expression plasmids into a mouse fibroblast cell line, L cells. As shown in Figure S6A, we found that the soluble form of Jagged-1 was enriched in the conditioned medium (here we used two different antibodies that recognize the N terminus of Jagged-1, to rule out any possibility of a none-specific signal with the use of a single antibody); this conditioned medium could promote the CSC phenotype of freshly isolated hCRC cells, as documented by CD133 FACS analysis (Figure S6B) and sphere-forming ability (Figure S6C). These data confirm that ADAM17 could cleave full-length Jagged-1, leading to extracellular release of the soluble form of Jagged-1, which is sufficient to promote the colorectal CSC phenotype.

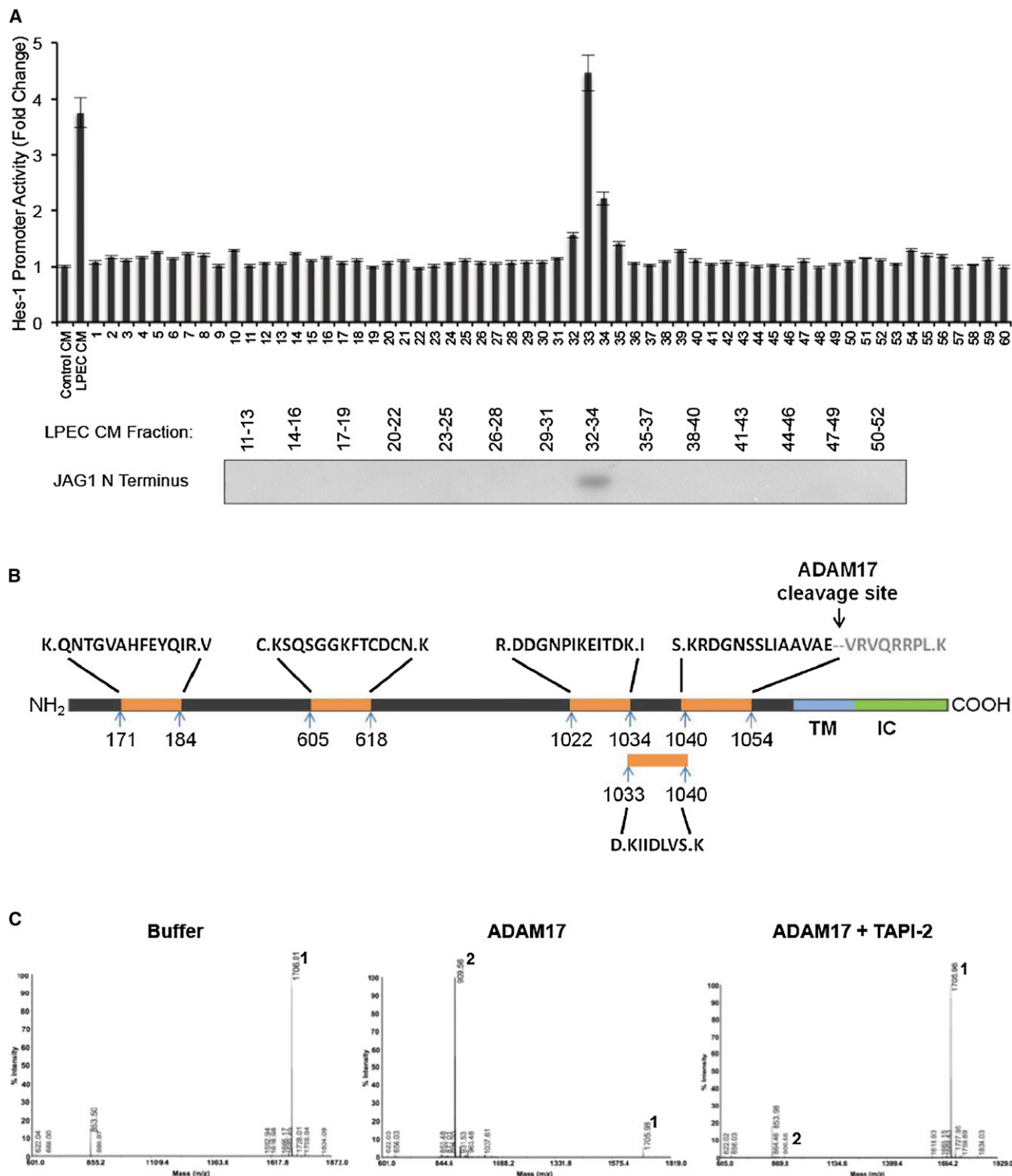


Figure 6. Proteomics Analysis Demonstrate that the EC-Secreted Soluble Form of Jagged-1 Is C-terminally Truncated by ADAM17

(A) Concentrated LPEC CM was fractionated by FPLC gel filtration. The fractions were applied to xhCRC cells containing the Hes-1 promoter-luciferase construct, and Hes-1 promoter activity was assessed (upper panel). Western blot detection of soluble Jagged-1 in combined adjacent fractions is shown in the lower panel.

(B) Jagged-1 from LPEC CM was immunoprecipitated using an N-terminal antibody and subjected to deglycosylation followed by digestion. Mass spectrometric analysis of Jagged-1 proteins was performed with multiple peptides identified to be consistent with the N-terminal region of Jagged-1 with a C terminus at amino acid E1054.

(legend continued on next page)

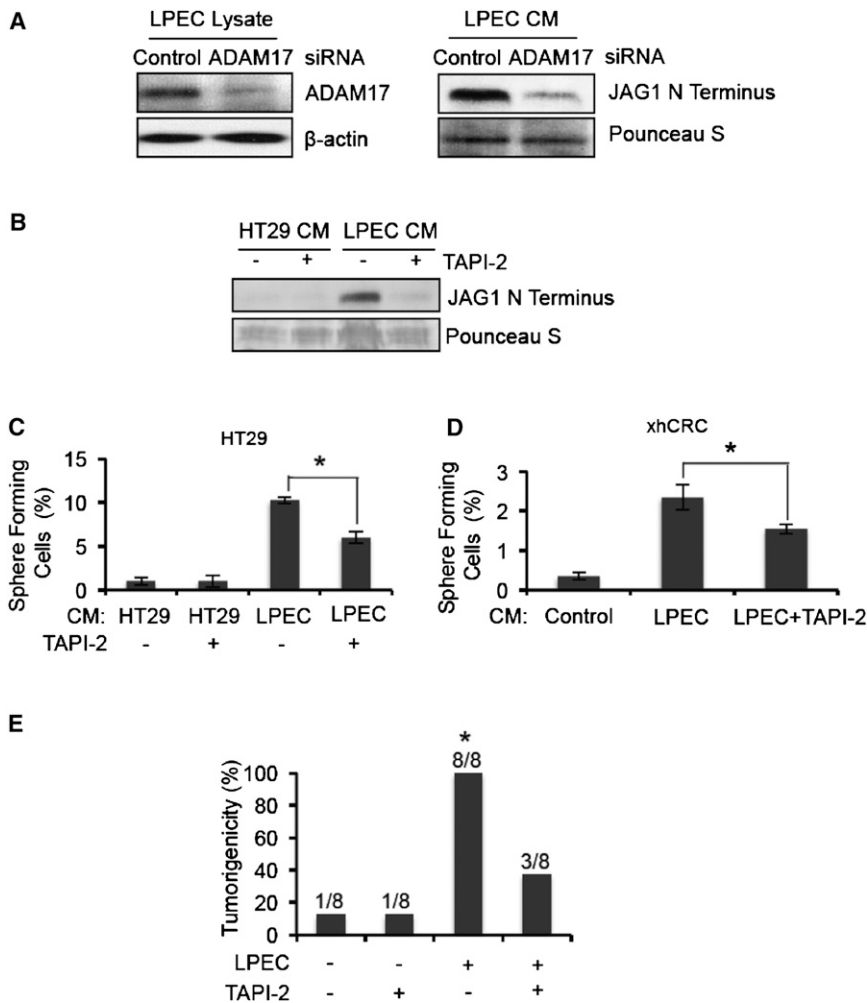


Figure 7. Inhibition of ADAM17 in Endothelial Cells Blocks the Conditioned Medium Promotion of the CSC Phenotype in Human CRC Cells

(A) Western blot detection of ADAM17 in the cell lysate of LPECs treated with control or ADAM17 siRNA (left panel). The soluble form of Jagged-1 in the CM from the cells shown in the left panel, are shown in the right panel.

(B) Secretion of the soluble form of Jagged-1 into the CM of HT29 cells and LPECs treated with the ADAM17 inhibitor TAPI-2.

(C and D) Sphere-forming assays on HT29 cells (C) and freshly isolated xhCRC cells (D) after treatment with CM from LPECs, with or without the ADAM17 inhibitor TAPI-2 (* $p < 0.05$, mean \pm SEM).

(E) In vivo tumorigenicity assay (day 10) using freshly isolated xhCRC cells coinjected with LPECs with/without daily TAPI-2 treatment (* $p < 0.05$, LPEC/no TAPI-2 versus all other groups). See also Figure S6.

confirm that ADAM17 is essential for soluble Jagged-1 production by ECs.

Finally, we performed an in vivo study using xenograft models to determine whether inhibition of ADAM17 can block the angiocrine promotion of tumorigenicity. We coinjected freshly isolated xhCRC cells with LPECs subcutaneously into mice and treated the animals with daily TAPI-2 by intraperitoneal (IP) injection. We found that TAPI-2 treatment significantly suppressed tumor initiation (Figure 7E). These data suggest that ADAM17 mediated shedding of Jagged-1

from ECs is an important mechanism that mediates the angiocrine effect on tumor initiation.

Taken together, our data suggest that ADAM17 is the protease that cleaves Jagged-1 in ECs, and the resultant soluble Jagged-1 functions in a paracrine manner to activate Notch signaling and promote the CSC phenotype of nearby CRC cells.

DISCUSSION

The concept of targeting the tumor vasculature as an antineoplastic strategy was developed ~40 years ago by Folkman (Folkman, 1971). However, therapeutic agents targeting classic angiogenic mediators, such as vascular endothelial growth factor, have only minimally improved progression-free and overall survival when added to chemotherapy regimens for patients with metastatic CRC (Saltz et al., 2008). Although tumor vascularity correlates with the aggressiveness of CRC, this does not

Inhibition of ADAM17 Blocks the Angiocrine Effect of ECs that Promotes the Colorectal CSC Phenotype by Blocking Soluble Jagged-1 Production

We sought to investigate whether inhibition of ADAM17 could suppress the EC-mediated promotion of colorectal CSC phenotype by blocking Jagged-1 production. We knocked down ADAM17 expression in LPECs by siRNA and found that this resulted in a significant decrease in the production of soluble Jagged-1 in LPEC CM (Figure 7A). We then used the ADAM17 inhibitor TAPI-2 to determine whether inhibition of ADAM17 activity would block production of soluble Jagged-1. Treatment of LPECs with TAPI-2 significantly reduced soluble Jagged-1 production in its CM (Figure 7B). Importantly, TAPI-2 also inhibited the angiocrine effect of LPECs that promotes the CSC phenotype of CRC cells, as demonstrated by decreased enrichment of sphere-forming populations in HT29 cells and freshly isolated xhCRC cells (Figures 7C and 7D). These studies

(C) Mass spectrometric analysis of the ADAM17 cleavage site of Jagged-1. A synthetic peptide corresponding to aa 1047–1061 of Jagged-1 was incubated with buffer only (left panel), ADAM17 (middle panel), or ADAM17 with its inhibitor TAPI-2 (right panel), and the reaction products were subjected to mass spectrometry. Peak 1 represents the intact substrate SLIAVAEVRVQRRP, and Peak 2 represents the ADAM17 cleavage product, a 906.56 Da peptide that was determined to be VRVQRRP.

See also Figure S5.

necessarily imply an associated increase in blood flow (Takahashi et al., 1995; Weidner et al., 1991). It is possible that ECs play a more active role in mediating tumor growth and metastasis than simply providing the physical structure that forms conduits for blood flow. The development of more effective agents targeting the vasculature may require approaches that go beyond targeting the classic angiogenic pathways by current means.

Here, we provide several lines of evidence demonstrating that ECs secrete soluble factors that promote the colorectal CSC phenotype via a paracrine effect: CM derived from ECs can (1) enrich the Aldefluor-positive CRC cell population, (2) enrich CRC cells expressing putative colorectal CSC surface marker CD133, (3) increase CRC cell sphere-forming capability, (4) enhance tumorigenicity, and (5) confer chemoresistance to CRC cells. We also determined that the major EC-secreted factor that promotes CSC phenotype is an unreported form of Jagged-1 that activates Notch signaling in neighboring CRC cells.

The identification (or existence) of CSCs remains a point of controversy. Numerous markers have been used to identify CSCs from CRC specimens, including the cell surface marker CD133, functional studies such as the Aldefluor assay and sphere-forming ability, and in vivo studies such as the serial dilution-based tumorigenicity assay. In our studies, we assessed all of these markers, and all confirmed that ECs secrete a factor(s) that increase the percentage of CRCs with CSC properties. We believe the tumorigenicity and chemoresistance assays are the most important studies that potentially have clinical implications.

Many studies suggest that CSCs originate from mutations in stem cells that cause malignant transformation (Barker et al., 2009; Dick, 2008; Korkaya and Wicha, 2010; Passequé et al., 2003). However, other investigators have noted that CSCs exist in a state of flux and that the CSC population can be enriched by microenvironmental influences (Chaffer et al., 2011; Rosen and Jordan, 2009; Vermeulen et al., 2010). In our studies, EC CM increased the percentage of cells with CSC characteristics, further supporting the idea that the microenvironment can regulate the CSC phenotype. Our findings that EC CM can convert a non-CSC to a cell with CSC properties are in line with recent studies showing that CSCs and non-CSCs do not exist in fixed states (Chaffer et al., 2011; Gupta et al., 2011). More importantly, we demonstrated that Notch signaling activation by a soluble ligand is an important mechanism through which the CSC population is enriched in CRC by the microenvironment.

The observation that CSCs accumulate in perivascular regions has been reported by several groups (Butler et al., 2010a; Calabrese et al., 2007; Krishnamurthy et al., 2010). EC-secreted factors have been shown to promote the self-renewal of CSCs in squamous cell carcinomas, as demonstrated by upregulated Bmi-1 expression and an increase in sphere formation in vitro (Krishnamurthy et al., 2010). Others have shown that ECs could promote glioblastoma stem-like cell expansion by secreting factors that activate mTOR signaling (Galan-Moya et al., 2011). These studies support the notion that tumor-associated ECs play a direct role in maintaining a population of CSCs. We demonstrated that ECs produce a truncated soluble form of Jagged-1 that activates Notch signaling in CRC cells to promote their CSC phenotype. We also showed that, in both primary and metastatic human CRC specimens, NICD- and CD133-positive cells are primarily located in perivascular areas. Our findings

suggest that ECs play an important role in establishing a perivascular niche for colorectal CSCs through inducing Notch signaling in tumor cells by releasing soluble Jagged-1 in a paracrine manner.

Rafii and colleagues reported that EC expression of Jagged-1 and Jagged-2 could stimulate the expansion of Notch-dependent hematopoietic stem cells (Butler et al., 2010b). Similarly, Fan's group reported that human brain microvascular ECs could activate Notch signaling in adjacent glioblastoma cells in a juxtacrine manner (Zhu et al., 2011). Taketo and colleagues also reported that tumor-associated ECs express Jagged-1 and DLL4 that activate Notch signaling on CRC cells (Sonoshita et al., 2011). In these studies, direct cell-cell contact (juxtacrine signaling) was required for ECs to maintain hematopoietic/cancer stem cell propagation (Butler et al., 2010b; Kobayashi et al., 2010). In our studies, however, we defined a previously unrecognized mechanism through which ECs activate Notch signaling to promote CRC cell stemness—namely, production of a soluble paracrine/angiocrine Notch ligand.

In this study, we were able to determine the identity of the soluble form of Jagged-1 secreted by ECs, produced through ADAM17 cleavage. In addition, we determined that this soluble form of Jagged-1 activates Notch signaling and, in turn, mediates the CSC phenotype of CRC cells. In the classic model of Notch signaling (Figure 8A), Notch is activated by cell surface-bound ligands, where cell-cell contact is required. We propose an alternative Notch activation model, as shown in Figure 8B, whereby the full-length Jagged-1 is cleaved by ADAM17, which results in the production of a truncated soluble form of Jagged-1 that can activate Notch signaling in nearby cells. This manner of Notch pathway activation does not require cell-cell contact, and therefore, we refer it as paracrine/angiocrine activation of Notch.

Several studies have reported contrasting biologic effects of soluble Notch ligands. Two groups generated soluble mutants of *Drosophila* Notch ligands Delta and/or Serrate and found that these forms could function as antagonists of Notch signaling (Hukriede and Fleming, 1997; Sun and Artavanis-Tsakonas, 1997). Similarly soluble forms of human Jagged-1 and DLL1 composed only of the extracellular domain were reported to inhibit Notch signaling (Small et al., 2001; Trifonova et al., 2004). An engineered soluble Notch ligand, DLL4-Fc, in which the extracellular domain of DLL4 was fused to a human IgG1 Fc fragment, has been shown to inhibit Notch activation (Lobov et al., 2007; Noguera-Troise et al., 2006). In contrast, several groups have shown that soluble Jagged1-derived peptides are able to activate Notch signaling in several cell types, leading to keratinocyte differentiation (Nickoloff et al., 2002), maturation of dendritic cells (Weijzen et al., 2002), apoptosis in B cell leukemia cells (Kannan et al., 2011), and inhibited differentiation of hematopoietic precursor cells (Li et al., 1998). Importantly, a naturally occurring soluble form of Jagged1 was found in human skin, inducing epithelial differentiation, a phenotype consistent with Notch activation (Aho, 2004). We found a naturally occurring soluble Jagged-1 that can activate Notch signaling in CRC cells. The reasons for the apparent discrepancies among different studies are not well understood. A major determinant of whether a soluble ligand activates or inhibits Notch signaling could be the specific structure of the ligand. Thus, we

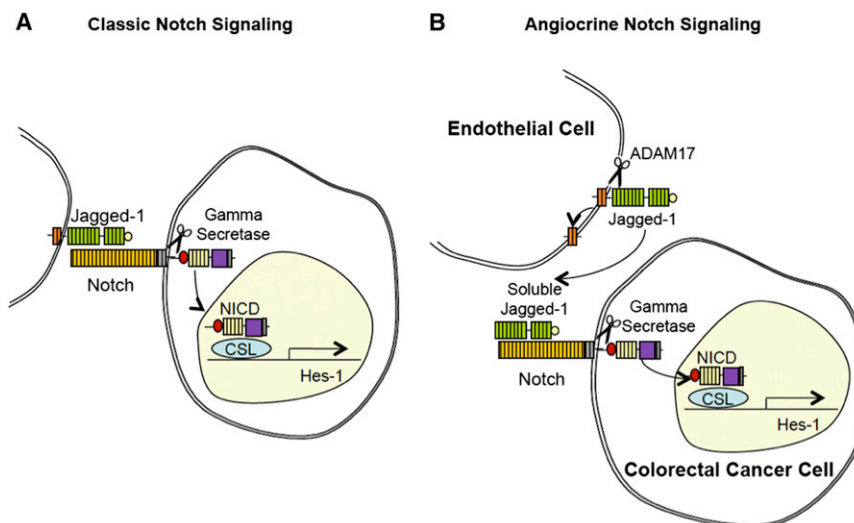


Figure 8. Proposed Model for EC-Mediated Paracrine Activation of Notch Signaling in Colorectal Cancer Cells

(A) The conical model for Notch pathway activation, where membrane bound ligands such as Jagged-1 activates Notch signaling in contacting cells.

(B) Schematic summarizing our proposed model for paracrine activation of the Notch pathway in CRC cells. ADAM17 cleaves membrane bound Jagged-1 on ECs, releasing an N-terminal soluble fragment that binds, and activates, Notch on CRC cells.

(MDACC) Institutional Review Board approved human specimen procurement, and informed consents were obtained.

Tumorigenicity Studies

All mice were housed in the MDACC animal facility, and all experiments were performed in

speculate that distinct forms of soluble Notch ligands, resulting from different species, cleavages, posttranslational modifications, and/or engineering strategies, may account for their different biologic behaviors.

Although Notch inhibitors are being studied in clinical trials, toxicity has been noted, limiting clinical development. Our discovery of truncated soluble form of Jagged-1 that activates Notch signaling in CRC cells has potential clinical implications. Neutralization of Notch activation triggered by soluble Jagged-1 may be a more specific and refined approach to sensitize tumors to antineoplastic therapies.

Although we believe that soluble Jagged-1 is the major factor that mediates the angiocrine effect that promotes the colorectal CSC phenotype, we do not exclude the possibility that other signaling events may also contribute to induction of the CSC phenotype. Given the obvious complexity of tumor microenvironment, we believe that other important angiocrine factors remain to be identified, and this will be important in the development and refinement of new therapeutic approaches.

In summary, our study defines a mechanism for the angiocrine function of ECs that leads to Notch activation that, in turn, promotes the CSC phenotype. This study reports the generation of an active, soluble form of Jagged-1 that is the product of ADAM17 protease activity. Our findings, along with other studies in the field of angiocrine signaling, suggest that ECs are more than simply conduits for nutrient and oxygen delivery—they also contribute soluble factors to promote the CSC phenotype and chemoresistance. It is possible that targeting angiocrine signaling, including soluble Jagged-1 and/or ADAM17, may improve the outcomes of therapy for patients with metastatic CRC.

EXPERIMENTAL PROCEDURES

Isolation of Human CRC Cells and Liver Parenchyma ECs

Human CRC (hCRC) cells and LPECs were isolated from CRC and liver parenchyma tissue from surgical specimens, respectively. Xenografted human CRC (hxCRC) cells were isolated from mice after a direct inoculation with freshly isolated human CRC cells derived from patients (see [Supplemental Experimental Procedures](#)). The M.D. Anderson Cancer Center

accordance with guidelines approved by the MDACC Institutional Animal Care & Use Committee. LPEC CM-pretreated hxCRC cells were injected subcutaneously into nude mice. Primary xenografts were harvested and treated with LPEC CM for 7 days before secondary xenograft passaging (see [Supplemental Experimental Procedures](#)). Tumor growth was monitored by a blinded investigator.

In Vivo Metastasis Studies

Luciferase-labeled CRC cells were pretreated with EC CM for 7 days and injected intravenously ([Saltz et al., 2008](#)) via tail vein or via the spleen (liver metastasis model). Luciferase activity was used to assess the relative tumor burden (see [Supplemental Experimental Procedures](#)).

Statistical Analysis

For all in vitro and ex vivo experiments, statistical analyses were conducted using Student's t test (Microsoft Excel). For in vivo studies, statistical analyses were performed using the Kaplan Meier test (Software R) (tumorigenicity), chi-square test (Microsoft Excel) (tumor incidence), and Mann Whitney-U test (number of metastatic sites and tumor burden). All statistical tests were two-sided, and p values ≤ 0.05 were considered to be significant.

SUPPLEMENTAL INFORMATION

Supplemental Information includes six figures and Supplemental Experimental Procedures and may be found with this article online at <http://dx.doi.org/10.1016/j.ccr.2012.12.021>.

ACKNOWLEDGMENTS

This work was supported in part by National Institutes of Health (NIH) Cancer Center support grant CA016672, NIH grant T32CA009599 (to S.B., F.T., and E.S.), NIH grant R01CA157880 (to L.M.E.), Department of Defense grant CA100879 (to L.M.E.), the William C. Liedtke, Jr., Chair in Cancer Research (to L.M.E.), and an R.E. "Bob" Smith Fellowship (to S.S.). The authors thank Li Huang and Menashe Bar-Eli, from the Department of Cancer Biology, M.D. Anderson Cancer Center (MDACC), for molecular subcloning of full-length Jagged-1 and ADAM17. The authors thank John Ladbury, from The Center of Biomolecular Structure and Function, for assistance in identification of the Jagged-1 cleavage site. The authors thank Francesco Stingo, from Department of Biostatistics, for statistical support. The authors thank Zach Bohannon, Sunita Patterson, and Claire Dawn from the Department of Scientific Publications, and Rita Hernandez from the Departments of Surgical Oncology and Cancer Biology for editorial assistance. All of the above are from the MDACC. L.M.E. serves as an ad hoc consultant for Genentech/Roche.

Received: September 16, 2011

Revised: March 12, 2012

Accepted: December 21, 2012

Published: January 31, 2013

REFERENCES

- Aho, S. (2004). Soluble form of Jagged1: unique product of epithelial keratinocytes and a regulator of keratinocyte differentiation. *J. Cell. Biochem.* 92, 1271–1281.
- Al-Hajj, M. (2007). Cancer stem cells and oncology therapeutics. *Curr. Opin. Oncol.* 19, 61–64.
- American Cancer Society. (2010). Cancer facts & figures 2010. <http://www.cancer.org/research/cancerfactsfigures/cancerfactsfigures/cancer-facts-and-figures-2010>.
- Barker, N., Ridgway, R.A., van Es, J.H., van de Wetering, M., Begthel, H., van den Born, M., Danenberg, E., Clarke, A.R., Sansom, O.J., and Clevers, H. (2009). Crypt stem cells as the cells-of-origin of intestinal cancer. *Nature* 457, 608–611.
- Butler, J.M., Kobayashi, H., and Rafii, S. (2010a). Instructive role of the vascular niche in promoting tumour growth and tissue repair by angiocrine factors. *Nat. Rev. Cancer* 10, 138–146.
- Butler, J.M., Nolan, D.J., Vertes, E.L., Varnum-Finney, B., Kobayashi, H., Hooper, A.T., Seandel, M., Shido, K., White, I.A., Kobayashi, M., et al. (2010b). Endothelial cells are essential for the self-renewal and repopulation of Notch-dependent hematopoietic stem cells. *Cell Stem Cell* 6, 251–264.
- Caescu, C.I., Jeschke, G.R., and Turk, B.E. (2009). Active-site determinants of substrate recognition by the metalloproteinases TACE and ADAM10. *Biochem. J.* 424, 79–88.
- Calabrese, C., Poppleton, H., Kocak, M., Hogg, T.L., Fuller, C., Hamner, B., Oh, E.Y., Gaber, M.W., Finklestein, D., Allen, M., et al. (2007). A perivascular niche for brain tumor stem cells. *Cancer Cell* 11, 69–82.
- Chaffer, C.L., Brueckmann, I., Scheel, C., Kaestli, A.J., Wiggins, P.A., Rodrigues, L.O., Brooks, M., Reinhardt, F., Su, Y., Polyak, K., et al. (2011). Normal and neoplastic nonstem cells can spontaneously convert to a stem-like state. *Proc. Natl. Acad. Sci. USA* 108, 7950–7955.
- Clarke, M.F., Dick, J.E., Dirks, P.B., Eaves, C.J., Jamieson, C.H., Jones, D.L., Visvader, J., Weissman, I.L., and Wahl, G.M. (2006). Cancer stem cells—perspectives on current status and future directions: AACR Workshop on cancer stem cells. *Cancer Res.* 66, 9339–9344.
- Dallas, N.A., Xia, L., Fan, F., Gray, M.J., Gaur, P., van Buren, G., 2nd, Samuel, S., Kim, M.P., Lim, S.J., and Ellis, L.M. (2009). Chemoresistant colorectal cancer cells, the cancer stem cell phenotype, and increased sensitivity to insulin-like growth factor-I receptor inhibition. *Cancer Res.* 69, 1951–1957.
- Davies, J.M., and Goldberg, R.M. (2008). First-line therapeutic strategies in metastatic colorectal cancer. *Oncology (Huntingt.)* 22, 1470–1479.
- Davies, J.M., and Goldberg, R.M. (2011). Treatment of metastatic colorectal cancer. *Semin. Oncol.* 38, 552–560.
- Dick, J.E. (2008). Stem cell concepts renew cancer research. *Blood* 112, 4793–4807.
- Du, L., Wang, H., He, L., Zhang, J., Ni, B., Wang, X., Jin, H., Cahuzac, N., Mehrpour, M., Lu, Y., and Chen, Q. (2008). CD44 is of functional importance for colorectal cancer stem cells. *Clin. Cancer Res.* 14, 6751–6760.
- Folkman, J. (1971). Tumor angiogenesis: therapeutic implications. *N. Engl. J. Med.* 285, 1182–1186.
- Galan-Moya, E.M., Le Guelle, A., Lima Fernandes, E., Thirant, C., Dwyer, J., Bidere, N., Couraud, P.O., Scott, M.G., Junier, M.P., Chneiweiss, H., and Gavard, J. (2011). Secreted factors from brain endothelial cells maintain glioblastoma stem-like cell expansion through the mTOR pathway. *EMBO Rep.* 12, 470–476.
- Gupta, P.B., Fillmore, C.M., Jiang, G., Shapira, S.D., Tao, K., Kuperwasser, C., and Lander, E.S. (2011). Stochastic state transitions give rise to phenotypic equilibrium in populations of cancer cells. *Cell* 146, 633–644.
- Huang, E.H., Hynes, M.J., Zhang, T., Ginestier, C., Dontu, G., Appelman, H., Fields, J.Z., Wicha, M.S., and Boman, B.M. (2009). Aldehyde dehydrogenase 1 is a marker for normal and malignant human colonic stem cells (SC) and tracks SC overpopulation during colon tumorigenesis. *Cancer Res.* 69, 3382–3389.
- Hukriede, N.A., and Fleming, R.J. (1997). Beaded of Goldschmidt, an antimorphic allele of Serrate, encodes a protein lacking transmembrane and intracellular domains. *Genetics* 145, 359–374.
- Jarriault, S., Brou, C., Logeat, F., Schroeter, E.H., Kopan, R., and Israel, A. (1995). Signalling downstream of activated mammalian Notch. *Nature* 377, 355–358.
- Kannan, S., Fang, W., Song, G., Mullighan, C.G., Hammit, R., McMurray, J., and Zweidler-McKay, P.A. (2011). Notch/HES1-mediated PARP1 activation: a cell type-specific mechanism for tumor suppression. *Blood* 117, 2891–2900.
- Kato, M., and Kato, M. (2007). Notch signaling in gastrointestinal tract (review). *Int. J. Oncol.* 30, 247–251.
- Kobayashi, H., Butler, J.M., O'Donnell, R., Kobayashi, M., Ding, B.S., Bonner, B., Chiu, V.K., Nolan, D.J., Shido, K., Benjamin, L., and Rafii, S. (2010). Angiocrine factors from Akt-activated endothelial cells balance self-renewal and differentiation of haematopoietic stem cells. *Nat. Cell Biol.* 12, 1046–1056.
- Korkaya, H., and Wicha, M.S. (2010). Cancer stem cells: nature versus nurture. *Nat. Cell Biol.* 12, 419–421.
- Krishnamurthy, S., Dong, Z., Vodopyanov, D., Imai, A., Helman, J.I., Prince, M.E., Wicha, M.S., and Nör, J.E. (2010). Endothelial cell-initiated signaling promotes the survival and self-renewal of cancer stem cells. *Cancer Res.* 70, 9969–9978.
- Li, L., Milner, L.A., Deng, Y., Iwata, M., Banta, A., Graf, L., Marcovina, S., Friedman, C., Trask, B.J., Hood, L., and Torok-Storb, B. (1998). The human homolog of rat Jagged1 expressed by marrow stroma inhibits differentiation of 32D cells through interaction with Notch1. *Immunity* 8, 43–55.
- Limkala, R., Yee, C., Terunuma, A., Martin, P., Kelly, K., and Vogel, J. (2009). Isolation of prostate cancer stem cells using developmental signaling pathway activities. *AACR Meeting Abstracts 2009*, LB-71.
- Lobov, I.B., Renard, R.A., Papadopoulos, N., Gale, N.W., Thurston, G., Yancopoulos, G.D., and Wiegand, S.J. (2007). Delta-like ligand 4 (Dll4) is induced by VEGF as a negative regulator of angiogenic sprouting. *Proc. Natl. Acad. Sci. USA* 104, 3219–3224.
- Nickoloff, B.J., Qin, J.Z., Chaturvedi, V., Denning, M.F., Bonish, B., and Miele, L. (2002). Jagged-1 mediated activation of notch signaling induces complete maturation of human keratinocytes through NF-kappaB and PPARgamma. *Cell Death Differ.* 9, 842–855.
- Noguera-Troise, I., Daly, C., Papadopoulos, N.J., Coetzee, S., Boland, P., Gale, N.W., Lin, H.C., Yancopoulos, G.D., and Thurston, G. (2006). Blockade of Dll4 inhibits tumour growth by promoting non-productive angiogenesis. *Nature* 444, 1032–1037.
- O'Brien, C.A., Pollett, A., Gallinger, S., and Dick, J.E. (2007). A human colon cancer cell capable of initiating tumour growth in immunodeficient mice. *Nature* 445, 106–110.
- Parr-Sturgess, C.A., Rushton, D.J., and Parkin, E.T. (2010). Ectodomain shedding of the Notch ligand Jagged1 is mediated by ADAM17, but is not a lipid-raft-associated event. *Biochem. J.* 432, 283–294.
- Passequé, E., Jamieson, C.H., Aliles, L.E., and Weissman, I.L. (2003). Normal and leukemic hematopoiesis: are leukemias a stem cell disorder or a reacquisition of stem cell characteristics? *Proc. Natl. Acad. Sci. USA* 100(Suppl 1), 11842–11849.
- Ricci-Vitiani, L., Lombardi, D.G., Pilozzi, E., Biffoni, M., Todaro, M., Peschle, C., and De Maria, R. (2007). Identification and expansion of human colon-cancer-initiating cells. *Nature* 445, 111–115.
- Rosen, J.M., and Jordan, C.T. (2009). The increasing complexity of the cancer stem cell paradigm. *Science* 324, 1670–1673.
- Saif, M.W., and Chu, E. (2010). Biology of colorectal cancer. *Cancer J.* 16, 196–201.
- Saltz, L.B., Clarke, S., Díaz-Rubio, E., Scheithauer, W., Figer, A., Wong, R., Koski, S., Lichinitser, M., Yang, T.S., Rivera, F., et al. (2008). Bevacizumab in



combination with oxaliplatin-based chemotherapy as first-line therapy in metastatic colorectal cancer: a randomized phase III study. *J. Clin. Oncol.* 26, 2013–2019.

Small, D., Kovalenko, D., Kacer, D., Liaw, L., Landriscina, M., Di Serio, C., Prudovsky, I., and Maciag, T. (2001). Soluble Jagged 1 represses the function of its transmembrane form to induce the formation of the Src-dependent chord-like phenotype. *J. Biol. Chem.* 276, 32022–32030.

Sonoshita, M., Aoki, M., Fuwa, H., Aoki, K., Hosogi, H., Sakai, Y., Hashida, H., Takabayashi, A., Sasaki, M., Robine, S., et al. (2011). Suppression of colon cancer metastasis by Aes through inhibition of Notch signaling. *Cancer Cell* 19, 125–137.

Sun, X., and Artavanis-Tsakonas, S. (1997). Secreted forms of DELTA and SERRATE define antagonists of Notch signaling in *Drosophila*. *Development* 124, 3439–3448.

Takahashi, Y., Kitadai, Y., Bucana, C.D., Cleary, K.R., and Ellis, L.M. (1995). Expression of vascular endothelial growth factor and its receptor, KDR, correlates with vascularity, metastasis, and proliferation of human colon cancer. *Cancer Res.* 55, 3964–3968.

Trifonova, R., Small, D., Kacer, D., Kovalenko, D., Kolev, V., Mandinova, A., Soldi, R., Liaw, L., Prudovsky, I., and Maciag, T. (2004). The non-transmembrane form of Delta1, but not of Jagged1, induces normal migratory behavior

accompanied by fibroblast growth factor receptor 1-dependent transformation. *J. Biol. Chem.* 279, 13285–13288.

Vermeulen, L., De Sousa E Melo, F., van der Heijden, M., Cameron, K., de Jong, J.H., Borovski, T., Tuynman, J.B., Todaro, M., Merz, C., Rodermond, H., et al. (2010). Wnt activity defines colon cancer stem cells and is regulated by the microenvironment. *Nat. Cell Biol.* 12, 468–476.

Weidner, N., Semple, J.P., Welch, W.R., and Folkman, J. (1991). Tumor angiogenesis and metastasis—correlation in invasive breast carcinoma. *N. Engl. J. Med.* 324, 1–8.

Weijzen, S., Velders, M.P., Elmishad, A.G., Bacon, P.E., Panella, J.R., Nickoloff, B.J., Miele, L., and Kast, W.M. (2002). The Notch ligand Jagged-1 is able to induce maturation of monocyte-derived human dendritic cells. *J. Immunol.* 169, 4273–4278.

Wicha, M.S., Liu, S., and Dontu, G. (2006). Cancer stem cells: an old idea—a paradigm shift. *Cancer Res.* 66, 1883–1890, discussion 1895–1886.

Zhu, T.S., Costello, M.A., Talsma, C.E., Flack, C.G., Crowley, J.G., Hamm, L.L., He, X., Hervey-Jumper, S.L., Heth, J.A., Muraszko, K.M., et al. (2011). Endothelial cells create a stem cell niche in glioblastoma by providing NOTCH ligands that nurture self-renewal of cancer stem-like cells. *Cancer Res.* 71, 6061–6072.

EphA3 Maintains Tumorigenicity and Is a Therapeutic Target in Glioblastoma Multiforme

Bryan W. Day,^{1,*} Brett W. Stringer,¹ Fares Al-Ejeh,² Michael J. Ting,¹ John Wilson,⁴ Kathleen S. Ensbey,¹ Paul R. Jamieson,¹ Zara C. Bruce,¹ Yi Chieh Lim,¹ Carolin Offenhäuser,¹ Sara Charmsaz,¹ Leanne T. Cooper,¹ Jennifer K. Ellacott,¹ Angus Harding,⁴ Lucie Leveque,³ Po Inglis,^{1,5} Suzanne Allan,^{1,5} David G. Walker,⁶ Martin Lackmann,⁷ Geoffrey Osborne,⁴ Kum Kum Khanna,² Brent A. Reynolds,⁸ Jason D. Lickliter,^{1,9} and Andrew W. Boyd^{1,4,10}

¹Brain Cancer Research Unit and Leukaemia Foundation Research Unit

²Signal Transduction Laboratory

³Antigen Presentation and Immunoregulation Laboratory

Queensland Institute of Medical Research, Brisbane 4006, Australia

⁴Queensland Brain Institute, University of Queensland, Brisbane 4067, Australia

⁵Cancer Services, Royal Brisbane and Women's Hospital, Brisbane 4024, Australia

⁶BrizBrain & Spine Research Foundation, Auchenflower, Brisbane 4066, Australia

⁷Department of Biochemistry and Molecular Biology, Monash University, Melbourne 3800, Australia

⁸McKnight Brain Institute, University of Florida, Gainesville, FL 32611, USA

⁹Centre for Cancer Research, Monash Institute of Medical Research, Melbourne 3168, Australia

¹⁰Department of Medicine, University of Queensland, Herston, Brisbane 4006, Australia

*Correspondence: bryan.day@qimr.edu.au

<http://dx.doi.org/10.1016/j.ccr.2013.01.007>

SUMMARY

Significant endeavor has been applied to identify functional therapeutic targets in glioblastoma (GBM) to halt the growth of this aggressive cancer. We show that the receptor tyrosine kinase EphA3 is frequently overexpressed in GBM and, in particular, in the most aggressive mesenchymal subtype. Importantly, EphA3 is highly expressed on the tumor-initiating cell population in glioma and appears critically involved in maintaining tumor cells in a less differentiated state by modulating mitogen-activated protein kinase signaling. EphA3 knockdown or depletion of EphA3-positive tumor cells reduced tumorigenic potential to a degree comparable to treatment with a therapeutic radiolabelled EphA3-specific monoclonal antibody. These results identify EphA3 as a functional, targetable receptor in GBM.

INTRODUCTION

Glioblastoma (GBM) is the most common primary brain cancer. Standard treatment involves surgical resection, followed by radiation and temozolomide chemotherapy (Behin et al., 2003). Therapy is rarely curative due to the infiltrative nature of these tumors and their resistance to radiation and chemotherapy. Median survival is <15 months and median progression-free survival is <7 months (Stupp et al., 2005). This dismal situation motivates a search for new therapies, in particular those that target tumor-propagating cells. Gene expression profiling, together with DNA mutation data, has identified four GBM subtypes (proneural, neural, classical, and mesenchymal) (Carro

et al., 2010; Verhaak et al., 2010). There is also accumulating evidence that at least some GBMs arise from developmentally arrested neural progenitor or stem cells (Pardal et al., 2003; Reya et al., 2001; Singh et al., 2004), although this may not be universally true (Visvader, 2011). Despite this controversy, cells with dedifferentiated properties are thought to be responsible for tumor recurrence following treatment (Dick, 2008), and their intrinsic resistance to both chemotherapy and radiation requires new strategies to eradicate them (Bao et al., 2006).

Eph receptors are the largest family of receptor tyrosine kinases and have vital functions, including cell adhesion, migration, and axon guidance, during development and homeostasis (Flanagan and Vanderhaeghen, 1998; Holder and Klein, 1999;

Significance

Although debate still surrounds the cancer stem cell hypothesis in solid tumors, such as GBM, there is agreement that cells in a less differentiated, tumorigenic state exist within these highly heterogeneous tumors. These cells are thought to be responsible for tumor recurrence following treatment. Here, we demonstrate that in EphA3-expressing GBM, EphA3 has a functional role in maintaining less differentiated, tumor-initiating cells by modulation of mitogen-activated protein kinase signaling. EphA3 is lowly expressed in adult tissues and therefore represents a relatively tumor-specific therapeutic target in GBM.

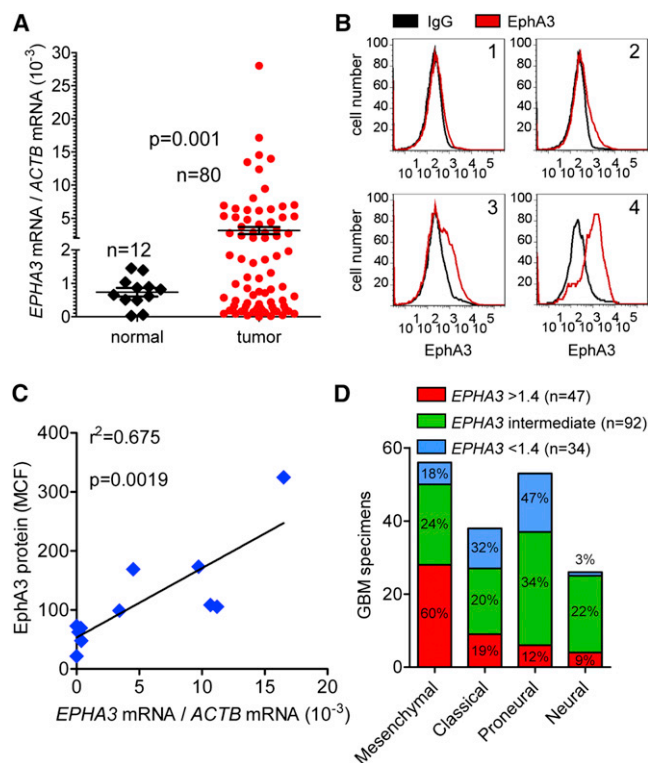


Figure 1. EphA3 Is Expressed Highly in Glioma and Is Overrepresented on Mesenchymal Tumors

(A) *EPHA3* overexpression was tested by qPCR in glioma clinical specimens ($n = 80$) compared to normal brain tissue ($n = 12$; $p = 0.001$; unpaired t test with Welch's correction). *EPHA3* mRNA levels were negligible in normal brain while 40% of clinical specimens (32/80) expressed detectable levels of *EPHA3* mRNA (more than two copies per 1,000 β -actin; further defined in Figure S1). Table S1 lists the specimens tested.

(B) Flow cytometric analysis of EphA3 protein expression in dissociated GBM clinical specimens.

(C) Linear regression analysis of *EPHA3* mRNA (qPCR) and EphA3 protein (mean channel fluorescence) levels in serum-free cultures ($n = 11$) shows a positive correlation ($r^2 = 0.675$, $p = 0.0019$). See also Figure S1.

(D) *EPHA3* microarray expression data were compared to GBM subtype classification (mesenchymal, classical, proneural, neural) in GBM specimens from the TCGA database ($n = 173$). Samples expressing *EPHA3* >1.4 -fold ($n = 47$) showed an overrepresentation of mesenchymal tumors (60%) and an underrepresentation of neural tumors (9%). The difference between each group was significant ($p = 0.001$) as assessed by multivariate analysis. See also Figures S1A–S1F.

Mann et al., 2002; Wilkinson, 2000). Eph receptors and ephrin ligands tend to be most highly expressed during development, and evidence suggests a role in regulation of stem cell differentiation and cell fate determination (Aoki et al., 2004; Conover et al., 2000; Holmberg et al., 2006; Lickliter et al., 1996; Wang et al., 2004). Ephrins and Eph receptors have been found to be aberrantly expressed in many cancers, including GBM (Pasquale, 2010). Family members implicated in gene deregulation and function in GBM include EphA2, EphA7, EphB2, and ephrin-A5 (Li et al., 2009; Nakada et al., 2004; Wang et al., 2008; Wykosky et al., 2005).

EphA3 is expressed in embryonic tissues including the brain, spinal cord, axial muscles, lungs, kidneys, and heart (Kilpatrick

et al., 1996) and appears to play a critical role in epithelial-to-mesenchymal transition (EMT) (Stephen et al., 2007). EphA3 mutations have been identified that suggest a tumor-suppressor role in some cancers (Davies et al., 2005). Conversely, overexpression of EphA3 has been observed in some cancers, including leukemia, lymphoma, lung cancers, melanomas, and gastric carcinoma (Boyd et al., 1992; Chiari et al., 2000; Dottori et al., 1999; Lawrenson et al., 2002; Wicks et al., 1992; Xi et al., 2012). EphA3 somatic mutations, which map to highly conserved regions of the gene, have been identified in GBM (Balakrishnan et al., 2007; Lisabeth et al., 2012).

Given the expression of EphA3 in many human cancers and its role in EMT, we explored the expression and function of EphA3 in GBM and, in particular, the mesenchymal subtype, which has a more aggressive and less differentiated phenotype with a poorer prognosis (Phillips et al., 2006).

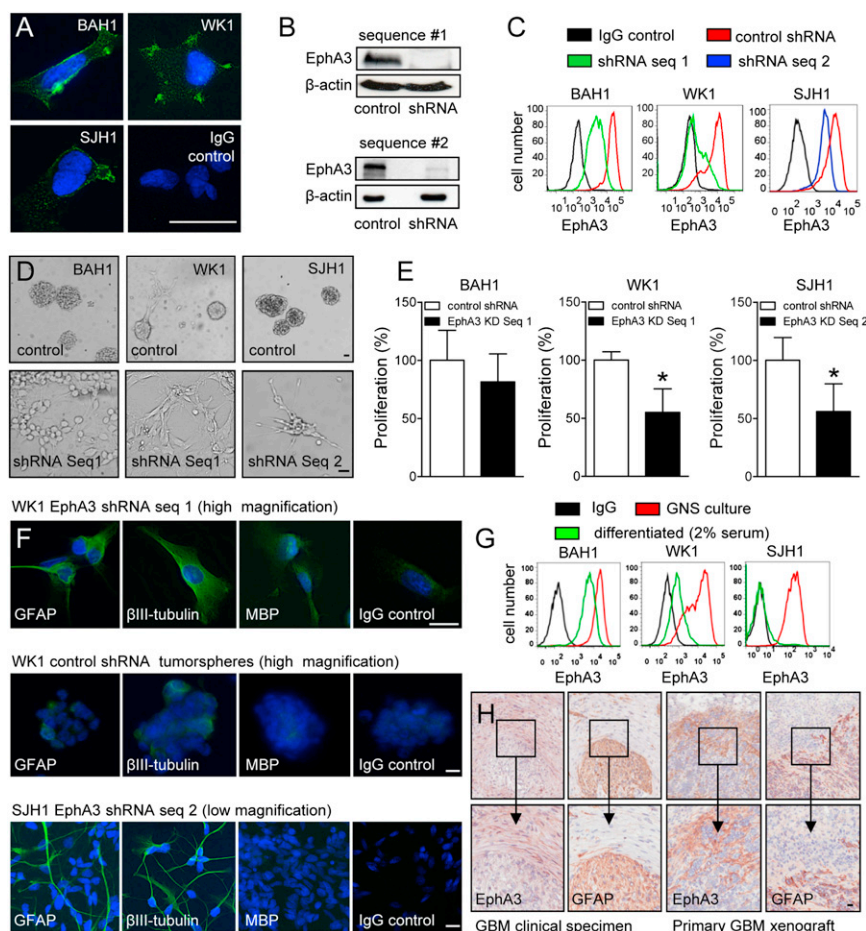
RESULTS

EphA3 Is Highly Expressed in Glioma and Is Overrepresented on Mesenchymal GBM

To investigate EphA3 expression in brain cancer, we assessed messenger RNA (mRNA) and protein levels in a series of clinical glioma specimens and specimen-derived early passage cell lines. A bank of 80 human glioma clinical specimens was collected of which 74% were GBM (WHO grade IV) (Table S1 available online). Quantitative PCR (qPCR) was performed on these tumors and 12 normal human brain specimens (Figure 1A). *EPHA3* mRNA levels were low in normal brain whereas 40% of clinical specimens (32/80) expressed significantly ($p < 0.01$) higher levels of *EPHA3* mRNA. EphA3 protein expression was assessed using flow cytometry of dissociated GBM tumor samples; representative expression profiles are shown in Figure 1B. In some cases essentially all cells were positive, whereas in others only a subset showed significant expression.

To further explore EphA3 expression, we analyzed a panel of early passage (less than five passages) cell lines from primary GBM specimens. Lines were grown in serum-free medium on a laminin substratum, because these conditions are reported to maintain the phenotype and genotype of the original tumor and enrich for tumor-initiating cells (Pollard et al., 2009). qPCR and flow cytometry were used to analyze EphA3 expression in these cultures (Figures S1A and S1B). Results showed that a greater proportion of cultures expressed *EPHA3* (60%, $n = 15$) compared to clinical specimens (40%, $n = 80$). Flow cytometry also revealed a greater than expected level of EphA3 expression when compared to the original tissue specimens (data not shown).

To determine the correlation between mRNA and protein expression, we analyzed primary serum-free cultures ($n = 11$) to compare mRNA (qPCR) and protein (mean channel fluorescence) levels (Figure 1C). Linear regression analysis showed a strong correlation ($r^2 = 0.675$, $p = 0.0019$) between mRNA and protein expression. EphA3 protein was detectable by flow cytometry when GBM lines expressed mRNA levels of two or more copies per 1,000 β -actin (Figure S1C). Additional analysis of ephrin expression by qPCR was performed in six primary serum-free cultures (Figure S1D). All samples had relatively low expression and, in particular, of the high-affinity *EPHA3* ligand *EPHRIN A5*.



To investigate if *EPHA3* expression correlated with glioma subtypes, we analyzed a data set of GBM specimens from The Cancer Genome Atlas Project (TCGA) ($n = 173$), which had been assigned GBM subtypes defined by a previous study (Verhaak et al., 2010). Samples expressing elevated *EPHA3* (>1.4 -fold; $n = 47$) showed an overrepresentation of mesenchymal tumors (60%) and an underrepresentation of neural tumors (9%), which was significant by multivariate analysis ($p = 0.0001$) (Figure 1D). Furthermore, analysis of *EPHA3* alterations, the majority being RNA upregulation, using the TCGA database revealed that altered *EPHA3* led to decreased survival in patients with mesenchymal subtype GBM ($n = 56$, $p = 0.017$; Figure S1E). Alternatively, using the Rembrandt database, *EPHA3* expression in all gliomas ($n = 454$) showed a significant correlation with survival (Figure S1F). Analysis revealed a 2-fold decrease in *EPHA3* expression ($n = 160$) correlated with increased survival ($p = 0.002$), whereas a 2-fold increase in *EPHA3* expression ($n = 34$) correlated with decreased survival ($p = 0.02$).

Loss of EphA3 Prevents Tumorsphere Formation and Induces Neuronal and Glial Cell Differentiation

Growth under neurosphere culture conditions selects against survival of terminally differentiated cells, whereas less differenti-

ated cells respond to growth factors to form “neurospheres” (Reynolds and Weiss, 1992). Under these conditions, a subset of GBM cells grow as “tumorspheres” and exhibit self-renewal and retain the capacity to differentiate (Galli et al., 2004). Consequently, to further explore EphA3 function in GBM, we generated three primary GBM cultures (BAH1, WK1, and SJH1), which were all shown to form orthotopic tumors in immune-compromised animals; we also used the established GBM cell line U251 grown as tumorspheres. The subtype of these primary lines was determined using the microarray method outlined by Verhaak et al. (2010). BAH1 and SJH1 were derived from GBMs of the neural subtype while WK1 was established from a mesenchymal GBM. Immunofluorescence staining for EphA3 showed strong membranous expression in all of the lines (Figure 2A).

We first investigated the effect of EphA3 knockdown (KD) on tumorsphere growth using two different *EPHA3* small hairpin RNA (shRNA) sequences, both of which resulted in $>90\%$ KD of EphA3 expression (Figures 2B, 2C, S2A, and S2B). In all four cell lines, following several passages the sphere-forming capability of the KD cells was reduced and was accompanied by increased cell spreading, adherence, and morphological changes (Figures 2D and S2C). Adherent cells in all three EphA3 KD primary lines grew slowly under tumorsphere culture conditions and died following subsequent cell passage. This

phenomenon was not observed in U251 cells, which grew slowly but remained viable (Figure S2D). In contrast, when EphA3 KD primary cells were grown under serum-free conditions on laminin, all three primary cultures were viable but proliferated slowly (Figure 2E). To determine whether the morphological changes following KD were the result of differentiation, cultures were stained with lineage-specific markers (Figures 2F and S2E). Positive staining for astrocytic (glial fibrillary acidic protein [GFAP]) and neuronal (β III-tubulin) markers, but minimal staining with the oligodendrocytic (myelin basic protein) lineage marker, was observed. Control tumorspheres showed minimal staining for differentiation markers (Figure S2F). We also established a tetracycline-inducible EphA3 KD system in U251 cells (Figures S2B–S2E). Whereas EphA3-positive U251 cells formed tumorspheres in the absence of tetracycline, tumorsphere formation and proliferation was greatly reduced following tetracycline-induced EphA3 KD and was accompanied by expression of differentiation markers. Following removal of tetracycline, EphA3 was re-expressed and tumorsphere formation was restored. As a specificity control for EphA3 KD, we performed a rescue experiment by re-expressing EphA3 with a mutated shRNA binding site in U251 constitutive EphA3 KD cells (Figures S2C and S2D). Following re-expression of shRNA-resistant EphA3, both proliferation and tumorsphere-forming capacity were restored.

We further compared EphA3 expression in the primary lines following growth factor withdrawal and addition of 2% fetal bovine serum (FBS), conditions that allow differentiation to occur (Figure 2G). In each case EphA3 levels decreased in serum-containing medium, providing further evidence that EphA3 is downregulated during GBM cell differentiation. When recultured in serum-free medium, EphA3 levels increased to preserum culture levels with a parallel decrease in differentiated cells (data not shown). To demonstrate that EphA3 was expressed on less differentiated cells, we assessed the expression of EphA3 compared to the expression of GFAP, a marker of astrocytes, in both patient specimens and GBM tumor xenografts. Immunohistochemistry (IHC) results are shown for sequential tissue sections from a GBM patient specimen and GBM xenograft using BAH1 cells (Figures 2H and S2G). These show a specific and discrete pattern of staining for EphA3 and GFAP, implying that EphA3 expression is high on less differentiated tumor cells and reduced on the differentiated population.

EphA3 Is Coexpressed with Markers of Undifferentiated Cells in GBM

Of the markers of less differentiated, highly proliferative cells in GBM that have been reported in the literature, among the most convincing have been CD133, integrin α 6, and CD15 (Lathia et al., 2010; Singh et al., 2004; Son et al., 2009). To investigate if EphA3 is coexpressed with these markers, we examined nine acutely dissociated GBM specimens using multiparameter flow cytometry, using the epidermal growth factor (EGF) receptor as a positive control (Figure 3A). Specimens did not show distinct subpopulations, but EphA3 appeared to be commonly coexpressed with integrin α 6 but not CD133 (complete analysis and controls shown in Figure S3A). Association with these markers was further confirmed in the primary lines using both Amnis expression analysis (Figure 3B) and flow cytometry (Figure 3C)

showing that EphA3 is most often coexpressed with integrin α 6 and CD133 but not with CD15 (for complete flow cytometry analysis and controls see Figure S3B). Given that primary serum-free cultures grown on laminin are reported to enrich for the dedifferentiated, highly proliferative cells known to express such markers as CD133, integrin α 6, and CD15, we assessed the expression of EphA3 using three primary GBM tissue specimens and the paired primary serum-free culture. Results show that EphA3 expression was increased under these culture conditions (Figure 3D). Despite two tissue specimens expressing low levels of EphA3, all samples showed a significant increase in EphA3 expression following culture for 3 weeks. We also assessed the expression by qPCR of neural and other progenitor cell markers in WK1 cells transfected with control shRNA versus *EPHA3* shRNA (Figure 3E). Results show a reduced expression of all these markers following EphA3 KD. Next, we sorted each primary culture into high and low EphA3 fractions and assessed the expression of progenitor cell markers, proliferation, and sphere-forming potential (Figures 3E and S3C). In each case, expression of at least one marker was elevated in the EphA3-high population; in the case of the mesenchymal line WK1, all markers were elevated in the EphA3-high fraction (Figure 3E). Moreover, in all lines tested, the EphA3-positive population showed a significantly ($p < 0.05$) higher capacity to form tumorspheres and to proliferate at a higher rate. Furthermore, IHC and immunofluorescence staining for CD31 and EphA3 in the same GBM xenograft section revealed that EphA3 was predominantly localized around the tumor vasculature (Figures 3F and S2G), a reported niche for GBM stem/progenitor cells (Calabrese et al., 2007). Thus, we have presented several lines of evidence that EphA3 is coexpressed with known markers of undifferentiated cells in both clinical specimens and primary cultures. This is in keeping with the finding that EphA3 is most commonly elevated in mesenchymal GBM, which are characterized by the presence of progenitor cell markers and lack of neural differentiation markers. Furthermore, EphA3 appears to be most commonly coexpressed with integrin α 6, a GBM progenitor cell marker known to be expressed in the vascular bed of GBM tumors (Lathia et al., 2010).

EphA3 Limits MAPK Pathway Activation

Previous studies have shown that EphA receptor activation can lead to increased differentiation of neural precursor cells through positive regulation of the extracellular signal-regulated kinase (ERK) mitogen-activated protein kinase (MAPK) pathway (Aoki et al., 2004). We examined ERK1/2 phosphorylation in both WK1 and U251 cells and found that the ERK/MAPK pathway was more highly activated in EphA3 KD cells compared to control (Figures 4A and S4A). In contrast, the phosphatidylinositol 3-kinases/protein kinase B and Janus-activated kinase/signal transducer and activator of transcription pathways showed no change following EphA3 KD (data not shown). Moreover, when cells had been cultured without EGF, activation of the MAPK pathway using either receptor tyrosine kinase (RTK)-dependent (EGF) or RTK-independent (PMA [phorbol-12-myristate-13-acetate]) stimulation resulted in prolonged and elevated MAPK pathway activation when EphA3 was downregulated (Figures 4B and S4B). This suggested that the differentiation observed when EphA3 was neutralized could be due to

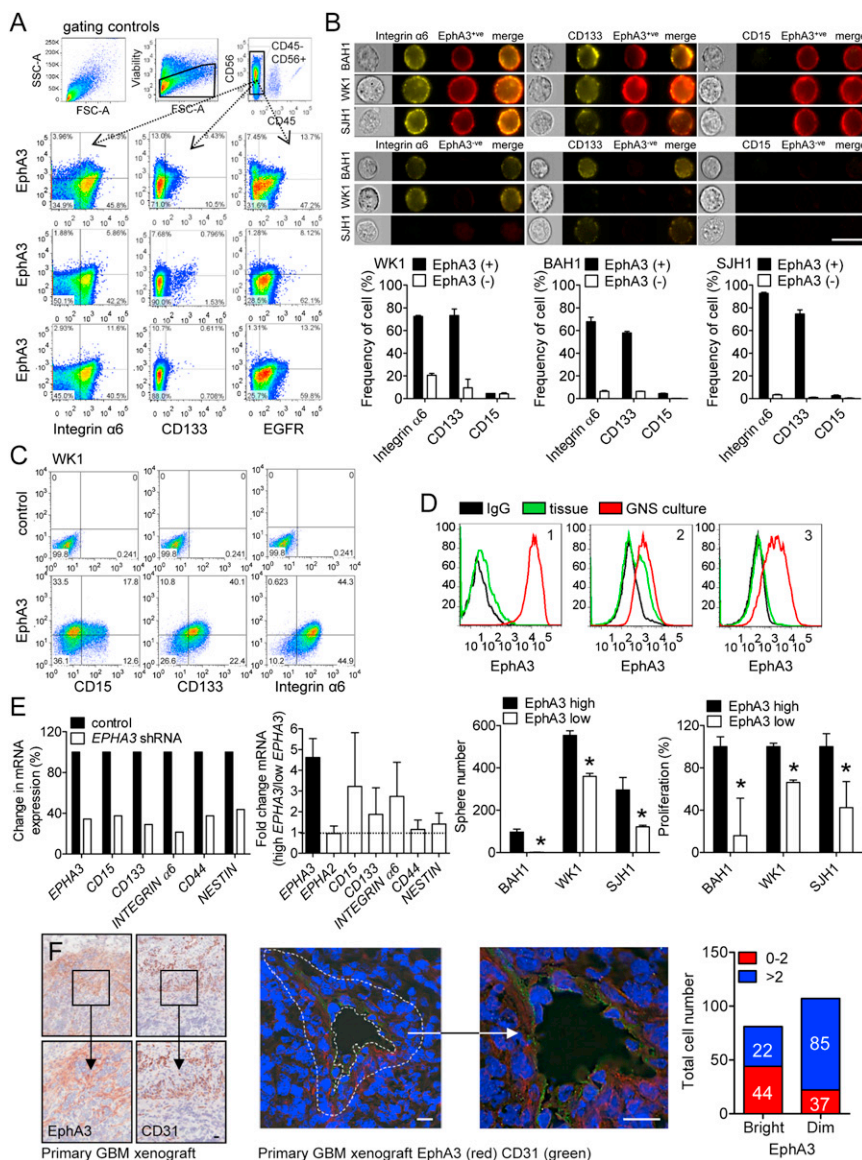


Figure 3. EphA3 Is Coexpressed with Markers of Undifferentiated Cells in GBM

(A) EphA3 coexpression with the markers integrin α6 and CD133 was assessed in GBM clinical specimens (n = 9); EGFR was used as a positive control. EphA3 was coexpressed with integrin α6, while distinct subpopulations of EphA3- and CD133-positive cells were observed in some of the samples. See Figure S3 for complete analysis and controls of nine specimens.

(B) Amnis expression analysis was performed on three primary GBM cultures for EphA3 and the markers integrin α6, CD133, and CD15; representative individual and merged fluorescent images are shown. Percentage of cells coexpressing EphA3 and the marker of interest is quantitated for each primary line (+SD, n = 3).

(C) EphA3 coexpression with the markers CD15, CD133 and integrin α6 was assessed by flow cytometry in three primary serum-free lines. Data are shown for WK1. See Figure S3 for analysis of BAH1 and SJH1.

(D) Flow cytometric analysis of paired GBM tumor tissue and serum-free culture showing expression of EphA3 is elevated under serum-free conditions compared to the original patient specimen.

(E) Stem cell-like marker expression was assessed in control shRNA versus *EPHA3* shRNA seq 1 WK1 cells. WK1 EphA3 KD cells showed a decrease in all markers tested. Expression shown as the percentage reduction in mRNA levels. Primary serum-free cultures (BAH1, WK1, and SJH1) were sorted into low and high EphA3 populations and qPCR undertaken to determine expression of undifferentiated markers, with expression shown as copy number per 1,000 β-actin. See Figure S3 for all primary lines tested. Sphere-forming potential and proliferation were also found to be significantly reduced in the EphA3-low cells compared to EphA3-high cells for each of the three primary lines (*p < 0.05, +SD; n = 3).

(F) Immunohistochemical and immunofluorescent staining of BAH1 GBM xenografted tumor shows coexpression of EphA3 and the endothelial cell marker CD31. EphA3 (red) bright cells are primarily found in close proximity to the tumor vasculature (CD31+, green). Number of bright EphA3+ versus

dim EphA3+ cells was quantitated in a localization-dependent fashion; cells in close proximity to the CD31+ cells (within two layers of cells; white dashed lines indicated boundaries) were compared to cells outside this region. Scale bar represents 20 μM. See also Figures S3A–S3D.

constitutively elevated ERK/MAPK activation. Furthermore, re-expression of EphA3 in U251 KD cells returned tumorsphere formation in parallel with a loss of constitutively activated ERK1/2 (Figure S4A). This suggested that EphA3 may be limiting MAPK signaling and thereby restricting differentiation. To further assess if ERK phosphorylation was indeed driving differentiation, we overexpressed wild-type and constitutively active mitogen-activated protein kinase kinases 1 and 2 (MEK1/2) in U251 wild-type tumorsphere cells and also downregulated ERK1/2 using small interfering RNA (siRNA) in EphA3 KD U251 tumorspheres (Figures S4C and S4D). MEK1/2 overexpression led to constitutively active ERK1/2, resulted in a loss of tumorsphere formation, and induced morphological changes indicative of differentiation and reduced cell growth. This phenomenon was reversed in EphA3 KD cells when ERK1/2 levels were reduced

by siRNA-mediated KD, restoring tumorsphere formation. Another Eph receptor, EphA2, has been shown to be frequently overexpressed in GBM (Wykosky et al., 2005). We found that EphA2 was coexpressed with EphA3 on many GBM patient samples (Table S1). Immunofluorescence staining of EphA2 and EphA3 in primary lines showed significant overlapping expression patterns (Figure S4F). Some degree of association of these proteins was demonstrated by immunoprecipitation of both EphA2 and EphA3 in U251 tumorspheres and primary serum-free cultures. Given the coexpression of the two receptors, we examined the effect of *EPHA2* shRNA-mediated KD in U251 tumorspheres. Results confirmed that, similar to EphA3 attenuation, EphA2 KD prevented tumorsphere formation, reduced proliferation (33%, p < 0.05), and resulted in sustained ERK activation following EGF stimulation (Figure S4G).

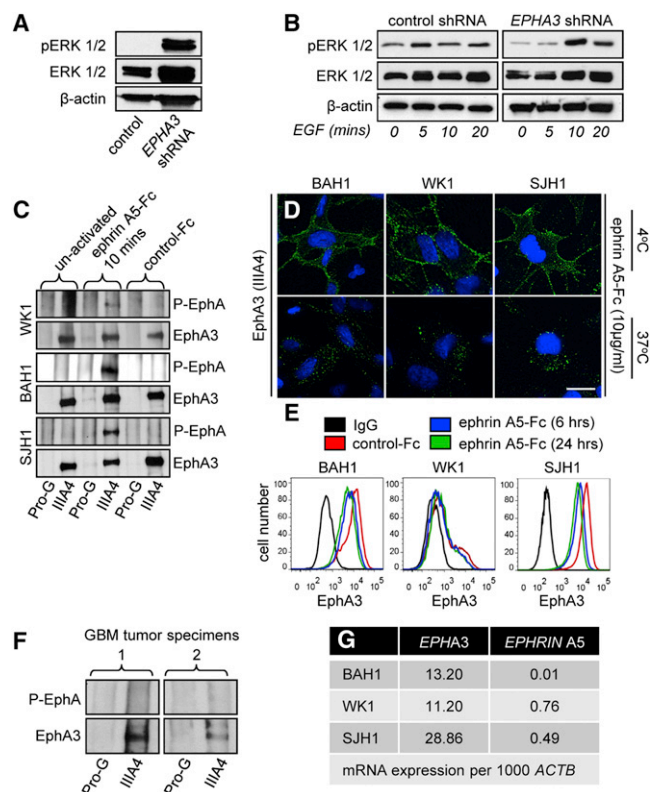


Figure 4. EphA3 Limits MAPK Pathway Activation and Exhibits Low Basal Receptor Activation In Vitro and In Vivo

(A) EphA3 KD in WK1 tumorspheres induces constitutive ERK1/2 activation. (B) EphA3 KD in WK1 tumorspheres induces elevated ERK1/2 activation following treatment with EGF (30 ng/ml). (C) Immunoprecipitation of EphA3 following treatment of BAH1, WK1, and SJH1 with soluble clustered ephrin-A5-Fc (1 μ g/ml) for 10 min revealed rapid receptor activation. No activation was detected in the unstimulated primary cultures. (D) Immunofluorescent staining of EphA3 in BAH1, WK1, and SJH1 cells showed rapid internalization of EphA3/ephrin-A5 receptor and ligand complexes following activation with ephrin-A5-Fc (10 μ g/ml) for 20 min at 37°C. EphA3 remained on the cell surface if activation was delayed by maintaining the cells at 4°C. Following ephrin-A5-Fc treatment, pronounced cell spreading and adhesion were observed. (E) Flow cytometric analysis revealed a mild reduction of EphA3 on the cell surface following treatment with ephrin-A5-Fc (10 μ g/ml) for 6 and 24 hr in BAH1 WK1 and SJH1 cells; expression is compared to control CD48-Fc (24 hr). (F) Immunoprecipitation of EphA3 in two GBM tissue specimens reveals total EphA3 was present while no receptor activation was detected. (G) qPCR expression analysis of *EPHA3* and *EPHRIN A5* in BAH1, WK1, and SJH1 shows elevated receptor expression compared to low ligand. Scale bar represents 20 μ m. See also Figures S4A–S4G.

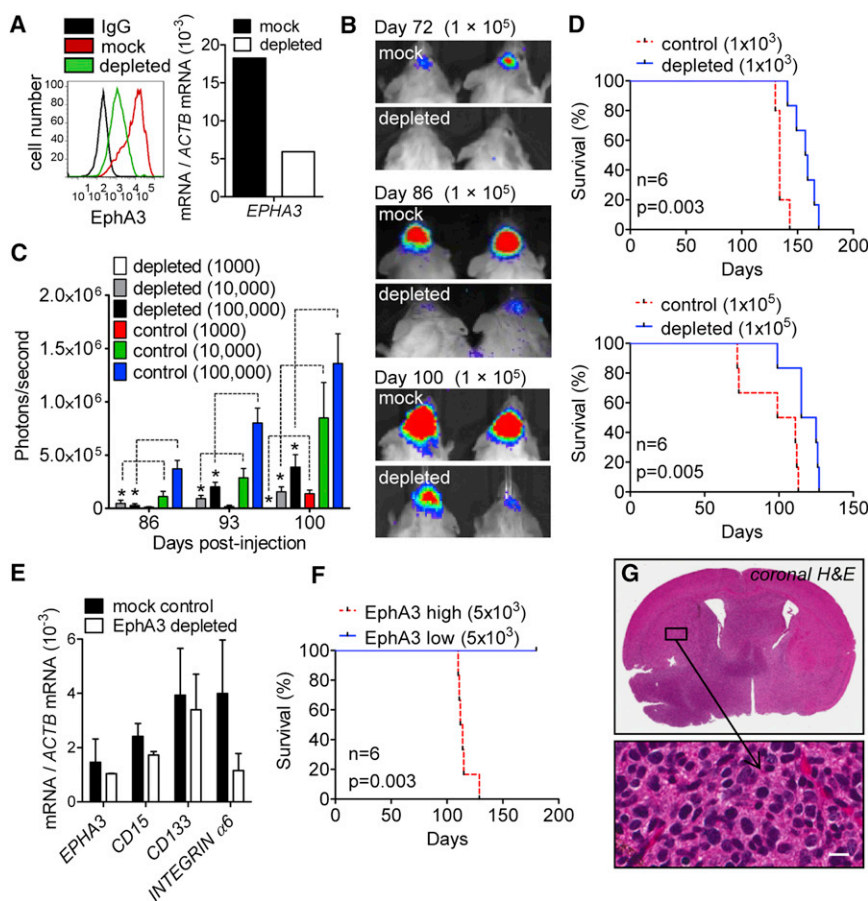
Aoki et al. (2004) showed that EphA3 activation could drive neural cell differentiation through increased MAPK pathway activation, whereas our data showed that EphA3 maintains an undifferentiated, self-renewing tumor population through a mechanism that limits MAPK signaling. We investigated the activation status of EphA3 in GBM cells with or without stimulation with the high-affinity ligand ephrin A5. The three primary lines tested showed low levels of kinase activity in unstimulated cultures, but the kinase was readily activated in response to

stimulation with clustered ephrin A5-Fc in all lines (Figure 4C). Furthermore, EphA3 activation also led to an increase in cell spreading and rapid internalization of receptor complexes (Figure 4D), and consequently a reduction in cell-surface EphA3 expression (Figure 4E). To determine if the low kinase activity in vitro reflected the activation status in vivo, we tested its activation state in GBM patient specimens. Although EphA3 was expressed in patient samples, we could not detect kinase activity (Figure 4F). qPCR expression analysis revealed that *EPHRIN A5* expression is low in all lines (Figure 4G), which is in keeping with the expression analysis in a larger group of primary lines tested (Figure S1). Receptor activation in U251 resulted in a reduction in proliferation when high concentrations of ephrin were used (Figure S4). Because the ephrin is cleaved during internalization, we assume the high concentration is needed to maintain continued internalization of Eph receptor. Ephrin A5-Fc may also activate EphA2. Therefore, to exclude an EphA2-mediated effect, we treated U251 cells with ephrin A5-Fc following EphA2 downregulation using shRNA (Figure S4H). The EphA2 KD cells showed an ephrin A5-Fc-stimulated reduction in proliferation similar to control cells. We also specifically activated EphA3 using the EphA3 monoclonal antibody (mAb) IIIA4, which, like ephrin, results in rapid internalization (Figure 4SH) (Vearing et al., 2005). An EphA3-specific reduction in proliferation was observed in U251 cells when stimulated with IIIA4, while an EphA3-negative primary GBM line (L1-NS) was unaffected. These data suggest that although EphA3 is present and functional in GBM, it is most likely functioning in a kinase-independent fashion to decrease MAPK signaling.

EphA3 Neutralization Attenuates Tumor Formation

Because EphA3 KD induced differentiation and reduced proliferation, we asked if tumorigenesis was affected. The U251 *EPHA3* shRNA sequence 1 versus control shRNA cells were injected subcutaneously into nonobese diabetic severe combined immunodeficiency (NOD/SCID) animals (Figure S5A). There was a dramatic reduction in tumor formation in the EphA3 KD group when compared with controls. Control tumors reached the 1 cm diameter endpoint at an average of 68 days. In contrast, all EphA3 KD animals survived beyond 100 days without tumor formation. The experiment was terminated at day 140, and at autopsy only one animal was found to have a small lesion. qPCR and IHC of EphA3 showed high expression in control tumors whereas low or negligible expression was detected in the single KD tumor. This small tumor also showed high expression of GFAP and β III-tubulin mRNA and GFAP and caspase-3 protein compared to the controls (Figures S5B and S5C).

Given the unique microenvironment in the brain, we also examined the antitumor potential of both EphA3 neutralization and depletion of EphA3 on the formation of intracranial xenografts. Initially, U251 EphA3 KD versus control shRNA cells were injected into the right hemisphere of NOD/SCID animals. As in the subcutaneous xenograft model, a failure of tumor formation was observed in mice injected with the KD cells (Figure 5SD), whereas control animals formed large, well-vascularized, invasive tumors at an average of 78 days after implantation. All EphA3 KD animals were free of tumor at autopsy on day 145 postimplantation. To exclude off-target shRNA effects, mutant EphA3 rescue cells were also analyzed. Control shRNA and



formed tumors with a median survival of 113 days, while no tumor formation was observed in EphA3-low cell-injected animals following 180 days ($p = 0.003$). (G) A representative coronal H&E section of a tumor formed after injection of EphA3-positive patient tumor cells. Tumors were highly infiltrative and invasive (complete H&E sections for each animal are shown in Figure S5). Scale bar represents 20 μ m. See also Figures S5A–S5H.

rescue U251 cells were injected subcutaneously and tumor formation was monitored (Figure S5E). The control tumors ($n = 3$) reached 1 cm in diameter in an average of 30 days, while the rescue tumors ($n = 4$) reached 1 cm in diameter in an average of 46 days. The somewhat slower growth of the rescue tumors may reflect the slightly lower EphA3 expression in the rescue cells but confirmed that EphA3 re-expression restored tumorigenic potential.

To confirm that EphA3 is present on tumor cells and not the stromal elements within the tumor, we orthotopically transplanted 5×10^4 tumor cells dissociated directly from a GBM patient specimen into an immune-compromised NOD/SCID animal. Five months following injection, a large invasive tumor was detected. We subsequently analyzed the expression of EphA3 in combination with the human-specific marker major histocompatibility complex class I, human leukocyte antigens (HLA) A, B, and C. Results show a clear separation between nonhuman (mouse) stromal elements that were negative for both EphA3 and HLA-A, B, and C within the tumor and EphA3-positive HLA-A, B, and C tumor cells (Figure 5SF).

To explore whether the observation that EphA3 expression was higher on less differentiated cells and therefore whether low-EphA3 cells might translate into reduced tumorigenicity,

we conducted an intracranial EphA3 depletion xenograft experiment using the WK1 primary line infected with a luciferase-encoding lentivirus. Because the EphA3 monoclonal antibody may have activating properties, we initially avoided positive fluorescence-activated cell sorting (FACS) selection and instead compared mock-depleted versus the EphA3 mAb (IIIA4) antibody-depleted cells. As expected, depletion reduced EphA3 levels and also reduced the proliferative and sphere-forming potential of the cells (Figures 5A and S5G). Cohorts of animals were injected intracranially with 1×10^3 , 1×10^4 , and 1×10^5 cells and tumor formation monitored using in vivo luminescence imaging (Figure 5B; for complete analysis see Figure S5G). Tumor luminescence was quantitated and showed a significant ($p < 0.05$) reduction in signal between mock and control for each injection group (Figure 5C). The protumorigenic effect of EphA3 expression was further confirmed by the survival curves, which showed a significant difference in survival. The median survival for the 1×10^3 group was mock 134 days versus depleted 158 days and for the 1×10^5 group was mock 105 days versus depleted 120 days (Figure 5D). When animals were culled, the tumor was resected and qPCR expression analysis performed for *EPHA3* and markers of less differentiated, highly proliferative cells (Figure 5E). Results showed a minimal

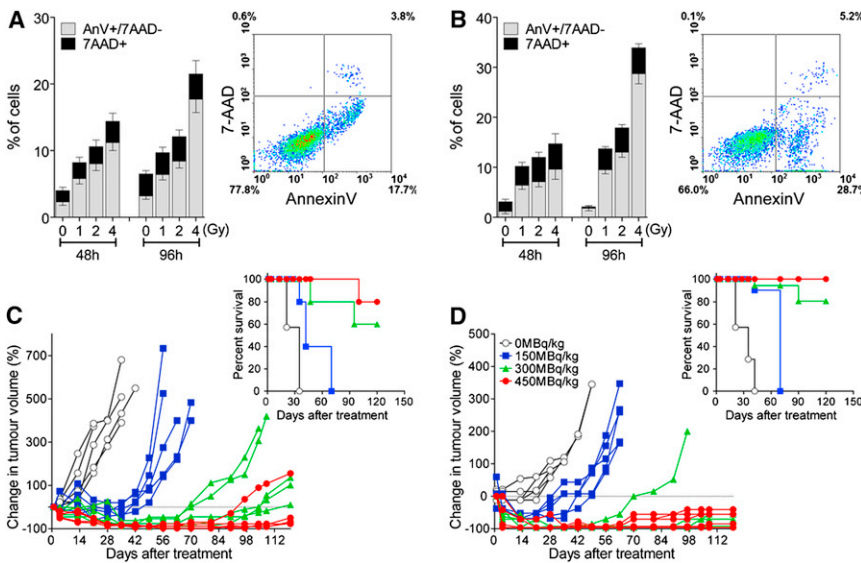


Figure 6. Lutetium-Radiolabelled Anti-EphA3 (III4) mAb Induces Apoptosis and Prevents Tumor Formation

(A and B) U251 (A) and BAH1 (B) cell cultures were treated with unlabeled DOTA-III4 mAb or escalating doses of ^{177}Lu -III4 mAb. At 48 and 96 hr, apoptosis and cell death were analyzed by Annexin V and 7-AAD staining. Representative density plots are shown for the 96 hr time point (inset) after treatment with 4 Gy of ^{177}Lu -III4 mAb. Early apoptotic cells were significantly ($p < 0.01$) higher for all doses and time points compared to cells treated with DOTA-III4 mAb (0 Gy).

(C and D) U251 (C) or BAH1 (D) tumors were grown subcutaneously in BALB/c nude mice (five animals per group). Tumors (50 mm³) were treated with DOTA-III4 mAb (50 μg per mouse) or escalating doses of ^{177}Lu -III4 mAb (50 μg per mouse). Data are shown as percentage change in tumor volume compared to day 0 (before treatments). Tumor growth curves are shown for individual mice in each treatment group. Insets show Kaplan-Meier survival plots based on tumor volume. One animal bearing a U251 tumor in the 150 MBq/kg showed

tumor regrowth and was humanely killed. The survival of 450 MBq/kg ^{177}Lu -III4 mAb-treated mice within the 120-day observation period was 80% and 100% for U251 and BAH-1 xenograft-bearing mice, respectively, whereas the survival after DOTA-III4 mAb (0 MBq/kg) was 0%.

reduction in EphA3 and other markers tested compared to mock-depleted tumors, implying that depleted cells had re-expressed EphA3 by the time the tumors had fully formed.

As a more stringent test of the involvement of EphA3 on the tumor-initiating cell population, a GBM patient tumor was dissociated and acutely sorted for high versus low EphA3 expression. A total of 5×10^3 cells from positive and negative fractions were injected orthotopically into NOD/SCID mice ($n = 6$). The median survival for the positive population was 113 days while no tumors had been detected in the negative fraction at 180 days (Figure 5F). Coronal hematoxylin and eosin (H&E) sections were prepared when animals showed signs of tumor formation. In each case, animals injected with high-EphA3-expressing cells uniformly developed highly infiltrative tumors (Figure 5G; for complete analysis, see Figure S5H). Two animals injected with low-EphA3-expressing tumor cells were culled due to signs of illness, but no tumor formation was detected (Figure S5H).

Radiolabelled Anti-EphA3 mAb Treatment Prevents Tumor Formation

The higher expression of EphA3 on dedifferentiated tumor cells suggested that an EphA3-targeted therapy might extinguish the tumor by eliminating the less differentiated, tumorigenic compartment. To test this idea, we used the EphA3 mAb (III4) radiolabelled with lutetium-177 (^{177}Lu) in mice bearing either U251 or early passage BAH1 cell xenografts. In vitro studies had shown that ^{177}Lu -III4 mAb treatment induced dose- and time-dependent apoptotic cell death in both U251 (Figure 6A) and BAH1 cells (Figure 6B) and reduced clonogenic survival (50% loss of clonogenic survival at 3.5 Gy over 48 hr, data not shown). In mice, following a single injection, the doubling time of U251 tumors was 9.9 ± 0.1 days in DOTA-III4 mAb-treated mice compared to 26.6 ± 0.2 days in mice treated with 150 MBq/kg ^{177}Lu -III4 mAb (Figure 6C). Similarly, in BAH1, 150 MBq/kg ^{177}Lu -III4 mAb lengthened the tumor-doubling

time from 12.7 ± 0.1 days in control DOTA-III4 mAb-treated mice to 30.1 ± 1 days (Figure 6D). Higher doses of ^{177}Lu -III4 mAb induced complete regression of both U251 (Figure 6C) and BAH1 (Figure 6D) tumors for up to 9 weeks following treatment. Between 9 and 17 weeks after treatments, regrowth was observed in one out five mice bearing U251 xenografts treated with 450 MBq/kg ^{177}Lu -III4 mAb (Figure 6C) and no regrowth was observed in mice bearing the patient-derived BAH1 xenografts (Figure 6D). Importantly, we observed no weight loss or any clinical signs of toxicity at any of the doses. Kaplan-Meier survival plots (Figures 6C and 6D) based on the defined tumor volume endpoint showed a significant increase in survival upon treatment with ^{177}Lu -III4 mAb ($p < 0.0001$). Given the prolonged follow up after treatment, these results suggest that all tumorigenic cells were effectively targeted by the therapy and at higher doses had extinguished the tumor.

DISCUSSION

The current investigation identifies the EphA3 receptor as being highly expressed on a significant proportion of gliomas and, in particular, on the mesenchymal subtype of GBM. Several lines of evidence show that EphA3 is often more highly expressed on the undifferentiated, tumor-initiating cells. In the first instance, EphA3 was shown to be more highly expressed in serum-free culture systems lacking differentiated cells and was downregulated when cells were differentiated. In tissue sections, the expression of EphA3 was high in areas with few differentiated (GFAP-positive) cells and lower in areas of positive GFAP expression. We observed an association of EphA3 with integrin $\alpha 6$ in patient specimens, a known marker of stem-like cells, but not so clearly with CD133, consistent with heterogeneity within the undifferentiated fraction in GBM (Lathia et al., 2010).

Importantly, we show that EphA3 has a critical role in maintaining GBM cells in an undifferentiated state by limiting MAPK

signaling (model shown in [Figure S4E](#)). EphA3 attenuation resulted in partial differentiation and decreased proliferation. Interestingly, if EphA3 was activated sufficiently to induce internalization, then the loss of EphA3 from the cell surface also resulted in reduced cell growth, implying that a relatively small loss of Eph receptor expression results in a shift in the balance between undifferentiated, highly proliferative cells and more differentiated, slowly dividing nontumorigenic cells. Indeed, we show that in lines that coexpress EphA2 or EphA3, loss of either is sufficient to alter this balance toward differentiation. Critically, the presence of EphA3 was shown to be needed for the function of tumor-initiating cells because loss of EphA3 was shown to markedly reduce tumorigenic potential.

Sustained MAPK signaling is able to drive differentiation of neural progenitors ([Aoki et al., 2004](#)). Moreover, EphA receptors have been shown to direct differentiation of neural stem cells via the MAPK pathway during CNS development. EphA3 is strongly coexpressed with nestin, a marker of undifferentiated neural cells, in the ventricular zone during murine development and in neurosphere cultures ([Aoki et al., 2004](#)). We show that in GBM, loss of EphA3 resulted in elevated MAPK signaling in parallel with partial loss of neurosphere formation, reduced proliferation, and the acquisition of differentiation markers. We show that regulation of ERK/MAPK signaling by EphA3 in GBM is kinase independent and also independent of the upstream activators of MAPK signaling.

The preferential expression of EphA3 in mesenchymal GBM is noteworthy. Mesenchymal tumors behave more aggressively and have a poorer prognosis ([Carro et al., 2010](#); [Phillips et al., 2006](#); [Thiery, 2002](#)). Notably, recurrent GBM is associated with a shift to a more mesenchymal state ([Phillips et al., 2006](#)). Studies of EphA3 knockout mice show that during heart development, EphA3 expression, induced by EMT, has a critical role in formation of atrioventricular valves and septa ([Stephen et al., 2007](#)). These findings suggest that EphA3 expression may increase as part of the switch to a more mesenchymal (sarcoma-tous) phenotype.

We noted that approximately 40% of GBM clinical specimens expressed significantly increased levels of EphA3 compared to normal brain. A further 20% of specimens expressed lower levels of EphA3 that were still elevated above normal brain tissues. Interestingly, most tumors, when cultured on laminin under conditions preventing differentiation, expressed EphA3 irrespective of subtype. Multiplex flow cytometric analysis of patient specimens revealed a positive association of EphA3 and integrin $\alpha 6$ but not other markers such as CD133. Based on these studies, EphA3 is not restricted to but it is more highly expressed on the less differentiated tumorigenic cells and more widely expressed in less differentiated tumors such as the mesenchymal subtype ([Phillips et al., 2006](#)). In some cases, EphA3 appeared to be prominently expressed around the tumor vasculature of GBM xenografts, a known stem cell niche in GBM ([Calabrese et al., 2007](#)). A recent study has shown that the laminin receptor integrin $\alpha 6$, a key protein in extracellular matrix modulation, is also localized in the perivascular niche and can regulate tumor-initiating cells ([Lathia et al., 2010](#)).

To explore the potential of EphA3 as a therapeutic target, we radiolabelled the EphA3 mAb (IIIA4) using lutetium-177. A single dose of the labeled antibody showed pronounced efficacy in

preclinical models with very low toxicity. The failure of tumors to regrow for 16 weeks following ^{177}Lu -IIIA4 mAb treatment strongly suggests that the treatment has targeted the tumor-initiating cell compartment. This supports the development of EphA3-based targeted therapies for the treatment of GBM.

Significantly, we demonstrate that EphA3 plays an active role in maintaining tumor cells in a dedifferentiated, tumorigenic state. Moreover, EphA3 is most highly expressed in the more aggressive and undifferentiated mesenchymal GBM subtype. What then might be the benefits of therapeutic targeting of this cell-surface receptor? EphA3 is expressed at low levels in adult tissues, making it relatively tumor specific. More importantly, our results suggest that such therapy can eliminate the tumor-initiating cells, thereby stopping the tumor at its source.

EXPERIMENTAL PROCEDURES

Patient Tumors

This study was approved by the human ethics committee of the Queensland Institute of Medical Research (QIMR) and Royal Brisbane and Women's Hospital (RBWH). All patients signed an approved consent form prior to surgery. Specimens were examined by a neuropathologist to verify tumor type and grade ([Table S1](#)).

GBM Cell Culture

Primary cell lines were derived from GBM specimens and maintained either as primary serum-free cultures grown on laminin ([Pollard et al., 2009](#)) or as tumorsphere cultures using StemPro NSC SFM (Invitrogen). The ATCC GBM cell line U251 was cultured in RPMI 1640 media containing 10% FBS or cultured as tumorspheres. All cultures were grown at 37°C under 5% CO₂/95% humidified air.

PCR Analysis

RNA was extracted using TRIzol (Invitrogen). First strand cDNA was synthesized using random hexamers and Superscript III (Invitrogen). Real-time PCR was carried out using SYBR Green (Applied Biosystems). Cycling conditions and primers are listed in [Supplemental Experimental Procedures](#).

shRNA Knock Down

EPHA3 shRNA seq 1 was cloned into pSuperior.neo+gfp (Oligoengine). The inducible KD system was generated using the tetracycline repressor construct pcDNA 6/TR (Invitrogen). *EPHA3* shRNA seq 2 and control construct was the mission lentivirus SCHLVN, Clone ID TRCN0000196830 (Sigma). shRNA sequences are listed in [Supplemental Experimental Procedures](#).

Multiplex Analysis

Two eight-color multiplex analysis was conducted on nine GBM specimens. Cells were selected using a viability dye, hematopoietic lineage cells were excluded using CD45, and CD56 was used to select cells of neural and glial lineage. Cells were analyzed on a LSR 2 (BD); data analysis was carried out using Treestar FlowJo software (version 7.6.4). Antibodies are listed in [Supplemental Experimental Procedures](#).

Amnis Image Stream

Samples were run on an ImageStream[®] as previously described ([Haney et al., 2011](#)) with minor modification. Briefly, 5,000 events were collected for each sample and single color controls used to create a compensation matrix to correct for spectral overlap. All data were then analyzed using IDEAS software (Amnis Corporation, Seattle, WA, USA).

Amnis, IHC, Immunofluorescence, FACS, and Western Blotting Antibodies

For IHC, GFAP (Biocare medical CM065B, 1:1,000), EphA3 in-house mAb (IIIA4, 1:100), and CD31 (Santa Cruz sc1506, 1:100) were used.



For FACS/immunofluorescence, EphA2 in-house mAb (1F7, 5 μ g/ml) and EphA3 in-house mAb (IIIA4, 5 μ g/ml), CD133 (Miltenyi AC133, 1:10), β III-tubulin (Promega G712A, 1:100), GFAP (DAKO 20334, 1:100), Integrin α 6 (Millipore CBL458, 1:100), myelin basic protein (Sigma M3821, 1:100), and control IgG1 (BD 349040, 1:400) were used.

For western blotting, we used EphA3 in-house rabbit polyclonal (1:2,000), Upstate antibodies ERK1/2 (06-182, 1:1,000), p-ERK1/2 (05-797, 1:1,000), Akt1 (AB3137, 1:1,000), and p-Akt1 (1:1,000), and Stat3 (Santa Cruz 81523, 1:1,000). β -actin was used as a loading control (Sigma, 1:2,000).

Subcutaneous and Orthotopic Xenografts

This study was approved by the QIMR animal ethics committee. Experiments were conducted using 5-week-old NOD/SCID mice. A total of 2×10^6 cells were injected subcutaneously and animals were sacrificed when tumors exceeded 1 cm in diameter. A total of 1×10^5 (for U251 experiments), 1×10^3 , 1×10^4 , 1×10^5 (for WK1 depletion experiments), and 5×10^3 (for acutely sorted clinical specimen) cells were injected intracranially using a stereotactic device at a depth of 3 mm into the right cerebral hemisphere. Animals were sacrificed when they showed signs of tumor formation (hunching, weight loss, rough coat).

In Vitro and In Vivo Treatment Using ^{177}Lu -IIIA4 mAb

For in vitro studies, ^{177}Lu -IIIA4 mAb (preparation described in [Supplemental Experimental Procedures](#)) was diluted to achieve a cumulative dose based on the dose rate constant of ^{177}Lu being 0.283 g.rad/ $\mu\text{Ci.hr}$ (Kocher, 1981). U251 and BAH1 GBM cultures were subjected to treatments with escalating doses (0–4 Gy) of ^{177}Lu -IIIA4 mAb for 48 or 72 hr and assayed for apoptosis using Annexin V and 7-ADD.

For in vivo studies, BALB/c nude mice were injected subcutaneously with 2×10^6 U251 or BAH1 cells. Treatments with unlabeled DOTA-IIIA4 mAb or escalating doses of ^{177}Lu -labeled DOTA-IIIA4 mAb were initiated when tumors reached 50 mm³. Unlabeled or labeled IIIA4 mAb was administered intravenously as a single dose. Animals were monitored for clinical signs of toxicity and tumor formation was monitored twice weekly by calliper measurement (detailed in [Supplemental Experimental Procedures](#)).

Immunoprecipitation

Serum-starved cultures were lysed in cold lysis buffer and precleared using CnBr inactivated beads. Total protein (2–5mg) was preincubated with either EphA2 (1F7), EphA3 (IIIA4), or EGFR (528) antibodies (1 μ g per 1 mg protein) for a minimum of 2 hr at 4°C. Prewashed protein G beads were added with further incubation for 1 hr at 4°C.

Statistical Analysis

A two-tailed Student's *t* test determined the probability of difference and a *p* value < 0.05 was considered significant. A χ^2 test was used to evaluate significance of GBM subtypes. Correlation coefficient was determined using parametric linear regression analysis.

SUPPLEMENTAL INFORMATION

Supplemental Information includes one table, five figures, and Supplemental Experimental Procedures and can be found with this article online at <http://dx.doi.org/10.1016/j.ccr.2013.01.007>.

ACKNOWLEDGMENTS

We thank neurosurgeons Dr. Rosalind Jeffree, Dr. Craig Winter, and Dr. Gert Tolleison from the RBWH, Grace Chojnowski and Paula Hall from the QIMR Flow Cytometry Facility, Dr. Leesa Wockner from the QIMR Statistics Department, Prof. Geoff Hill from the QIMR Bone Marrow Transplant Laboratory, Dr. Trina Yeadon from the QIMR Leukaemia Foundation Research Unit, and Dr. Thomas Robertson from the RBWH Pathology Department. This work was supported by project and program grants from the National Health and Medical Research Council (NHMRC; project grants to A.W.B. and senior principal research fellowship to K.K.K.). This work was supported in part by a grant from Kalabios Pharmaceuticals, Inc.

Received: August 5, 2011

Revised: March 21, 2012

Accepted: January 14, 2013

Published: February 11, 2013

REFERENCES

- Aoki, M., Yamashita, T., and Tohyama, M. (2004). EphA receptors direct the differentiation of mammalian neural precursor cells through a mitogen-activated protein kinase-dependent pathway. *J. Biol. Chem.* 279, 32643–32650.
- Balakrishnan, A., Bleeker, F.E., Lamba, S., Rodolfo, M., Daniotti, M., Scarpa, A., van Tilborg, A.A., Leenstra, S., Zanoni, C., and Bardelli, A. (2007). Novel somatic and germline mutations in cancer candidate genes in glioblastoma, melanoma, and pancreatic carcinoma. *Cancer Res.* 67, 3545–3550.
- Bao, S., Wu, Q., McLendon, R.E., Hao, Y., Shi, Q., Hjelmeland, A.B., Dewhirst, M.W., Bigner, D.D., and Rich, J.N. (2006). Glioma stem cells promote chemoresistance by preferential activation of the DNA damage response. *Nature* 444, 756–760.
- Behin, A., Hoang-Xuan, K., Carpentier, A.F., and Delattre, J.Y. (2003). Primary brain tumours in adults. *Lancet* 361, 323–331.
- Boyd, A.W., Ward, L.D., Wicks, I.P., Simpson, R.J., Salvaris, E., Wilks, A., Welch, K., Loudovaris, M., Rockman, S., and Busmanis, I. (1992). Isolation and characterization of a novel receptor-type protein tyrosine kinase (*hek*) from a human pre-B cell line. *J. Biol. Chem.* 267, 3262–3267.
- Calabrese, C., Poppleton, H., Kocak, M., Hogg, T.L., Fuller, C., Hamner, B., Oh, E.Y., Gaber, M.W., Finklestein, D., Allen, M., et al. (2007). A perivascular niche for brain tumor stem cells. *Cancer Cell* 11, 69–82.
- Carro, M.S., Lim, W.K., Alvarez, M.J., Bollo, R.J., Zhao, X., Snyder, E.Y., Sulman, E.P., Anne, S.L., Doetsch, F., Colman, H., et al. (2010). The transcriptional network for mesenchymal transformation of brain tumours. *Nature* 463, 318–325.
- Chiari, R., Hames, G., Stroobant, V., Texier, C., Maillère, B., Boon, T., and Coulie, P.G. (2000). Identification of a tumor-specific shared antigen derived from an Eph receptor and presented to CD4 T cells on HLA class II molecules. *Cancer Res.* 60, 4855–4863.
- Conover, J.C., Doetsch, F., Garcia-Verdugo, J.M., Gale, N.W., Yancopoulos, G.D., and Alvarez-Buylla, A. (2000). Disruption of Eph/ephrin signaling affects migration and proliferation in the adult subventricular zone. *Nat. Neurosci.* 3, 1091–1097.
- Davies, H., Hunter, C., Smith, R., Stephens, P., Greenman, C., Bignell, G., Teague, J., Butler, A., Edkins, S., Stevens, C., et al. (2005). Somatic mutations of the protein kinase gene family in human lung cancer. *Cancer Res.* 65, 7591–7595.
- Dick, J.E. (2008). Stem cell concepts renew cancer research. *Blood* 112, 4793–4807.
- Dottori, M., Down, M., Hüttmann, A., Fitzpatrick, D.R., and Boyd, A.W. (1999). Cloning and characterization of EphA3 (Hek) gene promoter: DNA methylation regulates expression in hematopoietic tumor cells. *Blood* 94, 2477–2486.
- Flanagan, J.G., and Vanderhaeghe, P. (1998). The ephrins and Eph receptors in neural development. *Annu. Rev. Neurosci.* 21, 309–345.
- Galli, R., Binda, E., Orfanelli, U., Cipelletti, B., Gritti, A., De Vitis, S., Fiocco, R., Foroni, C., Dimeco, F., and Vescovi, A. (2004). Isolation and characterization of tumorigenic, stem-like neural precursors from human glioblastoma. *Cancer Res.* 64, 7011–7021.
- Haney, D., Quigley, M.F., Asher, T.E., Ambrozak, D.R., Gostick, E., Price, D.A., Douek, D.C., and Betts, M.R. (2011). Isolation of viable antigen-specific CD8+ T cells based on membrane-bound tumor necrosis factor (TNF)- α expression. *J. Immunol. Methods* 369, 33–41.
- Holder, N., and Klein, R. (1999). Eph receptors and ephrins: effectors of morphogenesis. *Development* 126, 2033–2044.
- Holmberg, J., Genander, M., Halford, M.M., Annerén, C., Sondell, M., Chumley, M.J., Silvany, R.E., Henkemeyer, M., and Frisén, J. (2006). EphB receptors coordinate migration and proliferation in the intestinal stem cell niche. *Cell* 125, 1151–1163.

- Kilpatrick, T.J., Brown, A., Lai, C., Gassmann, M., Goulding, M., and Lemke, G. (1996). Expression of the Tyro4/Mek4/Cek4 gene specifically marks a subset of embryonic motor neurons and their muscle targets. *Mol. Cell. Neurosci.* 7, 62–74.
- Kocher, D.C. (1981). *Radioactive Decay Data Tables: A Handbook of Decay Data for Application to Radiation Dosimetry and Radiological Assessments* (Washington, DC: U.S. DOE Technical Information Center; DOE/TIC-11026).
- Lathia, J.D., Gallagher, J., Heddleston, J.M., Wang, J., Eyler, C.E., Macsworlds, J., Wu, Q., Vasanji, A., McLendon, R.E., Hjelmeland, A.B., and Rich, J.N. (2010). Integrin alpha 6 regulates glioblastoma stem cells. *Cell Stem Cell* 6, 421–432.
- Lawrenson, I.D., Wimmer-Kleikamp, S.H., Lock, P., Schoenwaelder, S.M., Down, M., Boyd, A.W., Alewood, P.F., and Lackmann, M. (2002). Ephrin-A5 induces rounding, blebbing and de-adhesion of EphA3-expressing 293T and melanoma cells by CrkII and Rho-mediated signalling. *J. Cell Sci.* 115, 1059–1072.
- Li, J.J., Liu, D.P., Liu, G.T., and Xie, D. (2009). EphrinA5 acts as a tumor suppressor in glioma by negative regulation of epidermal growth factor receptor. *Oncogene* 28, 1759–1768.
- Lickliter, J.D., Smith, F.M., Olsson, J.E., Mackwell, K.L., and Boyd, A.W. (1996). Embryonic stem cells express multiple Eph-subfamily receptor tyrosine kinases. *Proc. Natl. Acad. Sci. USA* 93, 145–150.
- Lisabeth, E.M., Fernandez, C., and Pasquale, E.B. (2012). Cancer somatic mutations disrupt functions of the EphA3 receptor tyrosine kinase through multiple mechanisms. *Biochemistry* 51, 1464–1475.
- Mann, F., Peuckert, C., Dehner, F., Zhou, R., and Bolz, J. (2002). Ephrins regulate the formation of terminal axonal arbors during the development of thalamocortical projections. *Development* 129, 3945–3955.
- Nakada, M., Niska, J.A., Miyamori, H., McDonough, W.S., Wu, J., Sato, H., and Berens, M.E. (2004). The phosphorylation of EphB2 receptor regulates migration and invasion of human glioma cells. *Cancer Res.* 64, 3179–3185.
- Pardal, R., Clarke, M.F., and Morrison, S.J. (2003). Applying the principles of stem-cell biology to cancer. *Nat. Rev. Cancer* 3, 895–902.
- Pasquale, E.B. (2010). Eph receptors and ephrins in cancer: bidirectional signalling and beyond. *Nat. Rev. Cancer* 10, 165–180.
- Phillips, H.S., Kharbanda, S., Chen, R., Forrest, W.F., Soriano, R.H., Wu, T.D., Misra, A., Nigro, J.M., Colman, H., Soroceanu, L., et al. (2006). Molecular subclasses of high-grade glioma predict prognosis, delineate a pattern of disease progression, and resemble stages in neurogenesis. *Cancer Cell* 9, 157–173.
- Pollard, S.M., Yoshikawa, K., Clarke, I.D., Danovi, D., Stricker, S., Russell, R., Bayani, J., Head, R., Lee, M., Bernstein, M., et al. (2009). Glioma stem cell lines expanded in adherent culture have tumor-specific phenotypes and are suitable for chemical and genetic screens. *Cell Stem Cell* 4, 568–580.
- Reya, T., Morrison, S.J., Clarke, M.F., and Weissman, I.L. (2001). Stem cells, cancer, and cancer stem cells. *Nature* 414, 105–111.
- Reynolds, B.A., and Weiss, S. (1992). Generation of neurons and astrocytes from isolated cells of the adult mammalian central nervous system. *Science* 255, 1707–1710.
- Singh, S.K., Hawkins, C., Clarke, I.D., Squire, J.A., Bayani, J., Hide, T., Henkelman, R.M., Cusimano, M.D., and Dirks, P.B. (2004). Identification of human brain tumour initiating cells. *Nature* 432, 396–401.
- Son, M.J., Woolard, K., Nam, D.H., Lee, J., and Fine, H.A. (2009). SSEA-1 is an enrichment marker for tumor-initiating cells in human glioblastoma. *Cell Stem Cell* 4, 440–452.
- Stephen, L.J., Fawkes, A.L., Verhoeve, A., Lemke, G., and Brown, A. (2007). A critical role for the EphA3 receptor tyrosine kinase in heart development. *Dev. Biol.* 302, 66–79.
- Stupp, R., Mason, W.P., van den Bent, M.J., Weller, M., Fisher, B., Taphoorn, M.J., Belanger, K., Brandes, A.A., Marosi, C., Bogdahn, U., et al.; European Organisation for Research and Treatment of Cancer Brain Tumor and Radiotherapy Groups; National Cancer Institute of Canada Clinical Trials Group. (2005). Radiotherapy plus concomitant and adjuvant temozolomide for glioblastoma. *N. Engl. J. Med.* 352, 987–996.
- Thiery, J.P. (2002). Epithelial-mesenchymal transitions in tumour progression. *Nat. Rev. Cancer* 2, 442–454.
- Vearing, C., Lee, F.T., Wimmer-Kleikamp, S., Spirkoska, V., To, C., Stylianou, C., Spanevello, M., Brechbiel, M., Boyd, A.W., Scott, A.M., and Lackmann, M. (2005). Concurrent binding of anti-EphA3 antibody and ephrin-A5 amplifies EphA3 signaling and downstream responses: potential as EphA3-specific tumor-targeting reagents. *Cancer Res.* 65, 6745–6754.
- Verhaak, R.G., Hoadley, K.A., Purdom, E., Wang, V., Qi, Y., Wilkerson, M.D., Miller, C.R., Ding, L., Golub, T., Mesirov, J.P., et al.; Cancer Genome Atlas Research Network. (2010). Integrated genomic analysis identifies clinically relevant subtypes of glioblastoma characterized by abnormalities in PDGFRA, IDH1, EGFR, and NF1. *Cancer Cell* 17, 98–110.
- Visvader, J.E. (2011). Cells of origin in cancer. *Nature* 469, 314–322.
- Wang, L.F., Fokas, E., Juricko, J., You, A., Rose, F., Pagenstecher, A., Engenhardt-Cabillic, R., and An, H.X. (2008). Increased expression of EphA7 correlates with adverse outcome in primary and recurrent glioblastoma multiforme patients. *BMC Cancer* 8, 79.
- Wang, Z., Cohen, K., Shao, Y., Mole, P., Dombkowski, D., and Scadden, D.T. (2004). Ephrin receptor, EphB4, regulates ES cell differentiation of primitive mammalian hemangioblasts, blood, cardiomyocytes, and blood vessels. *Blood* 103, 100–109.
- Wicks, I.P., Wilkinson, D., Salvaris, E., and Boyd, A.W. (1992). Molecular cloning of HEK, the gene encoding a receptor tyrosine kinase expressed by human lymphoid tumor cell lines. *Proc. Natl. Acad. Sci. USA* 89, 1611–1615.
- Wilkinson, D.G. (2000). Eph receptors and ephrins: regulators of guidance and assembly. *Int. Rev. Cytol.* 196, 177–244.
- Wykosky, J., Gibo, D.M., Stanton, C., and Debinski, W. (2005). EphA2 as a novel molecular marker and target in glioblastoma multiforme. *Mol. Cancer Res.* 3, 541–551.
- Xi, H.Q., Wu, X.S., Wei, B., and Chen, L. (2012). Aberrant expression of EphA3 in gastric carcinoma: correlation with tumor angiogenesis and survival. *J. Gastroenterol.* 47, 785–794.

Role of Macrophage Targeting in the Antitumor Activity of Trabectedin

Giovanni Germano,¹ Roberta Frapolli,^{2,10} Cristina Belgiovine,^{1,10} Achille Anselmo,¹ Samantha Pesce,¹ Manuela Liguori,¹ Eugenio Erba,² Sarah Uboldi,² Massimo Zucchetti,² Fabio Pasqualini,¹ Manuela Nebuloni,³ Nico van Rooijen,⁵ Roberta Mortarini,⁶ Luca Beltrame,² Sergio Marchini,² Ilaria Fuso Nerini,² Roberta Sanfilippo,⁷ Paolo G. Casali,⁷ Silvana Pilotti,⁸ Carlos M. Galmarini,⁹ Andrea Anichini,⁶ Alberto Mantovani,^{1,4} Maurizio D'Incalci,^{2,*} and Paola Allavena^{1,*}

¹Department Immunology and Inflammation, IRCCS Clinical and Research Institute Humanitas, 20089 Rozzano, Milan, Italy

²Department of Oncology, Mario Negri Institute for Pharmacological Research, 20156 Milan, Italy

³Pathology Unit, L. Sacco Department of Clinical Sciences

⁴Department of Medical Biotechnology and Translational Medicine University of Milan, 20122 Milan, Italy

⁵Department of Molecular Cell Biology, VU Medical Center, 1081 BT Amsterdam, The Netherlands

⁶Human Tumor Immunobiology Unit, Department of Experimental Oncology and Molecular Medicine

⁷Adult Sarcoma Medical Oncology Unit, Department of Cancer Medicine

⁸Pathology Department

Fondazione IRCCS, Istituto Nazionale dei Tumori, 20133 Milan, Italy

⁹PharmaMar, 28770 Madrid, Spain

¹⁰These authors contributed equally to this work

*Correspondence: maurizio.dincalci@marionegri.it (M.D.), paola.allavena@humanitasresearch.it (P.A.)
<http://dx.doi.org/10.1016/j.ccr.2013.01.008>

SUMMARY

There is widespread interest in macrophages as a therapeutic target in cancer. Here, we demonstrate that trabectedin, a recently approved chemotherapeutic agent, induces rapid apoptosis exclusively in mononuclear phagocytes. In four mouse tumor models, trabectedin caused selective depletion of monocytes/macrophages in blood, spleens, and tumors, with an associated reduction of angiogenesis. By using trabectedin-resistant tumor cells and myeloid cell transfer or depletion experiments, we demonstrate that cytotoxicity on mononuclear phagocytes is a key component of its antitumor activity. Monocyte depletion, including tumor-associated macrophages, was observed in treated tumor patients. Trabectedin activates caspase-8-dependent apoptosis; selectivity for monocytes versus neutrophils and lymphocytes is due to differential expression of signaling and decoy TRAIL receptors. This unexpected property may be exploited in different therapeutic strategies.

INTRODUCTION

The last decade witnessed an ever-growing awareness of the promoting role of chronic inflammation in cancer initiation and progression (Balkwill and Mantovani, 2001; Ben-Neriah and Karin, 2011; Coussens and Werb, 2002; Mantovani et al., 2008; Murray and Wynn, 2011). Cancer-related inflammation is now

recognized as a hallmark of tumors (Colotta et al., 2009; Hanahan and Weinberg, 2011). Tumor-associated macrophages (TAM) are present in large numbers in tumor tissues and are key promoters of cancer-related inflammation (Allavena and Mantovani, 2012; DeNardo et al., 2009; Joyce and Pollard, 2009; Mantovani et al., 2002; Martinez et al., 2009; Pollard, 2004; Qian and Pollard, 2010).

Significance

Tumor-associated macrophages (TAM) elicit cancer-promoting inflammation and have been implicated in cancer progression and resistance to therapies, thus representing attractive therapeutic targets. Trabectedin is a recently approved chemotherapeutic agent of marine origin that is clinically active in different tumors. Here, we report that trabectedin selectively depletes in vivo mononuclear phagocytes, including TAM. Evidence is provided that macrophage targeting is a key component of the antitumor activity of trabectedin. Selective mononuclear phagocyte depletion occurs in tumor patients who receive trabectedin-based therapy. These findings shed unexpected light on the mode of action of a clinically useful anticancer agent, provide strong proof-of-concept evidence for macrophage targeting in humans, and open interesting perspectives for the rational exploitation of this peculiar property in therapeutic settings.

Several mouse and human studies have shown that high TAM density is mostly associated with poor patient prognosis and resistance to therapies (DeNardo et al., 2011; Mazziere et al., 2011; Steidl et al., 2010). Based on these findings and general paradigms, TAM are considered attractive targets for antitumor interventions (Balkwill and Mantovani, 2010; Hanahan and Coussens, 2012). Strategies to exploit TAM as therapeutic target include re-education (Beatty et al., 2011; Duluc et al., 2009; Guiducci et al., 2005; Rolny et al., 2011), deletion by killing or blocking of recruitment (DeNardo et al., 2011; Qian et al., 2011; van Rooijen and van Kesteren-Hendrikx, 2003; Zhang et al., 2010), and modulation by chemotherapeutic agents (Apetoh et al., 2007). Monocyte/macrophage depletion in experimental settings has been successful in limiting tumor growth and metastatic spread and in achieving better responses to conventional chemotherapy and antiangiogenic therapy (Mazziere et al., 2011; Qian et al., 2011).

Trabectedin (ET-743) is a new DNA binder of marine origin that is approved in Europe and other countries as a single agent for the treatment of soft tissue sarcoma after failure of doxorubicin or ifosfamide and in relapsed platinum-sensitive ovarian cancer patients in combination with pegylated liposomal doxorubicin (Le Cesne et al., 2012; Grosso et al., 2007; Monk et al., 2010). From a mechanistic point of view, trabectedin shows features different from those of other conventional chemotherapeutic agents: it binds the minor groove of DNA and, in addition to blocking the cell cycle, it affects gene transcription and DNA-repair pathways (D'Incalci and Galmarini, 2010; Erba et al., 2001; Minuzzo et al., 2000). Furthermore, differentiation of human liposarcoma cells after therapy was described (Charytonowicz et al., 2012; Forni et al., 2009). We previously reported that trabectedin is selectively cytotoxic in vitro to human monocytes and inhibits the production of some cytokines (e.g., CC chemokine ligand 2 [CCL2], interleukin-6) functionally relevant in the tumor milieu (Allavena et al., 2005; Germano et al., 2010). These studies as well as clinical evidence (D'Incalci and Galmarini, 2010; Grosso et al., 2007) suggested that trabectedin may not only hit neoplastic cells but also affect the tumor microenvironment.

The present investigation was designed to elucidate the role of macrophage targeting in the antitumor activity of this drug in vivo by using four different mouse tumor models. We further studied the effect on mononuclear phagocytes in soft tissue sarcoma patients receiving trabectedin.

RESULTS

Trabectedin Selectively Decreases the Number of Mononuclear Phagocytes in Blood and Spleens of Tumor-Bearing Mice

We tested whether trabectedin affects mononuclear phagocytes upon treatment in vivo of tumor-bearing mice. Three transplantable tumor models were used (MN/MCA1 fibrosarcoma, ID8 ovarian carcinoma, and Lewis lung carcinoma [LLC]), as well as primary fibrosarcoma induced by injection of methylcholanthrene (MCA-fibrosarcoma). After each treatment (once per week for three cycles), blood was collected and leukocytes analyzed by flow cytometry. Figures 1A and 1B show representative experiments with MN/MCA1, ID8, and MCA-fibrosarcoma

tumors. Data for LLC tumors are shown in Figure S1A (available online). Treatment with trabectedin caused a rapid decrease (24–48 hr) in the number of blood monocytes (CD45⁺ CD11b⁺ CD115⁺ [macrophage colony-stimulating factor receptor]), while neutrophils (CD45⁺ CD11b⁺ CD115^{neg} SSC^{high}), CD3 T cells, and CD19 B lymphocytes were unaffected (Figure 1A; Figure S1A). Mean inhibition in the percentage of monocytes/CD45⁺ progressively increased after each treatment: 42%, 52%, and 86% after cycles 1, 2, and 3, respectively (Figure 1C; $p < 0.001$, Student's *t* test). Polymorphonuclear neutrophils (PMN)/CD45⁺ were not reduced after the first two cycles but were slightly inhibited (24%) after the third treatment. Next, we analyzed which monocyte subset was mostly affected. In untreated tumor-bearing mice, 71%–89% of CD115⁺ monocytes were Ly6C^{high}, while Ly6C^{inter} and Ly6C^{low} cells were 7%–13% and 1.7%–22%, respectively. After treatment, only the Ly6C^{high} subset (also defined as “inflammatory”) was strongly inhibited and the remaining monocytes had mostly a Ly6C^{inter}/Ly6C^{low} phenotype (Figure 1B).

The fibrosarcoma MN/MCA1 triggered a marked myelopoiesis that usually started at day +16 postinoculum and was significantly reduced by treatment, especially in terms of monocytes (Figure S1B). To rule out that the effect on monocytes was not merely due to a global inhibition of myelopoiesis, trabectedin was administered at day +25, when myelopoiesis was already full blown (total CD45⁺ cells increased up to 4-fold). A single injection caused, 48 hr later, a drastic decrease in the absolute number of monocytes but not in the number of PMN or CD45⁺ cells (Figure 1D). These results demonstrate that trabectedin directly affects circulating monocytes and that this rapid effect is not mediated via inhibition on bone marrow (BM) progenitors. Notably, trabectedin did not modulate the expression of relevant hematopoietic growth factors (macrophage colony-stimulating factor [M-CSF], granulocyte colony-stimulating factor, granulocyte-monocyte colony-stimulating factor, interleukin-3, and interleukin-6) in fibrosarcoma of treated mice (Figure S1C).

At the BM level, mature monocytes (CD11b⁺ CD115⁺), but not PMN or total CD45 cells, were significantly reduced (Figure S1D). We next checked whether this preferential effect on the monocytic lineage was also reflected on myeloid progenitors in comparison to other leukocyte lineages. After two cycles of treatment, all immature progenitors were reduced (Figure S1E). This effect is likely due to the cell-cycle-blocking activity of the drug on highly proliferating cells and was observed only after the second and third cycle of treatment.

We next checked the effect of trabectedin on tissue macrophages. The percentage of splenic F4/80⁺ macrophages was significantly decreased after treatment (Figure 2A). Furthermore, among CD11b⁺ GR1⁺ cells, the Ly6C^{high} component (monocytes) was reduced while Ly6C^{low} Ly6G⁺ cells (granulocytes) were not, underlining the peculiar selectivity of trabectedin for the monocytic lineage. To further validate this result, splenocytes from control tumor-bearing mice were treated in vitro with trabectedin. Annexin V⁺ apoptotic cells were present only in the Ly6C^{high} monocytic component, while Ly6G⁺ cells were not affected (Figure 2B). Because CD11b⁺ GR1⁺ Ly6C^{high} cells have been associated with the operationally defined myeloid derived suppressor cells (MDSC) (Movahedi et al., 2008; Sica and Bronte, 2007; Youn et al., 2012), we investigated whether

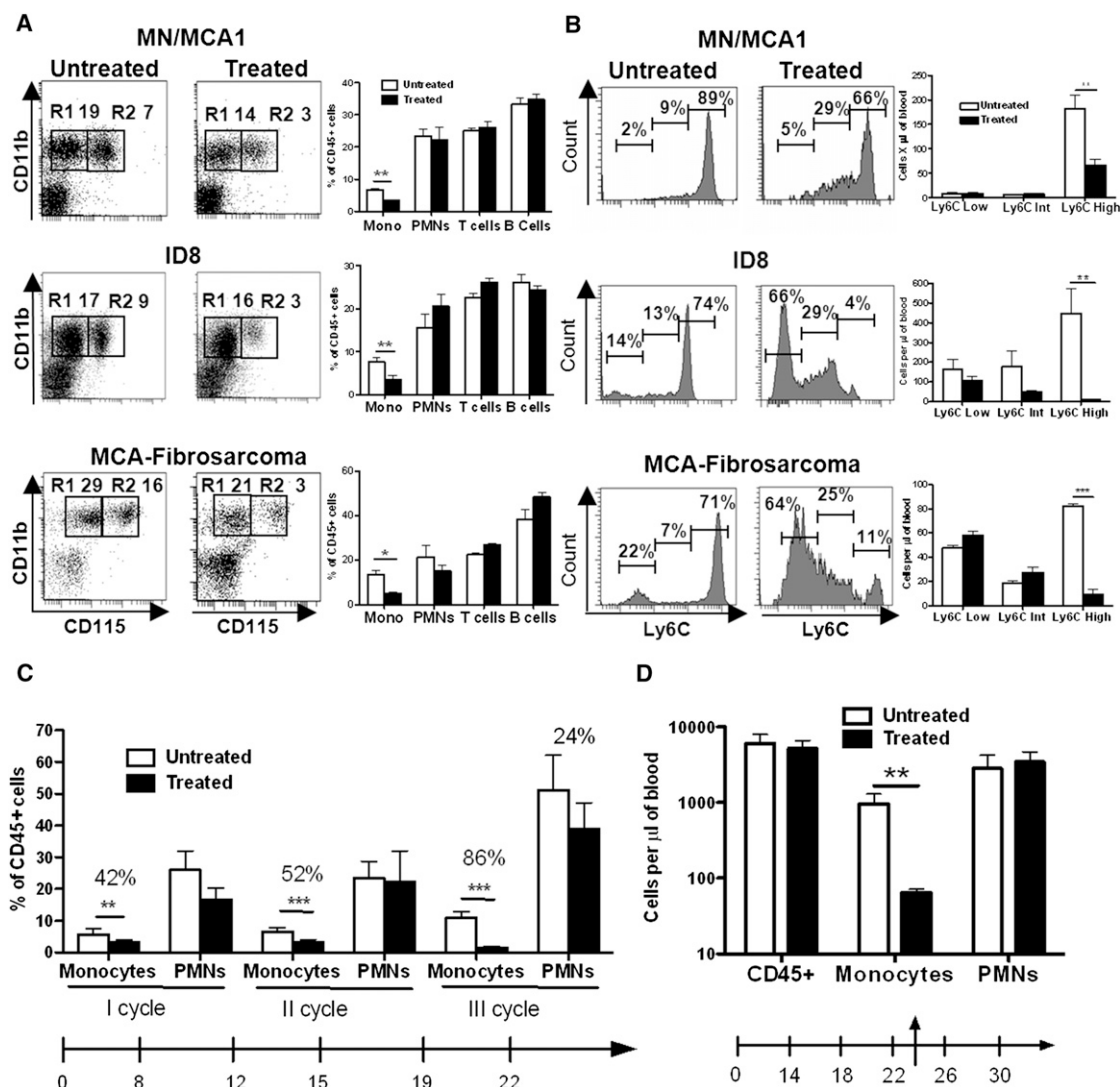


Figure 1. Trabectedin Decreases Blood Ly6C^{high} Monocytes in Tumor-Bearing Mice

The transplantable tumors fibrosarcoma MN/MCA1 and the ovarian carcinoma ID8 were intramuscularly inoculated. Primary MCA-fibrosarcomas were induced by intramuscular injection of methylcholanthrene. Trabectedin treatment (0.15 mg/kg) was given intravenously once per week for 3 weeks.

(A) Left: Flow cytometry analysis of blood leukocytes after two cycles of trabectedin (day +16). Monocytes (CD11b⁺ CD115⁺, gate R2) are reduced after treatment in all the three tumor models. Right: Percentage of monocytes, PMN (CD11b⁺ CD115^{neg} SSC^{high}), T cells (CD3⁺), and B cells (CD19⁺) relative to total CD45⁺ in control and treated mice (mean \pm SD of three experiments with six mice per group for MN/MCA1; mean \pm SD of six mice per group for ID8 and MCA-fibrosarcoma). Only monocytes are significantly reduced after treatment.

(B) Left: Representative histograms of blood Ly6C^{high}, Ly6C^{int}, and Ly6C^{low} monocytes (gated as CD11b⁺ CD115⁺ cells) in control and treated tumor-bearing mice. Right: Absolute number per microliter of blood of monocyte Ly6C subsets (mean \pm SE of four to six mice per group).

(C) Percentage of monocytes and PMN/CD45⁺ cells 24 hr after each treatment cycle (mean \pm SD of two experiments with six mice per group). Inhibition (%) after treatment is marked on top of the bars.

(D) Trabectedin is directly cytotoxic to blood monocytes. A single injection of trabectedin (day +25), when myelopoiesis is full blown, strongly reduces the number of monocytes. Absolute numbers per microliter of blood (mean \pm SD, six mice per group). Total CD45⁺ cells and PMN are not affected.

Statistical analysis: * $p < 0.05$, ** $p < 0.01$, *** $p < 0.001$ (Student's t test). See also Figure S1.

trabectedin modulated their immune-suppressive activity. Purified CD11b⁺ GR1⁺ Ly6C^{high} Ly6G^{neg} splenocytes from tumor-bearing mice were cocultured with lymphocytes from OT-1 mice in the presence of the model antigen ovalbumin. A similar dose-dependent inhibition of lymphocyte proliferation was observed in both control and in vivo-treated mice (Figure 2C). Therefore, trabectedin does not have an impact on the functional activity of MDSC but does significantly reduce the number of Ly6-

C^{high} cells, the most suppressive subset. Of note, Ly6C^{low} Ly6G⁺ cells did not have significant suppressive activity (not shown).

Antitumor Activity of Trabectedin and Selective Depletion of TAM

The antitumor activity of trabectedin on MN/MCA1 fibrosarcoma, lung LLC, and MCA-induced fibrosarcoma is shown in Figures S2A–S2D. Treatment significantly delayed tumor

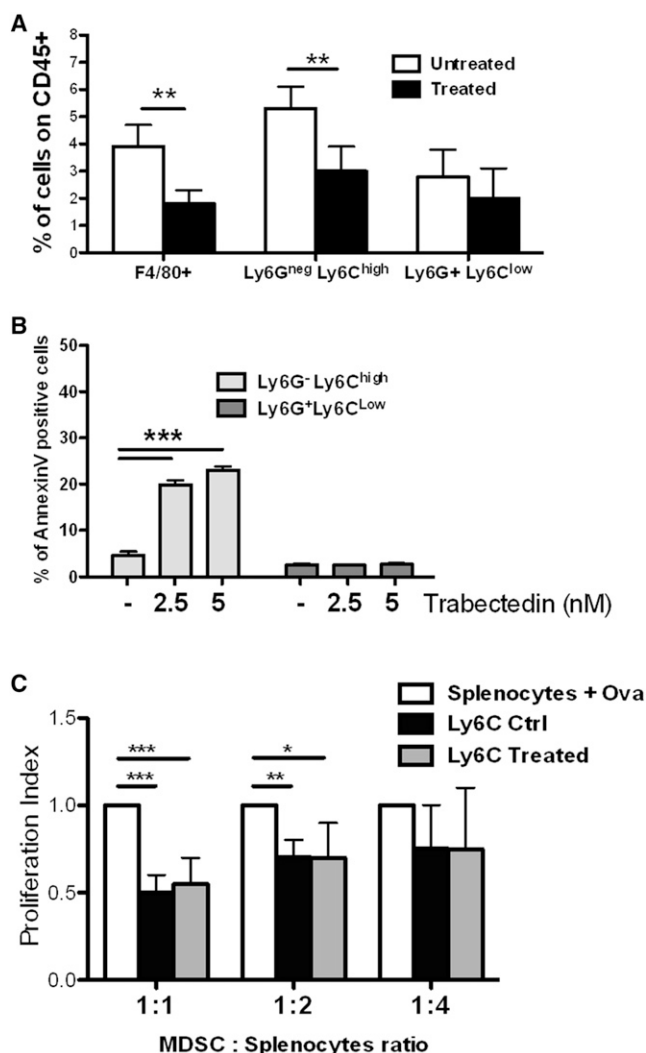


Figure 2. Effect of Trabectedin on Splenic Myeloid Cells from Tumor-Bearing Mice

(A) Spleen macrophages (CD11b⁺ F4/80⁺) and CD11b⁺ Ly6G^{neg} Ly6C^{high} myeloid cells are significantly decreased in treated mice bearing the MN/MCA1 fibrosarcoma (24 hr after two cycles of treatment, mean \pm SD of three experiments with six mice per group). CD11b⁺ Ly6G⁺ Ly6C^{low} cells are not reduced.

(B) Splenocytes of tumor-bearing mice treated in vitro with trabectedin (12 hr). Only CD11b⁺ Ly6G^{neg} Ly6C^{high} myeloid cells undergo significant apoptosis, evaluated as percentage of Annexin V⁺ cells. Statistical analysis: * p < 0.05, ** p < 0.01, *** p < 0.001 (Student's t test).

(C) Effect of trabectedin on the suppressive activity of spleen MDSC from tumor-bearing mice. Purified CD11b⁺ Ly6G^{neg} Ly6C^{high} MDSC significantly inhibit the proliferation of splenocytes from OT-1 mice stimulated with ovalbumin. MDSC from mice treated with trabectedin have similar suppressive activity compared with MDSC from untreated mice.

growth; lung metastasis from MN/MCA1 was also significantly reduced (Figure S2B). To assess the leukocyte infiltrate, tumors were excised at the end of treatment and analyzed by flow cytometry. The percentage of TAM (CD11b⁺ F4/80⁺ /CD45⁺) in treated mice was significantly lower in all four tumor models (mean inhibition: MN/MCA1, 38%; LLC, 46%; ID8, 43%; MCA-fibrosarcoma, 30%; Figure 3A). The percentage of T cells and

neutrophils was never reduced; T cells actually showed a tendency to increase.

Because tumors of treated mice were significantly smaller in size, we postponed tumor cell inoculum in control mice in order to have treated and untreated tumors of comparable size at the end of the experiment. As shown in Figure 3B, TAM (CD11b⁺ F4/80⁺) were strongly reduced after treatment, from 60% to 13%; of note, tumors excised 8 days after the last treatment still had lower TAM, indicating that the effect of trabectedin was long-lasting. The phenotype of TAM comprises mature (F4/80⁺ Ly6C^{low}) and immature (F4/80⁺ Ly6C^{int/high}) macrophages (Movahedi et al., 2010; Swirski et al., 2007). In untreated mice, most TAM had a mature phenotype (80% Ly6C^{low}; Figure 3C); in mice receiving trabectedin, up to 75% of TAM had an immature Ly6C^{high} profile. This finding suggests that trabectedin inhibits the local differentiation of tumor-recruited monocytes to fully mature macrophages. TAM are M2-like polarized macrophages (Mantovani et al., 2008; Solinas et al., 2010) with low expression of MHC II molecules (MHC^{low}), although a proportion of M1-like MHC^{high} macrophages are present as well (Movahedi et al., 2010). Treatment of MN/MCA1-bearing mice resulted in a similar inhibitory effect on CD11b⁺ Ly6C^{int} MHC^{high} (TAM/M1-like) and Ly6C^{int} MHC^{low} (TAM/M2-like) (Figure 3D).

Size-comparable tumors were used for immunohistochemistry studies. CD68⁺ and Dectin⁺ TAM in treated tumors were reduced by more than 50% (Figure 4A). The production of CCL2, a major determinant of monocyte recruitment in tumors, was also decreased in treated mice (Figure 4B). The predominant CCL2-expressing cells appeared as dispersed macrophages; sorted TAM from in vivo-treated tumors indeed showed significantly lower CCL2 messenger RNA levels (Figure S3A). The angiogenic network of treated tumors was also significantly decreased in terms of microvessel density and maturation, as assessed by the number of CD31 and CD105 (endoglin)-positive cells as well as staining for vascular endothelial growth factor (VEGF) (Figure 4C).

Given the capacity of TAM to promote tumor cell proliferation and metastasis (Joyce and Pollard, 2009; Sica and Mantovani, 2012), we investigated the impact of trabectedin on the functional TAM-tumor cell interaction. In vitro studies with fluorescence-activated cell-sorted TAM from untreated mice cocultured with MN/MCA1 cells showed that TAM significantly enhanced tumor cell proliferation and their migration through Matrigel-coated transwells (Figures S3B and S3C). When TAM were pretreated with trabectedin (under noncytotoxic conditions: 5 nM, 2 hr), these protumor properties were partially abrogated; of note, the expression of matrix metalloproteinases 9 and 12 by tumor cells was significantly downregulated (Figure S3D).

Role of TAM Targeting in the Antitumor Activity of Trabectedin

The results discussed above raised the question whether targeting of mononuclear phagocytes plays a major role in the antitumor activity of trabectedin. This was addressed by taking advantage of tumor cell lines that were rendered resistant to its cytotoxic activity upon continuous exposure to increasing drug concentrations. The trabectedin-resistant subline of the MN/MCA1 fibrosarcoma (MN/MCA1-RES) showed stable in vitro

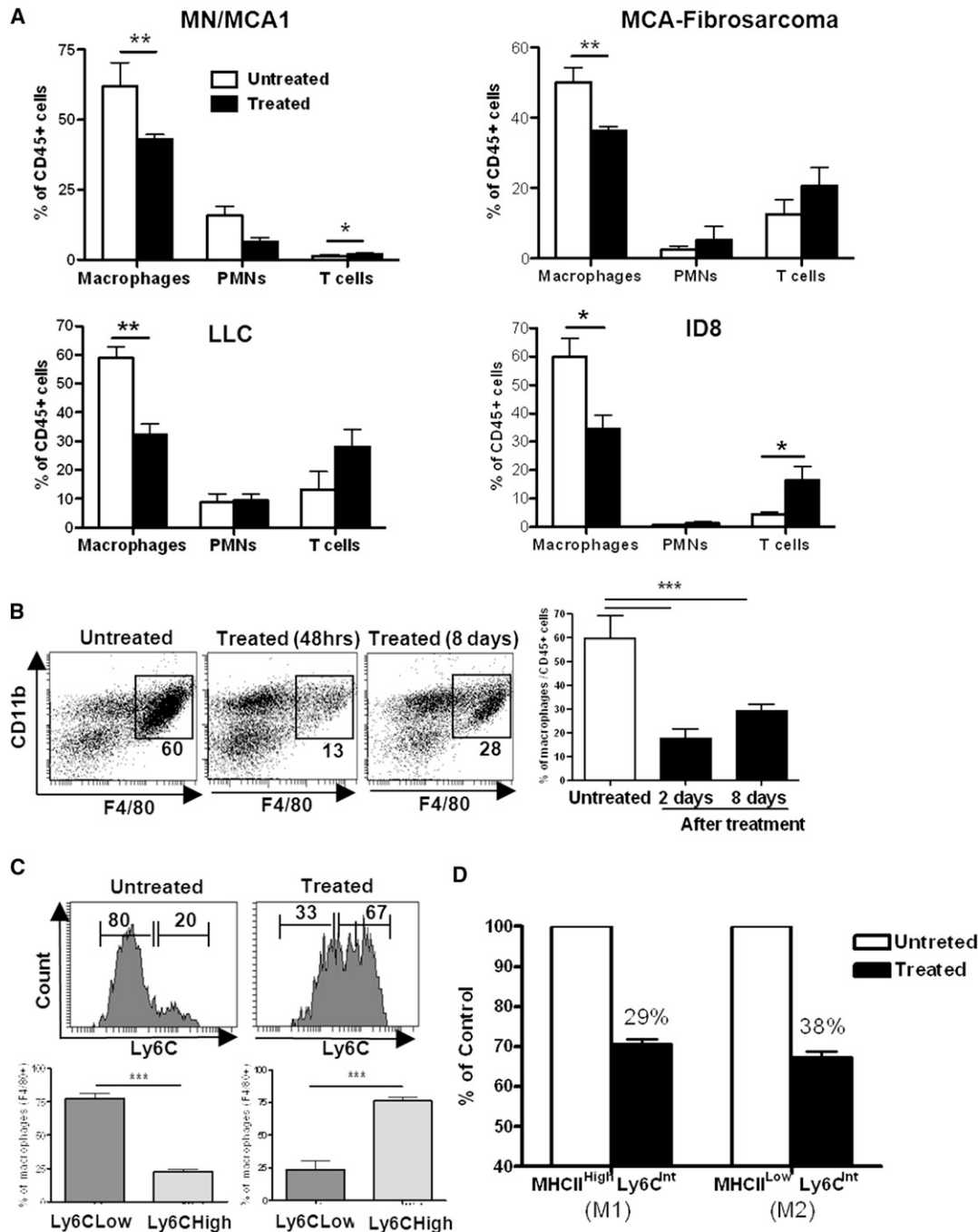


Figure 3. Trabectedin Decreases Tumor-Associated Macrophages after In Vivo Treatment

Transplantable tumors (MN/MCA1, LLC, ID8) and MCA-induced fibrosarcoma were excised 48 hr after the third cycle of trabectedin and analyzed in flow cytometry.

(A) Percentage of TAM (CD45⁺ CD11b⁺ F4/80⁺), PMN (CD45⁺ CD11b⁺ Ly6G⁺), and T cells (CD45⁺ CD3⁺) relative to total CD45 cells; (mean \pm SD with six to eight mice per group; for MN/MCA1, mean \pm SD of three experiments).

(B) Dot plots of TAM (CD45⁺ CD11b⁺ F4/80⁺) in treated and untreated size-comparable tumors. Tumor cell inoculum in untreated mice was postponed to have tumors of comparable size at the end of treatment (volume-untreated tumors: 2,900 \pm 537 mm³; volume-treated tumors: 3,220 \pm 407 mm³). Bars depict the percentage of CD11b⁺ F4/80⁺ on CD45⁺ live cells (mean \pm SD, six mice/group).

(C) Representative flow cytometry of Ly6C expression on F4/80⁺ TAM. In trabectedin-treated tumors, TAM contain more Ly6C^{high} macrophages. Data are expressed as percentage of F4/80⁺ cells (mean \pm SD of two experiments with six mice per group).

(D) Susceptibility of TAM subsets to trabectedin. TAM (CD45⁺ CD11b⁺ Ly6C^{Int}) from untreated or treated tumors were analyzed for MHC II expression. TAM MHC II^{High} (M1) and MHC II^{Low} (M2) were equally susceptible to trabectedin.

Statistical analysis: *p < 0.05, **p < 0.01, ***p < 0.001 (Student's t test). See also Figure S2.

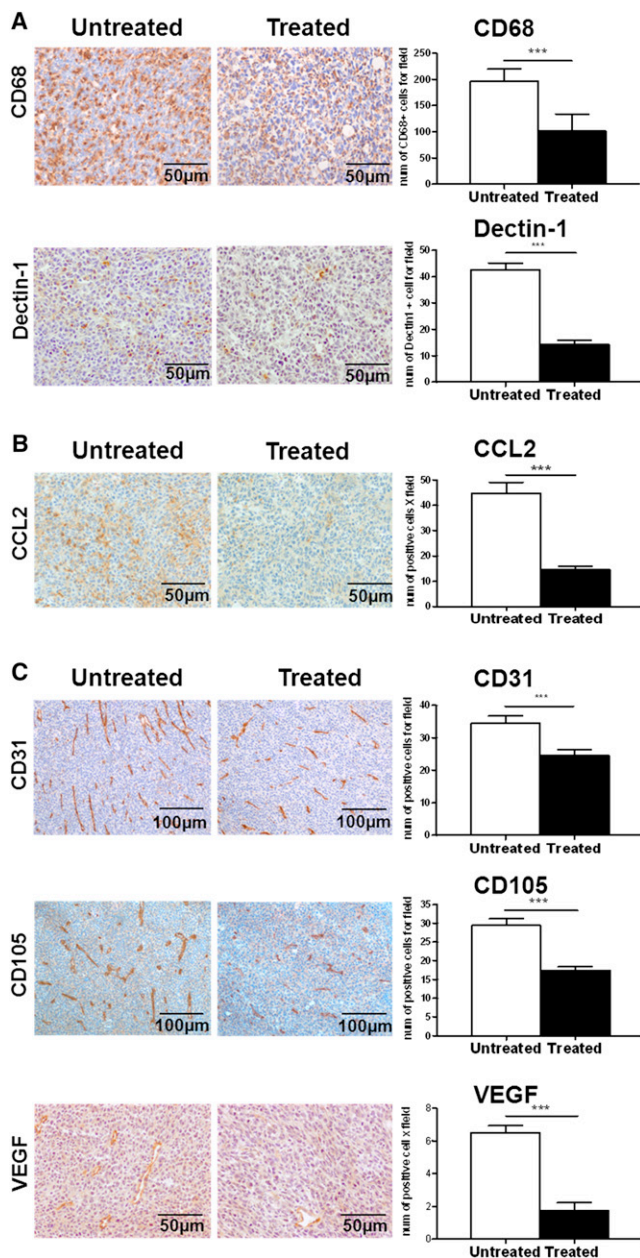


Figure 4. Trabectedin Decreases TAM, the Chemokine CCL2, and Angiogenesis in Treated Tumors

Immunohistochemistry was performed on size-comparable MN/MCA1 tumors (see legend to Figure 3) after three cycles of treatment. Results are shown as representative pictures (20×) and as mean values ±SD number of positive cells per five microscope fields for each sample, with six mice per group.

(A) Staining of intratumor macrophages with anti-CD68 monoclonal antibody (mAb) and anti-Dectin-1 mAb.

(B) Staining of tumor sections with anti-CCL2 mAb.

(C) Staining of intratumor vessels with anti-CD31, CD105 (endoglin) and VEGF. Statistical analysis: ** $p < 0.01$, *** $p < 0.001$ (Student's t test). See also Figure S3.

and ex vivo resistance (>8-fold) after growth in mice (Figure 5A; Figure S4A). Of note, trabectedin displayed strong in vivo antitumor activity on MN/MCA1-RES tumors (Figure 5A) similar to

that on wild-type MN/MCA1 cells (shown in Figure S2A). TAM density was also significantly decreased in MN/MCA1-RES tumors after treatment (Figure 5A). Comparable results were found in a xenograft model of ovarian cancer (IGROV) where an IGROV-RES subline, 5-fold resistant to trabectedin (Figure S4B), was at least as responsive to treatment in vivo as the wild-type one (Figure S4C). These results suggested that the antitumor efficacy of trabectedin in drug-resistant tumors could be mediated via its effects on the tumor microenvironment and associated myelomonocytic cells.

To further test this hypothesis, we adoptively transferred myeloid cells after each drug treatment; transfer of BM-derived in vitro-differentiated macrophages from tumor-bearing untreated mice significantly reinstated tumor growth in treated mice (Figure 5B). A similar finding was obtained when BM-derived monocytes were injected, although less marked than with already differentiated macrophages (Figure 5C). In contrast, the transfer of splenic MDSC had no significant effect (Figure 5D). In an effort to further explore the role of macrophage depletion in the antitumor activity of trabectedin, we compared its effects with the macrophage-depleting agent clodronate. Mice bearing MN/MCA1-RES tumors were treated with clodronate liposomes, alone or in combination with the drug. Clodronate single treatment delayed tumor growth initially (Figure 5E); however, when therapy was suspended (day +21), these tumors grew faster than those treated with trabectedin. Combined treatment with clodronate and trabectedin did not result in additive or synergistic antitumor activity. Clodronate liposomes reduced TAM density to a similar extent as trabectedin, but the latter caused a more persistent macrophage depletion (data not shown), possibly as a consequence of inhibition of CCL2 production. Overall, these results are consistent with the view that targeting of TAM is, at least in part, responsible for the antitumor activity of trabectedin under these conditions.

Selective Depletion of Monocytes and TAM in Tumor Patients Treated with Trabectedin

To assess the actual clinical relevance of the above observations, we investigated the impact of trabectedin on blood monocytes of soft tissue sarcoma patients receiving trabectedin as a single treatment.

Figure 6A shows a representative flow cytometry analysis from a leiomyosarcoma patient whose monocytes decreased after therapy from 9.4% to 3.2%, as well as the absolute number of monocytes but not that of granulocytes and lymphocytes (Figure 6B). Human CD14⁺ CD16^{low} monocytes are considered the counterpart of mouse CCR2⁺ Ly6C^{high} cells (Geissmann et al., 2010); this population was monitored throughout subsequent cycles of therapy and significant reduction after each cycle was seen in two different patients ($p = 0.0109$ for pre- versus post-therapy levels; Figure 6C). We also investigated by immunohistochemistry whether trabectedin caused a decrease of human TAM density. In selected soft tissue sarcoma patients receiving the drug as neoadjuvant treatment, we had access to tumor biopsy specimens before therapy and to post-therapy surgical samples. A strong decrease in the density of TAM and blood vessels was evident after treatment (Figure 6D), confirming that trabectedin-mediated depletion of mononuclear phagocytes also occurs in tumor patients.

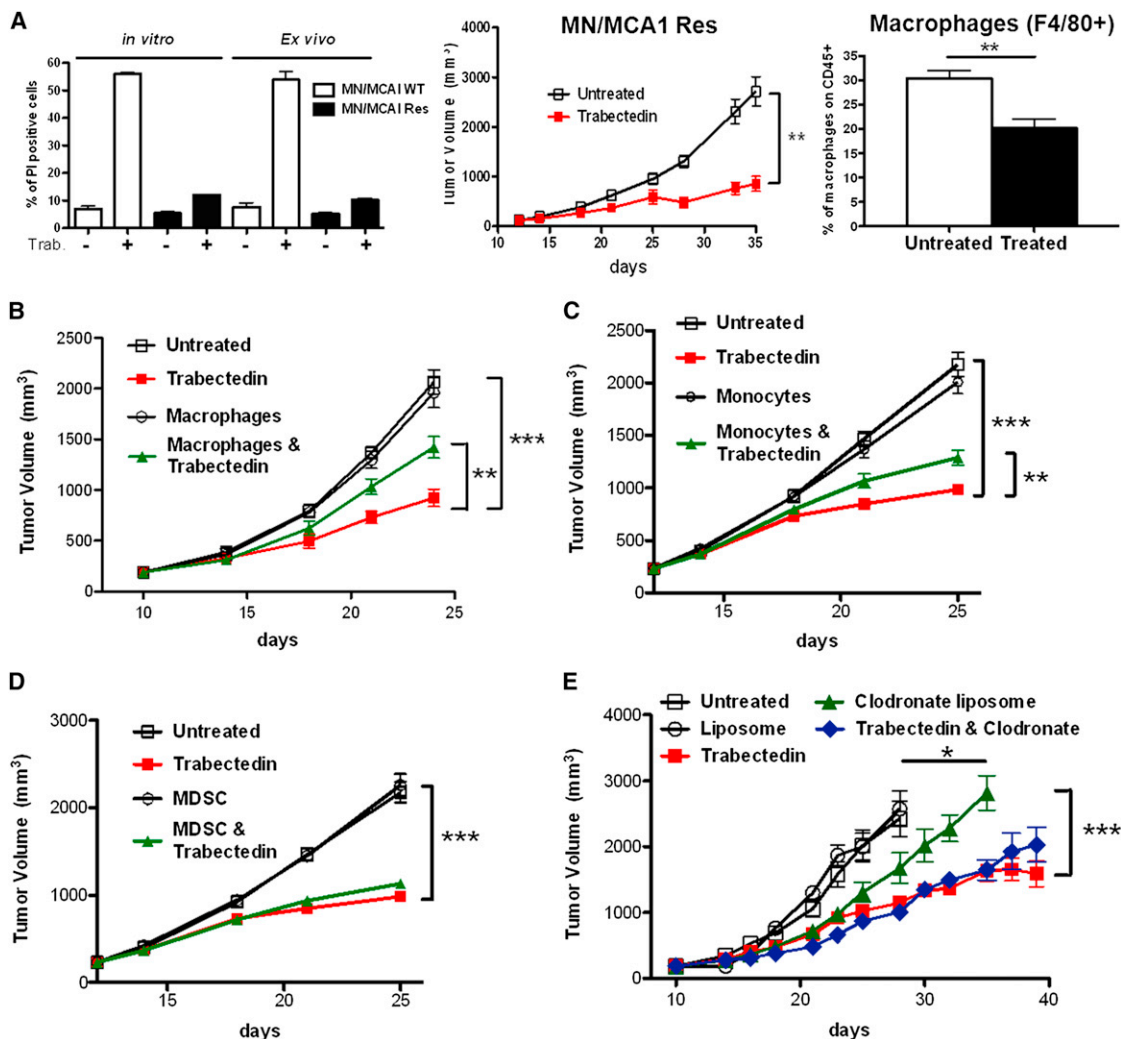


Figure 5. Role of Macrophage Targeting in the Antitumor Activity of Trabectedin

(A) Left: *In vitro* and *ex vivo* resistance to trabectedin of MN/MCA1-RES cells explanted from tumor-bearing mice and treated *in vitro* with trabectedin (5 nM). Results are percentage of propidium iodide-positive cells. Middle: Trabectedin has antitumor activity on the drug-resistant variant MN/MCA1-RES grown in mice. Right: Percentage of F4/80⁺ TAM is reduced in MN/MCA1-RES-bearing mice treated with trabectedin (mean \pm SD of six mice per group).

(B) Adoptive transfer of BM-derived *in vitro* M-CSF-differentiated macrophages into mice bearing MN/MCA1-RES tumors reinstates tumor growth. Macrophages (2×10^6 /mouse) were intravenously injected 72 hr after each of the three cycles of trabectedin (tumor volume, mean \pm SD of six mice per group).

(C) Adoptive transfer of BM-purified monocytes into mice bearing MN/MCA1-RES tumors reinstates tumor growth. Monocytes were intravenously injected (2×10^6 /mouse) 72 hr after each treatment (tumor volume, mean \pm SD of six mice per group).

(D) Adoptive transfer of purified spleen MDSC into mice bearing MN/MCA1-RES tumors does not reinstate tumor growth. MDSC were intravenously injected (2×10^6 /mouse) 72 hr after each treatment (tumor volume, mean \pm SD of six mice per group).

(E) Comparison of trabectedin treatment with clodronate liposomes. Mice bearing MN/MCA1-RES tumors were treated with trabectedin, clodronate liposomes, or their combination. The effect of trabectedin is similar to clodronate but lasts longer (tumor volume, mean \pm SD of six to eight mice per group).

Statistical analysis: * $p < 0.05$, *** $p < 0.001$ (Student's *t* test). See also Figure S4.

Mechanism of Macrophage Depletion by Trabectedin

In an effort to elucidate the peculiar selectivity of trabectedin for the myelomonocytic lineage, we investigated in depth the pathways of apoptotic death induced by the drug in different human leukocyte subsets. Mitochondrial depolarization and release of cytochrome C in the cytosol were observed only in treated monocytes, while PMN and T cells were unaffected (Figure 7A). Furthermore, trabectedin caused the cleavage of caspase-8 and caspase-9 selectively in monocytes (Figure 7B). In a kinetic analysis, activation of caspase-8 occurred earlier than caspase-9 or

mitochondria depolarization (Figures S5A and S5B) and Z-IETD-FMK (a caspase-8 inhibitor) strongly reduced Annexin V⁺ cells (Figure S5C). Thus, the first temporal event induced by trabectedin in monocytes is the activation of caspase-8. This caspase is the key effector molecule of the extrinsic apoptotic pathway mediated by membrane death receptors (Fas and tumor necrosis factor-related apoptosis inducing ligand [TRAIL] receptors [TRAIL-Rs]) (Bodmer et al., 2000). Expression of TRAIL and Fas receptors by purified human monocytes, neutrophils, and T lymphocytes is shown in Figure 7C (mean \pm SE, $n = 6$

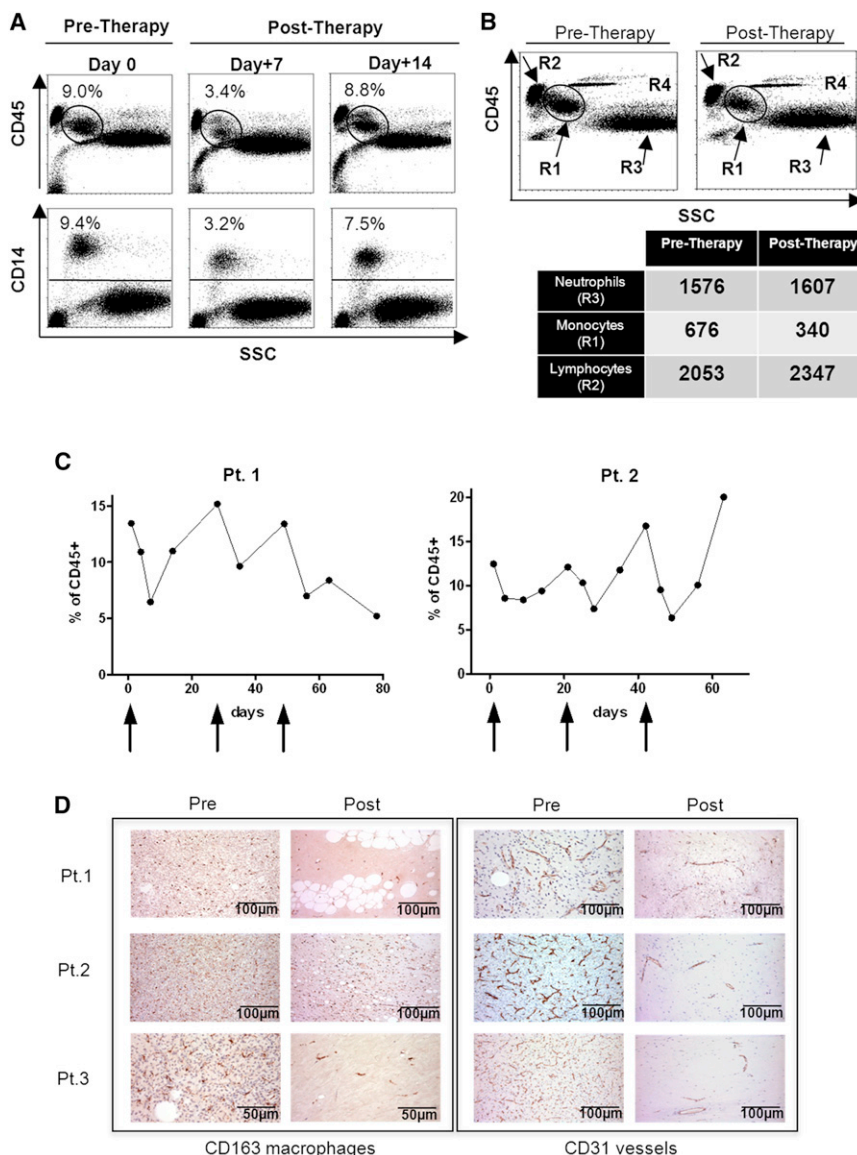


Figure 6. Trabectedin Decreases Blood Monocytes in Soft Tissue Sarcoma Patients

(A) Representative dot plots of peripheral blood samples stained for CD45 and CD14 from a leiomyosarcoma patient after trabectedin therapy. Blood was collected the day before therapy and 7 and 14 days postinfusion.

(B) Representative dot plots of peripheral blood samples before and after therapy; CD45 versus side scatter (SSC) dot plots showing decrease in the number of CD14 monocytes (circular gate).

(C) Reduction in the number of blood monocytes in two soft tissue sarcoma patients treated with trabectedin over different therapy cycles, indicated by the arrows. Results expressed as percentage CD14⁺ CD16⁺/CD45⁺.

(D) Immunohistochemistry of tumor sections from three different soft tissue sarcoma (STS) patients receiving trabectedin therapy prior to surgery. Sections marked (PRE) are biopsic samples before treatment. Sections marked (POST) are surgical samples after treatment. Tumor macrophages (CD163) and vessels (CD31) are reduced after treatment.

with blocking anti-R1 and anti-R2 (alone or in combination) strongly inhibited caspase-8 activation (Figure 7D). As reasonably expected, anti-R3 (decoy R) antibodies had no inhibitory effect. When used on neutrophils, pretreatment with anti-R3 did not result in higher susceptibility (not shown), in line with their lack of signaling R1 and R2 receptors. Anti-Fas antibodies had no significant effect. In parallel experiments, we verified that recombinant TRAIL ligand induced caspase-8 activation in monocytes and that anti-TRAIL-Rs antibodies properly blocked this activation (Figure S5E). These results indicated that caspase-8 activation via TRAIL-Rs was responsible

experiments). Fas receptor was very high and equally expressed in all three subsets. TRAIL receptor 1 (TNFRSF10A or R1) and especially TRAIL receptor 2 (TNFRSF10B or R2) were expressed in monocytes and low or absent in T cells and neutrophils. In contrast, the decoy nonsignaling TRAIL receptor 3 (TNFRSF10C or R3) was highly expressed by neutrophils and T cells but very low in monocytes. A second decoy receptor (TNFRSF10D or R4) was not expressed by any subset (not shown). Therefore, the expression pattern of TRAIL-Rs strikingly parallels the susceptibility of leukocytes to the cytotoxic action of trabectedin, with monocytes being susceptible and neutrophils and lymphocytes being resistant.

Next, the contribution of death receptors to trabectedin-induced apoptosis was investigated. We first set up a flow cytometry technique to specifically detect cleaved caspase-8 in leukocytes. Figure S5D shows a typical experiment where trabectedin dose- and time-dependently activates caspase-8 in monocytes but not in neutrophils and T cells. Cell pretreatment

for monocyte apoptosis induced by trabectedin. To further confirm our interpretation, we overexpressed the decoy R3 receptor, fused with green fluorescent protein, in the myeloid cell line HL60 and in 293T cells. In R3-expressing cells (Figure S5F), activation of caspase-8 was strongly reduced compared to mock-transfected cells, either with trabectedin and TRAIL ligand (Figure 7E; Figure S5G), confirming the involvement of TRAIL receptors in trabectedin-induced apoptosis.

We next investigated TRAIL-R expression in mouse leukocytes. In mice, only one signaling receptor is present (TRAIL-R2 or DR5). Blood monocytes with the phenotype Ly6C^{high} (which are more susceptible to the cytotoxic effect of trabectedin, see Figure 1B) expressed higher TRAIL-R2 compared to Ly6C^{low} monocytes and, in line with the human data, neutrophils and T cells had very low or no expression of TRAIL-R2 (Figure 8A). Activation of caspase-8 by trabectedin was confirmed in mouse macrophages differentiated in vitro from BM cells (Figure 8B). Upon in vivo treatment with trabectedin, TRAIL-R2⁺

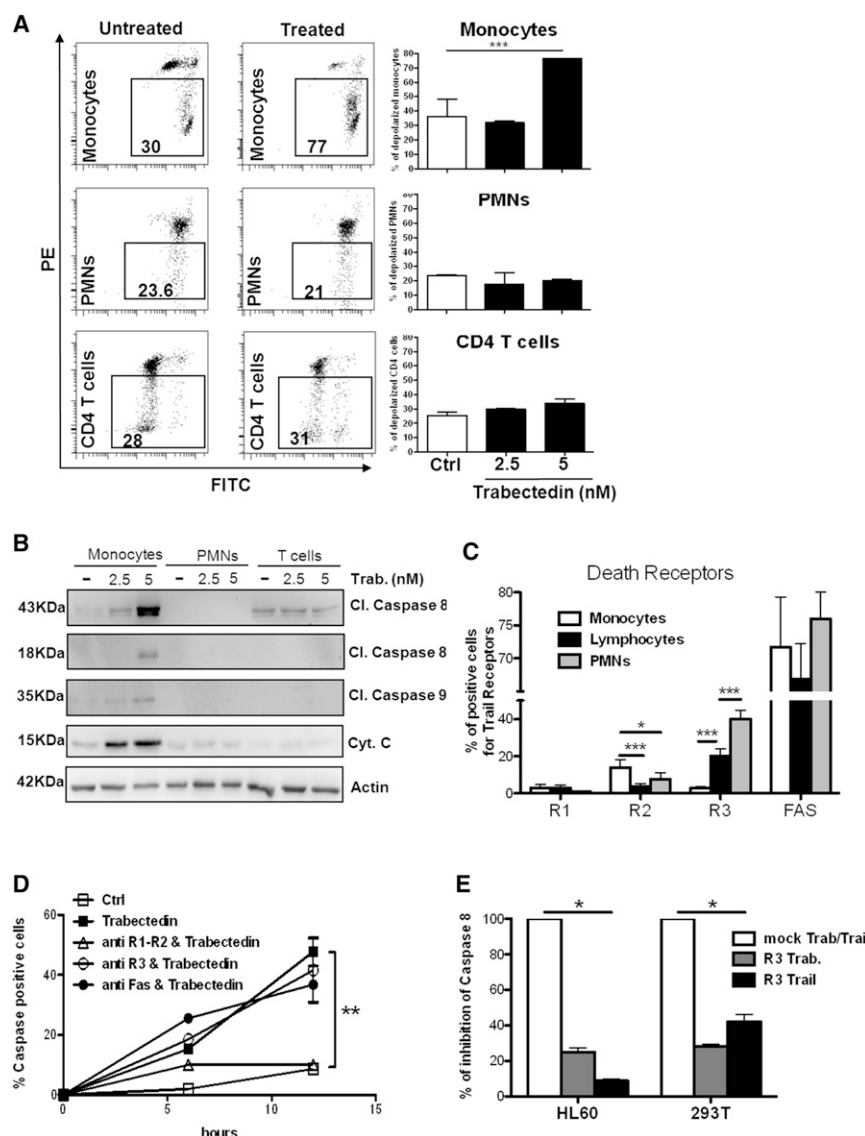


Figure 7. Mechanism of Apoptosis and Selective Effect of Trabectedin on Monocytes

(A) Mitochondrial membrane depolarization in human purified monocytes, PMN, and T cells treated with trabectedin (5 nM) for 12 hr.

(B) Western blot analysis of cleaved caspase-8, caspase-9, and cytochrome C in human monocytes, PMN, and T cells treated with trabectedin for 24 hr.

(C) Expression of TRAIL receptors in leukocyte subsets by flow cytometry. Monocytes express the functional TRAIL receptor (R2) and lack the non-signaling decoy receptor R3. Neutrophils and T cells express high levels of R3 and low or no R1 and R2. Mean \pm SD of six different experiments.

(D) Caspase-8 activation induced by trabectedin in purified monocytes is inhibited by anti-TRAIL-R1/2 antibodies. Anti-R3 or anti-Fas antibodies had no inhibitory effect. Results are percentage of cells with cleaved caspase-8 evaluated by flow cytometry.

(E) Overexpression of TRAIL-R3 strongly reduces the activation of caspase-8 in cells treated with trabectedin (10 nM, gray bars) and in cells treated with recombinant TRAIL ligand (500 ng/ml, black bars). Results are expressed as percentage of mock-transfected cells.

Statistical analysis: ** $p < 0.01$, *** $p < 0.001$ (Student's *t* test). See also Figure S5.

blood monocytes and TRAIL-R2⁺ TAM in tumors were dramatically reduced (Figure 8C). This result was confirmed also by immunohistochemistry: the density of TRAIL-R2⁺ tumor-infiltrating cells was significantly lower in treated mice (Figures 8D and 8E).

We conclude that trabectedin activates the extrinsic apoptotic pathway downstream of TRAIL receptors and that selectivity for mononuclear phagocytes versus neutrophils and lymphocytes is due to differential expression of signaling and decoy receptors.

DISCUSSION

Trabectedin is a recently approved drug of marine origin that is particularly active in soft tissue sarcoma and ovarian cancer (Carter and Keam, 2010; Grosso et al., 2007; Monk et al., 2010). Substantial clinical and experimental evidence suggests that this antitumor agent may importantly modulate the tumor microenvironment (D'Incalci and Galmarini, 2010; Germano

et al., 2010; Grosso et al., 2007). In this study, we demonstrate that trabectedin rapidly activates caspase-8, the key effector molecule of the extrinsic apoptotic pathway, in mononuclear phagocytes. This effect is remarkably selective for myelomonocytic cells, as neutrophils and lymphocytes are not affected. In four different mouse tumor models, including two lines representative of its clinical spectrum of action, and in a chemically induced fibrosarcoma model, trabectedin caused significant and selective reduction of blood monocytes, in particular of the Ly6C^{high} phenotype and of spleen and tumor macrophages. We also demonstrate that TAM targeting is a key determinant of its efficacy, as trabectedin retained antitumor activity *in vivo* against sarcoma and ovarian carcinoma cells rendered resistant to its cytotoxic action. This was demonstrated by cell transfer of monocytes and macrophages, after drug infusion, that re-established tumor growth in the fibrosarcoma model, supporting the concept that at least part of its antitumor activity is mediated via targeting of protumoral macrophages. Furthermore, the immune suppressive monocytic subset (CD11b⁺ Ly6C^{high}) of MDSC was significantly reduced by trabectedin.

The remarkable susceptibility of the myelomonocytic lineage was ascribed to a differential expression of signaling and decoy TRAIL receptors among leukocytes: monocytes express functional receptors and lack the decoy R3, whereas neutrophils and T cells predominantly express R3. Involvement of TRAIL-Rs

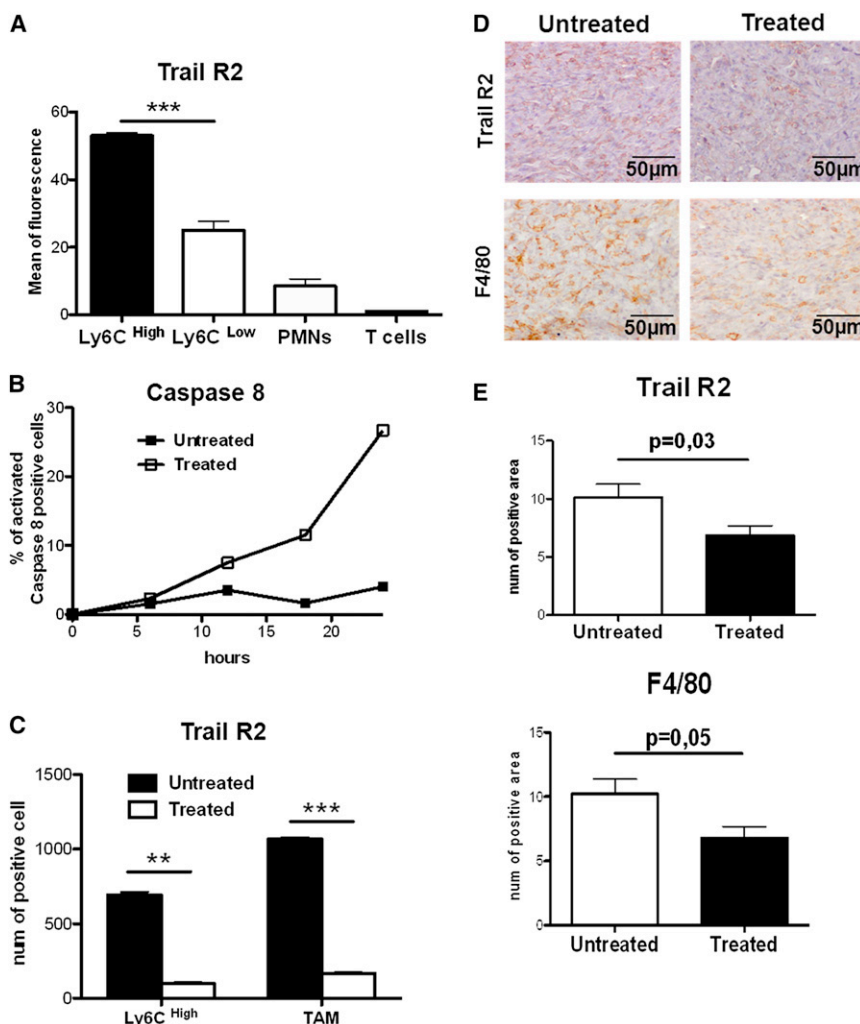


Figure 8. Mouse Blood Monocytes and TAM Expressing TRAIL-R2 Decrease in Trabectedin-Treated Mice

(A) Blood Ly6C^{high} monocytes express higher levels of TRAIL-R2; neutrophils and T cells have low or no expression, as evaluated by flow cytometry.

(B) Kinetic of caspase-8 activation induced by trabectedin (10 nM) in mouse macrophages differentiated in vitro from BM cells. Results are % of cells with cleaved caspase-8 evaluated by flow cytometry.

(C) In vivo treatment with trabectedin strongly reduces the number of blood Ly6C⁺ TRAIL-R2⁺ monocytes and F4/80⁺ TRAIL-R2⁺ TAM (mean \pm SD of four mice per group).

(D) Immunohistochemistry of MN/MCA1-RES tumors from untreated and treated mice stained with anti-TRAIL-R2 and anti-F4/80.

(E) The statistical analysis was performed on four different tumors for each group (mean of a total of 15 microscope fields).

Statistical analysis: **p < 0.01, ***p < 0.001 (Student's t test).

in trabectedin-induced apoptosis was demonstrated by reduced caspase-8 activation in the presence of anti-TRAIL-Rs antibodies and because overexpression of the decoy R3 resulted in marked inhibition of cleaved caspase-8 in trabectedin-treated cells. Furthermore, we demonstrate that mouse Ly6C^{high} monocytes and TAM express TRAIL-R2 and in vivo treatment with trabectedin strongly decreases the number of TRAIL-R2⁺ myelomonocytic cells both in blood and tumors.

Although it was previously claimed that normal cells are resistant to TRAIL, under pathological conditions, such as viral or bacterial infections, leukocytes can be killed, as shown for HIV-infected T cells and alveolar macrophages (Benedict and Ware, 2012; Herbeuval et al., 2005; Steinwede et al., 2012). The intriguing question is why mononuclear phagocytes express functional death receptors in homeostatic conditions and, unlike other leukocytes, are not protected by the presence of the decoy receptor. Activated macrophages can be very reactive cells and have a long life span in tissues, whereas neutrophils survive for just few days. It may be possible, therefore, that the presence of TRAIL-R on mononuclear cells is a checkpoint for controlling their overreactivity. Indeed, TRAIL-R^{-/-} mice have exaggerated innate immune responses with increased levels of interleukin-12,

interferon- α and interferon- γ (Diehl et al., 2004). We noticed that TRAIL-R2 is not expressed by all TAM within tumors. Further studies will clarify the nature of these TRAIL-R2⁺ macrophages. Of note, in human macrophages differentiated in vitro, both M1- and M2-polarized cells expressed TRAIL-Rs (not shown).

The precise mechanism by which trabectedin initiates caspase-8 cleavage remains to be elucidated. It is unlikely that this compound directly engages TRAIL-Rs on cell membrane (based on modeling experiments, not shown). Caspase-8 activation generally starts with the oligomerization of death receptors in response to ligand binding; however, there is evidence that receptor activation may occur independent of the cognate ligand. This ligand-independent activation has been described for several members of the tumor necrosis factor receptor family, including TRAIL-Rs (Cazanave et al., 2011; Chan et al., 2000; Clancy et al., 2005; Lim et al., 2011), and was mechanistically explained by the overexpression of death receptors and/or by their recruitment into lipid rafts on cell membrane. Receptor modulation has been widely studied using pharmacological or chemical/physical agents (Shirley et al., 2011; Siegelin, 2012). Interestingly, some active compounds that are able to upregulate TRAIL-Rs are derived from natural products: animal venoms and bacterial toxins (Park et al., 2012). In origin, trabectedin is also a natural product derived from a marine organism. In an effort to investigate its mode of action, a transcriptional profiling was conducted in mononuclear phagocytes, and key relevant data confirmed at the transcript and protein level. A short treatment (6 hr) upregulated *TRAIL-R2* and *FADD* (Fas-associated protein with death domain), an important proapoptotic gene, while *TRAIL* ligand was not modulated (Figure S5H). Enhanced levels of TRAIL-R2

and FADD, induced by trabectedin, may indeed facilitate the recruitment of caspase-8 and the activation of the apoptotic cascade.

Effects other than macrophage depletion may account for the antitumor efficacy of trabectedin. We show that in treated murine tumors the vessel network and the chemokine CCL2 were significantly downmodulated. TAM depend on the recruitment of monocytes from the blood compartment, mediated by signals including chemokines; although in situ proliferation has been recently identified as a determinant of macrophage accumulation at sites of M2-polarized inflammation (Jenkins et al., 2011) and can be sustained in tumors by paracrine circuits based on M-CSF and its receptor (Bottazzi et al., 1990), the role of CCL2 in tumors is of major importance (Bottazzi et al., 1983; Qian et al., 2011). In the fibrosarcoma model, CCL2 is produced mainly by TAM and its expression was dramatically reduced after treatment. Therefore, in addition to inducing direct cytotoxic activity on mononuclear phagocytes, trabectedin could downmodulate the recruitment of circulating monocytes into tumors.

It is well established that TAM drive angiogenesis and this represents a pathway of escape and resistance to anti-VEGF therapy (Ferrara, 2010; Mazzieri et al., 2011; Murdoch et al., 2008; Noonan et al., 2008). The reduced angiogenic network in treated tumors could be the result of an indirect effect due to the decrease in TAM numbers; however, in tumors treated with clodronate liposomes, where TAM were significantly reduced, the number of CD31⁺ vessels was not decreased (data not shown). VEGF was also downmodulated in trabectedin-treated tumors; therefore, both direct and indirect effects are likely to account for the reduced angiogenesis. As for the susceptibility of endothelial cells to the drug, we have evidence that they are relatively resistant in vitro (not shown). Interestingly, it was recently reported that tumor endothelial cells may be susceptible to TRAIL killing in a mouse model (Wilson et al., 2012).

In soft tissue sarcoma patients treated with trabectedin-based chemotherapy, a decrease of blood monocytes was observed. We retrospectively collected data from 34 patients from whom laboratory test results and clinical outcome were available, and found that 19 patients (56%) experienced monocyte reduction (range, 30%–77%). These results raised the question whether monocyte depletion correlates with drug responsiveness in treated patients. In a retrospective analysis, and in heavily pretreated patients, this was particularly difficult to address; a trend toward a correlation between decreased monocytes and response to therapy was indeed observed, but the association did not reach statistical significance ($p = 0.078$). Further analysis is needed to elucidate this issue. In addition to blood monocytes, in selected cases we had access to tumor biopsy specimens from patients receiving trabectedin as neoadjuvant therapy. When tumor biopsy specimens (before treatment) were compared to surgically explanted tumors (after treatment), a dramatic reduction of vessels and macrophages was observed. Although the drug may directly affect neoplastic cells in these patients, these results suggest that trabectedin may impact the tumor microenvironment, as observed in mouse tumor models.

In conclusion, we have reported that a clinically useful anti-tumor agent selectively depletes mononuclear phagocytes in blood and tumor tissues and that macrophage targeting is

a key component of its antitumor activity. These findings provide proof-of-concept evidence for the value of macrophage targeting in anticancer therapies in humans and shed unexpected light on the mode of action of an available anticancer agent. Moreover, these observations unveil a different perspective for the exploitation of trabectedin in cancer, for instance, in combination with antiangiogenic therapies or as a tool to limit myelomonocytic cell-mediated immune suppression.

EXPERIMENTAL PROCEDURES

Drug

Trabectedin (PharmaMar, Colmenar Viejo, Madrid, Spain) was dissolved in dimethylsulfoxide to 1 mM and kept at -20°C .

Mice, Tumors, and Primary Cells

Mice were used in compliance with national (4D.L.N.116, G.U., suppl. 40, 18-2-1992) and international law and policies (EEC Council Directive 86/609, OJ L 358, 1, 12-12-1987; NIH Guide for the Care and Use of Laboratory Animals, US National Research Council, 1996). This investigation was approved by the Animal Care and Use Committee of the Humanitas Clinical and Research Center.

C57/BL/6J mice were from Charles River (Calco, Como Italy). The transplantable MN/MCA1 mouse fibrosarcoma, the trabectedin-resistant variant MN/MCA1-RES, and the LLC were inoculated intramuscularly (10^5 cells). The mouse ovarian carcinoma ID8 (kindly provided by Prof. Balkwill, London, UK) was inoculated intraperitoneally (10^7 cells). The human ovarian carcinoma IGROV-1 and the trabectedin-resistant variant IGROV-1-RES were inoculated intramuscularly (10^6 cells) in nude mice. Primary fibrosarcomas were induced in C57/BL/6J mice by subcutaneous inoculation of 50 μg methylcholanthrene in 0.2 ml peanut oil (Sigma-Aldrich). Tumors growing progressively over 3 weeks were used. Treatment with trabectedin (0.15 mg/kg/body weight) was administered intravenously once per week for 3 weeks and started when tumors were palpable. For further details, please refer to [Supplemental Experimental Procedures](#).

Phenotype Analysis

Blood cells were collected from the eye vein of anesthetized mice and splenocytes from disaggregated spleen and filtered through Falcon strainers. Mouse tumors were cut into small pieces, disaggregated with collagenase (0.5 mg/ml), and filtered through strainers. Cells (10^6) were stained with specific antibodies and with live and dead dye (Invitrogen, Life Technology) (see [Supplemental Experimental Procedures](#) for an antibody list). Flow cytometry was performed by FACS Canto instrument and FACS Diva software version 6.1.1 (BD Biosciences).

Adoptive Transfer and Depletion of Myeloid Cells

Mouse macrophages were in vitro differentiated from BM cells cultured with 50 ng/ml murine M-CSF for 5 days as described elsewhere (Saccani et al., 2006). Monocytes were isolated from BM using CD115 MicroBead Kit (Miltenyi Biotec, Auburn, CA). GR1⁺ cells were isolated from spleen of MN/MCA1-bearing mice with a MDSC isolation kit (Miltenyi Biotec). Cells (2×10^6) were transferred intravenously 72 hr after each drug treatment for 3 weeks. Macrophage depletion was performed by clodronate liposome (200 μl) intraperitoneally three times per week for 3 weeks. Control mice received liposome alone (van Rooijen and van Kesteren-Hendriks, 2003). GR1⁺ cells were depleted using anti-Gr1 antibody (RB6-8C5, eBioscience, San Diego, CA) and control mice received the isotype-matched LTF-2 antibody (BioXcell, West Lebanon, NH). Antibodies (200 μg /mouse) were injected intraperitoneally three times a week for 3 weeks.

Apoptosis and Caspase Activation

Human monocytes, neutrophils, and T lymphocytes from blood of healthy donors were purified through density gradients as described previously (Allavena et al., 2005). Cells were treated with trabectedin (2.5–10 nM) or recombinant TRAIL (500 ng/ml; Enzo Lifesciences) for different time points and

apoptosis evaluated as caspase activation and mitochondrial depolarization. Cleavage of caspases was detected by western blotting with anti-cleaved caspase-8 and 9 (Germano et al., 2010). In flow cytometry, cleavage of caspase-8 was detected on permeabilized cells. Pretreatment with blocking antibodies used anti-human TRAIL-R1, TRAIL-R2 (Enzo Lifesciences, Farmingdale, NY), TRAIL R3 (R&D Systems, Minneapolis, MN), anti-human Fas (Millipore, Billerica, MA) at 1 μ g/ml. Mouse monocytes were treated with 10 nM trabectedin and stained with anti-mouse cleaved caspase 8 (Cell Signaling). Measurement of mitochondrial potential was performed with the Mito Probe JC-1 assay kit (Invitrogen, Life Technology, Carlsbad, CA) for 30 min at 37°C.

Human Patients

Soft tissue sarcoma patients received trabectedin therapy as single treatment at Fondazione IRCCS Istituto Nazionale Tumori, Milan. The study was approved by the Institutional Ethical Board and blood samples were obtained upon written informed consent. Patients received multiple cycles of therapy at the dose of 1.3 mg/m² every 3 weeks as 24 hr infusion (Casali et al., 2010). Leukocytes were collected immediately before and at different days after drug administration. Cells were stained with anti-CD45-FITC, anti-CD14-PerCp, and CD16-PE (BD Biosciences) and analyzed on a FACSCalibur (BD Biosciences) cytofluorimeter. Analysis (1–2 × 10⁶ events) was done by WinMDI 2.9 software.

SUPPLEMENTAL INFORMATION

Supplemental Information includes five figures and Supplemental Experimental Procedures and can be found with this article online at <http://dx.doi.org/10.1016/j.ccr.2013.01.008>.

ACKNOWLEDGMENTS

We thank N. Polentarutti and M. Sironi for helpful assistance with animal experiments, C. Buracchi for flow cytometry, S. Morlacchi and B. Savino for MDSC experiments, I. Bersani for immunohistochemistry, and Prof. Bolognesi's group (University Milano) for modeling experiments. This work was supported by Associazione Italiana Ricerca Cancro (AIRC) grants (to P.A., A.M., M.D., A.A., and R.M.) and grant AIRC 5 X 1000 (to A.M.), by Regione Lombardia (Agreement no. 14501A), and by a MIUR grant (to P.A.). C.M.G. is an employee and shareholder of PharmaMar, the company that distributes the drug trabectedin.

Received: July 7, 2011

Revised: November 23, 2012

Accepted: January 15, 2013

Published: February 11, 2013

REFERENCES

Allavena, P., and Mantovani, A. (2012). Immunology in the clinic review series: focus on cancer: tumour-associated macrophages: undisputed stars of the inflammatory tumour microenvironment. *Clin. Exp. Immunol.* 167, 195–205.

Allavena, P., Signorelli, M., Chieppa, M., Erba, E., Bianchi, G., Marchesi, F., Olimpico, C.O., Bonardi, C., Garbi, A., Lissoni, A., et al. (2005). Anti-inflammatory properties of the novel antitumor agent yondelis (trabectedin): inhibition of macrophage differentiation and cytokine production. *Cancer Res.* 65, 2964–2971.

Apetoh, L., Ghiringhelli, F., Tesniere, A., Obeid, M., Ortiz, C., Criollo, A., Mignot, G., Maiuri, M.C., Ullrich, E., Saulnier, P., et al. (2007). Toll-like receptor 4-dependent contribution of the immune system to anticancer chemotherapy and radiotherapy. *Nat. Med.* 13, 1050–1059.

Balkwill, F., and Mantovani, A. (2001). Inflammation and cancer: back to Virchow? *Lancet* 357, 539–545.

Balkwill, F., and Mantovani, A. (2010). Cancer and inflammation: implications for pharmacology and therapeutics. *Clin. Pharmacol. Ther.* 87, 401–406.

Beatty, G.L., Chiorean, E.G., Fishman, M.P., Saboury, B., Teitelbaum, U.R., Sun, W., Huhn, R.D., Song, W., Li, D., Sharp, L.L., et al. (2011). CD40 agonists

alter tumor stroma and show efficacy against pancreatic carcinoma in mice and humans. *Science* 331, 1612–1616.

Ben-Neriah, Y., and Karin, M. (2011). Inflammation meets cancer, with NF- κ B as the matchmaker. *Nat. Immunol.* 12, 715–723.

Benedict, C.A., and Ware, C.F. (2012). TRAIL: not just for tumors anymore? *J. Exp. Med.* 209, 1903–1906.

Bodmer, J.L., Holler, N., Reynard, S., Vinciguerra, P., Schneider, P., Juo, P., Blenis, J., and Tschopp, J. (2000). TRAIL receptor-2 signals apoptosis through FADD and caspase-8. *Nat. Cell Biol.* 2, 241–243.

Bottazzi, B., Polentarutti, N., Acero, R., Balsari, A., Boraschi, D., Ghezzi, P., Salmons, M., and Mantovani, A. (1983). Regulation of the macrophage content of neoplasms by chemoattractants. *Science* 220, 210–212.

Bottazzi, B., Erba, E., Nobili, N., Fazioli, F., Rambaldi, A., and Mantovani, A. (1990). A paracrine circuit in the regulation of the proliferation of macrophages infiltrating murine sarcomas. *J. Immunol.* 144, 2409–2412.

Carter, N.J., and Keam, S.J. (2010). Trabectedin: a review of its use in soft tissue sarcoma and ovarian cancer. *Drugs* 70, 355–376.

Casali, P.G., Sanfilippo, R., and D'Incalci, M. (2010). Trabectedin therapy for sarcomas. *Curr. Opin. Oncol.* 22, 342–346.

Cazanave, S.C., Mott, J.L., Bronk, S.F., Werneburg, N.W., Fingas, C.D., Meng, X.W., Finnberg, N., El-Deiry, W.S., Kaufmann, S.H., and Gores, G.J. (2011). Death receptor 5 signaling promotes hepatocyte lipoapoptosis. *J. Biol. Chem.* 286, 39336–39348.

Chan, F.K., Chun, H.J., Zheng, L., Siegel, R.M., Bui, K.L., and Lenardo, M.J. (2000). A domain in TNF receptors that mediates ligand-independent receptor assembly and signaling. *Science* 288, 2351–2354.

Charytonowicz, E., Terry, M., Coakley, K., Telis, L., Remotti, F., Cordon-Cardo, C., Taub, R.N., and Matushansky, I. (2012). PPAR γ agonists enhance ET-743-induced adipogenic differentiation in a transgenic mouse model of myxoid round cell liposarcoma. *J. Clin. Invest.* 122, 886–898.

Clancy, L., Mruk, K., Archer, K., Woelfel, M., Mongkolsapaya, J., Screaton, G., Lenardo, M.J., and Chan, F.K. (2005). Preligand assembly domain-mediated ligand-independent association between TRAIL receptor 4 (TR4) and TR2 regulates TRAIL-induced apoptosis. *Proc. Natl. Acad. Sci. USA* 102, 18099–18104.

Colotta, F., Allavena, P., Sica, A., Garlanda, C., and Mantovani, A. (2009). Cancer-related inflammation, the seventh hallmark of cancer: links to genetic instability. *Carcinogenesis* 30, 1073–1081.

Coussens, L.M., and Werb, Z. (2002). Inflammation and cancer. *Nature* 420, 860–867.

D'Incalci, M., and Galmarini, C.M. (2010). A review of trabectedin (ET-743): a unique mechanism of action. *Mol. Cancer Ther.* 9, 2157–2163.

DeNardo, D.G., Barreto, J.B., Andreu, P., Vaszquez, L., Tawfik, D., Kolhatkar, N., and Coussens, L.M. (2009). CD4(+) T cells regulate pulmonary metastasis of mammary carcinomas by enhancing protumor properties of macrophages. *Cancer Cell* 16, 91–102.

DeNardo, D.G., Brennan, D.J., Rexhepaj, E., Ruffell, B., Shiao, S.L., Madden, S.F., Gallagher, W.M., Wadhwani, N., Keil, S.D., Junaid, S.A., et al. (2011). Leukocyte complexity predicts breast cancer survival and functionally regulates response to chemotherapy. *Cancer Discov.* 1, 54–67.

Diehl, G.E., Yue, H.H., Hsieh, K., Kuang, A.A., Ho, M., Morici, L.A., Lenz, L.L., Cado, D., Riley, L.W., and Winoto, A. (2004). TRAIL-R as a negative regulator of innate immune cell responses. *Immunity* 21, 877–889.

Duluc, D., Corvaisier, M., Blanchard, S., Catala, L., Descamps, P., Gamelin, E., Ponsoda, S., Delneste, Y., Hebbard, M., and Jeannin, P. (2009). Interferon-gamma reverses the immunosuppressive and protumoral properties and prevents the generation of human tumor-associated macrophages. *Int. J. Cancer* 125, 367–373.

Erba, E., Bergamaschi, D., Bassano, L., Damia, G., Ronzoni, S., Faircloth, G.T., and D'Incalci, M. (2001). Ecteinascidin-743 (ET-743), a natural marine compound, with a unique mechanism of action. *Eur. J. Cancer* 37, 97–105.

Ferrara, N. (2010). Role of myeloid cells in vascular endothelial growth factor-independent tumor angiogenesis. *Curr. Opin. Hematol.* 17, 219–224.

- Forni, C., Minuzzo, M., Virdis, E., Tamborini, E., Simone, M., Tavecchio, M., Erba, E., Grosso, F., Gronchi, A., Aman, P., et al. (2009). Trabectedin (ET-743) promotes differentiation in myxoid liposarcoma tumors. *Mol. Cancer Ther.* 8, 449–457.
- Geissmann, F., Manz, M.G., Jung, S., Sieweke, M.H., Merad, M., and Ley, K. (2010). Development of monocytes, macrophages, and dendritic cells. *Science* 327, 656–661.
- Germano, G., Frapolli, R., Simone, M., Tavecchio, M., Erba, E., Pesce, S., Pasqualini, F., Grosso, F., Sanfilippo, R., Casali, P.G., et al. (2010). Antitumor and anti-inflammatory effects of trabectedin on human myxoid liposarcoma cells. *Cancer Res.* 70, 2235–2244.
- Grosso, F., Jones, R.L., Demetri, G.D., Judson, I.R., Blay, J.Y., Le Cesne, A., Sanfilippo, R., Casieri, P., Collini, P., Dileo, P., et al. (2007). Efficacy of trabectedin (ecteinascidin-743) in advanced pretreated myxoid liposarcomas: a retrospective study. *Lancet Oncol.* 8, 595–602.
- Guiducci, C., Vicari, A.P., Sangaletti, S., Trinchieri, G., and Colombo, M.P. (2005). Redirecting in vivo elicited tumor infiltrating macrophages and dendritic cells towards tumor rejection. *Cancer Res.* 65, 3437–3446.
- Hanahan, D., and Coussens, L.M. (2012). Accessories to the crime: functions of cells recruited to the tumor microenvironment. *Cancer Cell* 21, 309–322.
- Hanahan, D., and Weinberg, R.A. (2011). Hallmarks of cancer: the next generation. *Cell* 144, 646–674.
- Herbeuval, J.P., Grivel, J.C., Boasso, A., Hardy, A.W., Chougnet, C., Dolan, M.J., Yagita, H., Lifson, J.D., and Shearer, G.M. (2005). CD4+ T-cell death induced by infectious and noninfectious HIV-1: role of type 1 interferon-dependent, TRAIL/DR5-mediated apoptosis. *Blood* 106, 3524–3531.
- Jenkins, S.J., Ruckerl, D., Cook, P.C., Jones, L.H., Finkelman, F.D., van Rooijen, N., MacDonald, A.S., and Allen, J.E. (2011). Local macrophage proliferation, rather than recruitment from the blood, is a signature of TH2 inflammation. *Science* 332, 1284–1288.
- Joyce, J.A., and Pollard, J.W. (2009). Microenvironmental regulation of metastasis. *Nat. Rev. Cancer* 9, 239–252.
- Le Cesne, A., Cresta, S., Maki, R.G., Blay, J.Y., Verweij, J., Poveda, A., Casali, P.G., Balaña, C., Schöffski, P., Grosso, F., et al. (2012). A retrospective analysis of antitumor activity with trabectedin in translocation-related sarcomas. *Eur. J. Cancer* 48, 3036–3044.
- Lim, S.C., Duong, H.Q., Choi, J.E., Lee, T.B., Kang, J.H., Oh, S.H., and Han, S.I. (2011). Lipid raft-dependent death receptor 5 (DR5) expression and activation are critical for ursodeoxycholic acid-induced apoptosis in gastric cancer cells. *Carcinogenesis* 32, 723–731.
- Mantovani, A., Allavena, P., Sica, A., and Balkwill, F. (2008). Cancer-related inflammation. *Nature* 454, 436–444.
- Mantovani, A., Sozzani, S., Locati, M., Allavena, P., and Sica, A. (2002). Macrophage polarization: tumor-associated macrophages as a paradigm for polarized M2 mononuclear phagocytes. *Trends Immunol.* 23, 549–555.
- Martinez, F.O., Helming, L., and Gordon, S. (2009). Alternative activation of macrophages: an immunologic functional perspective. *Annu. Rev. Immunol.* 27, 451–483.
- Mazzieri, R., Pucci, F., Moi, D., Zonari, E., Ranghetti, A., Berti, A., Politi, L.S., Gentner, B., Brown, J.L., Naldini, L., and De Palma, M. (2011). Targeting the ANG2/TIE2 axis inhibits tumor growth and metastasis by impairing angiogenesis and disabling rebounds of proangiogenic myeloid cells. *Cancer Cell* 19, 512–526.
- Minuzzo, M., Marchini, S., Brogini, M., Faircloth, G., D'Incalci, M., and Mantovani, R. (2000). Interference of transcriptional activation by the antineoplastic drug ecteinascidin-743. *Proc. Natl. Acad. Sci. USA* 97, 6780–6784.
- Monk, B.J., Herzog, T.J., Kaye, S.B., Krasner, C.N., Vermorken, J.B., Muggia, F.M., Pujade-Lauraine, E., Lisyanskaya, A.S., Makhson, A.N., Rolski, J., et al. (2010). Trabectedin plus pegylated liposomal Doxorubicin in recurrent ovarian cancer. *J. Clin. Oncol.* 28, 3107–3114.
- Movahedi, K., Williams, M., Van den Bossche, J., Van den Bergh, R., Gysemans, C., Beschin, A., De Baetselier, P., and Van Ginderachter, J.A. (2008). Identification of discrete tumor-induced myeloid-derived suppressor cell subpopulations with distinct T cell-suppressive activity. *Blood* 111, 4233–4244.
- Movahedi, K., Laoui, D., Gysemans, C., Baeten, M., Stangé, G., Van den Bossche, J., Mack, M., Pipeleers, D., In't Veld, P., De Baetselier, P., and Van Ginderachter, J.A. (2010). Different tumor microenvironments contain functionally distinct subsets of macrophages derived from Ly6C(high) monocytes. *Cancer Res.* 70, 5728–5739.
- Murdoch, C., Muthana, M., Coffelt, S.B., and Lewis, C.E. (2008). The role of myeloid cells in the promotion of tumour angiogenesis. *Nat. Rev. Cancer* 8, 618–631.
- Murray, P.J., and Wynn, T.A. (2011). Protective and pathogenic functions of macrophage subsets. *Nat. Rev. Immunol.* 11, 723–737.
- Noonan, D.M., De Lerma Barbaro, A., Vannini, N., Mortara, L., and Albini, A. (2008). Inflammation, inflammatory cells and angiogenesis: decisions and indecisions. *Cancer Metastasis Rev.* 27, 31–40.
- Park, M.H., Jo, M., Won, D., Song, H.S., Song, M.J., and Hong, J.T. (2012). Snake venom toxin from *Vipera lebetina turanica* sensitizes cancer cells to TRAIL through ROS- and JNK-mediated upregulation of death receptors and downregulation of survival proteins. *Apoptosis* 17, 1316–1326.
- Pollard, J.W. (2004). Tumour-educated macrophages promote tumour progression and metastasis. *Nat. Rev. Cancer* 4, 71–78.
- Qian, B.Z., and Pollard, J.W. (2010). Macrophage diversity enhances tumor progression and metastasis. *Cell* 141, 39–51.
- Qian, B.Z., Li, J., Zhang, H., Kitamura, T., Zhang, J., Campion, L.R., Kaiser, E.A., Snyder, L.A., and Pollard, J.W. (2011). CCL2 recruits inflammatory monocytes to facilitate breast-tumour metastasis. *Nature* 475, 222–225.
- Rolny, C., Mazzone, M., Tugues, S., Laoui, D., Johansson, I., Coulon, C., Squadrito, M.L., Segura, I., Li, X., Knevels, E., et al. (2011). HRG inhibits tumor growth and metastasis by inducing macrophage polarization and vessel normalization through downregulation of PIGF. *Cancer Cell* 19, 31–44.
- Saccani, A., Schioppa, T., Porta, C., Biswas, S.K., Nebuloni, M., Vago, L., Bottazzi, B., Colombo, M.P., Mantovani, A., and Sica, A. (2006). p50 nuclear factor-kappaB overexpression in tumor-associated macrophages inhibits M1 inflammatory responses and antitumor resistance. *Cancer Res.* 66, 11432–11440.
- Shirley, S., Morizot, A., and Micheau, O. (2011). Regulating TRAIL receptor-induced cell death at the membrane: a deadly discussion. *Recent Patents Anticancer Drug Discov.* 6, 311–323.
- Sica, A., and Bronte, V. (2007). Altered macrophage differentiation and immune dysfunction in tumor development. *J. Clin. Invest.* 117, 1155–1166.
- Sica, A., and Mantovani, A. (2012). Macrophage plasticity and polarization: in vivo veritas. *J. Clin. Invest.* 122, 787–795.
- Siegelin, M.D. (2012). Utilization of the cellular stress response to sensitize cancer cells to TRAIL-mediated apoptosis. *Expert Opin. Ther. Targets* 16, 801–817.
- Solinas, G., Schiarea, S., Liguori, M., Fabbri, M., Pesce, S., Zammataro, L., Pasqualini, F., Nebuloni, M., Chiabrando, C., Mantovani, A., and Allavena, P. (2010). Tumor-conditioned macrophages secrete migration-stimulating factor: a new marker for M2-polarization, influencing tumor cell motility. *J. Immunol.* 185, 642–652.
- Steidl, C., Lee, T., Shah, S.P., Farinha, P., Han, G., Nayar, T., Delaney, A., Jones, S.J., Iqbal, J., Weisenburger, D.D., et al. (2010). Tumor-associated macrophages and survival in classic Hodgkin's lymphoma. *N. Engl. J. Med.* 362, 875–885.
- Steinwede, K., Henken, S., Bohling, J., Maus, R., Ueberberg, B., Brumshagen, C., Brincks, E.L., Griffith, T.S., Welte, T., and Maus, U.A. (2012). TNF-related apoptosis-inducing ligand (TRAIL) exerts therapeutic efficacy for the treatment of pneumococcal pneumonia in mice. *J. Exp. Med.* 209, 1937–1952.
- Swirski, F.K., Libby, P., Aikawa, E., Alcaide, P., Luscinskas, F.W., Weissleder, R., and Pittet, M.J. (2007). Ly-6Chi monocytes dominate hypercholesterolemia-associated monocytosis and give rise to macrophages in atherosclerosis. *J. Clin. Invest.* 117, 195–205.



van Rooijen, N., and van Kesteren-Hendrikx, E. (2003). "In vivo" depletion of macrophages by liposome-mediated "suicide". *Methods Enzymol.* 373, 3–16.

Wilson, N.S., Yang, A., Yang, B., Couto, S., Stern, H., Gogineni, A., Pitti, R., Marsters, S., Weimer, R.M., Singh, M., and Ashkenazi, A. (2012). Proapoptotic activation of death receptor 5 on tumor endothelial cells disrupts the vasculature and reduces tumor growth. *Cancer Cell* 22, 80–90.

Youn, J.I., Collazo, M., Shalova, I.N., Biswas, S.K., and Gabrilovich, D.I. (2012). Characterization of the nature of granulocytic myeloid-derived suppressor cells in tumor-bearing mice. *J. Leukoc. Biol.* 91, 167–181.

Zhang, J., Lu, Y., and Pienta, K.J. (2010). Multiple roles of chemokine (C-C motif) ligand 2 in promoting prostate cancer growth. *J. Natl. Cancer Inst.* 102, 522–528.

The LKB1-AMPK Pathway—Friend or Foe in Cancer?

D. Grahame Hardie^{1,*}

¹Division of Cell Signalling and Immunology, College of Life Sciences, University of Dundee, Dundee DD1 5EH, Scotland, UK

*Correspondence: d.g.hardie@dundee.ac.uk

<http://dx.doi.org/10.1016/j.ccr.2013.01.009>

Use of the biguanide metformin, an AMPK activator, is associated with a reduced incidence of cancer in diabetics, but it has been unclear whether this requires AMPK. In this issue of *Cancer Cell*, Shackelford and colleagues show, paradoxically, that biguanides are more effective in the treatment of mouse tumors that lack a functional LKB1-AMPK pathway.

Ten years ago, LKB1 was found to be the crucial upstream kinase required for activation of AMP-activated protein kinase (AMPK) (reviewed in [Hardie, 2004](#)). This finding placed a protein kinase known to be a tumor suppressor (LKB1) upstream of a kinase involved in regulation of metabolism in response to energy stress (AMPK). AMPK was already known to be activated by the anti-diabetic drug metformin. Putting these findings together, Morris and Alessi analyzed retrospective data from a cohort of patients with type 2 diabetes (T2D) and found that use of metformin rather than other medications was associated with a 30% lower cancer incidence ([Evans et al., 2005](#)). This association has since been observed in other diabetic cohorts, but the mechanism by which metformin might protect against cancer has been the subject of much debate. In a study reported in this issue of *Cancer Cell*, [Shackelford et al. \(2013\)](#) use a mouse model to show that the related drug phenformin appears, paradoxically, to be more effective in the treatment of non-small cell lung cancer (NSCLC) if the tumors lack a functional LKB1-AMPK pathway, suggesting that the latter can sometimes be a “foe” rather than a “friend” in cancer.

Metformin and phenformin, first used over 50 years ago for the treatment of T2D, are related biguanide drugs. Phenformin was withdrawn in most countries because of the serious but rare side effect of lactic acidosis, whereas metformin has become the drug of first choice in T2D. Both are cations that accumulate in mitochondria due to the charge gradient across the inner membrane, where they inhibit complex I of the respiratory chain ([Owen et al., 2000](#)). This causes depletion of cellular ATP and increases ADP and AMP, which is why they activate AMPK

([Hawley et al., 2010](#)). However, given the ubiquitous role of these nucleotides in cell function, it is not surprising that many AMPK-independent effects are now being documented.

At least three mechanisms can be proposed to explain the effects of metformin on cancer ([Figure 1](#)). Mechanism 1 is based on its known insulin-sensitizing and anti-hyperglycemic effects. Humans with T2D have an increased cancer incidence, and their high plasma insulin and/or glucose levels, which provide a cellular environment conducive to tumor growth, might be the culprits. By reversing hyperglycemia, and hence hypersecretion of insulin, metformin lowers plasma insulin as well as glucose. This could account in part for the protective effects of metformin in diabetics, but it cannot explain the effects in rodent models where the animals were not insulin-resistant. Two alternative hypotheses, both involving direct effects of metformin on tumor cells themselves, can be proposed in such cases. In mechanism 2, metformin activates AMPK in the tumor or pre-tumor cells, restraining their growth and proliferation. In addition, AMPK has been shown to oppose the Warburg effect, the switch from oxidative metabolism to glycolysis commonly observed in tumor cells ([Faubert et al., 2013](#)). Mechanism 3 is based on findings that LKB1-deficient cells are more prone to apoptosis in response to metabolic stress ([Shaw et al., 2004](#)) and that metformin causes a greater depletion of ATP in cells that are AMPK-deficient and therefore have defective energy homeostasis ([Foretz et al., 2010](#)). Up to 30% of NSCLCs ([Ji et al., 2007](#)) and smaller proportions of other cancers display loss-of-function mutations in LKB1. In such tumors, the ATP-depleting proper-

ties of metformin might promote cell death.

Although it focuses on phenformin rather than metformin, the new study by [Shackelford et al. \(2013\)](#) helps to distinguish between mechanisms 2 and 3. Starting with a K-Ras mutant and LKB1 null NSCLC cell line, they found that phenformin had a larger effect than metformin on ATP levels, while only phenformin triggered apoptosis. Similar results were obtained in other NSCLC lines, where apoptosis triggered by phenformin correlated strictly with LKB1 loss but not with other mutations. They went on to use a mouse model of NSCLC in which expression of mutant K-Ras, either alone or combined with loss of either LKB1 or p53, was selectively triggered in lung epithelial cells by intratracheal administration of viral vectors encoding Cre recombinase ([Ji et al., 2007](#)). As observed previously, the tumor burden was greatly increased when mutant K-Ras was combined with the loss of LKB1 or p53. In the tumors that still expressed LKB1, phenformin caused more AMPK phosphorylation than metformin, so further experiments focused on phenformin (although these results did confirm that both drugs were reaching the tumor cells and causing energy stress). They next tested two protocols, one giving phenformin in drinking water 6 weeks after tumor initiation and the other by daily oral gavage after 3 weeks. In the former, phenformin seemed to cause modest reductions in tumor burden and increased markers of tumor apoptosis in all three genotypes, although these effects were only statistically significant in the LKB1 null tumors. In the latter, phenformin enhanced overall survival of the mice by several weeks, while tumor volume and fluorodeoxyglucose uptake (a marker of

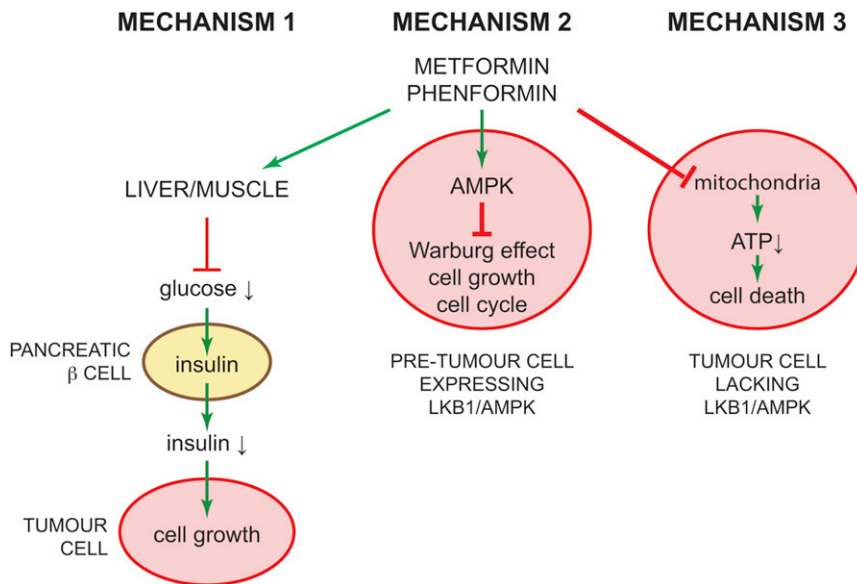


Figure 1. Three Alternate Mechanisms to Explain Protective Effects of Biguanides in Cancer
In mechanism 1, which would only operate in insulin-resistant individuals, the drugs lower plasma glucose, and thus increase the secretion of insulin from the pancreas. The consequent drop in plasma insulin and glucose reverses the favorable environment for tumor cell growth. In mechanism 2, they activate AMPK in the pretumor cell, exerting a cytostatic effect and preventing the metabolic switch to the Warburg effect. In mechanism 3, they selectively reduce ATP levels in tumor cells with a nonfunctional LKB1-AMPK pathway due to their inability to respond to energy stress, thus triggering cell death. All three mechanisms might operate in different cases of cancer, while mechanisms 1 and 2 or 1 and 3, could conceivably coexist in a single case.

the Warburg effect) were lower after 4 weeks of treatment, but, crucially, all of these effects were only seen in the tumors that had lost LKB1.

Because the mice used in these studies were not diabetic or insulin-resistant, phenformin did not reduce plasma glucose or insulin, ruling out mechanism 1. In addition, because the beneficial effects were only observed in the LKB1 null cancers, they had to be direct, cell-autonomous effects on the tumor cells themselves. Overall, the results clearly support mechanism 3 (i.e., that cells that have lost a functional LKB1-AMPK pathway are more sensitive to cell death induced by phenformin) and not mechanism 2 (i.e., that it works by activating AMPK in the tumors). In this mechanism, phenformin is effectively acting as a cytotoxic agent, but an attractive feature is that normal cells would be resistant because they have a functioning LKB1-AMPK pathway. This raises the exciting prospect that biguanides might be particularly useful for the treatment of those

tumors where the LKB1-AMPK pathway is downregulated. There are mechanisms by which this happens, other than by simple genetic loss of LKB1; for example, although mutations in the LKB1 gene appear to be rare in breast cancer, immunohistochemical analyses suggest that AMPK activation is frequently downregulated (Hadad et al., 2009).

These results do not rule out the occurrence of mechanisms 1 and 2 in other situations, particularly where biguanides may be used to prevent rather than treat cancer. Another caveat is that the beneficial effects on tumor burden and fluoro-deoxyglucose uptake observed after 4 weeks of phenformin treatment were no longer significant after 6 weeks, suggesting that phenformin resistance developed. This might arise as the cells start to make more of their ATP by glycolysis and become less dependent on mitochondrial function. All of the mice did also eventually succumb to cancer despite treatment, so phenformin is unlikely to be effective as a single therapy.

One of the most interesting features of this study was the focus on the use of phenformin rather than metformin. The effects of metformin on tumor burden or survival were not tested, although its smaller effects on AMPK in the tumors expressing LKB1, and its lack of effect on apoptosis in the cell culture models suggest that it would have been less effective than phenformin. A possible explanation of the greater effectiveness of phenformin is that it is more cell-permeable than metformin, and its uptake into cells is less dependent on expression of organic cation transporters (Hawley et al., 2010). Although phenformin was withdrawn for use in T2D because of cases of lactic acidosis, these were rare (<1 case per 1,000 patient years), and this frequency of side effect may be more acceptable for the treatment of cancer rather than diabetes.

REFERENCES

- Evans, J.M., Donnelly, L.A., Emslie-Smith, A.M., Alessi, D.R., and Morris, A.D. (2005). *BMJ* 330, 1304–1305.
- Faubert, B., Boily, G., Izreig, S., Griss, T., Samborska, B., Dong, Z., Dupuy, F., Chambers, C., Fuerth, B.J., Viollet, B., et al. (2013). *Cell Metab.* 17, 113–124.
- Foretz, M., Hébrard, S., Leclerc, J., Zarrinpashneh, E., Soty, M., Mithieux, G., Sakamoto, K., Andreelli, F., and Viollet, B. (2010). *J. Clin. Invest.* 120, 2355–2369.
- Hadad, S.M., Baker, L., Quinlan, P.R., Robertson, K.E., Bray, S.E., Thomson, G., Kellock, D., Jordan, L.B., Purdie, C.A., Hardie, D.G., et al. (2009). *BMC Cancer* 9, 307.
- Hardie, D.G. (2004). *J. Cell Sci.* 117, 5479–5487.
- Hawley, S.A., Ross, F.A., Chevzoff, C., Green, K.A., Evans, A., Fogarty, S., Towler, M.C., Brown, L.J., Ogunbayo, O.A., Evans, A.M., and Hardie, D.G. (2010). *Cell Metab.* 11, 554–565.
- Ji, H., Ramsey, M.R., Hayes, D.N., Fan, C., McNamara, K., Kozlowski, P., Torrice, C., Wu, M.C., Shimamura, T., Perera, S.A., et al. (2007). *Nature* 448, 807–810.
- Owen, M.R., Doran, E., and Halestrap, A.P. (2000). *Biochem. J.* 348, 607–614.
- Shackelford, D.B., Abt, E., Gerken, L., Vasquez, D.S., Seki, A., Leblanc, M., Wei, L., Fishbein, M.C., Czernin, J., Mischel, P.S., and Shaw, R.J. (2013). *Cancer Cell* 23, this issue, 143–158.
- Shaw, R.J., Kosmatka, M., Bardeesy, N., Hurley, R.L., Witters, L.A., DePinho, R.A., and Cantley, L.C. (2004). *Proc. Natl. Acad. Sci. USA* 101, 3329–3335.

Growth Factor Independence 1 Antagonizes a p53-Induced DNA Damage Response Pathway in Lymphoblastic Leukemia

Cyrus Khandanpour,^{1,3,9} James D. Phelan,^{4,9,10} Lothar Vassen,¹ Judith Schütte,⁶ Riyan Chen,¹ Shane R. Horman,^{4,11} Marie-Claude Gaudreau,^{1,2} Joseph Krongold,^{1,7} Jinfang Zhu,⁸ William E. Paul,⁸ Ulrich Dührsen,³ Bertie Göttgens,⁶ H. Leighton Grimes,^{4,5,*} and Tarik Möröy^{1,2,7,*}

¹Institut de recherches cliniques de Montréal (IRCM), 110 Avenue des Pins Ouest, Montréal, Québec H2W 1R7, Canada

²Département de Microbiologie et Immunologie, Université de Montréal, Montréal, Québec H3C 3J7, Canada

³Department of Haematology, University Hospital, University Duisburg-Essen, Hufelandstrasse 55, 45122 Essen, Germany

⁴Division of Cellular and Molecular Immunology

⁵Division of Experimental Hematology

Cincinnati Children's Hospital Medical Center, Cincinnati, OH 45229, USA

⁶Cambridge Institute for Medical Research and Wellcome Trust-Medical Research Council Cambridge Stem Cell Institute, University of Cambridge, Cambridge CB2 0XY, UK

⁷Division of Experimental Medicine, McGill University, Montreal, Québec H3A 1A3, Canada

⁸Laboratory of Immunology, National Institute of Allergy and Infectious Disease, National Institutes of Health, Bethesda, MD 20829, USA

⁹These authors contributed equally to this work

¹⁰Present address: Metabolism Branch, Center for Cancer Research, National Cancer Institute, National Institutes of Health, Bethesda, MD 20892, USA

¹¹Present address: Genomics Institute of the Novartis Research Foundation, San Diego, CA 92121, USA

*Correspondence: lee.grimes@cchmc.org (H.L.G.), tarik.moroy@ircm.qc.ca (T.M.)

<http://dx.doi.org/10.1016/j.ccr.2013.01.011>

SUMMARY

Most patients with acute lymphoblastic leukemia (ALL) fail current treatments highlighting the need for better therapies. Because oncogenic signaling activates a p53-dependent DNA damage response and apoptosis, leukemic cells must devise appropriate countermeasures. We show here that growth factor independence 1 (Gfi1) can serve such a function because Gfi1 ablation exacerbates p53 responses and lowers the threshold for p53-induced cell death. Specifically, Gfi1 restricts p53 activity and expression of proapoptotic p53 targets such as *Bax*, *Noxa* (*Pmaip1*), and *Puma* (*Bbc3*). Subsequently, Gfi1 ablation cures mice from leukemia and limits the expansion of primary human T-ALL xenografts in mice. This suggests that targeting Gfi1 could improve the prognosis of patients with T-ALL or other lymphoid leukemias.

INTRODUCTION

Many patients with acute lymphoblastic leukemia (ALL) and lymphoma die of tumor relapse (Gökbuget and Hoelzer, 2009). Experiments with mouse models have shown that T-ALL-like diseases can be accelerated by the overexpression of the transcriptional repressor growth factor independence 1 (Gfi1), which

is a well-established nuclear zinc finger protein and regulator of lymphoid development (Gilks et al., 1993; Zörnig et al., 1996; Li et al., 2010; Pargmann et al., 2007; Spooner et al., 2009; Yücel et al., 2003). Germline *Gfi1* deletion in mice modestly reduces thymic cellularity, with an accumulation of cells between double-negative 1 (DN1) and DN2 stages as well as a skew from CD4⁺ to CD8⁺ (Yücel et al., 2003). In contrast, the thymus is

Significance

Chemotherapy is nonspecific and highly toxic, damaging both host and tumor tissues. Even when effective, patients suffer dramatic side effects from standard treatments. Molecular-based targeted therapies have shown great promise but lack broad applicability due to the heterogeneity of oncogenic pathways mutated during transformation. Here, we demonstrate that ablation of Gfi1 broadly leads to lymphoid tumor regression and host survival independent of the transforming pathway. We demonstrate that Gfi1 limits the proapoptotic functions of the endogenous gatekeeper p53. Gfi1 inhibition amplifies p53-dependent proapoptotic responses driven by oncogenic stress; consequently, transformed lymphoid tissues are uniquely susceptible to Gfi1 inhibition. Thus, in combination with current therapies, Gfi1 inhibition may allow the use of lower cytotoxic doses, which would benefit patients directly.

relatively normal when *Gfi1* is deleted after the DN stage (Zhu et al., 2006), which suggests that Gfi1 mainly acts during early steps of T lymphopoiesis. Gfi1's ability to accelerate leukemogenesis in mice and its function in lymphoid development prompted us to explore the role of Gfi1 ablation in the initiation or maintenance of lymphoid malignancies.

RESULTS

GFI1 Is Associated with a Subgroup of Human T-ALL and Accelerates NOTCH1-Induced T-ALL in Mice

Although the oncogenic impact of high-level Gfi1 expression in murine T cell leukemogenesis is well established, an association of *GFI1* with human T-ALL has not been clearly shown. Because over 50% of human T-ALL displays mutated *NOTCH1* (Weng et al., 2004) or Notch1 regulatory proteins (O'Neil et al., 2007; Thompson et al., 2007) resulting in overexpression of Notch1 target genes (Palomero et al., 2006; Sharma et al., 2006; Weng et al., 2006), we performed hierarchical clustering of microarray data from independent cohorts of patients with T-ALL using *NOTCH1* mutation status (Ferrando et al., 2002), Notch1 target gene activation (Palomero et al., 2006; Van Vlierberghe et al., 2008), or early T cell precursor (ETP)-ALL diagnosis (Coustans-Smith et al., 2009) and examined *GFI1* expression (Figures 1A and 1B; Figures S1A–S1F available online).

We observed that patients with ETP-ALL had low levels of *GFI1* expression compared to those with a positive *NOTCH1* signature (Figures 1B, S1D, and S1E), suggesting a functional role for Gfi1 in *NOTCH1*-dependent human T-ALL. However, *GFI1* is unlikely a Notch1 target because intracellular Notch1 (ICN) does not occupy the *GFI1* locus nor was *GFI1* expression altered by γ -secretase inhibitors (GSIs) based on our own results as well as published data (Figure S1F) (Margolin et al., 2009; Medyouf et al., 2011). Also, we can show that mice transplanted with bone marrow (BM) cells overexpressing ICN and Gfi1 developed leukemia faster than mice transplanted with cells only overexpressing ICN (Figures S1G–S1I), corroborating previous reports on the function of Gfi1 in T cell leukemogenesis (Schmidt et al., 1998; Zörnig et al., 1996) and extending it to human ICN-mediated T-ALL.

Gfi1 Deletion Delays the Development of T-ALL

To test whether ablation of Gfi1 could inhibit the onset of T-ALL, we used five different mouse models, in which we could temporally delete *Gfi1*. First, we transplanted ICN-expressing BM cells from mice carrying a tamoxifen (OHT)-inducible *Rosa26* Cre-recombinase transgene (*Cre^{ERT2}*) (Hameyer et al., 2007) enabling inducible deletion of floxed *Gfi1* alleles (*Gfi1^{flf}*) (Horman et al., 2009; Velu et al., 2009) (Figure 1C). Although vehicle-treated animals died within 66 days, OHT-treated recipients developed leukemia within 87 days with similar T-ALL characteristics (Figures 1C–1F). However, all tumors emerging after OHT treatment had intact *Gfi1* alleles (Figure 1D), suggesting that ICN-induced T-ALL selects for Gfi1.

To confirm this, we used a T cell-specific Cre transgene (*LckCre⁺*) and *Gfi1^{flΔ}* transgenic mice, in which *Rosa26* locus-mediated expression of ICN and EGFP is blocked by a floxed STOP cassette (*Rosa^{ICN^{LSL}}*) (Murtaugh et al., 2003). We injected these mice with N-ethyl-N-nitrosourea (ENU), which

induces T cell leukemia and shortens the latency of leukemogenesis (Kundu et al., 2005; Yuan et al., 2001). Approximately 50% of all tumors arising in *LckCre⁺;Rosa^{ICN^{LSL}};Gfi1^{+/+}* mice were EGFP⁺ (i.e., expressing ICN and Gfi1, Figures S1J and S1K). However, ENU-induced tumors that arose in *LckCre⁺;Rosa^{ICN^{LSL}};Gfi1^{flΔ}* mice were always EGFP[−] (i.e., ICN[−] and Gfi1 wild-type, Figure S1K), also suggesting that ICN-mediated tumorigenesis selects for Gfi1. In yet another Notch-driven leukemogenesis model, in which constitutive absence of *Gfi1* was coupled with a *CD4* promoter-driven mutant Notch1 transgene (*Notch1^{ΔCT}*; Priceputu et al., 2006), T-ALL development was substantially decreased and delayed (Figures 1G–1I).

To explore the impact of *Gfi1* loss in mouse models of T-ALL that are not initiated by Notch, we either infected *Gfi1^{+/+}* and *Gfi1^{−/−}* newborn mice with Murine Moloney Leukemia (MMLV) (Scheijen et al., 1997) or injected adolescent mice with ENU. All MMLV-infected *Gfi1^{+/+}* mice developed lymphoid malignancies, whereas only 40% of MMLV-infected *Gfi1^{−/−}* mice did. The remaining mice were censored due to neurological problems consistent with reports on older *Gfi1^{−/−}* mice (unpublished data). Notably, *Gfi1^{−/−}* lymphoid malignancies were significantly less robust than *Gfi1^{+/+}* tumors (Figures 1J–1L). Similarly, >85% of the ENU-injected *Gfi1^{+/+}* mice, but only 20% of *Gfi1^{−/−}* mice, developed T cell leukemia (Figure S1L); the remaining mice succumbed to ENU-induced toxicity. As in other models, ENU-initiated *Gfi1^{−/−}* tumors developed slower and were significantly less robust than *Gfi1^{+/+}* tumors (Figures S1L–S1N). Neither *Gfi1^{+/+}* nor *Gfi1^{−/−}* ENU-induced tumors were found to harbor *Notch1* mutations in the HD or PEST domain (Table S1). Thus, results from these five independent T-ALL models, initiated by various oncogenic pathways, led us to conclude that ablation of *Gfi1* delays, impedes, or is counterselected during T-ALL formation.

T-ALL Disease Maintenance Is Gfi1 Dependent

Mx1-Cre⁺;Gfi1^{flf} or *Gfi1^{flf}* mice were treated with ENU to elicit T cell leukemia. After 50 days, both groups were injected with plpC (Horman et al., 2009). All *Gfi1^{flf}* mice developed T-ALL, but *Mx1-Cre⁺;Gfi1^{flf}* mice separated into two different subgroups following plpC injection. One subgroup remained healthy until the study was terminated (Figure 2A, *Mx1-Cre⁺;Gfi1^{flf}*, full excision) or died of ENU toxicity. The second subgroup displayed partial *Gfi1* deletion and succumbed to T cell leukemia similar to ENU/plpC-treated *Gfi1^{flf}* mice (Figure 2A, *Mx1-Cre⁺;Gfi1^{flf}* partial excision).

To investigate whether loss of *Gfi1* was causing tumor regression or preventing tumor formation, we used ultrasound imaging. Upon detection of a tumor (Figure 2B), *Gfi1* deletion was induced with plpC. All ENU-induced tumors in *Gfi1^{flf}* mice clearly showed increases in tumor size, whereas tumors that developed in *Mx1-Cre⁺;Gfi1^{flf}* animals showed variable changes in size (Figures 2C and S2A). Following plpC injection, disease-free survival, tumor growth, and blast cell detection all directly correlated with the degree of *Gfi1* deletion in the tumor (Figures 2B, 2C, and S2B) because we found that *Gfi1* deletion was incomplete in tumors that progressed but was complete in tumors that regressed (Figure S2A).

We verified this observation in a second T-ALL model, in which disease was induced by Notch1 activation and

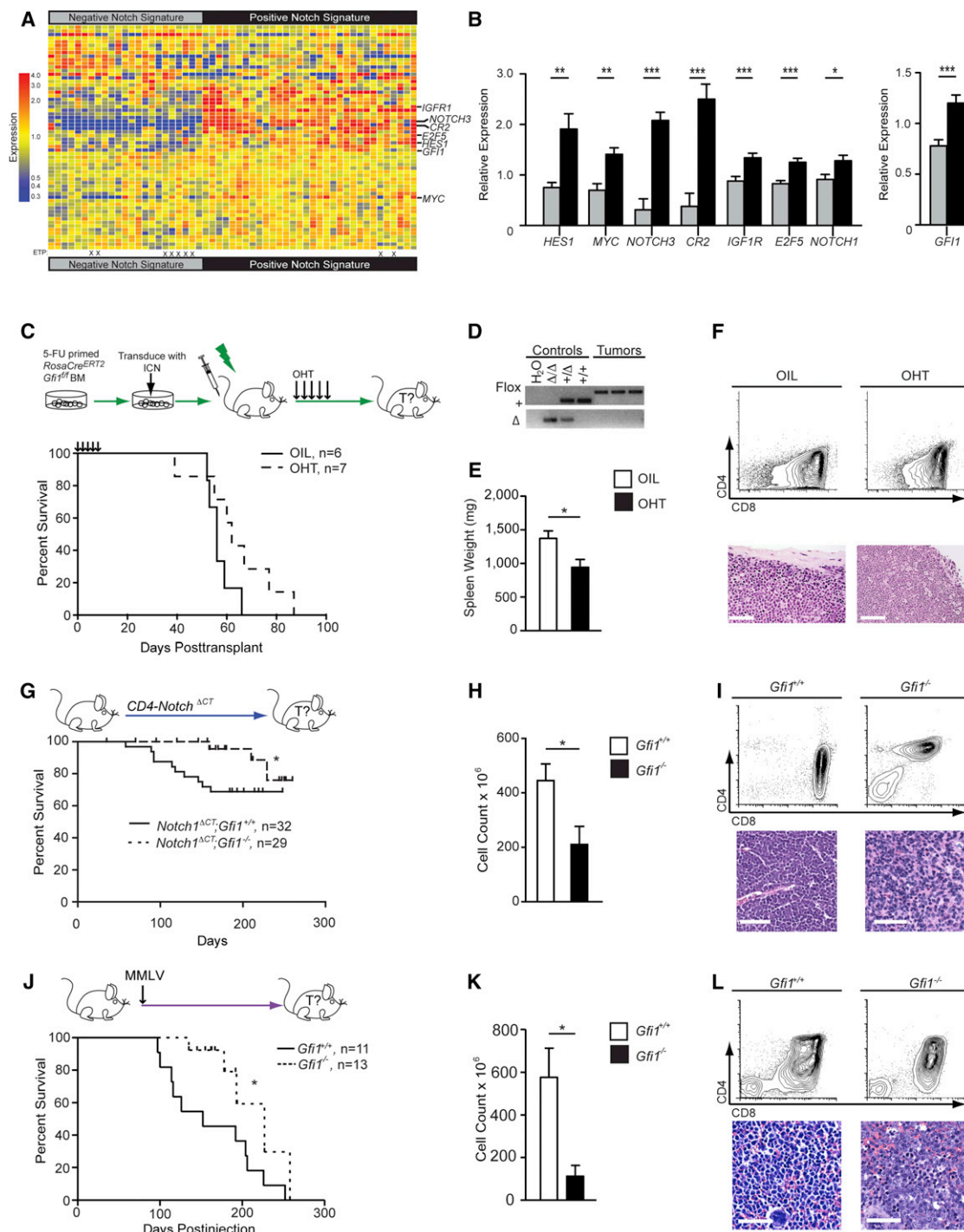


Figure 1. Gfi1 Associates with NOTCH1 in Human T-ALL, and Deletion Delays the Development of Disease

(A) Heatmap of expression of published Notch1 target genes used to classify gene expression array data from 55 patients with T-ALL (GSE8879) into two groups: "Negative Notch Signature" (left), and "Positive Notch Signature" (right). ETP-ALL diagnosis is designated by an "X."

(B) Quantification of relative expression of *NOTCH1*, *Gfi1*, and Notch1 target genes *HES1*, *MYC*, *NOTCH3*, *CR2*, *IGF1R*, and *E2F5* in 55 patients with T-ALL with either a "Negative Notch Signature" (gray) or a "Positive Notch Signature" (black).

(C) Top view shows *RosaCre^{ERT2};Gfi1^{fl/fl}* BM cells that were transduced with vectors expressing ICN and then transplanted. Mice were given vehicle or tamoxifen to induce Cre activity. Bottom view is a Kaplan-Meier curve.

(D) PCR genotype analysis of the *Gfi1* locus in control tissues (*Gfi1*^{Δ/Δ}, *Gfi1*^{+/-}, *Gfi1*^{+/+}) and in representative tumors from mice either treated with vehicle or OHT. FLOX, *Gfi1*^{fl} allele; +, the wild-type allele; Δ, deleted allele.

(E and F) Spleen weights (E; n = 6 each group) and flow cytometric analysis of thymic tumors (F, top panels) and spleen sections with H&E (F, bottom panels) collected during postmortems from indicated transplant groups.

(legend continued on next page)

accelerated by ENU injection. Mice were monitored by ultrasound and upon tumor detection, treated with plpC (Figure 2D). Although all plpC-injected *Notch1^{ΔCT};Gfi1^{fl/fl}* mice died, all plpC-injected *Notch1^{ΔCT};Mx1-Cre⁺;Gfi1^{fl/fl}* tumors with complete deletion of *Gfi1* regressed, and the mice survived (Figures 2D–2F). This regression also correlated with lower numbers of blast cells in the blood of plpC-treated *Notch1^{ΔCT};Mx1-Cre⁺;Gfi1^{fl/fl}* mice compared to *Notch1^{ΔCT};Gfi1^{fl/fl}* controls (Figure S2C).

Next, *Gfi1^{fl/fl}* or *Mx1-Cre⁺;Gfi1^{fl/Δ}* tumor cells were transplanted into syngeneic recipients. In recipients that did not receive plpC, only tumors with an intact floxed *Gfi1* allele emerged (data not shown). However, when recipient mice were treated with plpC, all mice that received *Gfi1^{fl/fl}* tumors died, whereas mice receiving *Mx1-Cre⁺;Gfi1^{fl/Δ}* tumors survived tumor free (Figure 2G). To demonstrate that loss of *Gfi1* specifically leads to tumor regression in a cell-autonomous manner, we inhibited *Gfi1* function in three Tal1-transformed murine T-ALL cell lines (Cullion et al., 2009) by overexpressing a dsRed-marked *Gfi1* dominant-negative mutant (*Gfi1^{N382S}*) (Horman et al., 2009; Person et al., 2003; Zarebski et al., 2008). Two days after the initial measurement of transduction, and in contrast to empty vector-transduced cells, only 15%–20% of cells transduced with dsRed⁺ *Gfi1^{N382S}*-expressing vectors were still dsRed⁺ (Figure 2H).

To determine the clinical potential of targeting *Gfi1*, we injected *Gfi1^{fl/fl}* and *Mx1-Cre⁺;Gfi1^{fl/fl}* mice (CD45.2⁺) with ENU, waited 50 days to allow tumor initiation, and then treated with plpC to delete *Gfi1*. Four weeks after the first plpC injection, both groups of mice were sublethally irradiated and transplanted with syngeneic CD45.1⁺ BM cells (BMT) to prevent BM failure associated with ENU (Figures 2I and 2J). The combination therapy was not sufficient to cure the mice of T-ALL because 80% of ENU-treated *Gfi1^{fl/fl}* mice still succumbed to disease (one died of nontumor-related reasons). However, when therapy was combined with *Gfi1* deletion, complete tumor remission was observed in every transplant recipient (Figures 2I and 2J). Taken together, our data strongly implicate *Gfi1* in the maintenance of established T cell malignancies, their ability to kill secondary hosts, and potentially in improving therapy.

Maintenance of B Cell Lymphoma Is Dependent on *Gfi1*

To test whether other lymphoid malignancies were also dependent on *Gfi1*, we used *Eμ-Myc* transgenic mice, which develop clonal B cell lymphomas (Adams et al., 1985). Loss of *Gfi1* did not affect the latency, incidence, or pathology of tumor initiation (Figures 3A and 3B) but completely blocked the ability of

lymphoma to kill secondary recipients (Figure S3A). Thus, similar to the T cell models, *Gfi1* is required for robust tumorigenesis. To determine whether *Gfi1* is required for B cell lymphoma maintenance, we used an inducible model (Zhu et al., 2006) to delete *Gfi1^{fl/fl}* after a lymphoma had formed. Although plpC injection had no effect on progression of disease in *Gfi1^{fl/fl};Eμ-Myc* mice, it led to tumor regression and a significant reduction of leukemic blasts in the peripheral blood of *Mx1-Cre⁺;Gfi1^{fl/fl};Eμ-Myc* mice (Figures 3C–3E and S3B), suggesting that *Gfi1* is indeed necessary to maintain a B cell lymphoma. Similar to the results with our T-ALL models, loss of *Gfi1* significantly improved the outcome of *Gfi1^{fl/fl};Eμ-Myc* mice treated with sublethal irradiation and BMT after detection of a tumor, whereas *Gfi1^{+/+};Eμ-Myc* animals died of tumor relapse (Figure 3F). These data suggest that targeting *Gfi1* could also be beneficial for treating B cell lymphoma.

Gfi1 Integrates the Cellular Transcriptional Response to DNA Damage/p53 Induction

To investigate how loss of *Gfi1* induces tumor regression, we compared gene expression profiles of T cell leukemia from two different models (Figures 2A and 2D) upon inducible deletion of *Gfi1* (Figure 4A). Gene Set Enrichment Analysis (GSEA) (Subramanian et al., 2005) demonstrated significant deregulation of multiple key leukemic pathways, including cell-cycle progression, NFκB signaling, and basal transcription among others (Table S2; data not shown). Normal thymocytes do not disappear upon loss of *Gfi1* as the tumors do. Therefore, to identify mechanisms that might explain tumor regression, we focused on those pathways that were similarly deregulated in both ENU and *Notch1^{ΔCT}*-induced tumors from *Gfi1^{fl/fl}* and *Gfi1^{+/+}* mice but were not enriched in normal nonmalignant *Gfi1^{fl/fl}* versus *Gfi1^{+/+}* thymocytes. We noticed a striking number of shared GSEA signatures that included deregulated p53 signaling, DNA damage/repair pathways, and a proapoptotic response (Figures 4B and 4C; Table S2), suggesting that an accelerated cell death program might be initiated in tumor cells that lack *Gfi1*.

An emerging concept proposes that oncogenic signaling induces uncoordinated cell division, generating collapsed replication forks and DNA double-strand breaks, which in turn initiate a DNA damage response, activating p53 and inducing apoptosis. Therefore, tumor cells must counteract cell death in order to survive (Bartek et al., 2007; Bartkova et al., 2007; Di Micco et al., 2006; Halazonetis et al., 2008). In agreement with this theory, leukemic cells from our tumor models displayed increased levels of phosphorylated H2AX (γH2AX), indicating DNA double-strand breaks, and higher levels of spontaneous

(G) Top view shows *Notch1^{ΔCT};Gfi1^{+/+}* and *Notch1^{ΔCT};Gfi1^{fl/fl}* mice that were monitored for tumor development and survival. Bottom view is a Kaplan-Meier curve.

(H and I) Spleen weights (H) and flow cytometric analysis (I, top panels) and histological sections (I, bottom panels) of *Notch1^{ΔCT};Gfi1^{+/+}* (n = 7) and *Notch1^{ΔCT};Gfi1^{fl/fl}* (n = 3) tumors.

(J) Top view shows *Gfi1^{+/+}* and *Gfi1^{fl/fl}* newborn mice that were injected with MMLV. Bottom view is a Kaplan-Meier curve.

(K) Thymic tumor cell numbers of *Notch1^{ΔCT}*-induced tumors.

(L) Flow cytometric analysis (top panels) and histological section (bottom panels) of MMLV-induced *Gfi1^{+/+}* versus *Gfi1^{fl/fl}* tumors.

Scale bars, 50 μm. Vertical line (|) in all Kaplan-Meier curves indicates censored mice. Mean and mean ± SEM are shown unless stated otherwise. *p < 0.05, **p < 0.01, ***p < 0.001.

See also Figure S1 and Table S1.

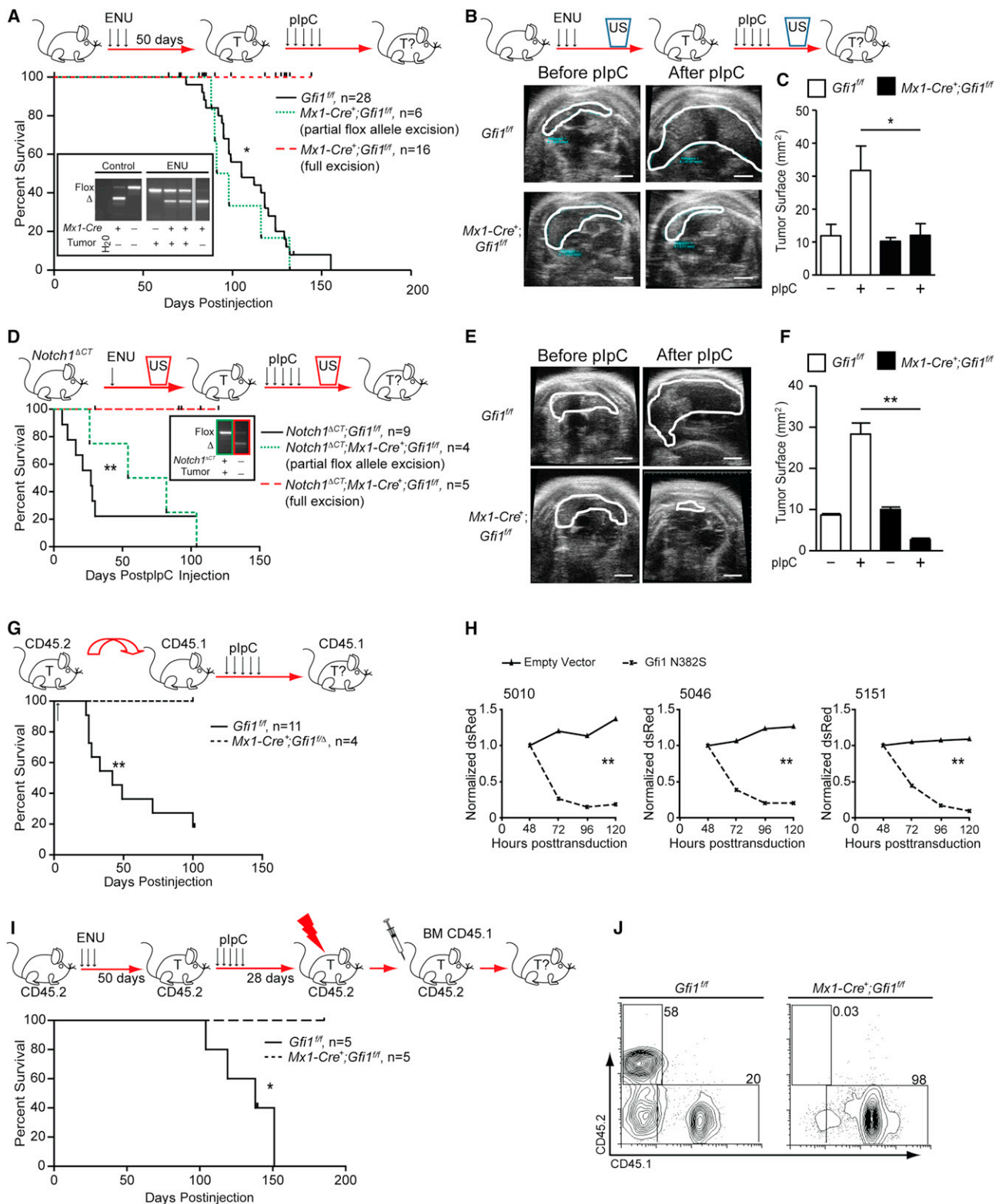


Figure 2. Gfi1 Is Required for T Cell Leukemia Maintenance

(A) Top view shows *Gfi1^{fl/+}* or *Mx1-Cre⁺; Gfi1^{fl/+}* mice that were treated with ENU and subsequently with plpC. Bottom view is a Kaplan-Meier curve. Inset presents PCR analysis of the *Gfi1* locus in control tissues and in representative tumors (T) for *Gfi1* flox and excised (Δ) alleles.

(B) Top view shows *Gfi1^{fl/+}* or *Mx1-Cre⁺; Gfi1^{fl/+}* mice that were treated with ENU and followed for tumors by ultrasound (US). Next, mice were treated with plpC, and tumor development was determined by ultrasound. Bottom view is representative ultrasound images. Scale bars, 20 mm.

(legend continued on next page)

apoptosis than untransformed thymocytes (Figures 4D–4F). We also noted that the number of apoptotic cells was further increased in those tumors where *Gfi1* was inducibly deleted (Figure 4F). Additionally, when we irradiated *Gfi1*^{−/−} leukemic cells, we observed decreased survival compared to *Gfi1*^{+/+} tumors (Figures 4G). Finally, when we overexpressed Bcl2 in Tal1-transformed T cell lines, counterselection of the dominant-negative mutant *Gfi1*^{N382S} was either absent or delayed (compare Figure 4H to Figure 2H). These data demonstrate that *Gfi1* is required in lymphoid tumors to counter DNA damage-induced death and suggest that DNA damage/p53-induced signals are dominant effectors of *Gfi1* loss-of-function apoptotic phenotypes in T-ALL.

In contrast to *Gfi1*-deleted tumors, *Gfi1*^{−/−} thymocytes display only mildly increased levels of apoptosis of c-Kit⁺ subsets (compared to *Gfi1*^{+/+}) (Yücel et al., 2003). In agreement with this observation, we noted that whereas GSEA of gene expression data of *Gfi1*^{−/−} versus *Gfi1*^{+/+} thymocytes is enriched for apoptotic signatures, the DNA damage and p53 signatures, which drive the execution of apoptosis, were not enriched (Figures 5A and 5B). Thus, we hypothesized that the introduction of a DNA damage signal (inherent to tumors) to *Gfi1*^{−/−} thymocytes may elicit the same increased apoptotic phenotype in thymocytes that was found in tumors. Indeed, gene expression analysis revealed that a comparison between γ -irradiated (to induce DNA damage) *Gfi1*^{−/−} versus *Gfi1*^{+/+} thymocytes recapitulated the exaggerated *Gfi1*^{−/−} GSEA DNA damage and p53 signatures found in leukemia cells (compare Figures 4B and 5B). Moreover, DNA damage induced by daunorubicin, etoposide, or by various doses of γ irradiation resulted in significantly decreased *Gfi1*^{−/−} thymocyte survival and mitochondrial potential (Figures S4A–S4E). Although *Gfi1*^{−/−} thymocytes showed similar levels of γ H2AX, p53 induction, and p53 phosphorylation compared to *Gfi1*^{+/+} controls (Figures S4F and S4G), *Gfi1*^{−/−} thymocytes displayed increased cleaved caspase-3 and PARP (Figures S4H and S4I). These data indicate that *Gfi1* antagonizes DNA damage-induced apoptotic pathways downstream of DNA damage detection but upstream of caspase and PARP1 cleavage.

To analyze this in more detail, the expression of cell death-associated p53 targets such as *Bax*, *Pmaip1* (Noxa), and *Bbc3* (Puma) was tested and found to be further induced in irradiated *Gfi1*^{−/−} thymocytes compared to *Gfi1*^{+/+} controls (Figure 5C).

These genes appear to be direct *Gfi1* targets because interrogation of *Gfi1* ChIP-seq data showed enriched *Gfi1* binding in the regulatory regions of *Bax*, *Pmaip1*, and *Bbc3* compared to IgG controls (Figure 5D). These data suggest that *Gfi1* co-occupies p53-responsive genes and regulates their expression. Interestingly, significant p53 binding to these same *Gfi1*-bound regions within the promoters (underscored in Figure 5D) of *Bax*, *Pmaip1*, and *Bbc3* was observed in thymocytes after induction of p53 by irradiation (Figure 5E). To assess whether *Gfi1* and p53 globally regulate the expression of proapoptotic p53 effector genes, we examined the leading edge of the GSEA *Gfi1*^{−/−}-irradiated thymocyte signature and found that >70% of the apoptotic genes were in fact proapoptotic effectors (Figure S4J). Moreover, combining the gene expression and ChIP-seq analyses revealed that *Gfi1* occupies 55 of 77 p53-effector genes (>70%) deregulated in irradiated *Gfi1*^{−/−} thymocytes (Figure 5F). We next validated the ChIP-seq data with ChIP-qPCR using primer sets for 14 of the 55 genes. These genes were (1) occupied by *Gfi1* according to ChIP-seq data with reads over 100 compared to Ig controls, (2) at least 1.5-fold differentially expressed between *Gfi1*^{−/−} and *Gfi1*^{+/+} thymocytes after irradiation, and (3) known p53 effector genes according to empirically tested data in the Molecular Signature Database (MSigDB). ChIP-qPCR confirmed binding of *Gfi1* in irradiated thymocytes with an enrichment of >1.5-fold in 10 of the 14 genes tested, suggested *Gfi1* binding in 3 genes with an enrichment of 1.3–1.5, and demonstrated little to no binding in only 1 of the 14 primer sets tested (Figure S4K). Co-occupation of the same loci by *Gfi1* and p53 was found in the majority of genes tested (9 of 14, Figure S4L). A time-dependent analysis on 4 of the 14 loci (*Bax*, *Pmaip1*, *Bbc3*, and *Cdkn1a*) revealed that a co-occupation by *Gfi1* and p53 is maintained over time but that p53 occupation clearly dominates at 120 min after the initial DNA damage signal over *Gfi1* (Figure S4M). This suggests that during the immediate response after DNA damage, *Gfi1* and p53 coregulate target genes, but if the DNA damage signal persists, a p53-dominated regulation prevails.

We investigated the involvement of the p53-activated apoptosis pathway in *Gfi1*^{−/−} thymocyte survival after DNA damage. To do so, we deleted *Trp53* or overexpressed *Bcl2* and found that either condition completely rescued the exaggerated *Gfi1*^{−/−} thymocyte apoptosis upon DNA damage signaling (Figure 5G). Further investigation into the underlying

(C) Change of thymic surface area before and after treatment with plpC for mice (see B).

(D) Top view shows *Notch1*^{ΔCT}; *Gfi1*^{fl/fl} or *Notch1*^{ΔCT}; *Mx1-Cre*⁺; *Gfi1*^{fl/fl} mice that were treated with ENU and subsequently monitored by ultrasound for tumor (T) development. Upon appearance of a mass, mice were injected with plpC and followed for tumor progression or regression by ultrasound. Bottom view is a Kaplan-Meier curve. Inset presents a PCR analysis of allele excision (Δ).

(E) Representative ultrasound images of mice before and after plpC injection. Scale bars, 20 mm.

(F) Change of thymic surface area before and after treatment with plpC (see E).

(G) Top view shows *Gfi1*^{fl/fl} tumors or tumors that had one *Gfi1* allele deleted (*Mx1-Cre*⁺; *Gfi1*^{fl/Δ}) were transplanted into CD45.1 recipient mice, which were then treated with plpC. Bottom view is a Kaplan-Meier curve.

(H) T-ALL cell lines 5151, 5046, and 5010 were transduced with retrovirus vectors expressing *Gfi1*^{N382S} and dsRed or dsRed alone. dsRed was measured over time by FACS and normalized to the level at 48 hr. One of three representative experiments is shown.

(I) Top view shows *Gfi1*^{fl/fl} or *Mx1-Cre*⁺; *Gfi1*^{fl/fl} mice that were injected with ENU. Fifty days later, they were treated with plpC. Twenty-eight days later, they were irradiated, and transplanted with wild-type CD45.1 BM cells, then followed for survival. Bottom view is a Kaplan-Meier curve. One *Gfi1*^{fl/fl} mouse was sacrificed for morbidity unrelated to leukemia.

(J) BM of mice in (I) at the end of observation was examined for contribution of the CD45.2 (host BM) and CD45.1 (donor BM).

Vertical line (|) in all Kaplan-Meier curves indicates censored mice. Mean and mean ± SEM are shown unless stated otherwise. *p < 0.05, **p < 0.01.

See also Figure S2.

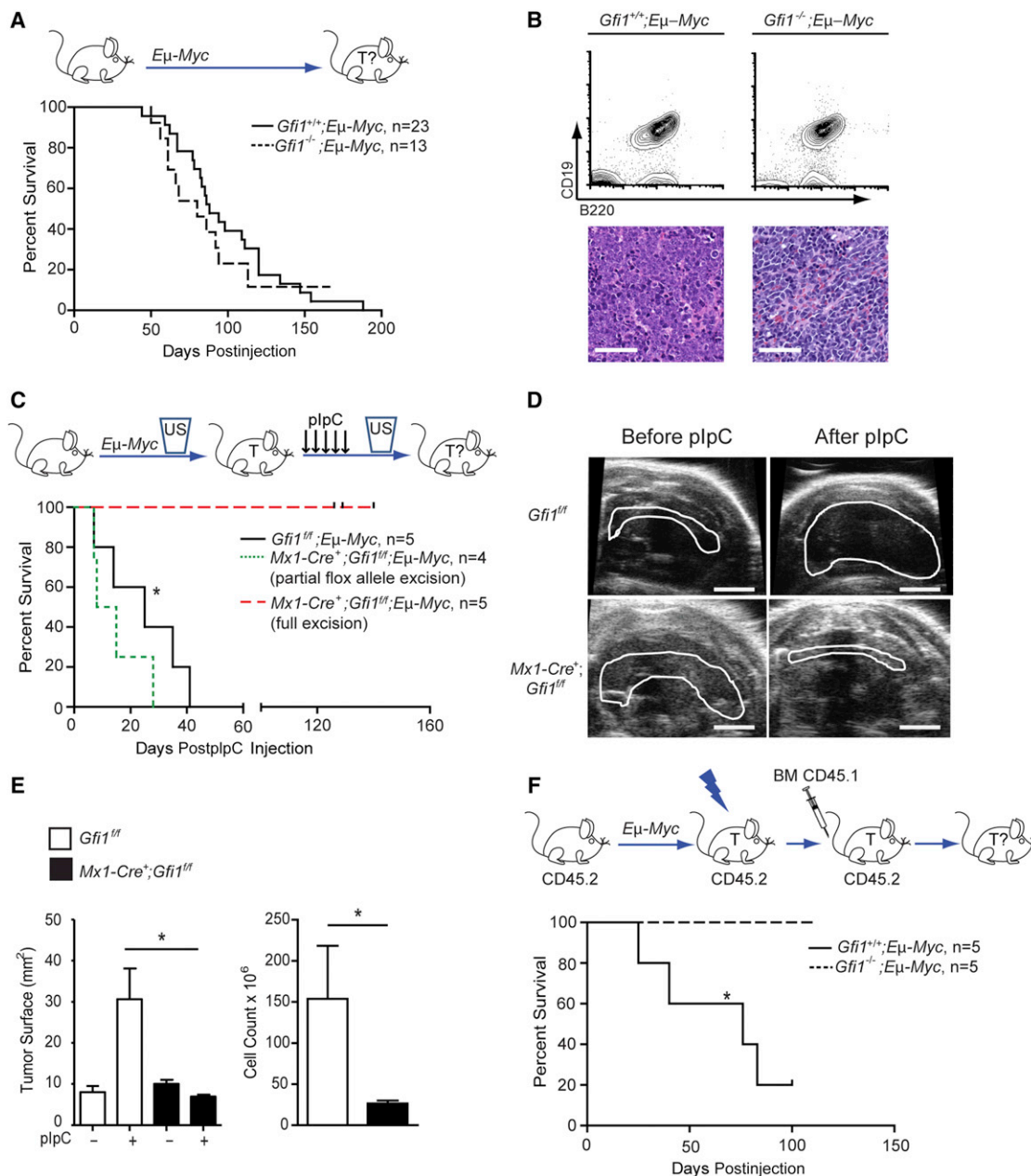


Figure 3. Gfi1 Is Required for Maintenance of B Cell Lymphoma

(A) Top view shows *Gfi1*^{+/+};Eμ-Myc and *Gfi1*^{-/-};Eμ-Myc mice that were monitored for tumor development and survival. Bottom view is a Kaplan-Meier curve.

(B) Flow cytometric analysis (top) and histological sections (bottom) of Eμ-Myc-induced *Gfi1*^{+/+} and *Gfi1*^{-/-} tumors. Scale bars, 50 μm.

(C) Top view shows *Mx1-Cre*⁺;Gfi1^{fl/fl};Eμ-Myc and *Gfi1*^{fl/fl};Eμ-Myc mice that were observed by ultrasound for appearance of B cell lymphoma. Upon appearance of a mass, mice were injected with plpC and monitored for tumor progression and survival. Bottom view is a Kaplan-Meier curve.

(D) Representative ultrasound images of tumors before and after plpC injection. Scale bars, 20 mm.

(E) Change of tumor surface area (left) before and after treatment with plpC for mice with the indicated genotypes as well as cellularity of mediastinal tumor after treatment (right).

(F) Top view shows *Gfi1*^{+/+};Eμ-Myc and *Gfi1*^{-/-};Eμ-Myc animals that were observed until enlarged lymph nodes evidenced tumor development, then they were irradiated and transplanted with CD45.1 BM cells and monitored for survival. Bottom view is a Kaplan-Meier curve.

Vertical line (|) in all Kaplan-Meier curves indicates censored mice. Mean and mean ± SEM are shown unless stated otherwise. *p < 0.05.

See also Figure S3.

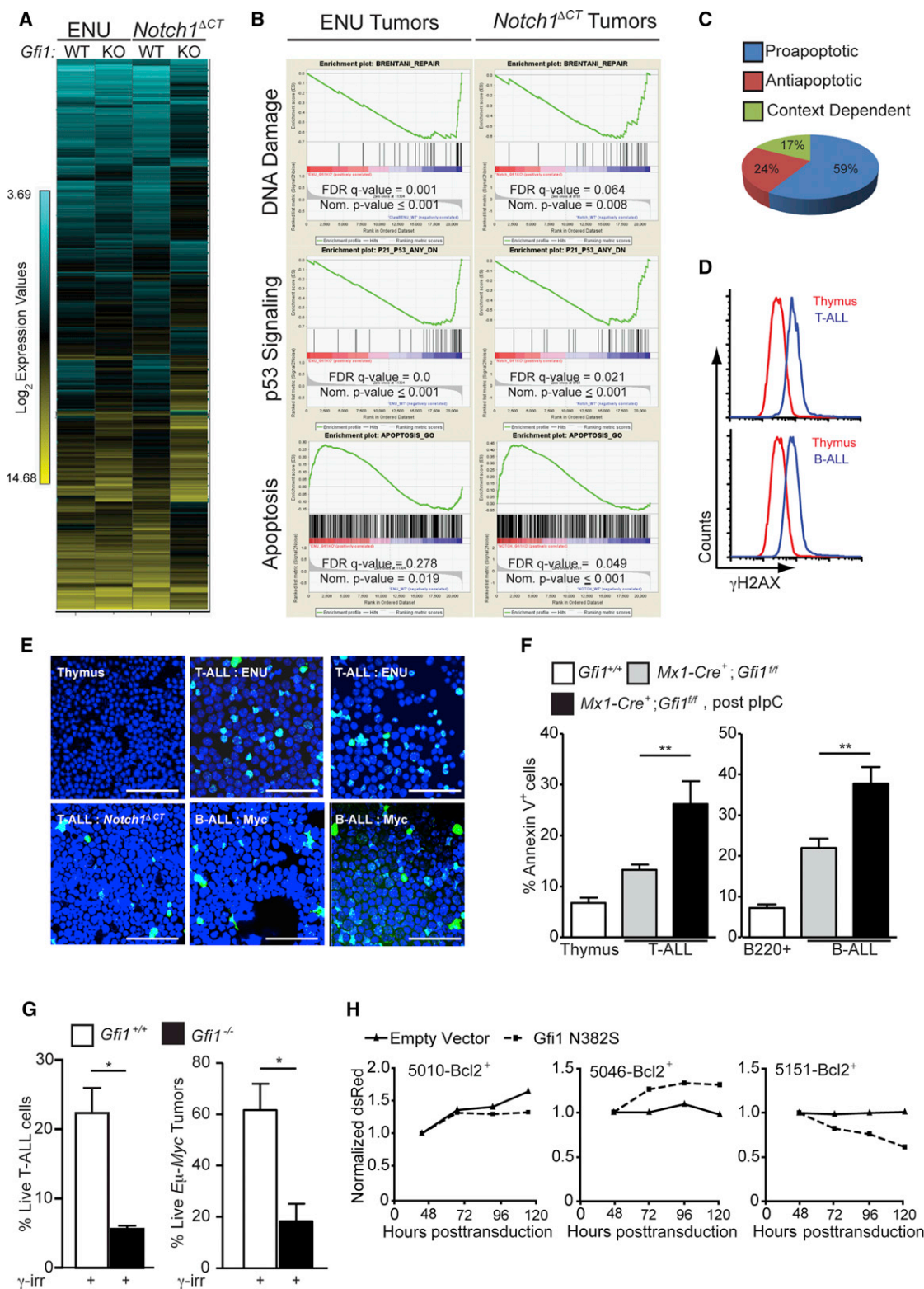


Figure 4. *Gfi1* Mediates DNA Damage and p53 Signaling to Control Apoptosis

(A) Unsupervised hierarchical clustering of the averaged normalized Log₂ gene expression values from ENU (n = 3) or ENU/*Notch1^{ΔCT}* (n = 2)-induced T-ALL arising in *Gfi1*^{fl/fl} (wild-type, WT) or *Mx1-Cre*⁺; *Gfi1*^{fl/fl} (knockout, KO) plpC-treated mice (ENU WT, n = 3; ENU KO, n = 3; ENU/*Notch1^{ΔCT}* WT, n = 2; ENU/*Notch1^{ΔCT}* KO, n = 2).

(B) GSEA butterfly plots for pathways related to DNA damage, p53 signaling, or apoptosis found in both ENU- and *Notch1^{ΔCT}*-initiated tumor signatures from (A).

(legend continued on next page)

mechanism demonstrated that Gfi1 and p53 can physically interact in transfected cells and in irradiated thymocytes (Figures 5H and 5I) and that Gfi1 was able to repress p53-mediated transcriptional activation of a model reporter gene (Figure 5J). Notably, methylation of p53 at K372 leads to increased stability of chromatin-bound p53 and to the activation of p53 target genes, whereas demethylation of K372 has an inhibitory effect on p53 (West and Gozani, 2011). Immunoprecipitation and immunoblot experiments with *Gfi1*^{+/+} and *Gfi1*^{-/-} thymocytes showed that absence of Gfi1 leads to a substantial increase of p53-K372me, regardless of irradiation (Figure 5K). Moreover, thymocytes from knockin mice expressing only a Gfi1^{P2A} mutant (Fiolka et al., 2006) that lacks the ability to bind LSD1 (Saleque et al., 2007) also displayed a substantial increase of p53-K372me (Figure 5L). These data suggest that Gfi1 restricts p53 activity through Gfi1 SNAG-dependent cofactor recruitment and p53 demethylation (Figure 5M).

Targeting GFI1 in Human ALL Leads to Tumor Death

To test whether Gfi1 could be a suitable target for therapy of human leukemia, we used human T-ALL cell lines and reduced Gfi1 expression either by transduction of previously described shRNA-expressing lentiviral vectors (Velu et al., 2009) or Vivo-Morpholinos (Morcos et al., 2008) specifically designed against *GFI1*. In both cases, reduction of Gfi1 impeded the growth of T-ALL cell lines, which correlated with a higher level of apoptosis (Figures 6A–6C and S5A–S5C), suggesting that T-ALL is sensitive to the induction of apoptosis. When we used the pan-Bcl2 inhibitors Obatoclastax and ABT-263 on three independent T-ALL lines, we observed IC₅₀ values approximately 10-fold lower than those observed in acute myeloid leukemia (AML), where the use of these drugs is currently in clinical trials (Figure 6D). Inhibition of Gfi1 further increased the efficiency of both Obatoclastax treatment (Figure 6E) and radiation therapy (Figure S5D). To demonstrate the contribution of p53 to Gfi1 loss-of-function apoptosis, we used Vivo-Morpholinos to first antagonize p53 expression then Gfi1 expression. We observed a significant decrease in the ability of the Gfi1 Vivo-Morpholinos to induce apoptosis after p53 Vivo-Morpholino pretreatment (Figure S5E). Similar results were obtained using p53-targeting shRNA lentiviruses followed by Gfi1 Vivo-Morpholino treatment (data not shown).

Next, we examined Gfi1 inhibition in primary patient samples. Due to the significant limitations of in vitro systems to support primary T-ALL cell survival, we transplanted primary patient specimens into immune-deficient Nod/Scid/IL2Rγ^{-/-}

(NSG) mice then tested whether targeting Gfi1 using morpholinos is a viable approach to treat leukemia. The cells were allowed to engraft and expand for 4 days before the mice were injected with Vivo-Morpholinos over a 3 week period and monitored for survival. Gfi1 Vivo-Morpholino-treated animals showed a trend toward increased survival after only three injections (Figures S5F–S5I). We repeated the assay with samples from a patient who failed to respond to current therapies but increased the treatment frequency. When control morpholino (NT)-treated mice became moribund, we analyzed the tissues of all of the transplanted mice for the presence of human T-ALL cells. Targeting Gfi1 significantly impeded the expansion of the human leukemia in the BM, peripheral blood, and the spleen of the transplanted NSG mice (Figures 6F–6H), whereas treatment of healthy mice with the same dosing regimen did not lead to adverse effects (Figure S5J).

DISCUSSION

Important roles for Gfi1 in normal lymphoid development and acceleration of murine T cell leukemia have previously been established (Blyth et al., 2001; Chakraborty et al., 2008; Dabrowska et al., 2009; Gilks et al., 1993; Scheijen et al., 1997; Schmidt et al., 1996; Uren et al., 2008; Yücel et al., 2003). Yet, questions remained whether Gfi1 was required for the development or maintenance of human lymphoid leukemia. In the current study, we found that ablation of Gfi1 leads to regression of already established murine lymphoid neoplasms occurring through the induction of p53-dependent apoptotic pathways. Our results indicate that leukemic cells in general require Gfi1 because the ablation of Gfi1 led to lymphoid tumor regression and host survival independently of the transforming pathway or tumor etiology. It is thus conceivable that Gfi1 is an “oncerequisite” factor, a normal cellular protein upon which malignant cells uniquely depend for their survival. This offers a different paradigm for cancer therapeutics and suggests that normal cellular proteins, independent of their mutation status in human tumors, can be excellent targets for clinical intervention.

Our findings are surprising given the recently identified function of Gfi1 in myeloproliferative disease (MPD) and AML, where Gfi1 loss of function derepresses HoxA9, Meis1, and Pbx1, and can cooperate with other oncogenic lesions to transform myeloid progenitors (Horman et al., 2009). Furthermore, a SNP in the human *GFI1* deregulates *HOXA9* expression and increases the risk for human AML by 60% (Khandanpour et al.,

(C) Classification of genes in the leading edge of the GSEA apoptosis signature in (B) as Proapoptotic, Antiapoptotic, or Context Dependent.

(D and E) Determination of γH2AX levels in normal tissue as well as in B and T cell leukemia by FACS (D) and immunofluorescence (E). One experiment was performed. Scale bars, 50 μm.

(F) Level of spontaneous apoptosis in the indicated tissues and tumors before and after *Gfi1* deletion. T-ALL: *Gfi1*^{+/+}, n = 4; *Gfi1*^{fl/fl}, n = 17; *Gfi1*^{Δ/Δ}, n = 5. B-ALL: *Gfi1*^{+/+}, n = 4; *Gfi1*^{fl/fl}, n = 13; *Gfi1*^{Δ/Δ}, n = 4.

(G) *Gfi1*^{+/+} (n = 7), *Gfi1*^{-/-} and *Gfi1*^{fl/Δ} (one constitutive Gfi1 KO tumor and two tumors, in which Gfi1 has been deleted with more than 50% excision, n = 3), thymic tumor cells and *Gfi1*^{+/+};Eμ-Myc⁺ (n = 7), and *Gfi1*^{-/-};Eμ-Myc⁺ (n = 3) lymphomas were explanted and irradiated (6 Gy), and examined for Annexin V staining by FACS.

(H) T-ALL cell lines 5151, 5046, and 5010 were transduced with retrovirus vectors MSCV-Bcl-2, expanded, and then transduced with vectors encoding Gfi1^{N382S} and dsRed or dsRed alone. dsRed was measured over time by FACS and normalized to the level at 48 hr. One of three representative experiments is shown.

Mean and mean ± SEM are shown unless stated otherwise. *p < 0.05, **p < 0.01.

See also Table S2.

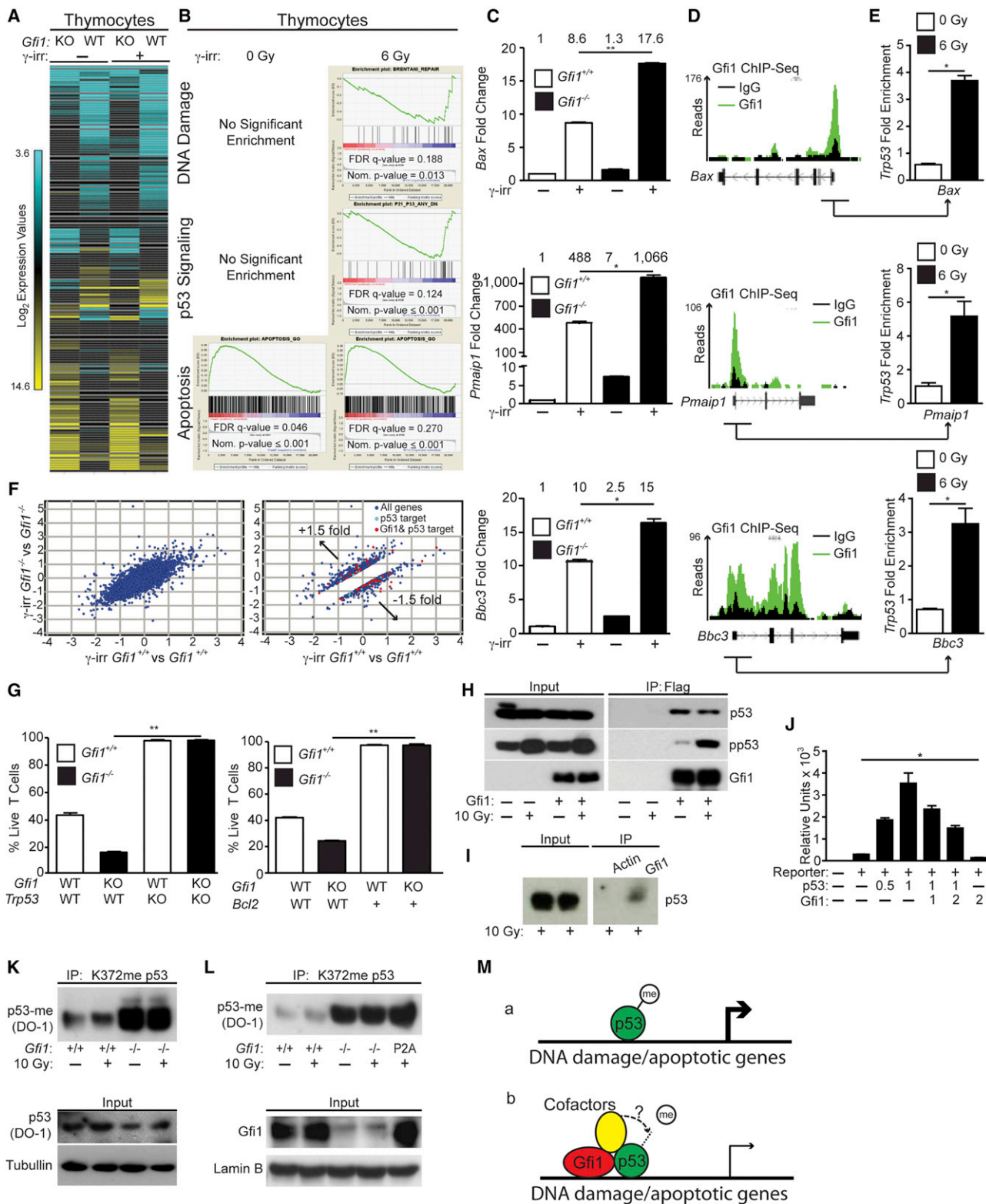


Figure 5. Gfi1 Restricts p53-Dependent Induction of Apoptosis

(A) Unsupervised hierarchical clustering of the averaged normalized Log₂ gene expression values from Gfi1^{+/+} (WT) and Gfi1^{-/-} (KO) thymocytes with or without irradiation (Gfi1^{+/+} control, n = 2; Gfi1^{-/-} irradiated, n = 3; Gfi1^{-/-} irradiated, n = 3). (B) GSEA butterfly plots for pathways related to DNA damage, p53 signaling, or apoptosis enriched in Gfi1-deficient tumors (Figure 4B) that emerge in Gfi1^{-/-} T cells only after irradiation.

(legend continued on next page)

2012); however, further experimentation is still necessary to incisively define a role for Gfi1 in human AML. HoxA9 signaling is present in mixed-lineage leukemia but is active in less than 10% of patients with T-ALL (Ferrando et al., 2002). Thus, patients with rare HoxA9-active T-ALL may not benefit from receiving Gfi1-targeting therapies. Therefore, careful molecular pathology will likely be important to stratify patients for Gfi1-targeted therapeutics.

Recent work suggested that oncogenic signaling in general causes uncoordinated cell division resulting in collapsed replication forks and the initiation of p53-dependent DNA damage responses causing cell death (Halazonetis et al., 2008; Bartek et al., 2007; Bartkova et al., 2007; Di Micco et al., 2006). Tumor cells have to counteract this “oncogenic stress” signal to avoid cell death, for instance by mutating *TP53*. However, *TP53* mutations are rare in T-ALL; hence, leukemic cells have to devise other measures to circumvent apoptosis. Our data offer an explanation as to how lymphoid malignancies can overcome p53 activation and why they are dependent on Gfi1. We propose that DNA damage, initiated by oncogenic stress during malignant transformation, induces p53 activity. High Gfi1-expressing subclones can thus be selected during transformation to enable global restriction of p53-mediated apoptosis. Gfi1 exerts this function by (1) co-occupying p53 target genes such as *Bax*, *Pmaip1*, and *Bbc3*; (2) binding to p53-bound transcriptional complexes; and (3) limiting the methylation of p53 at K372 thereby restricting the activity of p53 and the activation of p53 target genes.

The function of Gfi1 to limit p53-K372 methylation (p53-K369 in murine cells) (Kurash et al., 2008) appears to be dependent on its ability to bind SNAG-dependent cofactors such as LSD1. It is known that demethylation of p53 at K370 is mediated by LSD1 and prevents p53 association with coactivators such as p53BP1 (Huang et al., 2007). We propose that leukemic cells use a Gfi1-LSD1 or a Gfi1-SNAG-dependent cofactor complex to demethylate p53 at K372, which prevents

a full activation of p53 and its proapoptotic target genes. However, we cannot exclude the possibility that loss of Gfi1-SNAG-dependent transcriptional repression leads to the activation of factors, which may directly affect p53 activation/methylation status. In either case, ablation of Gfi1 leads to an accumulation of more active methylated p53, to a more efficient transactivation of proapoptotic p53 target genes, and as a consequence, to accelerated cell death. Several independent lines of evidence support this notion including reporter gene assays, ChIP-seq data, biochemical analyses, and expression data and offer a mechanistic explanation why Gfi1 ablation leads to regression of murine lymphomas and causes an inhibition of primary human T-ALL cell expansion in immune-deficient mice.

Our findings have direct implications for current ALL treatments, which consist of chemotherapy and irradiation. Both are nonspecific and highly toxic, damaging host and tumor tissues. These therapies function mainly through the induction of DNA damage and the initiation of p53-dependent DNA damage response pathways that cause cell death. Even when effective, patients can suffer dramatic side effects from standard ALL treatments. Therefore, reducing chemotherapeutic or irradiation dose and thus their side effects while maintaining their efficacy would directly benefit patients. The main result from our study suggests that this goal can be achieved by inhibiting the function of Gfi1 in patients with T-ALL because ablation of Gfi1 accelerates p53-induced cell death in leukemic cells. According to our data, leukemic cells lacking Gfi1 will be more sensitive to DNA damage-inducing chemo- or irradiation therapy and undergo accelerated apoptosis. It is thus conceivable that targeting Gfi1 will not only significantly improve response rates but may in particular allow lower effective doses of chemotherapeutic agents or irradiation. In summary, our findings suggest that Gfi1 represents an Achilles’ heel of lymphoid leukemias, and our approach to target Gfi1 may soon move to clinical trials.

(C) Expression of *Bax*, *Pmaip1* (*Noxa*), and *Bbc3* (*Puma*) in *Gfi1*^{+/+} and *Gfi1*^{-/-} thymocytes before and after irradiation. One representative experiment out of at least two experiments is shown. The numbers above the bars represent the mean values of the measurements.

(D) Peaks across the *Bax*, *Pmaip1*, and *Bbc3* loci from Gfi1 ChIP-seq of murine hematopoietic progenitor cells immortalized by retroviral transduction of an MLL-ENL expression vector (GSE31657).

(E) ChIP of p53 using primers from Gfi1-bound regions (underscored with arrow in D) of *Bax*, *Pmaip1*, and *Bbc3* before and after irradiation. Represented are the mean and SD of the fold difference compared to IgG control from one experiment with three technical repeats.

(F) Log₂ values of the fold change of the irradiated versus unirradiated gene expression values of all genes (left) or 1.5-fold differentially regulated (right) between *Gfi1*^{+/+} and *Gfi1*^{-/-} thymocytes. Gfi1-bound (identified in D) p53 target genes are shown in red.

(G) Percentage of live *Gfi1*^{+/+}; *Trp53*^{+/+}, *Gfi1*^{-/-}; *Trp53*^{+/+}, *Gfi1*^{+/+}; *Trp53*^{-/-}, and *Gfi1*^{-/-}; *Trp53*^{-/-} thymocytes after ex vivo γ irradiation (left, n = 3). Percentage of live *Gfi1*^{+/+}, *Gfi1*^{-/-}, *Gfi1*^{+/+}; *Vav-Bcl2*, and *Gfi1*^{-/-}; *Vav-Bcl2* thymocytes after ex vivo γ irradiation (right, n = 3).

(H) Immunoblot of total-cell lysate (left) and immunoprecipitation (right) were performed using p53, phospho-p53, or Gfi1 antibodies on lysates from untreated or irradiated 293T cells transfected as indicated with FLAG-tagged Gfi1 constructs. One representative experiment from at least two experiments is shown.

(I) Immunoblot of total-cell lysate (left) and immunoprecipitation using either Gfi1 or an isotype control (actin) antibody (right) were performed using phospho-p53 (Ser15) antibody on lysates from irradiated thymocytes cells. One representative experiment from at least two experiments is shown.

(J) Reporter expression assay using the *Bax* promoter and various amounts (μ g) of transfected vectors encoding p53 or Gfi1.

(K) Thymocytes from the indicated mice were irradiated or left untreated. After 30 min, total-cell lysates were immunoprecipitated with an anti-mono-methyl K372 p53 antibody, then immunoblotted with an anti-p53 antibody. p53 and tubulin in total-cell lysates are also shown. One experiment out of at least two experiments is shown.

(L) Thymocyte nuclear extracts from the indicated mouse strains were immunoprecipitated with an anti-mono-methyl K372 p53 antibody, then immunoblotted with an anti-p53 antibody. Input control shows the level of Gfi1 in thymocytes from *Gfi1*^{+/+}, *Gfi1*^{-/-}, and *Gfi1*^{P2A/P2A} mice and the loading control LaminB. One experiment out of at least two experiments is shown.

(M) Schematic representation showing methylated p53 binds to DNA and robustly activates the expression of target genes (a), and Gfi1 co-occupancy of a subset of p53 targets tethers a Gfi1 SNAG-dependent cofactor, which demethylates p53 to dampen the expression of p53 target gene (b).

Mean and \pm mean SEM are shown unless stated otherwise. *p < 0.05, **p < 0.01.

See also Figure S4.

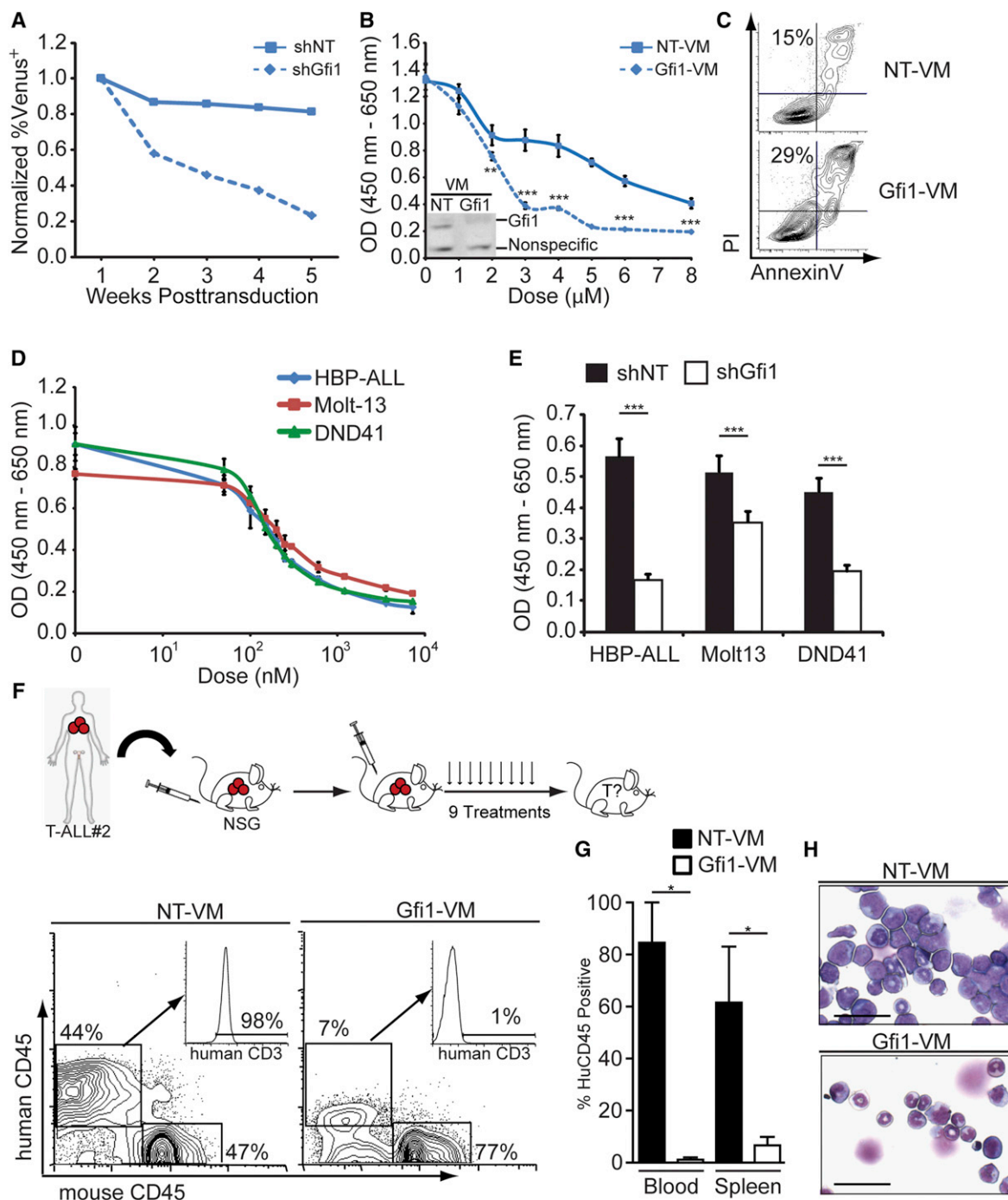


Figure 6. Gfi1 as a Target to Treat Human Leukemia

(A) HBP-ALL cells were transduced with Venus-marked shRNA-expressing lentiviral vectors targeting Gfi1 (shGfi1, dotted line) or nontargeting control (shNT, solid line). Expression of Venus was measured by FACS 72 hr posttransduction, which was set as 1, and subsequent measurements were taken by FACS over a 5 week period and normalized to the first reading, $p = 0.058$.

(B) Growth of HBP-ALL cells treated with Gfi1 or NT Vivo-Morpholinos (VM) as measured by WST assay for 48 hr. Inset shows immunoblot for Gfi1 in HBP-ALL cells treated with NT or Gfi1-VM (4μ M) for 16 hr.

(C) Annexin V and PI staining of HBP-ALL cells after 16 hr of Gfi1 or NT VM treatment (4μ M).

(D) Growth of T-ALL cell lines treated with indicated doses of the Obatoclax as measured by WST assay for 48 hr.

(E) Gfi1 knockdown was combined with Obatoclax treatment (200 nM), and growth was measured by WST assay for 48 hr. One representative experiment is shown; experiments were repeated two to three times (A–E).

(F) Top view shows primary patient T-ALL samples that were transplanted in NSG mice and then mice were injected with Gfi1 or NT VM three times per week for 3 weeks. Bottom view is a FACS analysis of human CD45 and human CD3 of NT ($n = 2$) or Gfi1-treated ($n = 3$) mice.

(legend continued on next page)

EXPERIMENTAL PROCEDURES

All other experimental procedures can be found in the [Supplemental Information](#).

Mice

LckCre⁺, *Mx1-Cre⁺*, C57BL/6, CD45.1, *Trp53^{-/-}*, and NSG mice were obtained from The Jackson Laboratory (Bar Harbor, ME, USA). Regarding other mouse strains, please refer to the [Supplemental Experimental Procedures](#). Mice were housed in either single ventilated cages with top filters or microisolator cages. The Institutional Animal Care, Use and Ethical Committees responsible for Cincinnati Children's Hospital Medical Center (CCHMC), the Institut de Recherches Cliniques de Montréal (IRCM), and University Clinic Essen (UKE) reviewed and approved all animal experimentation.

Xenograft Transplants and Morpholino Treatment

Diagnostic patient samples were obtained after informed consent according to Helsinki declaration and with approval from the institutional review boards at the IRCM, CCHMC, and UKE for the described experiments. One million T-ALL cells were transplanted (i.v.) into NSG mice that were injected 4 days later (i.v.) with Vivo-Morpholinos (Gene Tools) as described in [Figures 6 and S5](#) with 25 nM of control ("NT-VM," 5'-CCTCTTACCTCAGTTACAATT TATA-3') or Gfi1-specific ("Gfi1-VM," 5'-ATGGTGGTCCGGCACTTCCCCACT-3') Vivo-Morpholinos per injection.

In Vivo Deletion of Gfi1 and Ultrasound Observation

Gfi1^{fl/fl} or *RosaCre^{ERT2} Gfi1^{fl/fl}* mice were injected (i.p.) with 1 mg OHT (Sigma-Aldrich) dissolved in 100 μ l of corn oil the first 5 days following transplantation. *Gfi1^{fl/fl}* or *Mx1-Cre⁺;Gfi1^{fl/fl}* mice were either injected (i.p.) 4 weeks after the last ENU injection or 3 days after the transplantation of the tumor cells with 500 mg plpC (Sigma-Aldrich) seven times every other day. PCR validation of in vivo deletion was performed as previously described ([Horman et al., 2009](#)). Ultrasound observation was performed on anesthetized mice, and thymic tumors were measured using the Visualsonic ultrasound machine and the Vev0770 imaging software (Toronto). A tumor was called present if the thymic surface area measured in the horizontal and sagittal plane was larger than 8 mm² because average thymic surface of age-matched, untreated *Gfi1^{fl/fl}* control mice is 4 mm², and if the tumor exhibited growth of more than 50% during the last 2 weeks of observation.

Statistics

GraphPad Prism software (GraphPad Software, La Jolla, CA, USA) was used for most statistical analysis. Kaplan-Meier curves were analyzed using log rank tests. A p value ≤ 0.05 was considered significant for all analyses. Differences in incidences of leukemia or lymphoma among the different groups were determined using Fisher's exact test. Two-tailed unpaired Student's t tests were used to calculate the differences in the gene expression of patient data, WBC, and spleen weights of transplanted mice, as well as the differences in cell number or tumors in ENU and MMLV-treated mice. The Mann-Whitney U test was used to determine significance in counterselection assays. Two-way ANOVAs were used to calculate significance of Vivo-Morpholino dose-responsive curves. Differences in Annexin V staining of *Bcl2*-transgenic *Gfi1^{-/-}* mice and *Trp53p53^{-/-}Gfi1^{-/-}* were calculated using one-way ANOVAs. GSEA FDR Q values < 0.25 were used as a cutoff for enriched signatures.

ACCESSION NUMBERS

Array data are accessible under GEO accession number GSE32910.

SUPPLEMENTAL INFORMATION

Supplemental Information includes five figures, two tables, and Supplemental Experimental Procedures and can be found with this article online at <http://dx.doi.org/10.1016/j.ccr.2013.01.011>.

ACKNOWLEDGMENTS

We thank David Hildeman, Anil Jegga, Patrick Zweidler-McKay, Michelle Kelliher, Tom Look, and Paul Jolicouer for expertise and for kindly providing plasmids, cell lines, reagents, and mice. C.K. was supported by a fellowship of the Cole Foundation, the IFZ fellowship of the University Clinic of Essen, and a Max-Eder fellowship from the German Cancer fund. J.D.P. is a Pelotonia Fellow and was supported by the University of Cincinnati Cancer Therapeutics T32 training grant (T32-CA117846). J.S. was supported by a Gordon Piller PhD studentship from Leukaemia and Lymphoma Research UK, S.R.H. by a fellowship from CancerFree Kids, and J.Z. and W.E.P. by the Division of Intramural Research, National Institute of Allergy and Infectious Diseases. H.L.G. was supported by the Leukemia and Lymphoma Society of America, NIH CA105152, CA159845, Alex's Lemonade Stand, and thanks the Center of Excellence in Molecular Hematology P30 award (DK090971). T.M. was supported by a Canada Research Chair (Tier 1) and grants from the Canadian Institutes of Health Research (CIHR, MOP-84238, MOP-111011). C.K. and J.D.P. designed and performed experiments, analyzed data, and wrote the manuscript. M.-C.G., L.V., J.S., R.C., S.R.H., J.K., and B.G. performed experiments and assisted analyses. J.Z. and W.E.P. provided the *Gfi1^{fl/fl}* mouse strain. U.D. provided funding and oversaw research. H.L.G. and T.M. were responsible for concept and design of experiments, oversaw research, wrote the manuscript, and provided funding.

Received: December 22, 2011

Revised: September 11, 2012

Accepted: January 18, 2013

Published: February 11, 2013

REFERENCES

- Adams, J.M., Harris, A.W., Pinkert, C.A., Corcoran, L.M., Alexander, W.S., Cory, S., Palmiter, R.D., and Brinster, R.L. (1985). The c-myc oncogene driven by immunoglobulin enhancers induces lymphoid malignancy in transgenic mice. *Nature* 318, 533–538.
- Bartek, J., Bartkova, J., and Lukas, J. (2007). DNA damage signalling guards against activated oncogenes and tumour progression. *Oncogene* 26, 7773–7779.
- Bartkova, J., Horejsi, Z., Sehested, M., Nesland, J.M., Rajpert-De Meyts, E., Skakkebaek, N.E., Stucki, M., Jackson, S., Lukas, J., and Bartek, J. (2007). DNA damage response mediators MDC1 and 53BP1: constitutive activation and aberrant loss in breast and lung cancer, but not in testicular germ cell tumours. *Oncogene* 26, 7414–7422.
- Blyth, K., Terry, A., Mackay, N., Vaillant, F., Bell, M., Cameron, E.R., Neil, J.C., and Stewart, M. (2001). Runx2: a novel oncogenic effector revealed by in vivo complementation and retroviral tagging. *Oncogene* 20, 295–302.
- Chakraborty, J., Okonta, H., Bagalb, H., Lee, S.J., Fink, B., Changanamkandath, R., and Duggan, J. (2008). Retroviral gene insertion in breast milk mediated lymphomagenesis. *Virology* 377, 100–109.
- Coustan-Smith, E., Mullighan, C.G., Onciu, M., Behm, F.G., Raimondi, S.C., Pei, D., Cheng, C., Su, X., Rubnitz, J.E., Basso, G., et al. (2009). Early T-cell precursor leukaemia: a subtype of very high-risk acute lymphoblastic leukaemia. *Lancet Oncol.* 10, 147–156.

(G) Quantification of total human CD45⁺ cells in the blood and spleen from mice in (F).

(H) Cytospins of the BM from mice in (F). Scale bars, 50 μ m.

Mean and mean \pm SEM are shown unless stated otherwise. *p < 0.05, **p < 0.01, ***p < 0.001.

See also [Figure S5](#).



- Cullion, K., Draheim, K.M., Hermance, N., Tammam, J., Sharma, V.M., Ware, C., Nikov, G., Krishnamoorthy, V., Majumder, P.K., and Kelliher, M.A. (2009). Targeting the Notch1 and mTOR pathways in a mouse T-ALL model. *Blood* 113, 6172–6181.
- Dabrowska, M.J., Dybkaer, K., Johnsen, H.E., Wang, B., Wabl, M., and Pedersen, F.S. (2009). Loss of MicroRNA targets in the 3' untranslated region as a mechanism of retroviral insertional activation of growth factor independence 1. *J. Virol.* 83, 8051–8061.
- Di Micco, R., Fumagalli, M., Cicalese, A., Piccinin, S., Gasparini, P., Luise, C., Schurra, C., Garre', M., Nuciforo, P.G., Bensimon, A., et al. (2006). Oncogene-induced senescence is a DNA damage response triggered by DNA hyper-replication. *Nature* 444, 638–642.
- Ferrando, A.A., Neuberg, D.S., Staunton, J., Loh, M.L., Huard, C., Raimondi, S.C., Behm, F.G., Pui, C.H., Downing, J.R., Gilliland, D.G., et al. (2002). Gene expression signatures define novel oncogenic pathways in T cell acute lymphoblastic leukemia. *Cancer Cell* 1, 75–87.
- Fiolk, K., Hertzano, R., Vassen, L., Zeng, H., Hermesh, O., Avraham, K.B., Dührsen, U., and Möry, T. (2006). Gfi1 and Gfi1b act equivalently in haematopoiesis, but have distinct, non-overlapping functions in inner ear development. *EMBO Rep.* 7, 326–333.
- Gilks, C.B., Bear, S.E., Grimes, H.L., and Tschlis, P.N. (1993). Progression of interleukin-2 (IL-2)-dependent rat T cell lymphoma lines to IL-2-independent growth following activation of a gene (Gfi-1) encoding a novel zinc finger protein. *Mol. Cell. Biol.* 13, 1759–1768.
- Gökbüget, N., and Hoelzer, D. (2009). Treatment of adult acute lymphoblastic leukemia. *Semin. Hematol.* 46, 64–75.
- Halazonetis, T.D., Gorgoulis, V.G., and Bartek, J. (2008). An oncogene-induced DNA damage model for cancer development. *Science* 319, 1352–1355.
- Hameyer, D., Loonstra, A., Eshkind, L., Schmitt, S., Antunes, C., Groen, A., Bindels, E., Jonkers, J., Krimpenfort, P., Meuwissen, R., et al. (2007). Toxicity of ligand-dependent Cre recombinases and generation of a conditional Cre deleter mouse allowing mosaic recombination in peripheral tissues. *Physiol. Genomics* 31, 32–41.
- Horman, S.R., Velu, C.S., Chaubey, A., Bourdeau, T., Zhu, J., Paul, W.E., Gebelein, B., and Grimes, H.L. (2009). Gfi1 integrates progenitor versus granulocytic transcriptional programming. *Blood* 113, 5466–5475.
- Huang, J., Sengupta, R., Espejo, A.B., Lee, M.G., Dorsey, J.A., Richter, M., Opravil, S., Shiekhattar, R., Bedford, M.T., Jenuwein, T., and Berger, S.L. (2007). p53 is regulated by the lysine demethylase LSD1. *Nature* 449, 105–108.
- Khandanpour, C., Krongold, J., Schütte, J., Bouwman, F., Vassen, L., Gaudreau, M.C., Chen, R., Calero-Nieto, F.J., Diamanti, E., Hannah, R., et al. (2012). The human GFI136N variant induces epigenetic changes at the Hoxa9 locus and accelerates K-RAS driven myeloproliferative disorder in mice. *Blood* 120, 4006–4017.
- Kundu, M., Compton, S., Garrett-Beal, L., Stacy, T., Starost, M.F., Eckhaus, M., Speck, N.A., and Liu, P.P. (2005). Runx1 deficiency predisposes mice to T-lymphoblastic lymphoma. *Blood* 106, 3621–3624.
- Kurash, J.K., Lei, H., Shen, Q., Marston, W.L., Granda, B.W., Fan, H., Wall, D., Li, E., and Gaudet, F. (2008). Methylation of p53 by Set7/9 mediates p53 acetylation and activity in vivo. *Mol. Cell* 29, 392–400.
- Li, H., Ji, M., Klarmann, K.D., and Keller, J.R. (2010). Repression of Id2 expression by Gfi-1 is required for B-cell and myeloid development. *Blood* 116, 1060–1069.
- Margolin, A.A., Palomero, T., Sumazin, P., Califano, A., Ferrando, A.A., and Stolovitzky, G. (2009). ChIP-on-chip significance analysis reveals large-scale binding and regulation by human transcription factor oncogenes. *Proc. Natl. Acad. Sci. USA* 106, 244–249.
- Medyouf, H., Gusscott, S., Wang, H., Tseng, J.C., Wai, C., Nemirovsky, O., Trumpp, A., Pflumio, F., Carboni, J., Gottardis, M., et al. (2011). High-level IGF1R expression is required for leukemia-initiating cell activity in T-ALL and is supported by Notch signaling. *J. Exp. Med.* 208, 1809–1822.
- Morcos, P.A., Li, Y., and Jiang, S. (2008). Vivo-Morpholinos: a non-peptide transporter delivers Morpholinos into a wide array of mouse tissues. *Biotechniques* 45, 613–614, 616, 618 passim.
- Murtaugh, L.C., Stanger, B.Z., Kwan, K.M., and Melton, D.A. (2003). Notch signaling controls multiple steps of pancreatic differentiation. *Proc. Natl. Acad. Sci. USA* 100, 14920–14925.
- O'Neil, J., Grim, J., Strack, P., Rao, S., Tibbitts, D., Winter, C., Hardwick, J., Welcker, M., Meijerink, J.P., Pieters, R., et al. (2007). FBW7 mutations in leukemic cells mediate NOTCH pathway activation and resistance to gamma-secretase inhibitors. *J. Exp. Med.* 204, 1813–1824.
- Palomero, T., Lim, W.K., Odom, D.T., Sulis, M.L., Real, P.J., Margolin, A., Barnes, K.C., O'Neil, J., Neuberg, D., Weng, A.P., et al. (2006). NOTCH1 directly regulates c-MYC and activates a feed-forward-loop transcriptional network promoting leukemic cell growth. *Proc. Natl. Acad. Sci. USA* 103, 18261–18266.
- Pargmann, D., Yücel, R., Kusan, C., Saba, I., Klein-Hitpass, L., Schimmer, S., Heyd, F., Dittmer, U., and Möry, T. (2007). Differential impact of the transcriptional repressor Gfi1 on mature CD4+ and CD8+ T lymphocyte function. *Eur. J. Immunol.* 37, 3551–3563.
- Person, R.E., Li, F.Q., Duan, Z., Benson, K.F., Wechsler, J., Papadaki, H.A., Eliopoulos, G., Kaufman, C., Bertolone, S.J., Nakamoto, B., et al. (2003). Mutations in proto-oncogene GFI1 cause human neutropenia and target ELA2. *Nat. Genet.* 34, 308–312.
- Priceputu, E., Bouallaga, I., Zhang, Y., Li, X., Chrobak, P., Hanna, Z.S., Poudrier, J., Kay, D.G., and Jolicoeur, P. (2006). Structurally distinct ligand-binding or ligand-independent Notch1 mutants are leukemogenic but affect thymocyte development, apoptosis, and metastasis differently. *J. Immunol.* 177, 2153–2166.
- Saleque, S., Kim, J., Rooke, H.M., and Orkin, S.H. (2007). Epigenetic regulation of hematopoietic differentiation by Gfi-1 and Gfi-1b is mediated by the cofactors CoREST and LSD1. *Mol. Cell* 27, 562–572.
- Scheijen, B., Jonkers, J., Acton, D., and Berns, A. (1997). Characterization of pal-1, a common proviral insertion site in murine leukemia virus-induced lymphomas of c-myc and Pim-1 transgenic mice. *J. Virol.* 71, 9–16.
- Schmidt, T., Zörnig, M., Beneke, R., and Möry, T. (1996). MoMuLV proviral integrations identified by Sup-F selection in tumors from infected myc/pim bitransgenic mice correlate with activation of the gfi-1 gene. *Nucleic Acids Res.* 24, 2528–2534.
- Schmidt, T., Karsunky, H., Gau, E., Zevnik, B., Elsässer, H.P., and Möry, T. (1998). Zinc finger protein GFI-1 has low oncogenic potential but cooperates strongly with pim and myc genes in T-cell lymphomagenesis. *Oncogene* 17, 2661–2667.
- Sharma, V.M., Calvo, J.A., Draheim, K.M., Cunningham, L.A., Hermance, N., Beverly, L., Krishnamoorthy, V., Bhasin, M., Capobianco, A.J., and Kelliher, M.A. (2006). Notch1 contributes to mouse T-cell leukemia by directly inducing the expression of c-myc. *Mol. Cell. Biol.* 26, 8022–8031.
- Spooner, C.J., Cheng, J.X., Pujadas, E., Laslo, P., and Singh, H. (2009). A recurrent network involving the transcription factors PU.1 and Gfi1 orchestrates innate and adaptive immune cell fates. *Immunity* 31, 576–586.
- Subramanian, A., Tamayo, P., Mootha, V.K., Mukherjee, S., Ebert, B.L., Gillette, M.A., Paulovich, A., Pomeroy, S.L., Golub, T.R., Lander, E.S., and Mesirov, J.P. (2005). Gene set enrichment analysis: a knowledge-based approach for interpreting genome-wide expression profiles. *Proc. Natl. Acad. Sci. USA* 102, 15545–15550.
- Thompson, B.J., Buonamici, S., Sulis, M.L., Palomero, T., Vilimas, T., Basso, G., Ferrando, A., and Aifantis, I. (2007). The SCFFBW7 ubiquitin ligase complex as a tumor suppressor in T cell leukemia. *J. Exp. Med.* 204, 1825–1835.
- Uren, A.G., Kool, J., Matentzoglou, K., de Ridder, J., Mattison, J., van Uiter, M., Lagcher, W., Sie, D., Tanger, E., Cox, T., et al. (2008). Large-scale mutagenesis in p19(ARF)- and p53-deficient mice identifies cancer genes and their collaborative networks. *Cell* 133, 727–741.
- Van Vlierberghe, P., van Grotel, M., Tchinda, J., Lee, C., Beverloo, H.B., van der Spek, P.J., Stubbs, A., Cools, J., Nagata, K., Fornerod, M., et al. (2008).



- The recurrent SET-NUP214 fusion as a new HOXA activation mechanism in pediatric T-cell acute lymphoblastic leukemia. *Blood* 111, 4668–4680.
- Velu, C.S., Baktula, A.M., and Grimes, H.L. (2009). Gfi1 regulates miR-21 and miR-196b to control myelopoiesis. *Blood* 113, 4720–4728.
- Weng, A.P., Ferrando, A.A., Lee, W., Morris, J.P., 4th, Silverman, L.B., Sanchez-Irizarry, C., Blacklow, S.C., Look, A.T., and Aster, J.C. (2004). Activating mutations of NOTCH1 in human T cell acute lymphoblastic leukemia. *Science* 306, 269–271.
- Weng, A.P., Millholland, J.M., Yashiro-Ohtani, Y., Arcangeli, M.L., Lau, A., Wai, C., Del Bianco, C., Rodriguez, C.G., Sai, H., Tobias, J., et al. (2006). c-Myc is an important direct target of Notch1 in T-cell acute lymphoblastic leukemia/lymphoma. *Genes Dev.* 20, 2096–2109.
- West, L.E., and Gozani, O. (2011). Regulation of p53 function by lysine methylation. *Epigenomics* 3, 361–369.
- Yuan, Y., Zhou, L., Miyamoto, T., Iwasaki, H., Harakawa, N., Hetherington, C.J., Burel, S.A., Lagasse, E., Weissman, I.L., Akashi, K., and Zhang, D.E. (2001). AML1-ETO expression is directly involved in the development of acute myeloid leukemia in the presence of additional mutations. *Proc. Natl. Acad. Sci. USA* 98, 10398–10403.
- Yücel, R., Karsunky, H., Klein-Hitpass, L., and Mörröy, T. (2003). The transcriptional repressor Gfi1 affects development of early, uncommitted c-Kit⁺ T cell progenitors and CD4/CD8 lineage decision in the thymus. *J. Exp. Med.* 197, 831–844.
- Zarebski, A., Velu, C.S., Baktula, A.M., Bourdeau, T., Horman, S.R., Basu, S., Bertolone, S.J., Horwitz, M., Hildeman, D.A., Trent, J.O., and Grimes, H.L. (2008). Mutations in growth factor independent-1 associated with human neutropenia block murine granulopoiesis through colony stimulating factor-1. *Immunity* 28, 370–380.
- Zhu, J., Jankovic, D., Grinberg, A., Guo, L., and Paul, W.E. (2006). Gfi-1 plays an important role in IL-2-mediated Th2 cell expansion. *Proc. Natl. Acad. Sci. USA* 103, 18214–18219.
- Zörnig, M., Schmidt, T., Karsunky, H., Grzeschiczek, A., and Mörröy, T. (1996). Zinc finger protein GFI-1 cooperates with myc and pim-1 in T-cell lymphomagenesis by reducing the requirements for IL-2. *Oncogene* 12, 1789–1801.

Of note, the two studies identify different Eph receptors as key in CSC maintenance, although some level of crosstalk likely exists between the Eph receptors as well as other RTKs central to maintenance of the hierarchy. It would seem this difference could not be due to differential representation within the recently identified GBM subclasses as both have highest expression in the mesenchymal and classical groups (Verhaak et al., 2010). However, Eph receptors may be informative within these subgroups, although that hypothesis would require further exploration. Importantly, both groups validate the efficacy of targeting Eph receptors in preclinical models.

In conclusion, these two reports are not simply additions of new CSC markers but

rather help reinforce expanding opportunities for integrating features of normal tissue hierarchies and instructive micro-environmental cues in tumor development and maintenance that can inform advances in diagnosis and therapy.

REFERENCES

Binda, E., Visioli, A., Giani, F., Lamorte, G., Copetti, M., Pitter, K.L., Huse, J.T., Cajola, L., Zanetti, N., DiMeco, F., et al. (2012). *Cancer Cell* 22, 765–780.

Calabrese, C., Poppleton, H., Kocak, M., Hogg, T.L., Fuller, C., Hamner, B., Oh, E.Y., Gaber, M.W., Finklestein, D., Allen, M., et al. (2007). *Cancer Cell* 11, 69–82.

Chen, J., Li, Y., Yu, T.S., McKay, R.M., Burns, D.K., Kernie, S.G., and Parada, L.F. (2012). *Nature* 488, 522–526.

Day, B.W., Stringer, B.W., Al-Ejeh, F., Ting, M.J., Wilson, J., Ensbeys, K.S., Jamieson, P.R., Bruce,

Z.C., Lim, Y.C., Offenhäuser, C., et al. (2013). *Cancer Cell* 23, this issue, 238–248.

Genander, M., and Frisén, J. (2010). *Curr. Opin. Cell Biol.* 22, 611–616.

Miao, H., Li, D.Q., Mukherjee, A., Guo, H., Petty, A., Cutter, J., Basilion, J.P., Sedor, J., Wu, J., Daniel-pour, D., et al. (2009). *Cancer Cell* 16, 9–20.

Piccirillo, S.G., Reynolds, B.A., Zanetti, N., Lamorte, G., Binda, E., Broggi, G., Brem, H., Olivi, A., Dimeco, F., and Vescovi, A.L. (2006). *Nature* 444, 761–765.

Singh, S.K., Hawkins, C., Clarke, I.D., Squire, J.A., Bayani, J., Hide, T., Henkelman, R.M., Cusimano, M.D., and Dirks, P.B. (2004). *Nature* 432, 396–401.

Verhaak, R.G., Hoadley, K.A., Purdom, E., Wang, V., Qi, Y., Wilkerson, M.D., Miller, C.R., Ding, L., Golub, T., Mesirov, J.P., et al.; Cancer Genome Atlas Research Network. (2010). *Cancer Cell* 17, 98–110.

Wykosky, J., Palma, E., Gibo, D.M., Ringler, S., Turner, C.P., and Debinski, W. (2008). *Oncogene* 27, 7260–7273.

Breaking News on Fragile Sites in Cancer

Thomas W. Glover^{1,2,*} and Thomas E. Wilson^{1,2}

¹Department of Human Genetics

²Department of Pathology

University of Michigan, Ann Arbor, MI 48109, USA

*Correspondence: glover@umich.edu

<http://dx.doi.org/10.1016/j.ccr.2013.01.017>

Chromosome rearrangements in B lymphocytes can be initiated by AID-associated double strand breaks (DSBs), with others arising by unclear mechanisms. A recent study by Barlow and colleagues in *Cell* reports on genomic regions, termed early replicating fragile sites, that may explain many AID-independent DSBs and creates a compelling link between replication stress, transcription, and chromosome rearrangements.

Recurrent chromosomal translocations are common features of many cancers, especially lymphomas and leukemias. Most appear to be formed by the joining of two double strand breaks (DSBs). In developing B cells, DSBs are introduced into immunoglobulin loci during V(D)J recombination and class-switch recombination (CSR). Both CSR and immunoglobulin somatic hypermutation are initiated by AID, a single-strand-specific DNA cytidine deaminase targeted to DNA by transcription (Nussenzweig and Nussenzweig, 2010). AID-associated DSBs often generate one of the two breakpoints in the translocations observed in lymphoid tumors. This programmed DNA damage also puts the lymphocyte genome at risk

for rearrangements with bystander loci, such as the *C-MYC* locus. Nonetheless, while many translocations are driven by off-target AID-induced DSBs, others result from poorly defined factors that might include replication errors, oxidative stress, genotoxic agents, and involvement of chromosome fragile sites.

Common fragile sites (CFSs) have been recognized for decades as hotspots for breaks occurring on metaphase chromosomes following replication stress (Durkin and Glover, 2007). Following low doses of the DNA polymerase inhibitor aphidicolin (APH), chromosome breaks can be seen at discrete genomic regions that span hundreds of kilobases, often in large genes. CFS instability is dependent on

ATR signaling and associated with other DNA damage response factors (Durkin and Glover, 2007). Le Beau et al. (1998) and studies that followed showed that CFSs replicate late in S-phase and sometimes escape to metaphase with incomplete replication. For decades, two nonexclusive models have existed for CFS instability. One is that CFSs contain difficult-to-replicate sequences, leading to stalled replication forks. The second is that CFSs contain a paucity of replication origins, leading to late or incomplete replication. Support for the former came from the fact that CFSs are AT-rich and contain a high number of “flexibility peaks” (Zlotorynski et al., 2003) capable of forming secondary structures, especially when

replication is perturbed, that can act as barriers to replication. Recent experiments (Letessier et al., 2011) further provided evidence for a paucity of active origins at some CFSs, reflecting a failure to activate dormant origins in these regions following replication fork arrest. Importantly, replication and fragility patterns both differed among cell types.

Since their discovery, attempts have been made to link CFSs to translocations and other rearrangements in cancers. Whereas positive correlations were found at the chromosomal level, most did not stand up to higher resolution inspection. Nonetheless, CFS instability has been associated with gene amplifications and a small number of translocations in cancers (Arlt et al., 2006). Recently, replication stress induced by APH or hydroxyurea (HU) has been shown to be a potent inducer of submicroscopic deletions and duplications, i.e., copy number variants (CNVs), with some CNV hotspots at CFSs (Arlt et al., 2011). These CNVs can span hundreds of kilobases and model many CNVs that arise frequently in cancer cells and in the human germline.

Recently in *Cell*, Barlow et al. (2013) opened a new chapter in the fragile site and cancer saga that has important implications for cancer risk. The authors identified genome-wide early-firing replication origins, sites of RPA binding indicative of ssDNA accumulation and sites of active transcription in mouse splenic B cells after release from G1/S arrest induced with high doses of HU. Comparison of the data sets revealed a highly significant overlap. Thus, HU-induced RPA recruitment in early S phase preferentially occurred at early origins of actively transcribed genes. The sites were marked by γ H2AX binding and were associated with BRCA1 and SMC5, indicative of replication fork collapse and DNA damage response activation. The authors termed these sites “early replicating fragile sites” (ERFSs) because their analysis focused on the beginning of S phase, in contrast to the late replication associated with CFSs. Consistent with this difference, ERFSs arose at different genomic loci than previously mapped CFSs.

To investigate if ERFSs are prone to chromosome breaks like CFSs, they

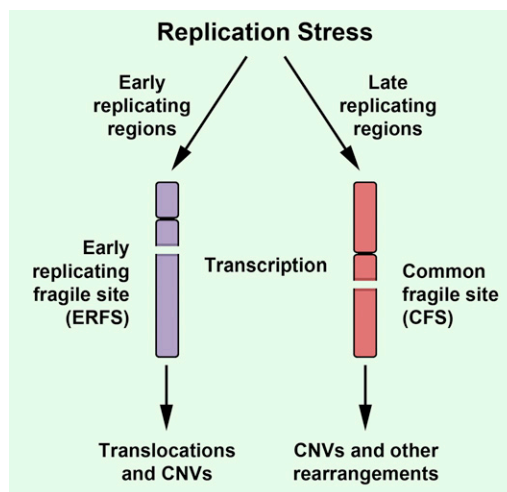


Figure 1. Comparison of Replication Stress-Induced Chromosome Breaks at ERFSs and CFSs

The difference in replication timing and the association with specific transcribed genomic regions are illustrated. ERFSs were found at regions that replicate early in S phase and are associated with early firing replication origins, whereas CFS regions replicate late and can be associated with intragenic, inactive origins and/or poor firing of dormant origins.

treated cells with high-dose HU and examined metaphases with FISH probes to ERFS hotspots. All six ERFS hotspots displayed CFS-like chromosomal breaks with 8%–15% of total damage at these six loci. Like CFSs, ATR inhibition and oncogene stress promoted ERFS breakage, consistent with the arrested replication and ssDNA observed at these sites. By studying breakage at an ERFS near *SWAP70* in cell types with different levels of transcription, the authors found a positive correlation between fragility and transcriptional activity despite similar replication timing, supporting a mechanistic link. Comparison of wild-type and AID knockout B cells demonstrated that ERFS fragility is AID independent.

How do ERFSs relate to chromosome rearrangements in cancer? To address this, the authors examined three ERFSs, including one in the lymphoma-associated *BACH2* locus, in metaphases from AID-overexpressing, 53BP1-deficient B cells, which have G1 *IgH* breaks that persist into S phase where they might be joined to ERFSs. They found chromosome breaks at both the *IgH* and *BACH2* loci. Furthermore, *BACH2* translocations to unidentified chromosomes were found in 1.2% of metaphases and to *IgH* in one cell. They then compared ERFSs with

copy number alterations (i.e., CNVs) detected in biopsies of diffuse large B cell lymphoma, the most common non-Hodgkin's lymphoma. Strikingly, 51.6% of the 190 common amplifications and deletions in the patient samples overlapped with ERFS regions.

These studies have a number of implications. First, they identify a new class of fragile sites that are similar to CFSs in terms of chromosome breaks, sensitivity to replication stress, and dependence on ATR signaling. A notable difference is that ERFSs are associated with early replication origins, often in promoters, whereas CFSs replicate late, and at least some are associated with poor firing of late and dormant origins within large genes. A model thus emerges in which impaired replication is a universal contributor to breakage and associated rearrangements with the timing of replication stress leading to different, cell type-specific outcomes (Figure 1).

Second, the association of ERFSs with gene transcription is of great interest. A similar association has been made for some CFSs and transcription of large genes (Helmrich et al., 2011). These correlations are consistent with recent findings (Dellino et al., 2013) that suggest two classes of replication origins: those associated with moderate to high transcription levels and firing in early S and those associated with low transcription levels and firing throughout S. These and other studies raise important questions about the mechanistic connections between replication, origin firing, and transcription and the need to identify the genetic factors and epigenetic modifications involved. They also highlight the need for a thorough evaluation of genomic lesions in different cancer types based on differential transcription of the regions involved.

Finally, the association among ERFSs, translocations, and CNVs in B cell cancers is compelling. The data suggest that ERFSs can provide AID-independent DSBs that can partner with AID-induced or other DSBs to promote translocations, highlighting the importance of understanding the synergy between multiple simultaneous intrinsic and exogenous

genotoxic factors. In addition, the strong correlation of ERFs with CNVs in B cell lymphomas strengthens the argument that common mechanisms likely underlie what might initially appear as distinct phenomena and suggest that replication arrest at ERFs can trigger CNV formation. This is indeed likely, because similar CNVs that mimic constitutional and cancer-related CNVs are induced in human and mouse cells following replication stress, including at some CFSs (Arlt et al., 2011). It would be interesting to similarly examine de novo CNVs in B-lymphocytes treated to express ERFs. The identity of the replication and repair factors that create the rearrangements and the endogenous conditions or environmental agents that lead to replication stress are unclear. These are important questions that are being ad-

ressed with regard to human germline CNVs and translocations, and they are equally important to understanding rearrangements in the cancer genome and the risk factors involved.

ACKNOWLEDGMENTS

We thank Martin Arlt for contributing to this article.

REFERENCES

- Arlt, M.F., Durkin, S.G., Ragland, R.L., and Glover, T.W. (2006). DNA Repair (Amst.) 5, 1126–1135.
- Arlt, M.F., Ozdemir, A.C., Birkeland, S.R., Wilson, T.E., and Glover, T.W. (2011). Proc. Natl. Acad. Sci. USA 108, 17360–17365.
- Barlow, J.H., Faryabi, R.B., Callén, E., Wong, N., Malhowski, A., Chen, H.T., Gitierez-Cruz, G., Sun, H.-W., McKinnon, P., Wright, G., et al. (2013). Cell 152, 620–632.

Dellino, G.I., Cittaro, D., Piccioni, R., Luzi, L., Banfi, S., Segalla, S., Cesaroni, M., Mendoza-Maldonado, R., Giacca, M., and Pelicci, P.G. (2013). Genome Res. 23, 1–11.

Durkin, S.G., and Glover, T.W. (2007). Annu. Rev. Genet. 41, 169–192.

Helmrich, A., Ballarino, M., and Tora, L. (2011). Mol. Cell 44, 966–977.

Le Beau, M.M., Rassool, F.V., Neilly, M.E., Espinosa, R., 3rd, Glover, T.W., Smith, D.I., and McKeithan, T.W. (1998). Hum. Mol. Genet. 7, 755–761.

Letessier, A., Millot, G.A., Koundrioukoff, S., Lachagès, A.M., Vogt, N., Hansen, R.S., Malfoy, B., Brison, O., and Debatisse, M. (2011). Nature 470, 120–123.

Nussenzweig, A., and Nussenzweig, M.C. (2010). Cell 141, 27–38.

Zlotorynski, E., Rahat, A., Skaug, J., Ben-Porat, N., Ozeri, E., Hershberg, R., Levi, A., Scherer, S.W., Margalit, H., and Kerem, B. (2003). Mol. Cell. Biol. 23, 7143–7151.

ABT-199: Taking Dead Aim at BCL-2

Matthew S. Davids¹ and Anthony Letai^{1,*}

¹Department of Medical Oncology, Dana-Farber Cancer Institute, 450 Brookline Avenue, Boston, MA 02215, USA

*Correspondence: anthony_letai@dfci.harvard.edu
<http://dx.doi.org/10.1016/j.ccr.2013.01.018>

ABT-199 is a new selective small molecule inhibitor of BCL-2 that appears to spare platelets while achieving potent antitumor activity. Assays that can predict the efficacy of ABT-199 in individual tumors will be critical in determining how best to incorporate this promising agent into the armamentarium of cancer therapies.

The B cell lymphoma/leukemia 2 (BCL-2) family regulates critical life or death decisions of cells via the mitochondrial pathway of apoptosis (Davids and Letai, 2012). BCL-2 inhibits death by binding the BH3 domains of pro-death BCL-2 family proteins, thus preventing mitochondrial outer membrane permeabilization, which can be considered the point of commitment to apoptosis. BCL-2 has several anti-apoptotic cousins, including BCL-XL, BCL-w, and MCL-1, each of which possesses a distinct, hydrophobic BH3-binding pocket. Lymphoid malignancies are frequently addicted to BCL-2 for their survival. Because most of these cancers, including chronic lymphocytic leukemia (CLL), remain incurable with

conventional therapies, agents that specifically target BCL-2 are under urgent investigation.

Early efforts to target the BCL-2 family were met with disappointment in the clinic. Agents such as the antisense oligonucleotide oblimersen sodium and the small molecule obatoclax showed promise as BCL-2 antagonists in pre-clinical testing but had little clinical activity. A potential mechanistic shortcoming of these agents is that they were never conclusively shown to specifically engage their purported BCL-2 family targets in patients.

Abbott Laboratories (now AbbVie) has developed a series of BH3-mimetic small molecules that bind to the BH3 bind-

ing sites of anti-apoptotic proteins like BCL-2. ABT-737, which binds BCL-2, BCL-XL, and BCL-w, was the first molecule studied extensively preclinically (Oltersdorf et al., 2005). Many subsequent experiments support its killing in an on-target fashion in cell lines, primary human cancer cells, and animal models. ABT-263 (navitoclax) was the first of this series to enter the clinic. Like ABT-737, it binds BCL-2, BCL-XL, and BCL-w, but it has the perceived advantage of being orally bioavailable. Clinical activity was observed, particularly in lymphoid cancers (Roberts et al., 2012); however, because navitoclax binds not only to BCL-2 but also to BCL-XL, the drug causes predictable,

genotoxic factors. In addition, the strong correlation of ERFs with CNVs in B cell lymphomas strengthens the argument that common mechanisms likely underlie what might initially appear as distinct phenomena and suggest that replication arrest at ERFs can trigger CNV formation. This is indeed likely, because similar CNVs that mimic constitutional and cancer-related CNVs are induced in human and mouse cells following replication stress, including at some CFSs (Arlt et al., 2011). It would be interesting to similarly examine de novo CNVs in B-lymphocytes treated to express ERFs. The identity of the replication and repair factors that create the rearrangements and the endogenous conditions or environmental agents that lead to replication stress are unclear. These are important questions that are being ad-

dressed with regard to human germline CNVs and translocations, and they are equally important to understanding rearrangements in the cancer genome and the risk factors involved.

ACKNOWLEDGMENTS

We thank Martin Arlt for contributing to this article.

REFERENCES

- Arlt, M.F., Durkin, S.G., Ragland, R.L., and Glover, T.W. (2006). DNA Repair (Amst.) 5, 1126–1135.
- Arlt, M.F., Ozdemir, A.C., Birkeland, S.R., Wilson, T.E., and Glover, T.W. (2011). Proc. Natl. Acad. Sci. USA 108, 17360–17365.
- Barlow, J.H., Faryabi, R.B., Callén, E., Wong, N., Malhowski, A., Chen, H.T., Gitierez-Cruz, G., Sun, H.-W., McKinnon, P., Wright, G., et al. (2013). Cell 152, 620–632.

Dellino, G.I., Cittaro, D., Piccioni, R., Luzi, L., Banfi, S., Segalla, S., Cesaroni, M., Mendoza-Maldonado, R., Giacca, M., and Pelicci, P.G. (2013). Genome Res. 23, 1–11.

Durkin, S.G., and Glover, T.W. (2007). Annu. Rev. Genet. 41, 169–192.

Helmrich, A., Ballarino, M., and Tora, L. (2011). Mol. Cell 44, 966–977.

Le Beau, M.M., Rassool, F.V., Neilly, M.E., Espinosa, R., 3rd, Glover, T.W., Smith, D.I., and McKeithan, T.W. (1998). Hum. Mol. Genet. 7, 755–761.

Letessier, A., Millot, G.A., Koundrioukoff, S., Lachagès, A.M., Vogt, N., Hansen, R.S., Malfroy, B., Brison, O., and Debatisse, M. (2011). Nature 470, 120–123.

Nussenzweig, A., and Nussenzweig, M.C. (2010). Cell 141, 27–38.

Zlotorynski, E., Rahat, A., Skaug, J., Ben-Porat, N., Ozeri, E., Hershberg, R., Levi, A., Scherer, S.W., Margalit, H., and Kerem, B. (2003). Mol. Cell. Biol. 23, 7143–7151.

ABT-199: Taking Dead Aim at BCL-2

Matthew S. Davids¹ and Anthony Letai^{1,*}

¹Department of Medical Oncology, Dana-Farber Cancer Institute, 450 Brookline Avenue, Boston, MA 02215, USA

*Correspondence: anthony_letai@dfci.harvard.edu
<http://dx.doi.org/10.1016/j.ccr.2013.01.018>

ABT-199 is a new selective small molecule inhibitor of BCL-2 that appears to spare platelets while achieving potent antitumor activity. Assays that can predict the efficacy of ABT-199 in individual tumors will be critical in determining how best to incorporate this promising agent into the armamentarium of cancer therapies.

The B cell lymphoma/leukemia 2 (BCL-2) family regulates critical life or death decisions of cells via the mitochondrial pathway of apoptosis (Davids and Letai, 2012). BCL-2 inhibits death by binding the BH3 domains of pro-death BCL-2 family proteins, thus preventing mitochondrial outer membrane permeabilization, which can be considered the point of commitment to apoptosis. BCL-2 has several anti-apoptotic cousins, including BCL-XL, BCL-w, and MCL-1, each of which possesses a distinct, hydrophobic BH3-binding pocket. Lymphoid malignancies are frequently addicted to BCL-2 for their survival. Because most of these cancers, including chronic lymphocytic leukemia (CLL), remain incurable with

conventional therapies, agents that specifically target BCL-2 are under urgent investigation.

Early efforts to target the BCL-2 family were met with disappointment in the clinic. Agents such as the antisense oligonucleotide oblimersen sodium and the small molecule obatoclax showed promise as BCL-2 antagonists in pre-clinical testing but had little clinical activity. A potential mechanistic shortcoming of these agents is that they were never conclusively shown to specifically engage their purported BCL-2 family targets in patients.

Abbott Laboratories (now AbbVie) has developed a series of BH3-mimetic small molecules that bind to the BH3 bind-

ing sites of anti-apoptotic proteins like BCL-2. ABT-737, which binds BCL-2, BCL-XL, and BCL-w, was the first molecule studied extensively preclinically (Oltersdorf et al., 2005). Many subsequent experiments support its killing in an on-target fashion in cell lines, primary human cancer cells, and animal models. ABT-263 (navitoclax) was the first of this series to enter the clinic. Like ABT-737, it binds BCL-2, BCL-XL, and BCL-w, but it has the perceived advantage of being orally bioavailable. Clinical activity was observed, particularly in lymphoid cancers (Roberts et al., 2012); however, because navitoclax binds not only to BCL-2 but also to BCL-XL, the drug causes predictable,

dose-dependent thrombocytopenia (Figure 1A). This is an on-target effect due to the reliance of platelets on BCL-XL for survival, and it provides pharmacodynamic evidence of the mechanism of action of the drug. Indeed, drugs claiming to inhibit BCL-XL that do not cause significant thrombocytopenia in vivo should be viewed with caution. The modest clinical activity of navitoclax is likely related to the inability to optimize its dose due to this dose-limiting thrombocytopenia.

Souers et al. (2013) recently reported the re-engineering of navitoclax to create ABT-199, a highly potent and selective inhibitor of BCL-2. Through an elegant structure-based reverse engineering process, ABT-199 maintains a sub-nanomolar affinity for BCL-2

but binds over three orders of magnitude less avidly to BCL-XL, suggesting the drug may not cause clinically significant thrombocytopenia (Figure 1B). In an in vitro cell culture model, the authors provide convincing evidence that ABT-199 selectively kills BCL-2 dependent, but not BCL-XL dependent, cells and kills through the mitochondrial pathway of apoptosis. ABT-199 also potently kills a diverse array of non-Hodgkin's lymphoma (NHL) and acute myelogenous leukemia cell lines, suggesting that the drug has the potential to be efficacious in a wide variety of hematologic malignancies. In vivo, ABT-199 suppresses tumor growth in several human hematologic tumor xenograft models and shows at least additive efficacy in combination with chemotherapy. Importantly, the authors also show compelling data from both in vitro and in vivo experiments that, as predicted, ABT-199 causes markedly less thrombocytopenia than navitoclax.

The true measure of a drug's efficacy must come from clinical trials, and the authors provide some very preliminary but promising data in three CLL patients. The rapid reduction of absolute lymphocyte count in just 8 hr along with a concomitant reduction in palpable lymphadenopathy in all three patients sug-

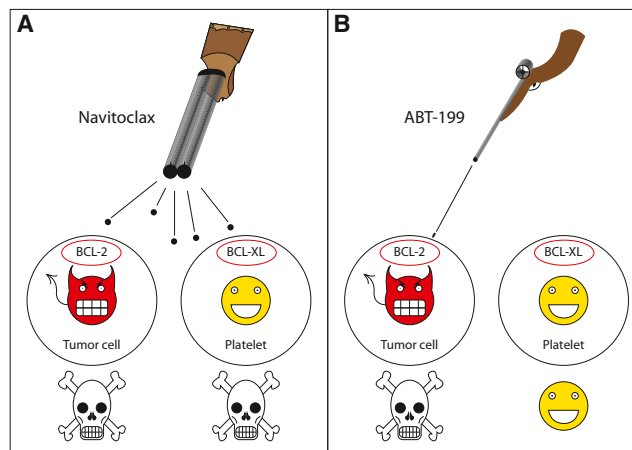


Figure 1. ABT-199 Selectively Kills BCL-2-Dependent Tumor Cells While Sparing Platelets

(A) Navitoclax (ABT-263) binds with high affinity to both BCL-2 and BCL-XL. Because many tumors, particularly lymphoid malignancies, are addicted to BCL-2 for survival, this potentially induces tumor cell apoptosis. Platelets depend primarily on BCL-XL for survival and, therefore, are also destroyed by navitoclax.

(B) ABT-199 is specific for BCL-2 and induces selective death of BCL-2 dependent tumor cells while sparing platelets. Figure created by Richard Oakley.

gests that the drug is more potent in CLL patients than navitoclax. The lack of thrombocytopenia in this limited data set is also a promising sign that the preclinical studies predicting less thrombocytopenia will be validated in the clinic. A similar lack of thrombocytopenia accompanied by significant anti-tumor activity was reported in an early interim analysis of a phase I study of ABT-199 in NHL patients at the 2012 American Society of Hematology Annual Meeting. Also notable in the Souers et al. (2013) article is that markedly elevated LDH and phosphate levels were seen during the same early time frame when the anti-tumor response was observed, reflecting significant tumor lysis, a clinical syndrome with potentially serious consequences if not managed aggressively. Whether modifications to the study design for future patients are adequate to reduce the risk of tumor lysis will be critical to the clinical development of ABT-199.

The use of rational biomarkers has become essential to optimizing the development of targeted cancer therapies, and ABT-199 is no exception. A challenge in developing a predictive biomarker for ABT-199 is understanding the molecular biology underlying BCL-2 addiction. The levels of over a dozen BCL-2 family pro-

teins, both pro- and anti-death, fluctuate rapidly, and protein-protein interactions or posttranslational modifications can have a major influence on the behavior of the system. Functional biomarkers are one way to probe the physiology of this dynamic system in real time. One such assay is BH3 profiling (Certo et al., 2006), which measures the mitochondrial response to different BH3-only peptides, each with its own selectivity of interaction with anti-apoptotic members. Results can be used to determine the relative dependence of a cell on a particular anti-apoptotic protein such as BCL-2, BCL-XL, or MCL-1. In many examples of primary cancer cells and cancer cell lines, BH3 profiling has cor-

rectly predicted sensitivity to ABT-737 (Del Gaizo Moore et al., 2007; Deng et al., 2007; Vo et al., 2012).

Central to the fate of a cancer cell exposed to chemotherapy is its proximity to the threshold of apoptosis, a cellular state also detected through BH3 profiling that is known as "mitochondrial priming". Mitochondrial priming helps explain why CLL cells are generally quite sensitive to chemotherapy despite having high levels of BCL-2 protein. Most BCL-2 in primed cells is bound by pro-death BCL-2 family members such as BIM, thereby perching these cells precariously near the precipice of apoptosis. Mitochondrial priming also provides insight into the reason why chemotherapy may be effective against primed malignant cells while sparing relatively less primed hematopoietic stem cells. Moreover, pretreatment priming levels in patient samples correlate with clinical response to cytotoxic chemotherapy (Davids et al., 2012; Ni Chonghaile et al., 2011; Vo et al., 2012). Agents like ABT-199 afford the exciting possibility of selectively increasing the mitochondrial priming of certain cancer cells, identified by the proper predictive biomarker, which might then be more effectively treated with conventional chemotherapy.

Clinical response to navitoclax was strongly associated with high BIM-MCL-1 or BIM-BCL-2 ratios, providing evidence of the selectivity of the drug for targeting the BCL-2 family in patients (Roberts et al., 2012). Additional correlative studies built into the ongoing clinical trials of ABT-199 include analysis of *BCL2* gains, *BCL2* amplification, as well as BH3 profiling. These assays have the potential to help predict the toxicities and efficacy of ABT-199, perhaps even one day to guide personalized therapy of cancer patients. Whether ABT-199 will be most effective as a single agent or in combination with other agents will be important to determine. Moreover, the biological insights gained through correlative studies will help inform the rational design of combination trials to determine

the optimal role for ABT-199 in the treatment of cancer.

ACKNOWLEDGMENTS

A.L. is a Leukemia and Lymphoma Society Scholar. M.S.D. is a Leukemia and Lymphoma Society Special Fellow in Clinical Research.

REFERENCES

- Certo, M., Del Gaizo Moore, V., Nishino, M., Wei, G., Korsmeyer, S., Armstrong, S.A., and Letai, A. (2006). *Cancer Cell* 9, 351–365.
- Davids, M.S., and Letai, A. (2012). *J. Clin. Oncol.* 30, 3127–3135.
- Davids, M.S., Deng, J., Wiestner, A., Lannutti, B.J., Wang, L., Wu, C.J., Wilson, W.H., Brown, J.R., and Letai, A. (2012). *Blood* 120, 3501–3509.
- Del Gaizo Moore, V., Brown, J.R., Certo, M., Love, T.M., Novina, C.D., and Letai, A. (2007). *J. Clin. Invest.* 117, 112–121.

Deng, J., Carlson, N., Takeyama, K., Dal Cin, P., Shipp, M., and Letai, A. (2007). *Cancer Cell* 12, 171–185.

Ni Chonghaile, T., Sarosiek, K.A., Vo, T.T., Ryan, J.A., Tammareddi, A., Moore, V., Deng, J., Anderson, K.C., Richardson, P., Tai, Y.T., et al. (2011). *Science* 334, 1129–1133.

Oltersdorf, T., Elmore, S.W., Shoemaker, A.R., Armstrong, R.C., Augeri, D.J., Belli, B.A., Bruncko, M., Deckwerth, T.L., Dinges, J., Hajduk, P.J., et al. (2005). *Nature* 435, 677–681.

Roberts, A.W., Seymour, J.F., Brown, J.R., Wierda, W.G., Kipps, T.J., Khaw, S.L., Carney, D.A., He, S.Z., Huang, D.C., Xiong, H., et al. (2012). *J. Clin. Oncol.* 30, 488–496.

Souers, A.J., Levenson, J.D., Boghaert, E.R., Ackler, S.L., Catron, N.D., Chen, J., Dayton, B.D., Ding, H., Enschede, S.H., Fairbrother, W.J., et al. (2013). *Nat. Med.* Published online January 6, 2013. <http://dx.doi.org/10.1038/nm.3048>.

Vo, T.T., Ryan, J., Carrasco, R., Neuberg, D., Rossi, D.J., Stone, R.M., Deangelo, D.J., Frattini, M.G., and Letai, A. (2012). *Cell* 151, 344–355.

Molecular Archeology: Unearthing Androgen-Induced Structural Rearrangements in Prostate Cancer Genomes

Francesca Demichelis,^{1,6} Levi A. Garraway,^{2,3,4,5} and Mark A. Rubin^{7,8,9,*}

¹Centre for Integrative Biology, University of Trento, Povo, Trento, 38123, Italy

²Department of Medicine, Brigham and Women's Hospital, Harvard Medical School, Boston, MA 02115, USA

³The Broad Institute of Harvard and MIT, Cambridge, MA 02142, USA

⁴Department of Medical Oncology

⁵Center for Cancer Genome Discovery

Dana-Farber Cancer Institute, Boston, MA 02215, USA

⁶Institute for Computational Biomedicine, Department of Physiology and Biophysics

⁷Department of Pathology and Laboratory Medicine

⁸Brady Foundation Department of Urology

⁹Institute for Precision Medicine

Weill Cornell Medical College of Cornell University and New York Presbyterian Hospital, New York, NY 10065, USA

*Correspondence: rubinma@med.cornell.edu

<http://dx.doi.org/10.1016/j.ccr.2013.01.019>

In this issue of *Cancer Cell*, Weischenfeldt and colleagues report on the whole genome sequencing of 11 early-onset prostate cancers. Compared to elderly onset prostate cancer, these tumors demonstrate enrichment for androgen-driven structural rearrangements involving ETS family genes. This study confirms observations that prostate cancer manifests discrete genomic subclasses.

Prostate cancer remains the most common type of cancer and a frequent cause of cancer-related mortality in men worldwide. Although prostate cancer predominantly affects older men, a subset of prostate cancer arises in men below the age of 50. Early-onset cancers often display hereditary links to germline mutations; well-known examples include *BRCA2* mutations in breast and ovarian cancers and *p53* mutations in Li-Fraumeni syndrome. Among common solid tumors, prostate cancer has been shown to have the largest estimated effect of heritability (Lichtenstein et al., 2000). Despite suggestions that hereditary prostate cancer genes exist, most studies have failed to yield reproducible germline variants that account for early onset prostate cancer. Rare germline variants have been discovered, such as in *HOXB13*, but may only account for a small percentage of early-onset prostate cancer cases. No single germline variant accounts for a substantial proportion of prostate cancer.

In the search for a genetic basis for early-onset prostate cancer, Weischenfeldt et al. (2013) describe, in this issue of *Cancer Cell*, whole genome sequencing of 11 early-onset prostate cancer (median age 47 years) selected

from a German cohort. They compared their results to seven previously published whole genomes meeting their definition for elderly-onset prostate cancer (median age of 65 years) (Berger et al., 2011). A side-to-side evaluation revealed a statistically significant increase in somatic structural rearrangements (SRs) in general and balanced rearrangements in particular in the 11 early onset-prostate cancer tumors as compared to the elderly-onset prostate cancer tumors. Interestingly, 91% (10/11) early-onset prostate cancer harbored an ETS gene rearrangement involving either *ERG* (n = 9) or *ETV1* (n = 1), which is significantly higher than the estimated 50% for all prostate cancers (Rubin et al., 2011; Tomlins et al., 2005).

Androgen stimulation and genotoxic stress (e.g., radiation) have previously been shown to induce the *TMPRSS2-ERG* gene fusion, the most common prostate cancer ETS rearrangement (Mani et al., 2009). By exploiting a map of publicly available androgen receptor (AR) binding sites, Weischenfeldt et al. (2013) observed that the early-onset prostate cancer tumors exhibited SR break points situated nearer to AR binding sites than those in the seven elderly-onset prostate cancer tumors from Berger

et al. (2011). This finding raises the possibility that androgen stimulation preferentially induces certain types of SRs in early-onset prostate cancer, leading to a cascade of oncogenic molecular events such as recurrent ETS rearrangements. The authors conclude that early-onset prostate cancer may be more likely to harbor androgen-driven SRs, whereas elderly onset prostate cancers display a distinct rearrangement landscape.

The notion that androgen-triggered DNA damage might explain the majority of early-onset prostate cancer is certainly intriguing. However, comprehensive assessment of causal components should also account for how prostate cancer is often diagnosed. Today, most prostate cancer is detected through prostate-specific antigen (PSA) screening. Widespread screening has increased the detection of low risk cancers. In fact, recent U.S. and European screening studies have questioned if the benefits of PSA screening outweigh the attendant morbidities and costs. Relevant to the Weischenfeldt et al. (2013) study, prostate cancer detected by PSA screening may be diagnosed up to 15 years earlier than may have been the case without PSA screening. Thus, a 50-year-old man diagnosed with prostate cancer by PSA

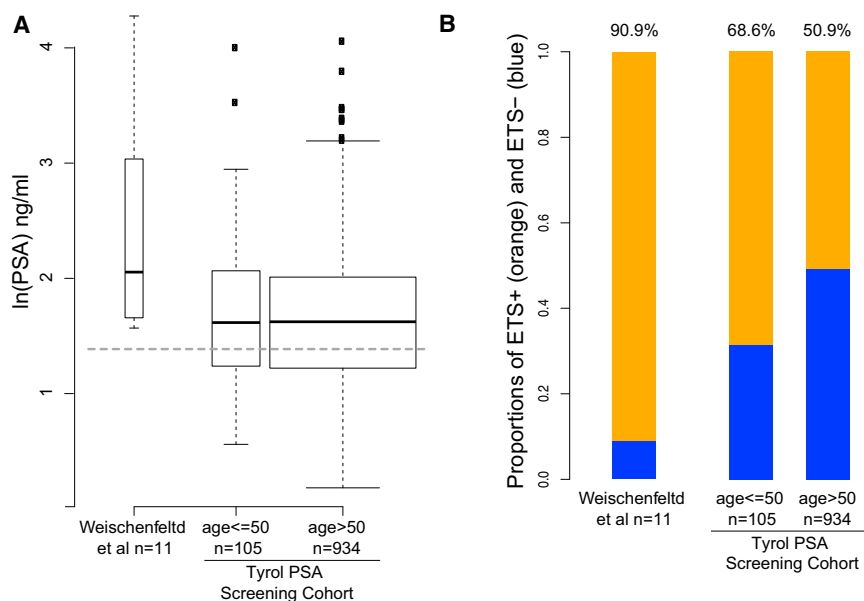


Figure 1. Comparison of PSA Levels and ETS Rearrangement Frequencies of the 11 Cases from the Weischenfeldt and Colleagues Study and Data from the Tyrol PSA Screening Population

(A) Significantly higher PSA levels were found in the Weischenfeldt et al. (2013) cases than observed in the Tyrol PSA screening population of men with prostate cancer. The width of the boxes reflects differences in sample sizes: the dotted horizontal gray line corresponds to 4 ng/ml, and age indicates years.

(B) The percentage of ETS rearrangement positive prostate cancer in the 11 whole genomes from the Weischenfeldt et al. (2013) study is shown compared to men from the Tyrol screening cohort stratified by age. The numbers at the top of each bar indicates the percent of cases that are ETS positive.

screening might not have presented clinically until he was 65 years old. In such a case, the “early onset” versus “elderly onset” comparison might represent a distinction without a difference.

PSA vagaries aside, results of the Weischenfeldt et al. (2013) study also suggest that the constellation of genomic alterations (i.e., increased somatic androgen-related SRs and ETS rearrangements) influence earlier clinical detection. We recently completed a population-based study determining *ERG* overexpression, used as a surrogate for *ERG* rearrangements, in 1,039 radical prostatectomy tumor samples from the Tyrol PSA screening cohort (Schaefer et al., 2013). This study showed that early *ERG* rearranged tumors manifest clinically at lower PSA levels, and their prevalence is age-dependent. Figure 1 shows the comparison of PSA levels and the *ETS/ERG* rearrangement frequencies of the 11 cases from the Weischenfeldt et al. (2013) study with the Tyrol PSA screening population, distinguishing between men of 50 years of age at diagnosis or younger versus patients above 50 years of age and using the cutoff

defined by Weischenfeldt et al. (2013). Their ten ETS rearrangement positive cases demonstrate significantly higher PSA levels than those observed in prostate cancer cases in the Tyrol PSA screening population. The higher PSA level, high tumor grade, and stage might therefore reflect a particularly virulent subset of prostate cancer identified from a larger population of men with early-onset disease diagnosed by PSA screening. The question of whether or not a similar virulent, high-PSA subset may also exist among elderly prostate cancer patients—and at what prevalence—will be an important follow-up question.

A corollary of the Weischenfeldt et al. (2013) study findings posits that SRs arising from androgen-driven DNA damage also give rise to the *TMPRSS2-ERG* (and other ETS) rearrangements. This important study extends previous work that ETS-rearranged prostate cancer comprises a distinct molecular subclass. The *TMPRSS2-ERG* rearrangement can be observed in the prostate cancer precursor lesion (Perner et al., 2006) and is associated with distinct

somatic copy number aberrations (Demicelis et al., 2009). *TMPRSS2* is highly androgen regulated and drives *ERG* expression in the fusion gene. Berger et al. (2011) noted that *ERG*-rearrangement positive cases contained somatic SR breakpoints located near AR binding sites, whereas ETS-negative prostate cancer harbored SR breakpoints significantly distant from AR binding sites. They also observed that these SRs in *ERG* rearranged tumors could exist as interwoven chains that involved cancer related genes, suggesting a possible selective growth advantage (Berger et al., 2011). More recent work suggests that *ERG* overexpression may mediate three-dimensional DNA conformational changes through active transcription, putatively facilitating SRs under genotoxic conditions (Rickman et al., 2012). The Weischenfeldt et al. (2013) study now suggests an alternative scenario where androgenic events drive SRs, which leads to ETS rearrangements. This would imply the early-onset “gene” might really represent a susceptibility to androgenic DNA damage.

Disentangling the effect of cancer screening from age may prove challenging for the foreseeable future, given widespread PSA testing. Regardless, Weischenfeldt et al. (2013) confirm observations that prostate cancer manifests discrete genomic subclasses. The telltale molecular fingerprints are emerging through advances in whole genome sequencing that encompass important non-coding regulatory regions not captured by exome sequencing and innovations in large data analysis. Future studies should help elucidate the genomic events predisposing to androgen-driven SR breakpoints, genomic events that may trigger a cascade of prostate cancer alterations including the recurrent *TMPRSS2-ERG* rearrangements, and the development of balanced chained loop rearrangements. One can imagine that germline polymorphisms (i.e., SNPs or copy number variants) could deleteriously hinder DNA repair mechanisms, thus phenocopying *BRCA2* deficiency. Epigenetic or environmental effects may play some modifying role in this process. Knowledge of somatic SRs may also have important implications with regards to diagnosis and response to targeted treatment after disease progression. Overall, the

Weischenfeldt et al. (2013) study extends a growing paradigm regarding the links between complex rearrangements and prostate carcinogenesis, while also considering the age dimension as a possible player in the spectrum of clinical features that contribute to disease biology.

ACKNOWLEDGMENTS

Work cited in this article was supported by the Starr Cancer Consortium (to M.A.R., F.D., and L.A.G.), the Prostate Cancer Foundation (to M.A.R.), US Department of Defense Synergy awards (PC101020 to F.D., L.A.G., and M.A.R.), and the Early Detection Research Network (U01CA111275 and NCI EDRN to F.D. and M.A.R.). L.A.G. is an equity holder and consultant in Foundation Medicine, a consultant to Novartis and Millenium/Takeda, and a recipient of a grant from Novartis. F.D. and M.A.R. are listed as co-inventors of the patent on the detection of gene fusions in prostate cancer, filed by The University of Michigan and the Brigham and Women's

Hospital. The diagnostic field of use for ETS gene fusions has been licensed to Hologic Gen-Probe. The authors would like to thank Helmut A. Klocker and Scott M. Tomlins for their thoughtful comments.

REFERENCES

Berger, M.F., Lawrence, M.S., Demichelis, F., Drier, Y., Cibulskis, K., Sivachenko, A.Y., Sboner, A., Esquivela, R., Pflueger, D., Sougnez, C., et al. (2011). *Nature* 470, 214–220.

Demichelis, F., Setlur, S.R., Beroukhi, R., Perner, S., Korbel, J.O., Lafargue, C.J., Pflueger, D., Pina, C., Hofer, M.D., Sboner, A., et al. (2009). *Genes Chromosomes Cancer* 48, 366–380.

Lichtenstein, P., Holm, N.V., Verkasalo, P.K., Iliadou, A., Kaprio, J., Koskenvuo, M., Pukkala, E., Skythe, A., and Hemminki, K. (2000). *N. Engl. J. Med.* 343, 78–85.

Mani, R.S., Tomlins, S.A., Callahan, K., Ghosh, A., Nyati, M.K., Varambally, S., Palanisamy, N., and Chinnaiyan, A.M. (2009). *Science* 326, 1230.

Perner, S., Demichelis, F., Beroukhi, R., Schmidt, F.H., Mosquera, J.M., Setlur, S., Tchinda, J., Tomlins, S.A., Hofer, M.D., Pienta, K.G., et al. (2006). *Cancer Res.* 66, 8337–8341.

Rickman, D.S., Soong, T.D., Moss, B., Mosquera, J.M., Dlabal, J., Terry, S., MacDonald, T.Y., Tripodi, J., Bunting, K., Najfeld, V., et al. (2012). *Proc. Natl. Acad. Sci. USA* 109, 9083–9088.

Rubin, M.A., Maher, C.A., and Chinnaiyan, A.M. (2011). *J. Clin. Oncol.* 29, 3659–3668.

Schaefer, G., Mosquera, J.M., Ramoner, R., Park, K., Romanel, A., Steiner, E., Hominger, W., Bektic, J., Ladurner-Rennau, M., Rubin, M.A., et al. (2013). *Prostate Cancer Prostatic Dis.* Published online February 5, 2013. <http://dx.doi.org/10.1038/pcan.2013.4>.

Tomlins, S.A., Rhodes, D.R., Perner, S., Dhanasekaran, S.M., Mehra, R., Sun, X.W., Varambally, S., Cao, X., Tchinda, J., Kuefer, R., et al. (2005). *Science* 310, 644–648.

Weischenfeldt, J., Simon, R., Feuerbach, L., Schlangen, K., Weichenhan, D., Minner, S., Wuttig, D., and Warnatz, H.-J. (2013). *Cancer Cell* 23, this issue, 159–170.

Growth Factor Receptors Define Cancer Hierarchies

Monica Venere,¹ Justin D. Lathia,^{2,3} and Jeremy N. Rich^{1,3,*}

¹Department of Stem Cell Biology and Regenerative Medicine

²Department of Cellular and Molecular Medicine

Lerner Research Institute, Cleveland Clinic Foundation, Cleveland, OH 44195, USA

³Department of Molecular Medicine, Cleveland Clinic Lerner College of Medicine at Case Western Reserve University, Cleveland, OH 44106, USA

*Correspondence: richj@ccf.org

<http://dx.doi.org/10.1016/j.ccr.2013.01.020>

Normal and neoplastic tissues display cellular hierarchies that integrate extracellular cues to maintain tissue function through bidirectional signals mediated via cell surface proteins. Two papers in *Cancer Cell*, one in this issue (Day and colleagues) and one in a recent issue (Binda and colleagues), describe how Eph receptor tyrosine kinases critically define and regulate the growth of cancer stem cells.

Tumors display cellular heterogeneity through the integration of multiple supportive cell types—vasculature, stroma, and immune components—as well as diversity within the neoplastic compartment derived from genetic and epigenetic variability. Cancers co-opt transcriptional programs normally active in development and wound responses, processes in which stem and progenitor cells contribute, so it is not surprising that cancers display characteristics of stem and progenitor cells.

Recent data from human and murine models support the presence of cellular

hierarchies in some advanced cancers with cancer stem cells (CSC) at the apex (Chen et al., 2012; Singh et al., 2004). The CSC field currently lacks a coherent set of criteria to define these cells. Many reports mistakenly hold that CSCs simply represent cells that form spheres in culture and tumors upon transplantation (i.e., tumor initiating cells). Rather, CSCs also mimic normal stem cells to create a dysfunctional cellular hierarchy with non-tumorigenic cells derived from the self-renewing CSC. To fulfill this feature, the CSC hypothesis needs to employ strategies to prospectively segregate

tumorigenic and non-tumorigenic cells or perform functional lineage tracing studies. A critical aspect of these studies is the requirement to identify and separate discrete populations and perform functional analyses. In response, researchers have defined a number of surface molecules that are preferentially expressed by CSCs and can be interrogated in live cells. At first blush, the increasing number of these markers may engender skepticism as to the validity of the CSC hypothesis, but this viewpoint is derived from our desire to impose simplicity on an inherently complex and dynamic system. First,